Le rôle des éléments d'alliage sur la passivation des alliages Ni-Cr-Mo

Xuejie Li

▶ **To cite this version:**

Xuejie Li. Le rôle des éléments d'alliage sur la passivation des alliages Ni-Cr-Mo. Chimie analytique. Université Paris sciences et lettres, 2020. Français. NNT : 2020UPSLC022 . tel-03553307

HAL Id: tel-03553307
https://pastel.hal.science/tel-03553307

Submitted on 2 Feb 2022

HAL is a multi-disciplinary open access archive for the deposit and dissemination of scientific research documents, whether they are published or not. The documents may come from teaching and research institutions in France or abroad, or from public or private research centers.

L'archive ouverte pluridisciplinaire **HAL**, est destinée au dépôt et à la diffusion de documents scientifiques de niveau recherche, publiés ou non, émanant des établissements d'enseignement et de recherche français ou étrangers, des laboratoires publics ou privés.

PSL UNIVERSITÉ PARIS

THÈSE DE DOCTORAT
DE L'UNIVERSITÉ PSL

Préparée à Chimie ParisTech

Le rôle des éléments d'alliage sur la passivation des alliages Ni-Cr-Mo

The role of alloying elements on the passivation of Ni-Cr-Mo alloys

Soutenue par
Xuejie LI
Le 13 Novembre 2020

Ecole doctorale n° 388
Chimie Physique et Chimie Analytique de Paris-Centre

Spécialité
Chimie Analytique

Composition du jury :

Vincent, VIVIER Directeur de Recherche, Sorbonne Universités	*Président*
Nick, BIRBILIS Professeur, Australian National University	*Rapporteur*
Michael, ROHWERDER Privatdozent, Max-Planck-Institut für Eisenforschung GmbH	*Rapporteur*
Judith, MONNIER Maître de Conférences, Université Paris-Est Créteil	*Examinatrice*
Kevin, OGLE Professeur, Chimie ParisTech	*Directeur de thèse*

Chimie Paris ParisTech | PSL

这个世界会好吗?

伯特兰·亚瑟·威廉·罗素（1872－1970）
梁漱溟（1893－1988）
李志（1978－）

Has man a future?

Bertrand Arthur William Russell (1872 – 1970)
Shuming Liang (1893 – 1988)
Zhi Li (1978 –)

LIST OF ACRONYMS

AES	Auger electron spectroscopy
AESEC	atomic emission spectroelectrochemistry
AFO	air-formed oxide
AP	anodic passivation
B.E.	binding energy
BCC	body-centered cubic
CA	cathodic activation
CCD	charge-coupled device
CCT	critical crevice temperatures
C.E.	counter electrode
CID	charge injection device
CR	corrosion rate
CTD	charge-transfer device
DCP	direct current plasma
EIS	electrochemical impedance spectroscopy
FCC	face-centered-cubic
GD-OES	glow discharge optical emission spectroscopy
GDP	gross domestic product
HCP	hexagonal closed-pack
HEA	high entropy alloy
HER	hydrogen evolution reaction
ICP	inductively coupled plasma
ICP-AES	inductively coupled plasma atomic emission spectroscopy
ICP-MS	inductively coupled plasma mass spectroscopy
K.E.	kinetic energy
LSV	linear sweep voltammetry
MIP	microwave-induced plasma
Mono	monochromator
NHE	normal hydrogen electrode
OCP	open-circuit potential
ORR	oxygen reduction reaction
PD-GS-PD	potentiodynamic-galvanostatic-potentiodynamic
PDP	potential dynamic polarization
PMT	photomultiplier tube
Poly	polychromator
PREN	pitting resistance equivalent number
R.E.	reference electrode
RF	radio frequency

RTD	residence time distribution
SCC	stress corrosion cracking
SCE	saturated calomel electrode
SEM	scanning electron microscopy
SP	spontaneous passivation
STM	scanning tunneling microscopy
UHV	ultra-high vacuum
W.E.	working electrode
XPS	X-ray photoelectron spectroscopy
XRD	X-ray diffraction

LIST OF SYMBOLS

σ	standard deviation of the ICP-OES background signal
A	reaction surface
c	speed of light
C_M	instantaneous emission intensity for element M
E	electrical potential
E°	standard electrode potential
E_{ap}	applied potential
E_{corr}	corrosion potential
$E_{j=0}$	potential where $i_a = i_c$
E_{oc}	open circuit potential
E_r	repassivation potential
F	Faraday constant
f	flow rate of the electrolyte in the flow cell
h	Planck constant
h(t)	residence time distribution function
i_a	anodic current density
i_c	cathodic current density
i_{crit}	critical current density
I_λ	elemental intensity signal
I_λ°	background intensity signal
j_a	anodic current density
j_{BG}	calculated background current density caused by the RTD of the flow cell
j_c	cathodic current density
j_e	electrical current density
j_e^*	convoluted electrical current density
j_M	equivalent elemental current density
j'_M	normalized elemental current
j_{M°	assumed congruent element current for M
j_{ox}	partial current due to oxide formation
j_Δ	mass balance equation: $j_e^* - j_\Sigma$
$j_{\Delta M}$	excess element current for M
j_Σ, Σj_M	sum of elemental current densities
m_M	molar mass of an element
n	number of exchanged electrons in the oxidation reaction
Q_M	total quantity of dissolved M
X_M	mass fraction of element M
z	oxidation state of an element

α	sensitivity factor for a measured element determined from the calibration standards of the ICP-OES
β	time constant defined for h(t)
Θ_M	total quantity of surface excess M
$\varkappa_\lambda$	sensitivity factor for a given wavelength
ν_M	elemental dissolution rate
ν'_M	normalized dissolution rate for M
ν_{M°	assumed congruent dissolution rate for M
τ	experimentally determined RTD parameter
χ_M	molar fraction of element M

RESUME

L'ORIGINE ET LES OBJECTIFS DE LA THESE

La corrosion fait généralement référence à la réaction chimique ou électrochimique entre un matériau et son environnement qui produit une détérioration du matériau et de ses propriétés[1]. Le coût global de la corrosion estimé par NACE international[2] est d'environ 2,5 billions de dollars américains. Cela équivaut à 3,4% du produit intérieur brut (PIB) mondial, ce qui fait de la lutte contre la corrosion une entreprise essentielle. La corrosion peut avoir lieu dans des environnements liquides et gazeux pour divers matériaux. Comme cette thèse se concentre sur la passivation des alliages liés au Ni dans des solutions aqueuses, la discussion suivante sera limitée à la corrosion dans les solutions aqueuses.

Le contrôle de la corrosion peut être réalisé par de nombreuses méthodes différentes, notamment en utilisant des alliages résistants à la corrosion, des revêtements, l'ajout d'inhibiteurs, l'application d'une protection cathodique, etc. Le moyen le plus direct est peut-être de concevoir directement un alliage résistant à la corrosion et, dans certains cas, l'utilisation d'alliages résistant à la corrosion est la seule solution technique pratique. Les alliages Fe-Cr, appelés aciers inoxydables, sont les plus courants. Cependant, les alliages Ni-Cr sont peuvent également être trouvés dans une grande variété d'applications, en particulier pour les hautes températures et des environnements extrêmes, comme les industries chimiques et pétrochimiques, les usines de pâtes et papiers, des équipements de contrôle de la pollution, etc.[3] en raison de leur extraordinaire résistance à la corrosion à haute température et aqueuse.

L'effort pour développer d'excellents alliages résistant à la corrosion ne s'est pas relâché. Au cours des dernières décennies, les alliages à haute entropie (HEA) ont fait l'objet d'une attention considérable en raison de leurs propriétés uniques. Les HEA sont généralement définis comme des alliages contenant au moins cinq éléments principaux en pourcentage atomique égal ou presque égal[4], tout en conservant une ou plusieurs phases de solution solide. La capacité à accueillir plusieurs éléments majeurs dans des phases simples de solution solide fait des HEA des candidats prometteurs pour obtenir une résistance supérieure à la corrosion.

Tous ces alliages résistants à la corrosion ont le même mécanisme de résistance à la corrosion, qui se fait par la formation d'un film d'oxyde nanométrique en surface, appelé film passif. Ce film forme une barrière entravante l'échange d'électrons et d'ions entre le métal et l'environnement. Le processus de formation de ce film est appelé passivation. Des recherches considérables ont été menées pour étudier les mécanismes de passivation ainsi que les propriétés du film passif avec une grande variété de techniques[5-12]. Certaines des questions les plus fréquentes concernent la décomposition du film passif[13-19], l'influence des éléments d'alliage sur la passivation[20-27], l'épaisseur, la composition, la structure du film passif[12, 28-33], et les propriétés électroniques et mécaniques du film passif[34-37]. De toutes ces études, on peut soutenir que la compréhension de l'influence des éléments d'alliage sur la passivation a le potentiel de percée le plus significatif pour la conception de nouveaux alliages. Par exemple, l'enrichissement en Cr en surface est responsable de la passivation de la plupart des alliages résistants à la corrosion[38-47]. L'ajout de Mo améliore considérablement la résistance des alliages à la corrosion localisée[13, 24, 26, 27, 48-63]. Cependant, de nombreuses questions restent floues concernant le rôle des éléments d'alliage sur la passivation, comme le mécanisme spécifique de la façon dont Mo prend effet.

Le rôle des différents éléments d'alliage devient encore plus critique à mesure que l'accent est mis sur les HEA, qui sont également des objectifs à étudier dans cette thèse. Le concept d'élément principal n'est plus applicable aux HEA et, par conséquent, la stratégie conventionnelle d'essais et d'erreurs est trop lente à développer de nouvelles HEA. Une meilleure approche consiste à clarifier le rôle des éléments individuels, puis à concevoir les alliages en conséquence. En ce qui concerne les HEA résistants à la corrosion, cela soulignerait la nécessité de comprendre la contribution des éléments individuels à la passivité.

Des études antérieures sur le rôle des éléments d'alliage pour la passivation ont été principalement réalisées par des méthodes électrochimiques conventionnelles combinant des techniques sensibles à la surface ex situ, telles que la x-ray photoelectron spectroscopy (XPS)[10, 12, 42, 64-72]. L'influence des éléments d'alliage sur le comportement électrochimique tel que la passivation peut être déterminée par des méthodes électrochimiques conventionnelles. Le film passif résultant peut être caractérisé par une

analyse de surface ex situ. Cependant, les expériences électrochimiques ne donnent que le comportement global de l'alliage sans mesure directe de la contribution des éléments individuels. De plus, l'analyse de surface est principalement effectuée ex situ. Il n'y a pas d'accès aux informations cinétiques concernant la formation du film. De plus, il existe un risque d'oxydation de la surface pendant le processus de transfert d'échantillon pour conduire XPS, ce qui rend la surface de l'échantillon non représentative de la façon dont elle était dans l'électrolyte.

Cette thèse tente de contribuer à la compréhension de certains éléments d'alliage lors de la passivation d'une série d'alliages à base de Ni de complexité variable, allant du Ni pur au Ni contenant des alliages à haute entropie, y compris le Ni-Cr binaire synthétique et le Ni-Cr-Mo ternaire alliages et alliages Ni commerciaux. Comment des éléments spécifiques influencent le comportement de passivation et comment ils interagissent les uns avec les autres sont les principaux objectifs à étudier. À cette fin, atomic emission spectroelectrochemistry (AESEC) a été utilisée en raison de sa capacité à mesurer les taux de dissolution élémentaire in situ tout en appliquant l'électrochimie. Les informations cinétiques de formation et de dissolution du film ont été obtenues en appliquant un bilan massique et un bilan charge-masse au profil de dissolution AESEC. L'épaisseur du film a été calculée par bilan massique et bilan masse-charge en tenant compte de l'enrichissement d'éléments spécifiques par rapport au Ni. Les états d'oxydation des éléments ont été vérifiés par XPS avec des échantillons préparés dans une boîte à gants sans oxygène et transférés soigneusement avec une boîte d'échantillons sous vide.

LA STRUCTURE DE LA THESE

Cette thèse commence par trois chapitres d'introduction (**chapitre 1, chapitre 2 et chapitre 3**). Dans le **chapitre 1** (le présent chapitre), l'origine et le but du travail de thèse et la structure de la thèse ont été présentés. Dans le **chapitre 2**, les connaissances actuelles (enregistrées dans la littérature) sur le sujet étudié dans cette thèse ont été examinées. Il peut être divisé en deux parties principales : 1) la passivation des alliages Ni-Cr-Mo, et 2) le rôle du Mo sur la passivation. Des questions essentielles non résolues ont été soulevées. Le **chapitre 3** décrit les méthodes expérimentales utilisées dans les chapitres sur les résultats. En tant que technique principale utilisée dans cette thèse, l'AESEC a

d'abord été présentée en détail. Ensuite, quelques techniques de caractérisation ex situ ont été brièvement introduites.

Après les chapitres d'introduction se trouvent cinq chapitres sur les résultats (**chapitre 4-8**). Un diagramme schématique (**Fig. 1**) donne les principaux résultats obtenus à partir de chaque chapitre. L'idée générale utilisée pour étudier la passivation des alliages Ni-Cr-Mo est d'analyser la libération d'ions pendant le processus électrochimique, comme le montre la **Fig. 1**. La dissolution élémentaire taux, ν_M, le peignage avec du bilan massique, peut être utilisée pour calculer l'accumulation de la surface élémentaire, Θ_M. En supposant que l'état d'oxydation de l'élément détecté, ν_M peut être converti en courant élémentaire, j_M. En comparant j_M avec le courant extérieur, j_e, enregistré par le potentiostat, le rendement faradique peut être obtenu.

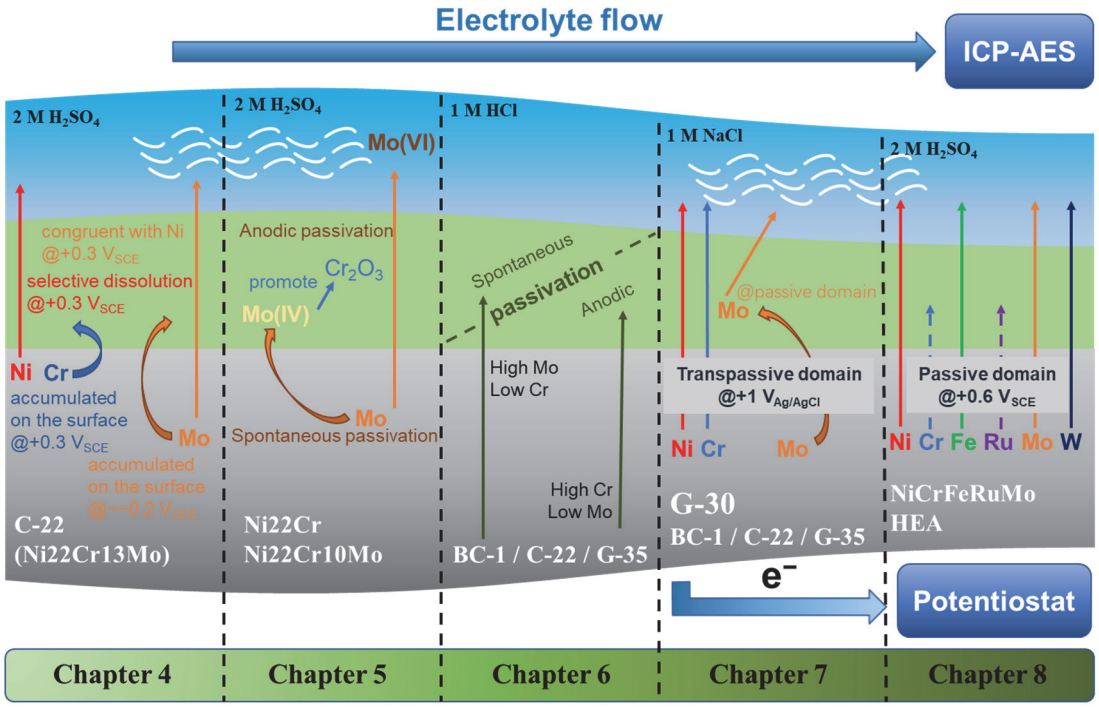

Fig. 1 Schéma montrant les principaux résultats obtenus du **chapitre de 4-8**.

En utilisant la méthodologie mentionnée ci-dessus, la mesure directe de la cinétique de passivation peut être réalisée avec une résolution élémentaire, donnant ainsi de nouvelles perspectives sur le mécanisme de passivation.

Au **chapitre 4**, le comportement de passivation d'un alliage commercial C-22 Ni-

Cr-Mo a été étudié par l'AESEC. Une cinétique de dissolution élément-résolue a été observée in situ pendant l'activation cathodique, la passivation spontanée et la passivation anodique.

La courbe de polarisation résolue par élément pour l'alliage C-22 représentée sur la **Fig. 2A** donne le comportement élémentaire général de l'alliage dans une large plage de potentiel. Il est intéressant de mentionner deux domaines dans lesquels une dissolution sélective a été observée. Au cours du domaine de transition actif-passif, Mo s'est accumulé à la surface tandis que d'autres éléments se sont dissous ‹ Bnanière presque congruente. Dans le domaine passif, Mo a montré un pic de dissolution, tandis que d'autres éléments se sont dissous de manière congruente. Une expérience potentiostatique à 0,3 V_{SCE} (**Fig. 2B**) a prouvé que Cr s'est accumulé sur la surface pendant la passivation, tandis que Mo a montré une dissolution excessive par rapport au Ni. Le rendement faradique de passivation a également été obtenu en comparant la somme du courant élémentaire, j_M, et du courant externe alambiqué, j_e^*. L'activation cathodique (**Fig. 2C**) a démontré la dissolution du film passif sous une polarisation cathodique à −0,8 V_{SCE}. Lors de la libération du potentiel, une passivation spontanée a été observée avec les accumulations de Mo et Cr.

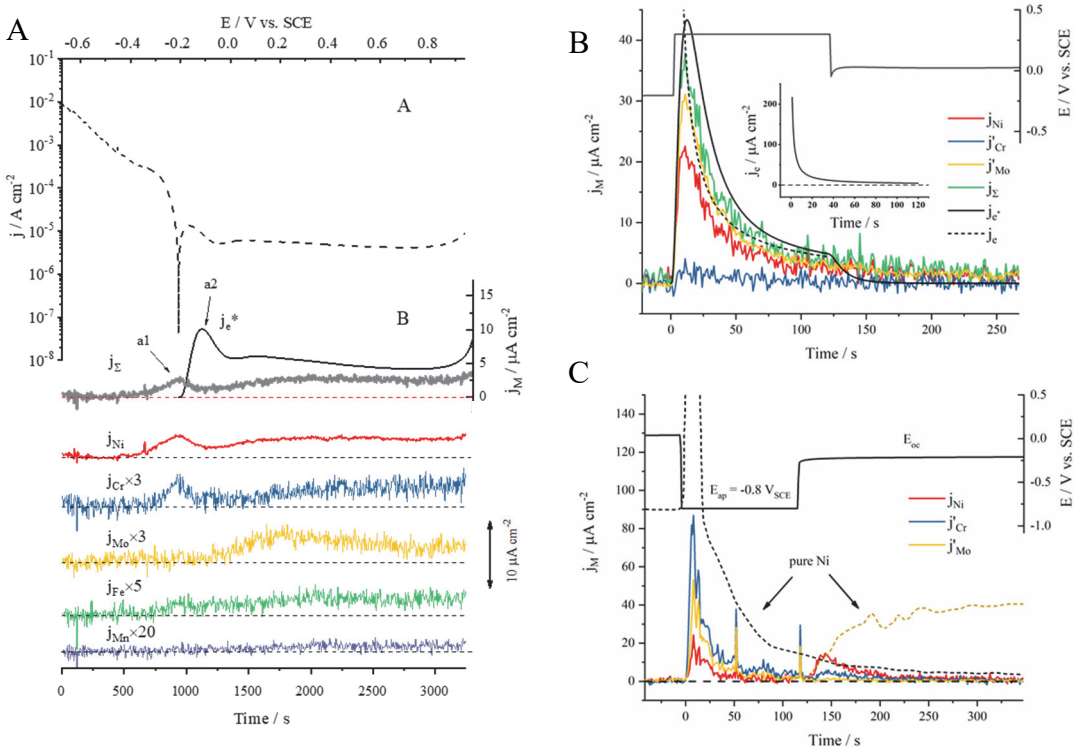

Fig. 2 La courbe de polarisation résolue par élément (A), la passivation anodique (B) et l'activation cathodique et la passivation spontanée (C) pour l'alliage Ni-Cr-Mo commercial C-22 en 2 M H_2SO_4 aéré à une vitesse de balayage de 0,5 mV/s.

Le **chapitre 4** a établi un protocole pour étudier la passivation spontanée et la passivation anodique des alliages Ni-Cr-Mo. Ce protocole a été appliqué au **chapitre 5** suivant, dans lequel les alliages synthétiques Ni22Cr et Ni22Cr10Mo (en poids%) ont été étudiés par AESEC en combinaison avec XPS. L'électrochimie du Ni et du Mo purs a également été examinée pour avoir une compréhension globale du rôle du Mo, **Fig. 3**. Il est clair que dans le domaine de potentiel A1, dissolution de Mo élémentaire était inférieure à la limite de détection of AESEC tandis que la densité de courant externe est d'environ 0,1 mA cm^{-2}, indiquant la formation d'oxydes de Mo insolubles. Au même domaine potentiel, Ni avait un pic actif. Dans le domaine potentiel A 2 où Cr est généralement considéré comme passif, Mo avait un comportement transpassif. Les résultats de XPS à différentes étapes avec dans les expériences de passivation spontanée et de passivation anodique de l'alliage Ni-Cr-Mo ont confirmé que le Mo insoluble peut être attribué à Mo(IV) et la dissolution de Mo en Mo(VI).

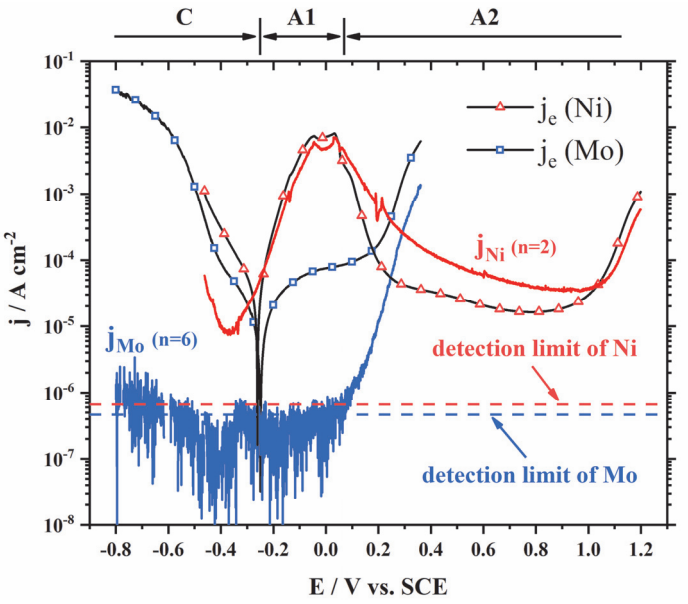

Fig. 3 Les courbes de polarisation résolues élémentaires de Ni et Mo purs dans 2 M H_2SO_4. Les données Ni sont reproduites à partir de la référence[45].

Dans le **chapitre 6**, l'objet de l'étude a été étendue à une série d'alliages Ni commerciaux avec différentes combinaisons de teneur en Cr et Mo dans la solution de HCl à 75 °C. L'utilisation de la solution de HCl était de mimique un peu l'environnement de la corrosion caverneuse. Les alliages utilisés étaient BC-1 (Cr bas et Mo élevé), C-22 (Cr

et Mo moyens) et G-35 (Cr élevé et Mo faible). La passivation spontanée et la passivation anodique de ces alliages ont été étudiées par AESEC en combinaison avec XPS.

Les courbes de polarisation résolues par élément de la **Fig. 4** montrent le comportement élémentaire pour BC-1 (A), C-22 (B) et G-35 (C). L'influence des éléments d'alliage sur le comportement à la corrosion de l'alliage a été illustrée. L'alliage BC-1 avec la teneur en Mo la plus élevée n'avait pas de pic actif dans le domaine de transition actif-passif, tandis que les alliages C-22 et G-35 avaient des pics de dissolution évidents. La dissolution au cours du domaine passif a été décidée par la teneur en Cr, indiquée par l'alliage avec la dissolution la plus faible étant le G-35.

Des expériences de passivation spontanée ont montré que l'alliage BC-1 pouvait rapidement établir un état passif stable à partir d'une surface active. Ce processus a pris plus de temps pour le C-22 que pour le BC-1, tandis que pour le G-35, aucun état passif stable n'a pu être établi, indiquant le rôle important du Mo pour la passivation spontanée. La passivation anodique a entraîné la dissolution excessive de Mo et l'accumulation de Cr. Mo a été identifié comme Mo(IV) pour la passivation spontanée et Mo(VI) pour la passivation anodique, a confirmé la théorie proposée au **chapitre 4**.

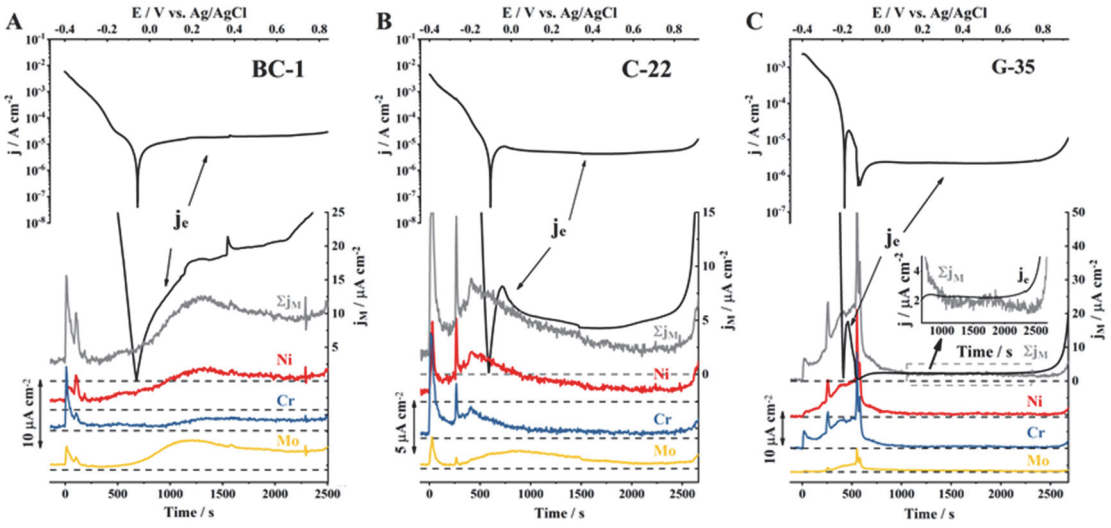

Fig. 4 Les courbes de polarisation résolues par élément de BC-1 (A), C-22 (B) et G-35 (C) dans du 1 M HCl aéré à la vitesse de balayage de 0,5 mV/s à 75 ° C.

Au **chapitre 7**, l'accumulation de Mo pendant la dissolution transpassive a été

observée pour quatre alliages de Ni commerciaux. Un Mo accumulé se dissoudrait partiellement lors de la repassivation dans le domaine passif. Parmi ces quatre alliages, l'alliage G-30 présentait l'accumulation la plus importante de Mo. Le Mo accumulé et ensuite dissous ont été quantifiés et comparés, **Fig. 5**. On montre que le Mo accumulé ne s'est pas complètement dissous lors de la repassivation. Ce phénomène était associé au changement du pH local en milieu acide lors de la transpassivation, dû à l'hydrolyse des cations métalliques. L'accumulation importante Mo pour l'alliage G-30 a été attribuée à sa teneur élevée en Fe, en tant que Fe serait pourrit plus rapidement et avec plus d'eau par rapport à Ni, conduisant ainsi à un pH inférieur.

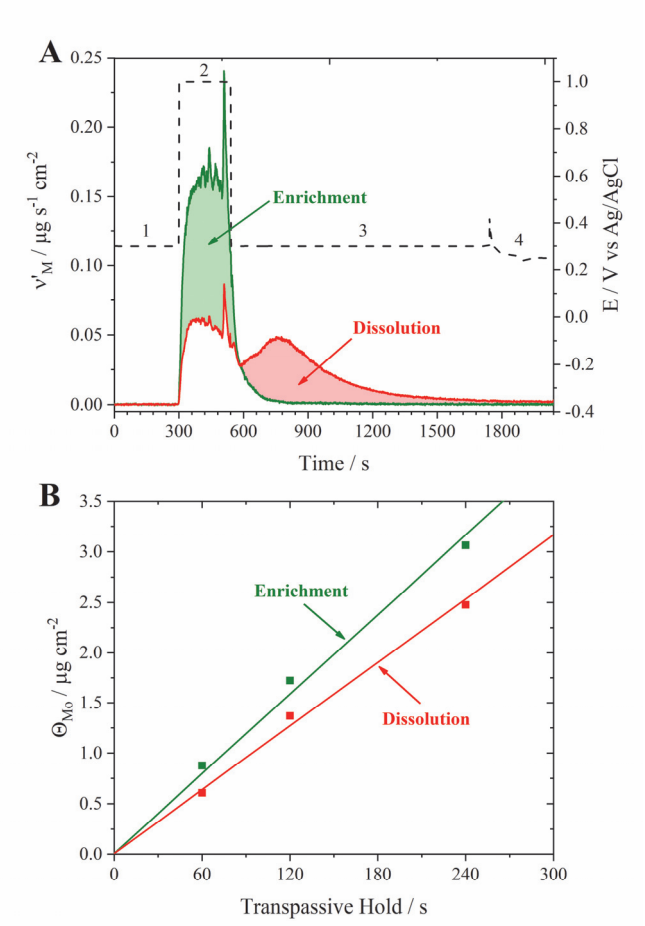

Fig. 5 Comparaison de l'accumulation et de la dissolution des espèces Mo pendant la dissolution transpassive et la repassivation de l'alliage G-30, respectivement. (A) représentation graphique des zones considérées comme accumulation / dissolution d'espèces de molybdène. (B) Comparaison de l'accumulation et de la dissolution en fonction du temps polarisé dans la région transpassive.

La passivation d'un nouveau NiCrFeRuMoW HEA a été étudiée au **chapitre 8**. Le HEA a montré une excellente résistance à la corrosion, sans dissolution élémentaire active détectée au cours de l'expérience de polarisation dynamique potentielle AESEC. Des accumulations de surface de Cr et Ru ont été observées pendant la passivation anodique à 0,6 V_{SCE}, tandis que l'activation cathodique de l'oxyde formé dans l'air n'a montré aucun

enrichissement en Ru. La passivation spontanée du HEA était différente de celle observée pour l'alliage Ni-Cr-Mo. La surface était inerte (indiquée par aucune dissolution détectable) après l'activation cathodique, pendant laquelle le film passif d'origine a été retiré. Le pic de dissolution s'est produit environ 300 s après avoir montré l'excès de dissolution de Ni, Fe et Mo et l'accumulation de Cr et Ru, **Fig. 6**.

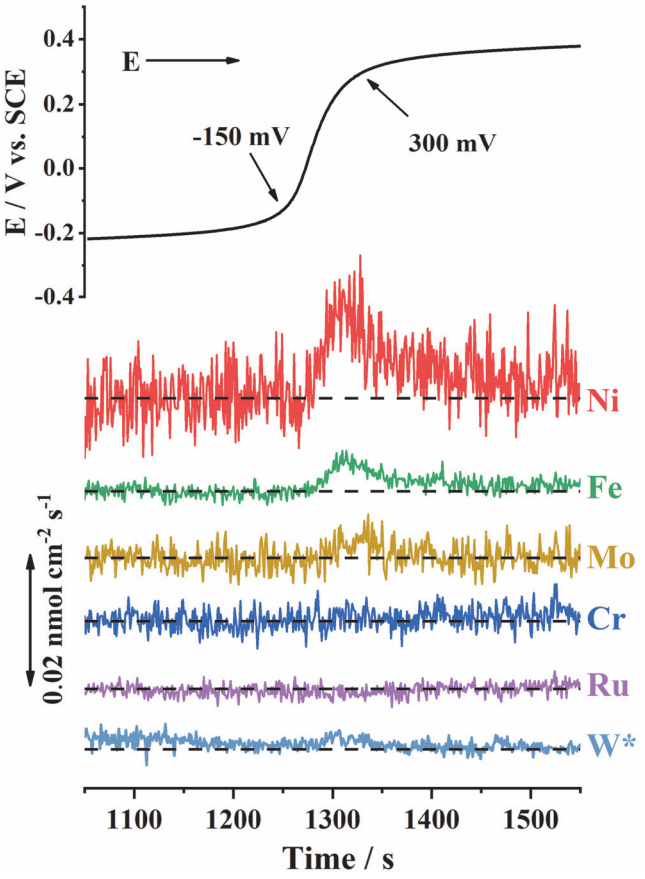

Fig. 6 Taux de dissolution élémentaire lors de la passivation spontanée en circuit ouvert après activation cathodique (−1,0 V_{SCE}). La ligne pointillée indique zéro. Les taux de dissolution de Cr, Fe, Ru, Mo et W sont compensés.

*W a été mesuré dans une expérience distincte.

En fin de compte, le **chapitre 9** donne la conclusion générale résumée de tous les chapitres sur les résultats. De nouvelles perspectives sur le rôle de Mo et le phénomène de passivation spontanée ont été proposées. Les perspectives issues de cette thèse ont également été présentées au **chapitre 9**.

Le mécanisme de Mo en passivation pourrait être résumé un de potentiel dépendant et dépendante du pH dynamique d'accumulation et de dissolution. Lorsque la surface est activée, la dissolution peut être entravée par la formation d'insolubles Mo(IV) oxyde et de l'oxyde de Cr(III) formée ultérieurement, représenté sur la **chapitres 4, 5 et 6**

à la fois pour l'acide sulfurique et l'acide chlorhydrate. Lorsque la surface est passivée, Mo(IV) serait oxydé en Mo(VI), partiellement dissoudre. De même, la solubilité de Mo(VI) espèce peut être influencée par le pH. Dans le domaine de pH faible, la diminution de la solubilité provoque le dépôt de Mo(VI) espèces sur la surface, comme le montre le **chapitre 7**. La repassivation a entraîné une augmentation du pH, conduisant à la redissolution de l'espèce Mo (VI) déposée. Le rôle du Mo était plus compliqué dans la HEA, comme l'indiquent les résultats du **chapitre 8**.

TABLE OF CONTENTS

1. Introduction 1
- 1.1 The origin and objectives of the dissertation work 1
- 1.2 The structure of the dissertation 3
- 1.3 List of publications 5
  - 1.3.1 Full articles 5
  - 1.3.2 Article in preparation 6
  - 1.3.3 Oral presentation 6

2. State of the art 7
- 2.1 Ni alloys 7
- 2.2 High entropy alloys 10
- 2.3 Passivation of Ni alloys 11
  - 2.3.1 Polarization curve of passive alloy 11
  - 2.3.2 Passivity of binary Ni-Cr alloys 15
  - 2.3.3 Passivity of ternary Ni-Cr-Mo alloys 19
  - 2.3.4 Crevice corrosion of Ni-Cr-Mo alloys 20
- 2.4 The role of molybdenum 26
  - 2.4.1 The influence of Mo on the electrochemical behavior of alloys 26
  - 2.4.2 The influence of Mo on active dissolution 28
  - 2.4.3 The influence of Mo for passivation 29
  - 2.4.4 Mo in the passive film 31
  - 2.4.5 The influence of Mo on pitting corrosion 33
- 2.5 Summary 34

3. Experimentation 36
- 3.1 Atomic emission spectroelectrochemistry (AESEC) 36
  - 3.1.1 Overview 36
  - 3.1.2 The electrochemical flow cell 37
  - 3.1.3 ICP-AES 39
  - 3.1.4 Data treatment 49
- 3.2 Other techniques 50
  - 3.2.1 X-ray diffraction 50
  - 3.2.2 X-ray photoelectron spectroscopy 51

4. The passivation of Ni-Cr-Mo alloys: Time resolved surface accumulation and dissolution of Cr and Mo during passive-active cycles 53
- Abstract 53
- 4.1 Introduction 54
- 4.2 Experimental 55
  - 4.2.1 Materials 55
  - 4.2.2 Instrumentation 56
  - 4.2.3 Data treatment 57
- 4.3 Results 59
  - 4.3.1 Overview of electrochemical behavior 59
  - 4.3.2 Passivation at an applied potential 63
  - 4.3.3 Activation and spontaneous passivation at open circuit 65
  - 4.3.4 Elemental accumulations during active-passive cycles 67
- 4.4 Discussion 69
- 4.5 Conclusions 71

5. The contribution of Cr and Mo to the passivation of Ni22Cr and Ni22Cr10Mo

alloys in sulfuric acid 73
Abstract 73
5.1 Introduction 74
5.2 Experimental 75
5.2.1 Sample preparation 75
5.2.2 Atomic emission spectroelectrochemistry 76
5.2.3 Electrochemical setup 77
5.2.4 Data treatment 77
5.2.5 XPS characterization 79
5.3 Results 80
5.3.1 Overview of Electrochemical Behavior 80
5.3.2 Elemental electrochemistry of Ni22Cr and Ni22Cr10Mo 81
5.3.3 Electrochemistry of pure Mo and Ni 84
5.3.4 Passive film formation and dissolution 85
5.3.5 XPS characterization 91
5.4 Discussion 97
5.5 Conclusions 101
6. Investigating the role of Mo and Cr during the breakdown and repassivation of oxide films formed on Ni-based alloys in hydrochloric acid 103
Abstract 103
6.1 Introduction 104
6.2 Experimental 105
6.2.1 Materials 105
6.2.2 Electrochemical Methods 106
6.2.3 AESEC Measurements and Data Treatment 107
6.2.4 XPS measurements 110
6.3 Results and Discussion 111
6.3.1 Potentiodynamic Polarization Behavior 111
6.3.2 Potentiostatic Polarization Behavior 115
6.3.3 Surface Analysis 122
6.4 Conclusions 126
6.5 Supplementary Information 128
7. Molybdenum surface accumulation and release during transpassive dissolution of Ni-based alloys 129
Abstract 129
7.1 Introduction 130
7.2 Experimental 131
7.2.1 Materials 131
7.2.2 Electrochemical Measurements 132
7.2.3 AESEC Measurements and Data Treatment 133
7.3 Results 135
7.3.1 Cyclic polarization 135
7.3.2 Potentiostatic Polarization 138
7.3.3 Mo Accumulation 142
7.4 Discussion 145
7.5 Conclusions 148
8. Dissolution and Passivation of a Ni-Cr-Fe-Ru-Mo-W High Entropy Alloy by Elementally Resolved Electrochemistry 149
Abstract 149
8.1 Introduction 150

8.2 Experimentation 150
8.3 Results and discussion 151
8.4 Conclusions 157
9. Conclusions and perspectives 158
9.1 Enrichment of Cr during passivation 158
9.2 The role of Mo 158
9.2.1 Potential-dependent Mo enrichment and dissolution 159
9.2.2 Mo enrichment and dissolution during transpassive domain 160
9.3 Passivation of a novel NiCrFeRuMoW HEA 160
9.4 Perspectives 161
9.4.1 Mechanisms 161
9.4.2 The future of the AESEC technique 162
Appendix A. The effect of N on the passivation of the Cantor alloy investigated by elementalally resolved electrochemistry. 164
A1. Introduction 164
A2. Experimentation 165
A3. Results and discussion 165
A4. Conclusions 171
Reference 173

1. INTRODUCTION

1.1 THE ORIGIN AND OBJECTIVES OF THE DISSERTATION WORK

Corrosion generally refers to the chemical or electrochemical reaction between a material and its environment that produces a deterioration of the material and its properties[1]. The global cost of corrosion, estimated by NACE international[2], is approximately 2.5 trillion US dollars (2013). This is equivalent to 3.4% of the global gross domestic product (GDP), making corrosion control a critical endeavor.

Aqueous corrosion is the corrosion of a material in contact with an electrolyte or a humid atmosphere. Aqueous corrosion may be controlled by many different methods, including using corrosion-resistant alloys, coatings, adding inhibitors, applying cathodic protection, and so forth. Perhaps the most direct way is to design corrosion-resistant alloys directly, and in some cases, the use of corrosion-resistant alloys is the only practical engineering solution. Fe-Cr alloys, with the Cr content higher than 11 wt.% know as stainless steel, are the most common. However, Ni-Cr alloys may also be found in a wide variety of applications, especially for high temperatures and extreme environments, such as chemical and petrochemical industries, pulp and paper mills, pollution control equipment, etc.[3] due to their extraordinary resistance to high-temperature and aqueous corrosion[3].

The effort to develop excellent corrosion-resistant alloys has not slackened. In the last few decades, high entropy alloys (HEAs) have received considerable attention due to their unique properties. HEAs are generally defined as alloys that contain five or more principal elements in equal or near-equal atomic percent[4], while still keeping one or more solid solution phases. The ability to accommodate multiple major elements in simple solid solution phases makes HEAs promising candidates for achieving superior corrosion resistance.

All these corrosion-resistant alloys have a similar mechanism of resisting corrosion, which is by the formation of a nanometric oxide film on the surface, referred to as a passive film. This film forms a barrier hindering the exchange of electrons and ions between the

metal and the environment. The process of forming this film is called passivation. Considerable research has been carried out to investigate the mechanisms of passivation as well as the properties of the passive film with a wide variety of techniques[5-12]. Some of the more frequent questions concern the breakdown of the passive film[13-19], the influence of alloying elements on passivation[20-27], the thickness, the composition, the structure of the passive film[12, 28-33], and the electronic and mechanical properties of the passive film[34-37]. Of all these studies, arguably, understanding the influence of alloying elements on passivation has the most significant breakthrough potential for the design of new alloys. For example, enrichment of Cr on the surface is responsible for most corrosion-resistant alloys to achieve passivation[38-47]. The addition of Mo considerably improves alloys' resistance to localized corrosion[13, 24, 26, 27, 48-63]. However, many questions remain unclear regarding the role of alloying elements on passivation, such as the specific mechanism of how Mo takes effect.

The role of the different alloying elements becomes even more critical as the focus changes to HEAs, which are also investigated in this dissertation. The concept of a principal element is no longer applicable to the HEAs, and therefore the conventional trial and error strategy is too slow in developing new HEAs. A better approach is to clarify the role of individual elements, then design alloys accordingly. As regards the corrosion-resistant HEAs, this would emphasize the necessity of understanding the contribution of individual elements to passivity.

Previous studies on the role of alloying elements for passivation were mainly carried out by conventional electrochemical methods combining ex situ surface sensitive techniques, such as X-ray photoelectron spectroscopy (XPS)[10, 12, 42, 64-72]. The influence of alloying elements on the electrochemical behavior, such as passivation, can be determined by conventional electrochemical methods. The resulting passive film can be characterized by ex situ surface analysis. However, electrochemical experiments only give the alloy's overall behavior without a direct measurement of the contribution of individual elements. Moreover, surface analysis is mostly conducted ex situ. There is no access to the precise kinetic information as regards the film formation. Additionally, there is a risk of oxidizing the surface during the sample transfer process for conducting XPS, making the sample's surface not representative of how it was in the electrolyte.

This dissertation tries to contribute to the understanding of certain alloying elements on passivation of a series of Ni-based alloys with varying complexity, ranging from pure Ni to Ni containing high entropy alloys, including synthetic binary Ni-Cr and ternary Ni-Cr-Mo alloys, and commercial Ni alloys. How specific elements influence passivation behavior and how they interact with each other are the main objectives to be investigated. To this end, atomic emission spectroelectrochemistry (AESEC) was employed due to its ability to measure elemental dissolution rates in situ while applying electrochemistry. The kinetics of film formation and dissolution was obtained by applying mass-balance and charge-mass balance to the elemental dissolution results. Film thickness was calculated by mass-balance and charge-mass balance considering the accumulation of specific elements relative to Ni. The oxidation states of the elements were verified by XPS with samples prepared in an oxygen-free glove box and transferred carefully with a vacuum sample box.

1.2 THE STRUCTURE OF THE DISSERTATION

This dissertation begins with three introductory chapters (**chapter 1, chapter 2, and chapter 3**). In **chapter 1** (the present chapter), the origin and the purpose of the dissertation work and the structure of the dissertation are introduced. In **chapter 2**, the current knowledge (recorded through literature) about the subject studied in this dissertation is reviewed. It can be divided into two major parts: 1) the passivation of Ni-Cr-Mo alloys, and 2) the role of Mo on passivation. Essential questions that remain unsolved are raised. **Chapter 3** describes the experimental methods that were used in the results chapters. As a principal technique used in this dissertation, AESEC is introduced in detail firstly. Then some ex situ characterization techniques are briefly introduced.

Following the introductory chapters are five results chapters (**chapter 4-8**). A schematic diagram (**Fig. 1.1**) gives the principal results obtained from each chapter. The general idea used to investigate the passivation of Ni-Cr-Mo alloys is to obtain the elemental information on the ion released during the electrochemical process, as shown in **Fig. 1.1**. The elemental dissolution ν_M, combing with mass-balance, may be used to calculate the surface accumulation for an individual alloy element M, Θ_M. By assuming the oxidation state of the detected element, ν_M may be converted to elemental current, j_M.

Comparing j_M with the external current, j_e, recorded by the potentiostat, the faradaic yield may be obtained.

Using the methodology mentioned above, in **chapter 4**, the passivation behavior of a commercial C-22 Ni-Cr-Mo alloy was investigated by AESEC. Elemental dissolution kinetics were observed in situ during cathodic activation, spontaneous passivation, and anodic passivation. This chapter established a protocol for investigating spontaneous passivation and anodic passivation. This protocol was applied to the ensuing **chapter 5**, in which synthetic Ni22Cr and Ni22Cr10Mo (wt.%) alloys were investigated by AESEC combining with XPS. By comparing the synthetic Mo-free and Mo-containing alloys, the specific behavior of Mo was further elucidated. Meanwhile, the influence of minor alloying elements was clarified. In **chapter 6**, the object of study was expanded to a series of commercial Ni alloys with different combinations of Cr and Mo content. Spontaneous passivation and anodic passivation of these alloys were investigated by AESEC combining with XPS. In **chapter 7**, Mo accumulation during transpassive dissolution was observed for a series of commercial Ni alloys. The accumulated Mo partially dissolved during repassivation. This phenomenon was associated with the change of the local pH. The passivation of a novel NiCrFeRuMoW HEA was studied in **chapter 8**. The HEA showed excellent corrosion resistance, with no active elemental dissolution detected. Surface accumulation of Cr and Ru was observed during anodic passivation.

Finally, **chapter 9** gives the overall conclusion summarized from all the results chapters. New insights into the role of Mo and the spontaneous passivation phenomenon were offered. Perspectives generated from this dissertation were also given in **chapter 9**.

Overall this dissertation presents a methodology and scientific strategy that may be used to analyze corrosion, dissolution, and passivation phenomena for corrosion-resistant alloys, especially adapted for compositional complex alloys such as HEA. **Appendix A** gives an example of a "routine" characterization of the well-known Cantor alloy, CoCrNiFeMn.

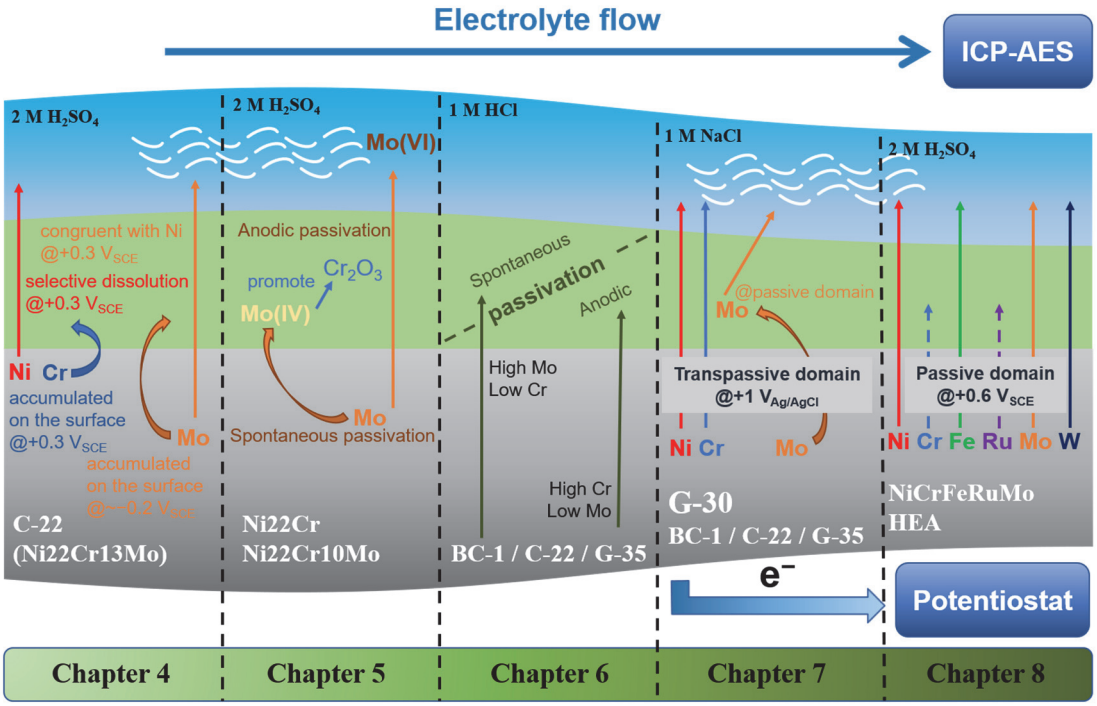

Figure 1.1 Schematic diagram showing the principal results obtained from **chapters 4-8**.

1.3 LIST OF PUBLICATIONS

1.3.1 FULL ARTICLES

1. X. Li, K. Ogle, The Passivation of Ni-Cr-Mo Alloys: Time Resolved Enrichment and Dissolution of Cr and Mo during Passive-Active Cycles, Journal of The Electrochemical Society, 166 (2019) C3179-C3185 (**chapter 4**).
2. X. Li, J. D. Henderson, F. P. Filice, D. Zagidulin, M. C. Biesinger, F. Sun, B. Qian, D. W. Shoesmith, J. J. Noël, K. Ogle, The contribution of Cr and Mo to the passivation of Ni22Cr and Ni22Cr10Mo alloys in sulfuric acid, Corrosion Science, in press (**chapter 5**).
3. J. D. Henderson*, X. Li*, D.W. Shoesmith, J.J. Noël, K. Ogle, Molybdenum surface enrichment and release during transpassive dissolution of Ni-based alloys, Corrosion Science, 147 (2019) 32-40 (**chapter 7**). *: equal contribution.
4. X. Li, J. Han, P. Lu, J.E. Saal, G.B. Olson, G.S. Frankel, J.R. Scully, K. Ogle, Communication—Dissolution and Passivation of a Ni-Cr-Fe-Ru-Mo-W High Entropy Alloy by Elementally Resolved Electrochemistry, Journal of The Electrochemical Society, 167 (2020) **(chapter 8)**.

5. X. Li, P. Zhou, K. Ogle, S. Proch, M. Paliwal, A. Jansson, J. Westlinder, Transient stainless-steel dissolution and its consequences on ex-situ bipolar plate testing procedures, International Journal of Hydrogen Energy, 45 (2020) 984-995.
6. Y.M. Yan, A. Maltseva, P. Zhou, X.J. Li, Z.R. Zeng, O. Gharbi, K. Ogle, M. La Haye, M. Vaudescal, M. Esmaily, N. Birbilis, P. Volovitch, On the in-situ aqueous stability of an Mg-Li-(Al-Y-Zr) alloy: Role of Li, Corrosion Science, 164 (2020).

1.3.2 ARTICLE IN PREPARATION

1. J. D. Henderson*, X. Li*, F. P. Filice, D. Zagidulin, M. C. Biesinger, B. Kobe, D. W. Shoesmith, K. Ogle, J. J. Noël, Investigating the role of Mo and Cr during the breakdown and repassivation of oxide films formed on Ni-based alloys in acidic media. *: equal contribution.
2. X. Li, P. Zhou, K. Ogle, The role of N on the passivation of the CoCrFeCoMn high entropy alloys (**Appendix A**).

1.3.3 ORAL PRESENTATION

1. X. Li, J. D. Henderson, D. W. Shoesmith, J. J. Noël, K. Ogle, Surface enrichment of Mo during transpassive dissolution of Ni-alloys, European Corrosion Congress (Eurocorr), 9-13 September 2019, Seville, Spain.

2. STATE OF THE ART

2.1 NI ALLOYS

Ni has been used in alloys since the beginning of our civilization. In ancient China, Pai-Thong, or white copper, a copper alloy with white color containing a certain amount of Ni was used to fabricate weapons. In the third century B.C., those copper alloys were believed to be introduced to the ancient kingdom of Bactria, part of what is now Afghanistan, to make coins[73]. Ni was unknown as an element until 1751, when a Swedish scientist named Cronstedt discovered it from the ore that was called "Kupfer-Nickel" by the superstitious miners, meaning "Old Nick's Copper"[74]. The modern Ni industry started when the mines in New Caledonia opened in 1875, and those in Sudbury, Ontario, Canada opened in 1886. **Table 2.1** gives the consumption of nickel for different uses.

Table 2.1 Consumption of Nickel for different uses[74]

Use	Stainless steel	Alloy steel	Nickel-base alloys	Copper-base alloys	Plating	Foundry	Other
Amount consumed / %	57	9.5	13	2.3	10.4	4.4	3.3

The first developed Ni-based alloy was Monell Metal, a trademark registered in 1906. It is a nickel-copper alloy with a nominal nickel composition of 67% and the balance copper[3]. This alloy was highly resistant to atmospheric corrosion, saltwater, and various acid and alkaline solutions. From then, many Ni-base alloys were developed. In addition to commercially pure nickel, three binary alloy systems providing exceptional corrosion resistance were also designed. These include nickel-chromium (Ni-Cr), nickel-copper (Ni-Cu), and nickel-molybdenum (Ni-Mo). The advantages of Ni as a base for corrosion-resistant alloys are not only due to its being inherently resistant to certain chemicals, but also it can be highly alloyed with elements known to enhance corrosion performance. **Fig. 2.1** gives the phase diagram of Ni-Cr[75], and Ni-Mo[75] systems. In a wide range of compositions, Ni could form a single-phase solid solution with these elements. **Table 2.2** gives a summary of the corrosion behaviors of the most often used commercial binary Ni

alloys.

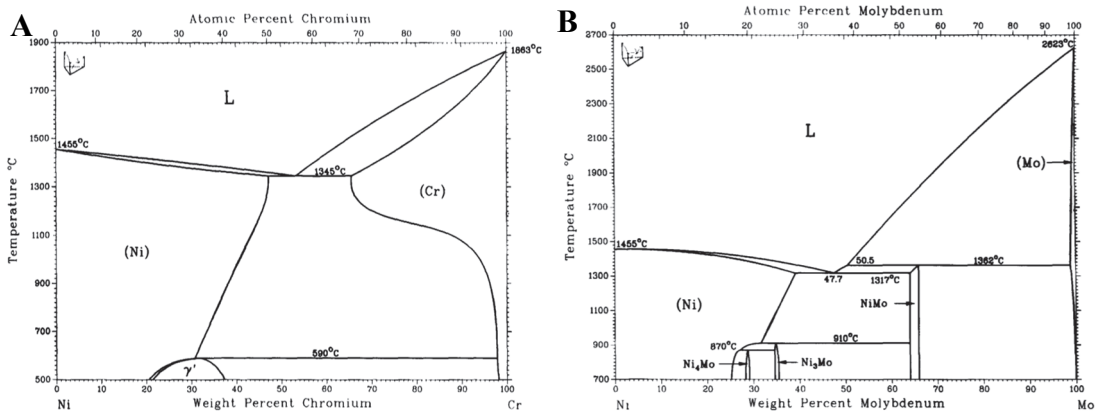

Figure 2.1 (A) Ni-Cr and (B) Ni-Mo binary phase diagrams

Table 2.2 Summary of the typical commercial binary Ni alloys

Alloy	Trade name	UNS No.	Major components / %	General corrosion behavior	Specification	Ref.
Ni-Cr	Inconel 600	N06600	Ni: balance Cr: 14-17 Fe: 6-10	Resistant to oxidizing acids. Oxidation resistant under high temperature.	Excellent resistance to sodium hydroxide and good resistance to stress corrosion cracking (SCC)	[76]
	Inconel 690	N06690	Ni: balance Cr: 27-31 Fe: 7-11		Resistant to SCC inpure water at temperatures more than ~300°C	[77]
Ni-Cu	Monel 400	N04400	Ni: balance Cu: 28-34	Resistance to seawater, brackish water and hydrofluoric acid		[78]
	Monel K-500	N05500	Ni: balance Cu: 27-33		Can be strengthened by age-hardening, three times the yield strength as compared to Monel 400	[79]
Ni-Mo	Hastelloy B-2	N10665	Ni: balance Mo: 28	High resistance to reducing acids.		[80]

The most common ternary nickel alloy systems are Ni-Cr-Mo and Ni-Cr-Fe systems. Cr and Mo could offer corrosion resistance to oxidizing acids and reducing acids, respectively, which makes the Ni-Cr-Mo alloy the most versatile ternary nickel alloy system.

Fig. 2.2 gives the calculated isothermal section at 1000°C for the Ni-Cr-Mo ternary phase diagram. It is shown that Ni can accommodate reasonably large amounts of Cr and Mo while keeping face-centered-cubic (fcc) single phase at 1000°C. Fcc single phase of Ni-Cr-Mo alloys may be obtained at room temperature using heat treatment. The purpose of having a single phase is to have a homogeneous distribution of the composition to prevent corrosion issues, such as galvanic corrosion, from happening. It is generally accepted that single phase alloys have better corrosion resistance, as compared to the multiphase alloys of the same composition[81].

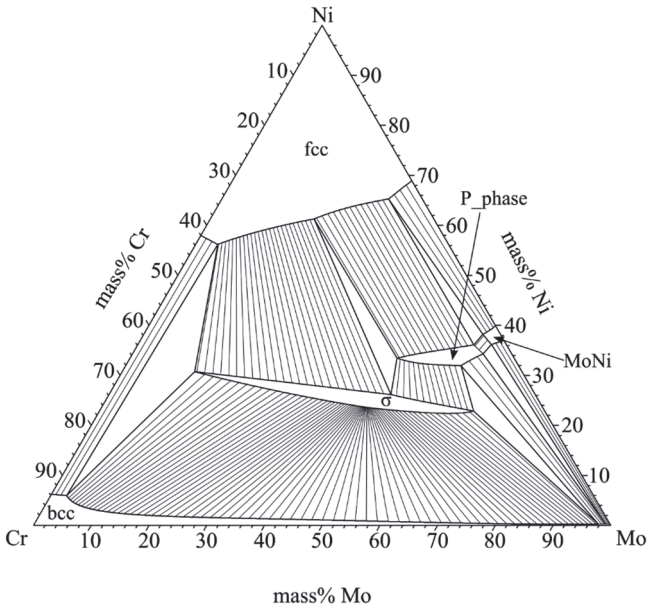

Figure 2.2 Calculated isothermal section at 1000 °C for the Ni-Cr-Mo ternary phase diagram.

The Ni-Cr-Fe family was designed to bridge the performance and cost gaps between the Ni-Cr alloys and the austenitic stainless steels. They can be divided into two groups, i.e., 1) the Ni-Cr-Fe alloys with Cr content ranging from 20 wt.% to 30 wt.% and Fe content ranging from 15 wt.% to 20 wt.%; 2) the Ni-Fe-Cr alloys with Fe content of approx. 30 wt.% and Cr content approx. 20 wt.%. Their benefits over the stainless steels include enhanced resistance to stress corrosion cracking. **Table 2.3** gives a summary of the most widely used ternary Ni alloys.

Table 2.3 Summary of the typical commercial ternary Ni alloys

	Trade name	UNS No.	Nominal components / % (major elements)	General corrosion behavior	Specification	Ref.
Ni-Cr-Mo	C-4	N06455	Ni: 65 Cr: 16 Mo: 16	Excellent resistance to both oxidizing acids and reducing acids.	The first Ni-Cr-Mo material developed in the early 1930s.	[82]
	C-22	N06022	Ni: 56 Cr: 22 Mo: 13		Higher Cr content to better cope with industrial environments containing oxidizing impurities.	[83-86]
	C-2000	N06200	Ni: 59 Cr: 23 Mo: 16 Cu: 1.6		Copper was added to improve resistance to sulfuric and hydrofluoric acids.	[29, 47]
Ni-Cr-Fe	G-3	N06985	Ni: 44 Cr: 22 Fe: 19.5	Good resistance to chloride-induced phenomena, such as pitting, crevice corrosion, and stress corrosion cracking, and exhibit moderate resistance to the halogen acids, in particular hydrochloric.	Cold-reduced tubes of G-3 alloy became standard for moderately sour oil and gas wells. Also, G-3 alloy was applied in evaporators for concentrating fertilizer-grade phosphoric acid.	[87]
	825	N08825	Ni: 42 Cr: 21.5 Fe: 30		High Fe content results in reduced resistance to environmental cracking. Low cost.	[88]

2.2 HIGH ENTROPY ALLOYS

High entropy alloys (HEAs) usually contain five or more principal elements in equal or near-equal atomic percent. Due to the high mixing entropy effect, HEAs tend to form disordered solid solutions of fcc[89], body-centered cubic (bcc)[90], or hcp hexagonal closed-pack (hcp)[91] structures rather than complex intermetallic compounds.

The first results reported on HEAs maybe dating back to the year 2004, on which several critical articles were pulished[92-97]. The following years have seen rapid development in this domain. Many HEAs with unique properties were invented. **Table 2.4**

below gives short descriptions of two HEAs. The first one is an equiatomic CrMnFeCoNi quinary fcc alloy, also called the Cantor alloy, named after the researcher who first reported it. The second one is a recently developed high corrosion-resistant HEA, with the composition of Ni38Cr21Fe20Ru13Mo6W2 (at.%)[44].

Table 2.4 Brief introduction of the Cantor alloy and a Ni-based HEA.

Alloy composition	Phase structure	Corrosion behaviors
Cr Mn Fe Co Ni in equimolar	fcc	1. Similar corrosion behavior as compared to 304L stainless steel with higher passive current density[98]. 2. Investigation of its variant with different Mn content showed that Mn suppressed the passivation process by increasing the current density during active-passive transition[99].
Ni38Cr21Fe20Ru13Mo6W2 (at.%)	fcc	1. Strong passivity in HCl solution up to 6 M. Immune to pitting corrosion in HCl solution[100]. 2. A broad passive potential range in 0.1 M Na_2SO_4 at pH 1, 4, and 12[44].

2.3 PASSIVATION OF NI ALLOYS

2.3.1 POLARIZATION CURVE OF PASSIVE ALLOY

The corrosion-resistant alloys, such as stainless steels and Ni-Cr alloys, owe their excellent corrosion resistance to the phenomenon of passivity. The definition of passivity provided by ASTM is: "passive—the state of metal surface characterized by low corrosion rates in a potential region that is strongly oxidizing for the metal"[1].

Passivation occurs spontaneously by the reaction of the material with an oxidizing environment. For a given metal M, passivation reaction in aqueous solution can be expressed as the following equations

$$M + xH_2O \rightarrow M(OH)_x + xH^+ + xe^- \quad (2.1)$$

$$M + xH_2O \rightarrow MO_x + 2xH^+ + 2xe^- \quad (2.2)$$

Such passivation can be considered as the process of forming insoluble oxide/hydroxide on the surface of the metal through an electrochemical reaction. Consequently, electrochemical techniques are frequently used to investigate passivation.

Basic electrochemical techniques used for characterizing passivation are those potential step methods. The potential may be held constant (potentiostatic) or may be varied with time (potentiodynamic) as the current is measured as a function of time or potential. Potential dynamic polarization (PDP, or linear scanning voltammetry, LSV) may be used to characterize the overall electrochemical behavior of an alloy over a wide potential range. The potential of the working electrode (specimen) is controlled by the potentiostat. A potential sweep is applied, which in passivation studies will usually begin in the cathodic domain (negative external current) and increase in the positive direction at a constant scan rate. Meanwhile, the current is recorded.

The resulting graph of current vs. potential is referred to as a polarization curve. If we ignore capacitive effects, the measured current reflects the faradaic reactions at the alloy/electrolyte interface. At any given potential, the current reflects the difference between the total anodic and the total cathodic currents :

$$i = i_a - |i_c| \tag{2.3}$$

An example of the decomposition of a polarization curve into anodic and cathodic components is shown in **Fig. 2.3**. The black line shows a typical polarization curving recorded for a passive alloy characterized by an active-passive transition (the anodic peak) and a passive domain (where the current). It represents the total current as a function of potential. The red and the blue dashed lines indicate the anodic and the cathodic partial current, i_a, and i_c, respectively.

It shows a phenomenon in **Fig. 2.3** that the onset of i_a is covered by i_c. Similarly, the current peak during the active-passive transition is lowered by i_c. These are the issues using the polarization curve to study the passivation of alloys, which will cause the consequent inaccurate understanding of the passivation phenomenon. In this dissertation, these issues were addressed by employing elemental resolved polarization curves, in which the anodic branch of the curve was separated by identifying the elemental dissolution.

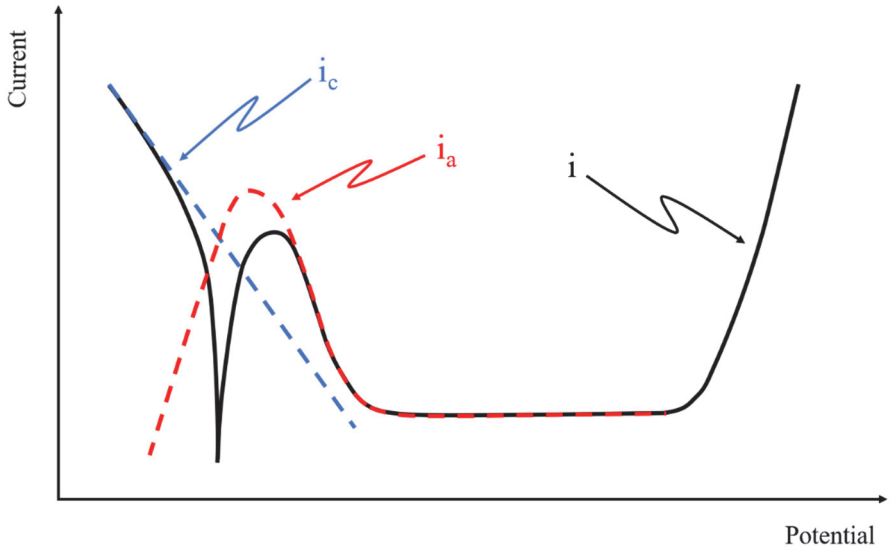

Figure 2.3 The schematic diagram showing the decomposed polarization curve.

Fig. 2.4 gives an experimentally measured PDP curve for Ni22Cr (wt.%) in deaerated 2 M H_2SO_4 solution at a scan rate of 0.5 mV/s. Some features are apparent in the figure. The cathodic domain in which $|i_c| > i_a$ thus the anodic reaction may not be determined directly by electrochemistry. In acidic solution used in **Fig. 2.4**, the main reaction is the hydrogen evolution reaction (HER) as shown below

$$2H^+ + 2e^- \rightarrow H_2 \tag{2.4}$$

The oxygen reduction reaction (ORR), **eq. (2.5)**, contributes little since the electrolyte was deaerated. However, it is the dominant cathodic reaction in neutral and alkaline solutions.

$$O_2 + 2H_2O + 4e^- \rightarrow 4OH^- \tag{2.5}$$

At the corrosion potential (E_{corr}) $|i_c| = i_a$. The anodic domain, in which $|i_c| < i_a$. The anodic domain may be further divided into three different parts: the active domain, the passive domain, and the transpassive domain. In the active domain, the current increases while increasing potential. The main reaction in this domain is the metal oxidation, forming soluble metal species. In the case under consideration, the reactions are Ni and Cr dissolution, **eq. (2.6)**, and **eq. (2.7)**.

$$Ni \rightarrow Ni^{2+} + 2e^{-} \quad (2.6)$$

$$Cr \rightarrow Cr^{2+} + 2e^{-} \quad (2.7)$$

When the current reaches the critical current, i_{crit}, the passive film nucleates and begins to grow. Once the stable passive film is formed, the current is a weak function of potential, and the material is in the passive state. The passive film, in the electrolyte without detrimental species such as Cl^-, is usually stable. However, the presence of detrimental species such as Cl^- will sometimes result in the loss of passivity, i.e., the breakdown of the passive film. Localized corrosion, including pitting corrosion[19, 101], crevice corrosion[102, 103], stress corrosion[104], and so forth, is the most common mode. Mo, to this end, is added to reinforce the alloys' resistance to localized corrosion[26, 60, 62]. The typical influence of alloying with Mo on the polarization curve of an alloy is the decrease of i_{crit}. In some cases, i_{pass} also decreases with the addition of Mo[26, 105], which will be discussed in the following section.

In the transpassive domain, the anodic current increases as the film begin to break down and/or oxygen formation occurs. The oxygen evolution reaction is shown as **eq. (2.8)**. Transpassive dissolution of the passive film formed on Ni22Cr is due to the oxidation of Cr^{3+} to Cr^{6+}, **eq. (2.9)**.

$$2H_2O \rightarrow O_2 + 4H^+ + 4e^- \quad (2.8)$$

$$Cr_2O_3 + 6H^+ \rightarrow Cr^{6+} + 3H_2O \quad (2.9)$$

Note that for Ni in the alkaline solutions, a secondary passivation phenomenon was observed due to the formation of $Ni(OH)_2$[106] or Ni_2O_3[107].

When exposed to the electrolyte, the passive alloy may exist in two states: passive or active, with very different corrosion rates. In the **passive state**, the corrosion rate is determined by the passive current, i_{pass} shown in **Fig. 2.4**. Typically, this is relatively low and is the desirable state of the material. If the passive film is damaged or removed, the system reverts to the **active state** at a more negative potential, which involves a higher corrosion rate. If the redox potential of the electrolyte is sufficient for the alloy to reach

E_{pp}, **Fig. 2.4**, where the current corresponds to i_{crit}, the material will undergo **spontaneous passivation** and return to the passive state. Otherwise, it will remain in the active state.

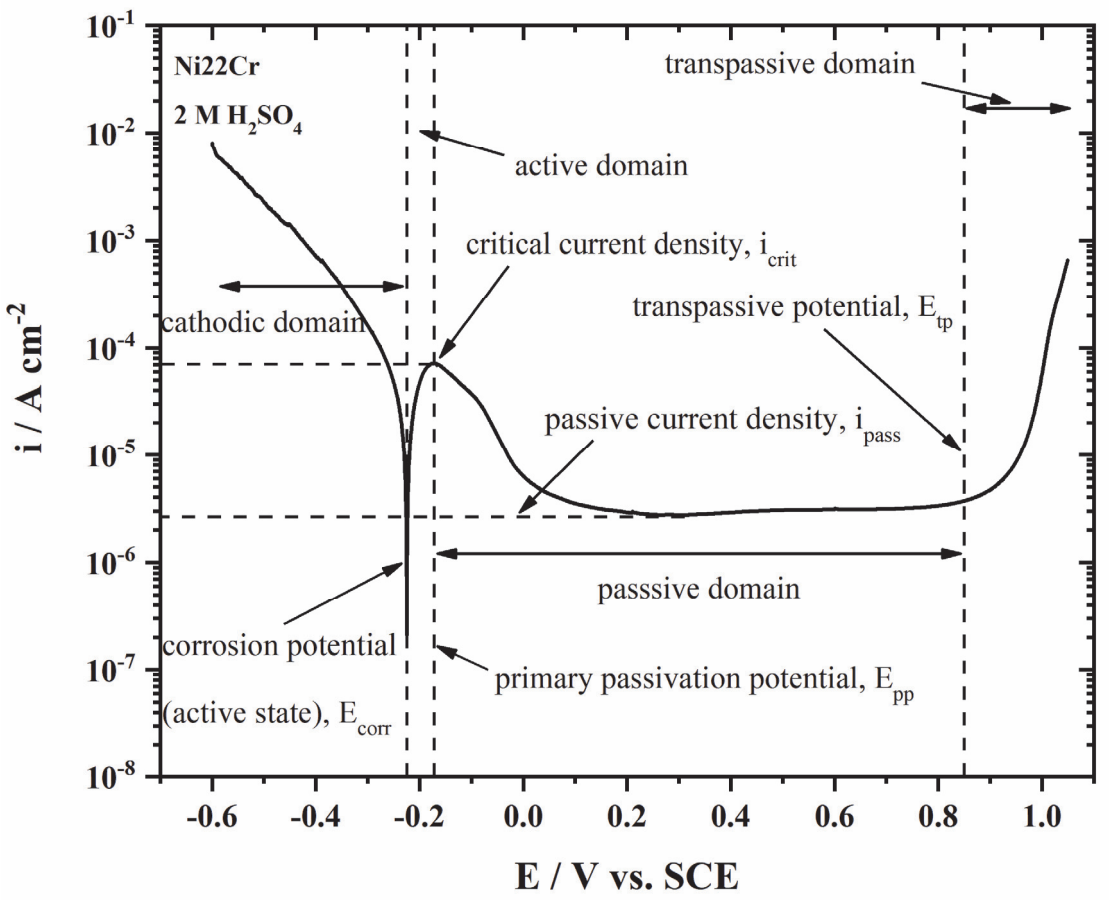

Figure 2.4 The polarization curve of Ni22Cr in 2 M H_2SO_4 at a scan rate of 0.5 mV/s at ambient temperature. The solution was naturally aerated.

2.3.2 PASSIVITY OF BINARY Ni-Cr ALLOYS

One of the pioneering work related to the passivation of binary Ni-Cr alloys was by A. Paul Bond and H. H. Uhlig[108]. In their study, pure Ni-Cr alloys with the composition of Cr ranging from 2 to ~29 wt.% were investigated in H_2SO_4 and HNO_3. The corrosion rate, the corrosion potential, and the critical current density of the alloys were studied. In all the oxidizing media used in their work, the Ni-Cr alloys exhibited a critical composition, that is, alloys containing less than the critical amount of chromium corroded relatively rapidly compared to those containing more than the critical percent. This composition varies with the concentration of the acid, as shown in **Table 2.5**. The

wide variation in the amount of Cr needed to passivate these alloys in different acidic media was believed to result from the different corrosion rates, anode-cathode area ratios, and critical current densities which prevail in these media. In the case of aerated sulfuric acid, the critical current densities decreased as the acid concentration was reduced while the corrosion rates remained at the same level. In nitric acid, corrosion rates, as well as critical currents, were raised as acid concentration was increased. The increase in the corrosion rate was attributed to the increase in the concentration of nitrate ion, which is reduced at the local cathodes. The increase in hydrogen ion concentration increased observed critical current densities in nitric acid.

Table 2.5 The relationship between the concentration of H_2SO_4 and the critical composition of Cr[108].

Concentration of sulfuric acid (normality)	0.01	0.1	1.1
Critical composition of Cr (wt. %)	12	18	24

Later in 1965, more systematic work by J. R. Myers, F. H. Beck, and M. G. Fontana was done to investigate the anodic polarization behavior of Ni-Cr alloys in sulfuric acid[109]. They studied different combinations of Ni and Cr in 1 to 20 N sulfuric acid solutions. Their work demonstrated that the addition of more than 20%Cr wt.% to Ni significantly reduced the passive current density by approximately two orders of magnitude as compared to 0% Cr. The influence of chloride ion on the passivity of Ni-Cr alloys was first investigated by F. G. Hodge and B. E. Wilde[110]. They tested Ni-Cr alloys with different Cr content from 0 to 100 wt.% in H_2SO_4 containing NaCl. They conclude that the presence of chloride accelerated the cathodic partial process. The alloy with increased Cr content improved the stability of the passive state and the resistance to pitting corrosion. It can be concluded from the above works that a threshold value for the composition of Cr exists for the alloys to realize passivation through alloying with Cr. The corrosion resistance is usually better with increased content of Cr, in terms of the passive current density as well as the resistance to pitting corrosion.

The characterization of the passive film for Ni-Cr binary alloys appeared far later. In 1994, S. Boudin et al. reported the surface analysis of the passive film on a series of Ni-xCr alloys (x = 0-30 at.%)[111]. The passive film was electrochemically formed in a borate buffer solution (pH = 9.2). Auger electron spectroscopy (AES) and XPS were employed

to study the depth distribution and oxidation state of the elements within the passive film. They proposed a model with Ni oxide-hydroxide and some Cr hydroxide at the outside layer and an internal Cr_2O_3 anhydrous layer at the film/alloy interface. The metallic substrate beneath the film was depleted in Cr but enriched in Ni. A critical Cr content of 15 at.% was reported, above which a protective Cr_2O_3 barrier layer was established on the surface. This could be an explanation of what was discussed above for the critical Cr content in decreasing the i_{pass}, the slight change in the value of Cr content may be attributed to the difference in the electrolyte. The thickness of the film depended on the content of Cr. The higher Cr content resulted in the thicker film with the highest value for Ni30Cr at 2.1 nm.

The passive film formed in acidic and alkaline media (1 M NaOH and 0.5 M H_2SO_4) on Ni20Cr wt.% alloy were studied by T. Jabs, P. Borthen, and H. H. Strehblow[112]. They calculated the thickness and the concentrations of the components of the film based on the two-layer model shown in **Fig. 2.5**. The maximum thickness of the passive layer is about 6 nm in NaOH and 3.5 nm in H_2SO_4. Based on XPS analysis, they proposed a multilayer model of the passive film, as shown in **Fig. 2.6**. They found that in H_2SO_4, the passive film consisted mainly of Cr oxide/hydroxide, with a minor contribution of Ni(II). Ni hydroxide was not detected due to its high solubility in acid solution. In alkaline solution, the film consisted of a Ni hydroxide outer layer and Cr_2O_3 and NiO inner layer.

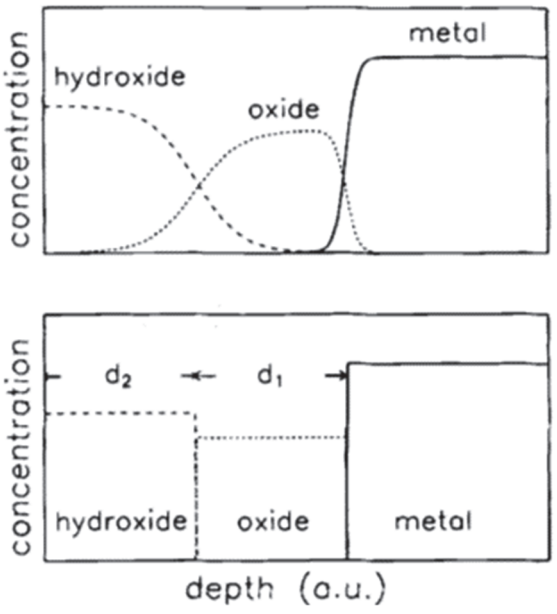

Figure 2.5 Realistic concentration profile of the passive layer (top) and the simplified two-layer model (bottom) for Ni-Cr alloys[112].

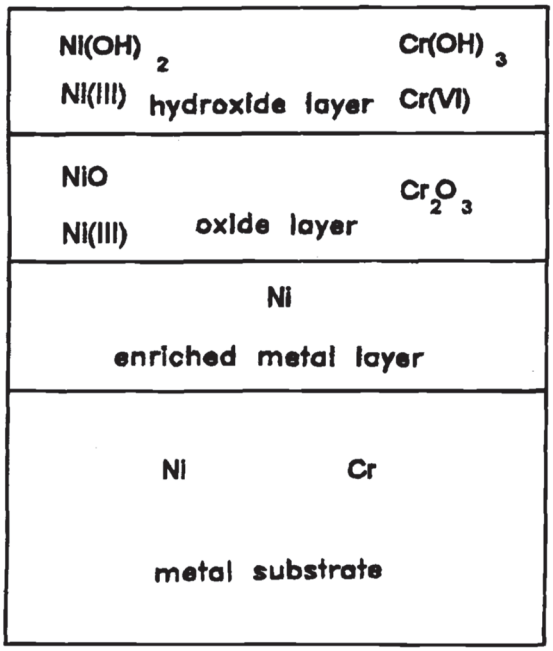

Figure 2.6 Passive layer model for Ni-Cr alloys[112] developed based on the XPS results in 1 M NaOH and 0.5 M H_2SO_4.

A series of work by Benoît Ter-Ovanessian etc. studied the electronic and transport properties of the passive films[36], the role of Cr on passive film formation[113], and pitting corrosion[114] for synthetic Ni-Cr alloys using a point-defect model. In this model, the passive film formation and breakdown are described by the movement of point defects under the influence of an electrostatic field[115]. The major point defects in the passive film are assumed to be electrons, holes, and metal and oxide vacancies. They found that the electronic properties and resistance to point-defect migration are the principal properties governing pit nucleation[36]. Multi-frequency Mott-Schottky analysis revealed that the passive films formed on Ni-Cr alloys in pH 2 sulfuric acid behaved as p-type semiconductors and possessed two high charge carrier populations (10^{20}-10^{21} cm^{-2})[113]. It was shown that the NiCr alloy with the highest Cr content showed the highest corrosion resistance to pitting corrosion. Ni cation incorporated into the passive film was responsible for deleterious interactions between the surface and chloride ions leading to metastable pit events. Migration resistance is a good indicator of the passivity breakdown process based on the electrochemical impedance spectroscopy (EIS) results[114].

2.3.3 PASSIVITY OF TERNARY Ni-Cr-Mo ALLOYS

The first Ni-Cr-Mo material was introduced in the early 1930s[116]. After that, the research was mainly carried out on optimization of the composition[82, 117, 118], the influence of heat treatment on the corrosion behavior[119] etc. The work by G. Lorang in 1990 represents the earliest work concerning the surface characterization of the surface oxide on Ni-Cr-Mo alloys[11]. They employed AES with ion sputtering to investigate depth distribution within the surface film in 5 M NaCl. The film was found to consist of mainly Cr oxide at the film-alloy interface covered with a small amount (< 10% of the total atomic density of the film) of Ni oxide. Only very few Mo atoms were found in the film.

Since the US government approved the Yucca Mountain nuclear waste repository project in 2002, the Ni-Cr-Mo type of alloys started to receive more and more attention. Because one of those alloys named C-22 was chosen as the candidate to fabricate the package for storing the nuclear waste[120]. To this end, in terms of the corrosion behavior, the alloy must be immune to aqueous corrosion attack in its lifetime, which was designed to be more than 100,000 years. Many research works were therefore carried out to study the corrosion behaviors of the Ni-Cr-Mo alloys, especially C-22 alloys[83, 84, 86, 121-124]. The passivity of the Ni-Cr-Mo alloys was extensively studied concerning the structure and composition of the passive film, the electronic properties of the film etc.

Lloyd et al. studied the film composition and structure of the commercial Ni-Cr-Mo alloys using electrochemical techniques combined with surface characterizations in 1.0 mol L^{-1} NaCl + 0.1 mol L^{-1} H_2SO_4[50, 85, 125]. The role of Cr was emphasized. They divided those alloys into two groups depending on their Cr content. The high-Cr alloys contain more than 20 wt.% Cr while the low-Cr alloys have less than 20 wt.% Cr. For high-Cr alloys, much lower passive dissolution currents and much slower attainment of steady-state conditions were observed. Also, they showed a little temperature dependence of the i_{pass} as compared to the low-Cr alloys. The results of XPS and TOF-SIMS showed the passive films formed at 200 mV and 500 mV (vs. Ag/AgCl) for the high-Cr alloys were thicker than the low-Cr alloys, meanwhile they had a layered structure consisting of an inner Cr-Ni oxide layer and an outer Mo oxide. However, this layered structure was not found on the low-Cr alloys[50]. They had no tendency to segregate Cr and Mo to the inner

and outer regions of the film. At 75°C, the high-Cr alloys exhibit E_{corr} values that are 300 to 400 mV vs. Ag/AgCl more positive than those of the low-Cr alloys. This is attributed to the Cr/Mo segregation process, and the suppression of defect injection at the alloy/oxide interface for those high-Cr alloys[125]. The role of Mo, as well as W, was also studied. It was found that, at low passive potential (200 mV), Mo and W exert little influence on passive current densities. While at high passive potential (500 mV), when Cr(VI) release appears to start, the presence of Mo and W in the outer regions of the oxide suppresses passive dissolution[50]. The work by Lloyd described a model for the passive film structure formed on Ni-Cr-Mo alloys, which is the segregation of Cr and Mo in the inner and outer layers, respectively. Many works on Ni-Cr-Mo alloys reported similar results.

Zagidulin et al. characterized the surface composition of C22 Ni alloys in 5 M NaCl solution with XPS and TOF-SIMS[30]. At the potential range of −0.4V to 0.2 V vs. Ag/AgCl, Cr(III) oxide film was built at the oxide/alloy interface. At the potential above 0.2 V vs. Ag/AgCl, the film thickens considerably due to the accumulation of Mo(VI) and W(VI) in the outer region of the film. The passive film of a Ni-Cr-Mo alloy, Alloy C-2000 (Ni-23Cr-16Mo-1.6Cu, wt.%), was studied by Zhang et al. with surface-sensitive techniques[29]. The outermost surface of the film was found to be enriched in Cu and Mo oxide, the intermediate region dominated by Cr/Ni hydroxides, and the inner region comprising Cr/Ni oxide. In the transpassive domain, the passive film broke down non-uniformly due to the electrochemical conversion of Cr(III) to Cr(VI).

Hayes et al. studied the influence of Cr and Mo on a series of synthetic Ni-Cr-Mo alloys in 1 M NaCl at different pH from 3 to 11[48]. Alloy C-22 was also studied as a comparison. The composition of the synthetic Ni-Cr-Mo alloys used were Ni-20Cr, Ni-11Cr-7Mo, and Ni-11Cr-13Mo wt.% alloys. The primary finding of this study is that Cr is responsible for the passive behavior and high breakdown potential, whereas Mo is responsible for repassivation after breakdown occurs.

2.3.4 CREVICE CORROSION OF Ni-Cr-Mo ALLOYS

Although they possess relatively high corrosion resistance in a variety of aqueous solutions, including oxidizing and reducing acids, alkaline solutions etc., the Ni-Cr-Mo alloys are somewhat fragile in Cl^--containing solutions. The chloride ions are extremely

aggressive for the Cr-enriched passive film, which will result in the breakdown of the film and finally cause damage to the material. The worst scenario is when the corrosion reactions lead to the formation of a low pH, high chloride electrolyte in the occluded region, e.g., a crevice, at which the passive film will deteriorate rapidly.

The mechanism of crevice corrosion may be illustrated in **Fig. 2.7**, in which a Ni alloy is exposed to NaCl solution in the presence of a crevice. The anodic reaction inside the crevice is **eq. (2.10)**.

The electrons given up by the anodic reaction are consumed by the cathodic reaction outside the crevice, which is the oxygen reduction reaction, shown as **eq. (2.5)**. As a result of these reactions, the electrolyte inside the crevice gains positive electrical charges in contrast to the electrolyte surrounding the crevice, which is electrically balanced by the migration of chloride ions from outside the crevice into the crevice. This results in an increase in chloride ion concentration with time.

The hydrolysis reaction of metal cation, in this case, Ni^{2+}, is shown as **eq. (2.10)**, results in the increase of the acidity within the crevice.

$$Ni^{2+} + 2H_2O \rightarrow Ni(OH)_2 + 2H^+ \qquad (2.10)$$

The combination of the increased concentration of Cl^- and the decrease of the pH inside the crevice destabilizes the passive film and accelerates the corrosion process.

The consumption of oxygen inside the crevice and the impossibility to restore it contrasts with the area outside the crevice, where oxygen is supplied constantly. This difference in the concentration of dissolved oxygen in the solution creates the electrochemical concentration cell, makes the crevice corrosion self-sustained.

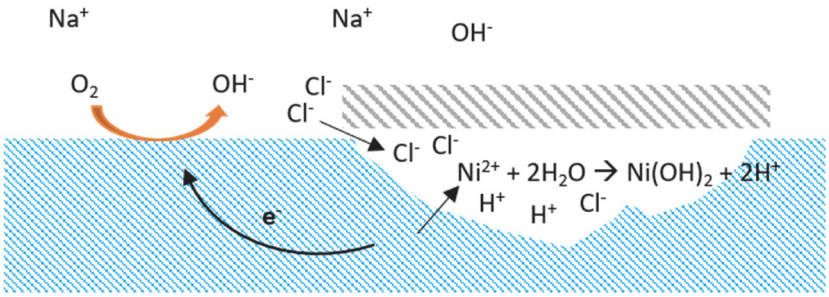

Figure 2.7 The schematic diagram of crevice corrosion taking Ni alloys in NaCl solution as an example.

The crevice corrosion initiation and propagation were studied by Lillard et al. for three Ni-Cr-Mo alloys (alloy 625, alloy G-3 and alloy C-276) in chlorinated ASTM artificial ocean water[103]. The role of Mo was emphasized. Alloyed Mo lowered passive current densities, decreased the tendency for the primary passive potential to increase with increasing acidity, and lower the anodic dissolution rate in the active polarization region. It was proposed that the improved crevice corrosion resistance ranking of alloy C-276 > alloy 625 > alloy G-3 was partly a result of the production of MoO_4^{2-} ions, a protective oxidation product of Mo, within the crevice during the initial passive dissolution of the alloy and perhaps thereafter if MoO_4^{2-} migrates to the active crevice from other occluded regions.

The susceptibility of C-22 Ni-Cr-Mo alloy in chloride solutions was examined by Dunn et al.[121] at different temperatures from 60°C to 150°C. The crevice corrosion repassivation potentials were compared with corrosion potentials measured in separate tests. Crevice corrosion repassivation potentials, the potentials at which the current density in the reverse potentiodynamic scan reached passive current density measured on the forward potentiodynamic scan, were found to be strongly dependent on temperature, chloride concentration, and nitrate-to-chloride molar concentration ratio. Corrosion potentials were dependent on solution pH but independent of chloride concentration.

Critical potentials, E_{crit}, for crevice corrosion initiation were predicted for Ni-22Cr-XMo alloys (X = 0, 3, 6, 9, 13%), Alloy 625 (UNS N06625), and Alloy 22 (UNS N06022) based on electrochemical oxidation behavior in various artificial crevice solutions using an adaptation of a previously developed approach[126]. The calculated E_{crit} was compared to experimental values from the literature. The effect of Mo on the passive film stability in

the investigated conditions was discussed, especially its impact when present in quantities larger than 6%. The exchange current density estimated from the extrapolation of experimentally determined 10 M HCl data at 50°C and 85°C to estimated equilibrium potentials using compositional averaged Nernst potentials assumption of Mo^{3+} and Cr^{3+}, Ni^{2+}, dissolution valence states, congruent dissolution, Tafel dissolution behavior, and neglecting effects of temperature from 25°C to 85°C on standard chemical potentials or, hence, use of standard free energies for the half-cell reactions. The calculations show that the estimated exchange current density is reduced significantly by the addition of Mo. This effect was more pronounced in HCl + LiCl solution (pH equivalent to 0.1 M HCl with the Cl^- concentration of 12.87 M) compared to 10 M HCl solution, and was strongly affected by Mo alloying level, especially as alloyed Mo was increased to 9 wt.%. Rather than the formation of protective Mo oxides, the effect of alloying Mo was explained with respect to two aspects. First, Mo atoms in zero valence block active surface sites against dissolution. Second, Mo changes the chemical environment near Ni and Cr atoms rendering bond cleavage more difficult, thereby suppressing the exchange current density at E_{corr}.

Zadorozne et al. studied C-22, C-22HS, and HYBRID-BC1 Ni-Cr-Mo commercial alloys in several chloride solutions at 90°C[127]. Repassivation potentials (E_r) were measured by potentiodynamic-galvanostatic-potentiodynamic (PD-GS-PD) experiments. An experimental example is shown in **Fig. 2.8**. The PD-GS-PD method consists of three stages: (1) a potentiodynamic polarization (at a scan rate of 0.167 mV/s) in the anodic direction up to reaching an anodic current of 30 or 300 μA, (2) the application of a constant anodic current of 30 μA or 300 μA (approximately 2 $\mu A/cm^2$ or 20 $\mu A/cm^2$) for 2 hours, and (3) a potentiodynamic polarization (at 0.167 mV/s) in the cathodic direction, from the potential at the end of stage 2 until reaching alloy repassivation. Enhanced crevice corrosion resistance was indicated by an increase of E_r and a decrease in the corrosion rate (CR). Their results showed that the i_{crit} was inversely proportional to the molybdenum content, while the i_{pass} was inversely proportional to the chromium content. They concluded that the crevice corrosion resistance of these alloys increased with PREN (Pitting Resistance Equivalent Number, PREN = %Cr + 3.3(%Mo + 0.5%W)), which is mainly affected by the Mo content in the alloys.

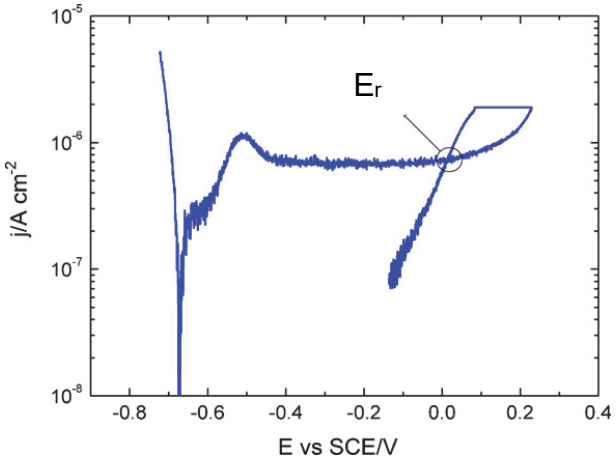

Figure 2.8 PD–GS–PD test for an alloy HYBRID-BC1 specimen, in pH 6, 1 M NaCl at 90°C[127].

The crevice corrosion kinetics of the three alloys were studied using the localized acidification model by Galvele[128] with the following equation

$$E_r = E^*_{Corr} + \eta + \Delta\Phi \tag{2.11}$$

where E_r is the repassivation potential, E^*_{CORR} is the corrosion potential in the acidified solution within the crevice, η is the polarization necessary to obtain a current density high enough to maintain a critical acidity within the crevice, and $\Delta\Phi = IR$ is the ohmic potential drop within the crevice. It was found that the crevice corrosion propagation was controlled by ohmic drop in dilute chloride solutions and by charge transfer in the more concentrated chloride solutions.

The influence of temperature on the initiation of crevice corrosion was studied by Hornus et al. for alloys 625, C-22, C-22HS, and HYBRID-BC1[129], using **eq. (2.11)**. Crevice corrosion was found in the PD-GS-PD experiments at 20-60°C, depending on the specific alloys. These values are below the reported critical crevice temperatures (CCT), ranging from 40-125°C, obtained through standard immersion tests. The crevice corrosion repassivation potential, determined by the PD-GS-PD technique, decreased as the temperature and chloride concentration increased. The high dependence of the repassivation potential on chloride concentration was attributed to the ohmic potential drop caused by passivating species at the alloy/solution interface.

The effects of the alloying elements Cr, Mo, and W on the crevice corrosion of commercial Ni-Cr-Mo(W) alloys in 1.0 mol/L NaCl solution were studied using the PD-

GS-PD technique by Mishra et al[130]. Cr was found to be the critical element determining resistance to the initiation of crevice corrosion, but a substantial Mo alloy content is required to achieve maximum film stability, especially at temperatures > 60°C. Meanwhile, Mo is the major element controlling crevice propagation and repassivation.

Henderson et al. clarified that the H^+ reduction reaction is a significant contributor to the crevice corrosion by investigating a series of Ni-Cr-Mo alloys using a galvanostatic crevice corrosion technique in conjunction with weight loss analyses[131]. A constant current was applied to the sample assembled to a single-crevice approach. Crevice corrosion occurred after the incubation time, during which the sample was protected by the passive film. The schematic diagram of this technique was shown in **Fig. 2.9**. By comparing the charge that equivalent to the mass loss with the applied charge, the contribution of proton reduction reaction may be determined. It was found that the addition of Mo and W not only stifles active dissolution but also limits the ability of H^+ reduction to intensify the damage.

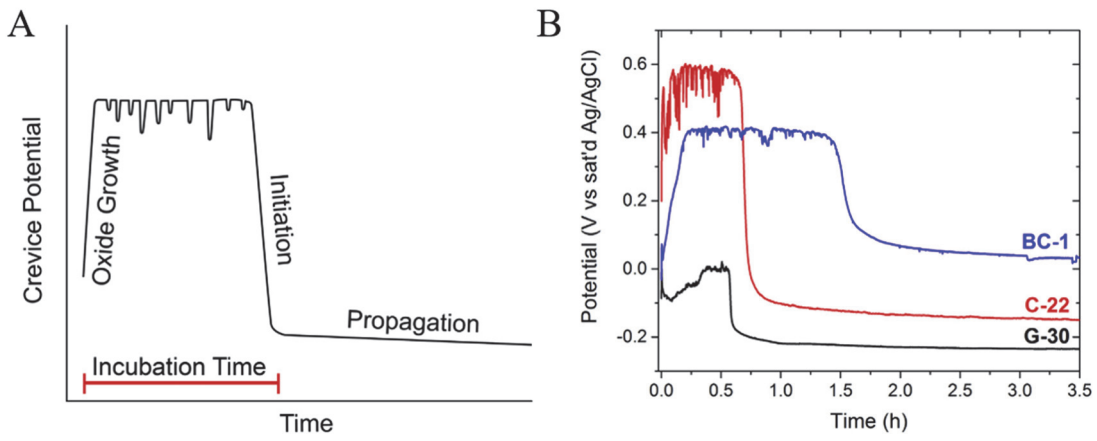

Figure 2.9 The schematic diagram of the galvanostatic crevice corrosion technique (A) and a real example including BC-1, C-22, and G-30 under galvanostatic control at 100 μA (B)[131].

SUMMARY OF THE SECTION

For binary Ni-Cr alloys, passivation was found to involve the enrichment of Cr on the surface. Increasing Cr content has a positive influence on passivity, including the effects of decreasing the critical current density and the passive current density. NiCr alloys with higher Cr content also showed better pitting corrosion resistance. For Ni-Cr-Mo alloys, Cr oxide is still the dominant species in the passive film. For the high Cr-containing alloys, the passive film may consist of a bilayer structure with the segregated Mo outer and Cr inner layer. Alloying element Mo was a critical factor that influences the crevice corrosion of the Ni-Cr-Mo alloys, while Cr also plays a role.

Studies carried out on the Ni-Cr-Mo alloys mainly used EC techniques and ex situ surface characterizations. The passivation process with elemental-resolved information has not yet been accessed so far. Understanding the passivation process with elemental information is of importance to understand the role of alloying elements.

2.4 THE ROLE OF MOLYBDENUM

Mo is known to be effective in improving the resistance to localized corrosion, such as pitting corrosion and crevice corrosion for stainless steels[17, 24, 26, 52, 54, 59], and Ni alloys[21, 48, 103]. The research concerning the role of Mo has been conducted for decades, and various mechanisms have been proposed accordingly[21, 23, 26, 59]. V. Maurice et al. concluded that Mo might either inhibit passive film breakdown or promote passive film repair[132]. The role of Mo is complex and cannot be explained by a single mechanism. Instead, it becomes more and more clear that Mo, as an alloying element, takes effect in various ways at various situations to improve the corrosion resistance of the alloy. In the following sections, the research related to the role of Mo on stainless steels and Ni alloys will be reviewed.

2.4.1 THE INFLUENCE OF MO ON THE ELECTROCHEMICAL BEHAVIOR OF ALLOYS

The thermodynamically stable Mo species in water may be illustrated by **Fig. 2.10**, the potential-pH equilibrium diagram (also known as the Pourbaix diagram) for the Mo-water system at 25°C. It should be noted that many of the chemical and electrochemical

phenomena associated with the formation and dissolution of the passive film are far from the thermodynamic equilibrium. For example, Cr is predicted to be soluble by the pH-potential diagram at pH 1. However, in practice, Cr oxide enriched passive film was experimentally determined to exist in such an environment. Considering that the passive film is a dynamic stationary state with constant dissolution and reformation, this "intermediate" state of insoluble Cr_2O_3 cannot be predicted by the Pourbaix diagram. Thus, considerable caution must be used in applying the Pourbaix diagram. Still, it is worth checking the thermodynamic prediction of the Mo species in aqueous solution. From the diagram, it is shown that Mo has a relatively narrow pH-potential domain in which the predominant species is a solid MoO_2 oxide. MoO_3 also exists as a solid form in the low pH domain. Other than that, Mo is soluble in the form of Mo(III) and Mo(VI) species.

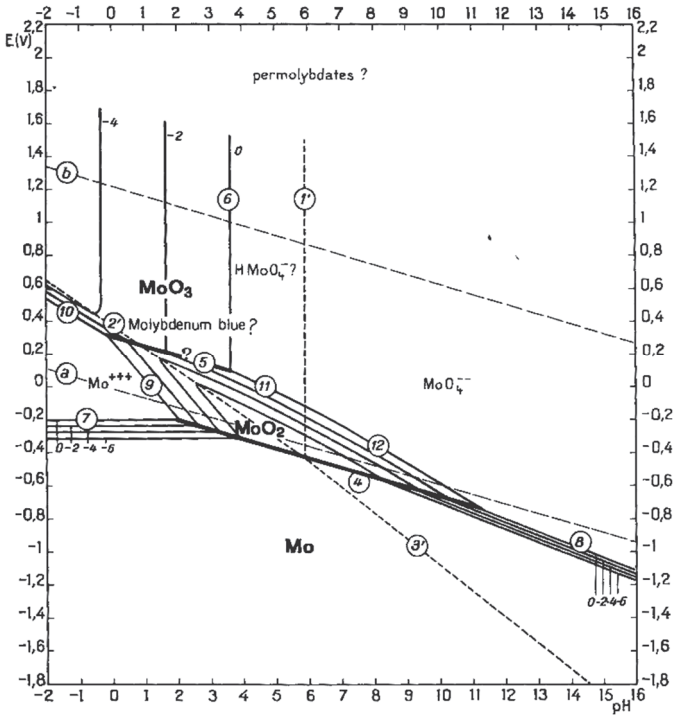

Figure 2.10 Potential-pH equilibrium diagram for the Mo-water system at 25°C[133].

The electrochemical behavior of Mo in aqueous solutions has already been examined by many researchers. One example is shown in **Fig. 2.11**, in which the electrochemical behavior of Mo as well as Fe, Ni, Cr, and stainless steels with and without Mo in 1 N HCl was determined by LSV. It can be concluded that Mo itself does not passivate in 1 N HCl. However, the addition of Mo in stainless steel considerably lowered the passive current density in the potential range where Cr was supposed to be passivated.

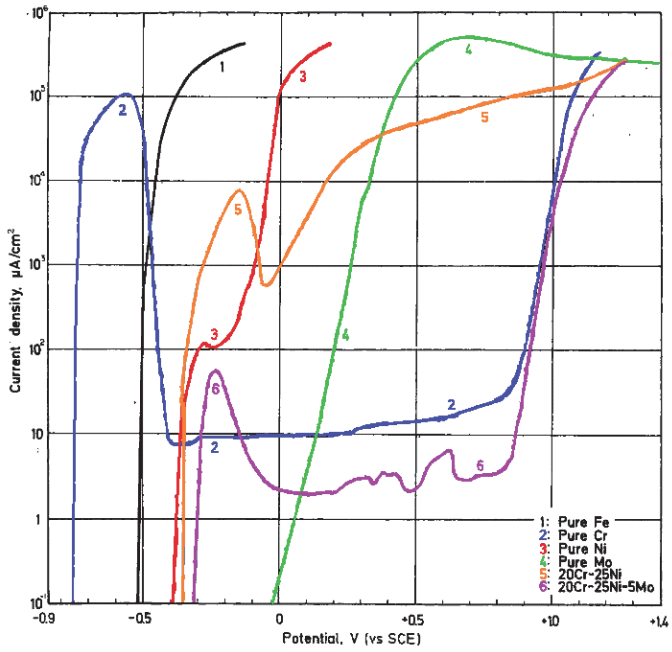

Figure 2.11 The polarization curves of 1: Pure Fe, 2: Pure Cr, 3: Pure Ni, 4: Pure Mo, 5: Fe-20Cr-25Ni and 6: Fe-20Cr-25Ni-5Mo in 1 N HCl at 25°C[26]. Reproduced with colors.

2.4.2 THE INFLUENCE OF MO ON ACTIVE DISSOLUTION

One of the consequences of alloying Mo is the effect of lowering the critical current density as has demonstrated that on Fe-Cr and Ni-Cr alloys[26, 60, 105, 134, 135]. **Fig. 2.12** shows anodic polarization curves for 17% chromium, 17% Cr-1% Mo, and 17% Cr-3% Mo alloys in 0.1 N hydrochloric acid. The critical current density decreased with the increase of Mo content. The electrochemistry results were combined with the results obtained from surface-sensitive techniques to suggest possible mechanisms. Hashimoto et al. characterized the surface composition by XPS. It was shown that a large amount of hexavalent Mo existed in the surface film on 30Cr-2Mo stainless steel during the active domain[60]. Based on this result, they proposed that during the active domain, molybdenum oxy-hydroxide or chromium or iron-molybdate formed on the active sites. This leads to the appearance of a homogeneous steel surface and hence to the formation of a uniform passive film. Based on the XPS results, they suggested the formation of Mo(VI) during active dissolution. However, that is contradicted with many other works[136-138]. For example, Olefjord et al. reported the formation of Mo(IV) on stainless steel with the Mo content of 1.7 and 3.6 wt.% during active domain in 0.1 M HCl + 0.4 M NaCl solution[136]. They concluded that the enrichment of Mo lowered the dissolution rate preceding passivation and thereby provoked passivation.

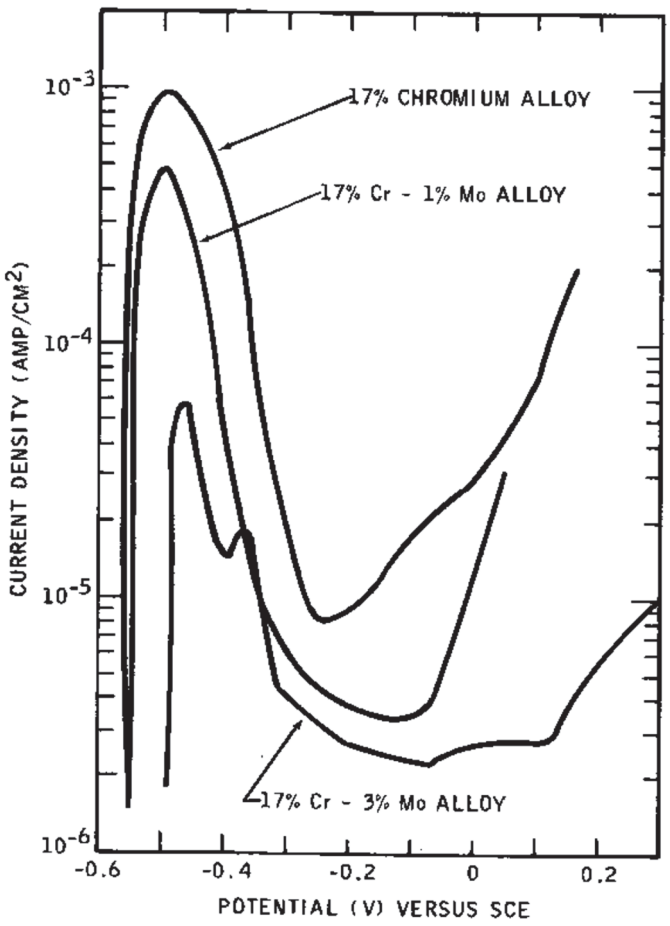

Figure. 2.12 Anodic polarization curves for 17% chromium, 17% Cr-1% Mo, and 17% Cr-3% Mo alloys in 0.1 N hydrochloric acid at 29.6°C[105].

2.4.3 THE INFLUENCE OF MO FOR PASSIVATION

In HCl solution, alloying with Mo in stainless steels lowered both the critical and passive current densities[26, 60, 105, 139]. Without Mo, the Fe-Cr alloy either had a very high passive current density (~1 mA cm^{-2} in 1 M HCl) in the passive domain[60], or suffered from pitting corrosion at low potentials in 0.1 N HCl solution[105]. As the Mo content increased (from 0 to ~3 wt.%), the passive current density decreased the pitting potential increased[60, 105, 139]. **Fig. 2.13** shows the polarization curves of stainless steels with different Mo contents in 1 M HCl at 20°C. The addition of 1 and 2% (wt.%) Mo decreased the passive current densities by approximately two orders of magnitude. Also shown is that the passive current density was more stable for the stainless steel with 2% Mo than with 1% Mo.

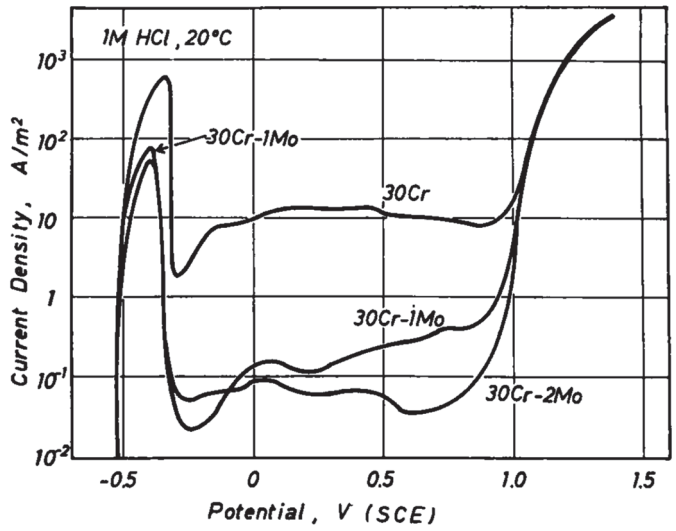

Figure. 2.13 The polarization curves recorded in 1 M HCl at 20°C for stainless steels containing different contents of Mo[60].

In the H_2SO_4 solution, however, the effect of Mo in the passive domain in terms of the passive current density was less obvious[46, 140-142]. The polarization curves of Fe-Cr alloys with different Mo content in 1 N H_2SO_4 are shown in **Fig. 2.14**. With the increase of the Mo content from 2 to 8 wt.%, the critical current density decreased, similar to that in HCl solution. However, the passive current densities of the Fe-Cr alloys with Mo content ranging from 2 to 8 wt.% were not much different and higher than that of the Fe-Cr alloy without Mo. In a recent study by Cwalina et al.[46], the polarization curves of Ni22Cr and Ni22CrMo (wt.%) showed no significant difference in i_{pass} in 0.1 M NaCl at pH 4 and pH 10, respectively.

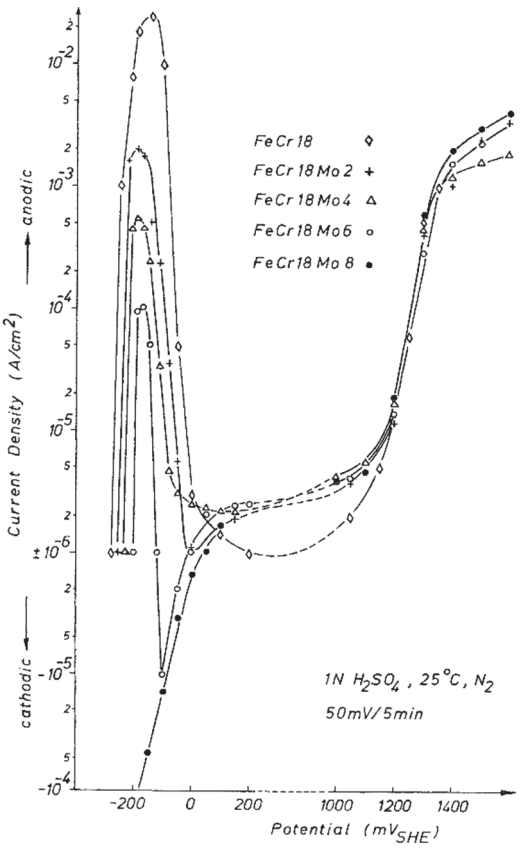

Figure 2.14 Polarization curves of Fe-Cr alloys with different Mo content in 1 N H_2SO_4 solution at 25°C, N_2 purged[140].

2.4.4 MO IN THE PASSIVE FILM

By lowering the i_{crit}, it was inferred that Mo promoted the formation of the Cr-enriched passive film[139, 141, 143]. However, the fate of Mo in the passive film remains controversial, and some of the results are contradictory. Different experimental works may be classified by the Mo/Cr composition of the oxide as compared to that of the bulk alloy: (a) absent (Mo/Cr ≈ 0); (b) enriched (Mo/Cr > bulk ratio); or (c) depleted (Mo/Cr < bulk ratio).

Though some results showed the absence of Mo in the passive film[5], Mo is usually considered to be incorporated into the film during passivation. However, whether it's enriched (Mo ratio higher than the bulk) or depleted (Mo ratio lower than the bulk) in the film is still in debate[24]. A number of early works on stainless steel by AES showed that Mo was depleted in the film[8, 144-146]. Similarly, XPS results from the work by Hashimoto also suggested that Mo was depleted in the passive film[60]. By contrast, Olefjord et al. characterized the passive film formed on austenitic stainless steels polarized

in the passive domain in 0.1 M HCl + 0.4 M NaCl[139]. They found that, for the high Mo alloyed steel (6 wt.%), Mo was enriched in the passive film.

It is no doubt that all the factors, such as electrolyte, passive potential and passivation time etc. will influence the fate of Mo. It is, therefore, difficult to draw a unified conclusion as compared to the presence of Cr in the passive film. To sum up, those results are of importance to gain insight into the role of Mo in the passive film. Thus, **Table 2.6** was made to give an overview of the studies related to the presence of Mo in the passive film. The conditions used to obtain the results were emphasized.

Table 2.6 Summary of the research concerning the state of Mo in the passive film

Alloy	Electrolyte	Potential (SCE)	Time	Technique	Presence of Mo	Ref.
316 SS (2.3%Mo)	1 M NaCl + 0.1 M Na_2SO_4	0.442 mV (H)	1000 min	AES	absent	[5]
Austenitic 20Cr-25Ni steels (0-5 wt.% Mo)	1 N HCl, 1 N H_2SO_4	0.3 V (HCl), 0 V (H_2SO_4)	60 min	XPS	depleted	[26]
Ferritic SS (0-5 wt.% Mo)	1 N H_2SO_4, 1 N Na_2SO_4 + H_2SO_4 (pH 3), 1 N NaCl + H_2SO_4 (pH 3.45), and pH 14 NaOH	60, 150, −150, and −700 mV (NHE) respectively (corresponding to the solution on the left	60 min	AES	depleted	[8]
SS with 0-3 wt.% Mo	5% H_2SO_4 at 35°C saturated with N_2 / 5% H_2SO_4 + 3% NaCl	0, 0.4, 0.8 V	5 min	AES	absent	[145]
Ferritic SS (3 wt.% Mo)	3.5% NaCl deaerated with N_2	0.65 V	6 h	AES	depleted	[147]
Ferritic SS (with 0, 1, 2 wt.% Mo)	1 M HCl	−0.2, 0, 0.2, 0.4, 0.5, 0.6, 0.7, 0.8, 0.9 V	6 min	XPS	depleted	[60]
Austenitic SS (with 1.3, 2.7, 2.8 wt.% Mo)	Ringer's physiological solution (pH 7.4) at 37°C	Immersed for 4 days	4 days	AES	absent	[146]
Austenitic SS (with 1.7 and 3.6 wt.% Mo)	0.1 M HCl + 0.4 M NaCl	−0.1, 0.5 V	Not mentioned	XPS	enriched	[139]
Single crystals of Fe19Cr and Fe24Cr2Mo	0.5 M H_2SO_4 at 25°C, deoxygenated and stirred	0, 0.5 V	6 min	XPS	enriched	[141]
SS (20Cr18Ni6Mo0.2N)	0.1 M HCl + 0.4 M NaCl	−0.1 and 0.5 V	10 min	XPS	enriched	[143]
304L and 316L SS	5% NaCl	−0.01 V (for 304L and 316L) and 0.07 V (for 316L)	Not mentioned	XPS	depleted	[51]
Single crystal austenitic SS (2.3 wt.% Mo)	0.05 M H_2SO_4	0.5 V	2 h and 20 h	XPS	enriched	[132]
Hastelloy C4 (Ni-16Cr-16Mo wt.%)	0.5 M NaCl deaerated with N_2	−0.2 V	2 h	AES	absent	[11]
C22, C-2000, 625, C-276, C-4 (Ni-Cr-Mo alloys)	1 M NaCl + 1 M H_2SO_4 at 75°C	0.35 V (vs. Ag/AgCl, 0.1 M KCl)	3 days	XPS	enriched	[125]
C22 Ni-Cr-Mo alloy	5 M NaCl	−0.4, −0.2, 0, 0.2, 0.4, 0.6 V (vs. Ag/AgCl, saturated KCl)	120 min	XPS	enriched	[30]
C-2000 Ni-Cr-Mo-Cu alloy	5 M NaCl, argon purged	0 V (vs. Ag/AgCl, saturated KCl)	44 h	XPS	enriched	[29, 47]

Another question that remains unclear is whether or not the film thickness is influenced by the addition of Mo. Sugimoto et al. reported that on the Fe-20Cr-25Ni (wt.%)

alloys containing 0 to 5 wt.% Mo, the film thickness increased with increasing the Mo content[27]. However, in another work by Hashimoto, they found that the film thickness of the Fe-Cr alloys with 1 and 2 wt.% Mo was the same[60]. Olefjord et al. also gave the same conclusion. They studied stainless steel with 1.7 wt.% and 3.6 wt.% Mo in 1 M HCI + 0.4 M NaCl solution. Their results showed that the film thickness was not changed by Mo content[139].

Mo can also influence the structure of the passive film. It was reported that the addition of Mo in the stainless steel resulted in a bipolar passive film with a cation-selective outer layer containing CrO_4^{2-} and MoO_4^{2-} and the anion-selective inner layer[57]. Lloyd demonstrated that for Mo containing Ni alloys with > 20 wt.% Cr, a layered structure consisting of an inner Cr-Ni oxide layer and an outer Mo/Cr oxide layer, could be built on the surface[50].

2.4.5 THE INFLUENCE OF MO ON PITTING CORROSION

Alloying with Mo may also improve pitting corrosion. The beneficial effects include many of what has been mentioned above, such as its influence on the active domain, the passive current density in Cl^- containing solutions, and its role in the passive film. Besides all this, the other beneficial effects of Mo on localized corrosion can be concluded as follows:

1. Shifting the pitting potential to a more noble value[27, 55, 103, 105, 126, 148];
2. Increasing the critical pitting temperature[27, 63, 149];
3. Decreasing the number, the diameter, and the depth of the pits grown on the surface of the alloy[53];
4. Ennobling of the repassivation potential[48].

SUMMARY OF THE SECTION

Various effects of Mo on the corrosion behaviors of stainless steel and Ni alloys are discussed in this section. The mechanism of how Mo takes effect, as well as its presence in the passive film, remains unclear, though many possible theories have been proposed. It is still a challenge to understand precisely how Mo influences the corrosion behavior of alloys.

2.5 SUMMARY

In this literature review chapter, binary NiCr, and ternary NiCrMo alloys were briefly introduced firstly, as well as the Ni related high entropy alloys. It was shown that Cr and Mo play important roles in improving the corrosion resistance of the alloy. The corrosion performance may be controlled by adjusting the composition of the alloy. For example, a critical Cr composition is needed to achieve passivation for NiCr alloy. Research concerning the role of alloying elements was mainly carried out by using convention electrochemistry and surface sensitive techniques. It was found that passivation involves the formation of Cr-enriched oxide film on the surface due to the selective dissolution of Ni. While Cr is the major component of the passive film, the role of Mo is also important, especially in the context of the localized corrosion. However, many ambiguities exist in the state-of-the-art interpretation of the role of Mo. The exact mechanism of how Mo takes effect is unclear. Even the presence of Mo in the passive film is in dispute. These questions are important for understanding the role of Mo, which is necessary for developing new corrosion-resistant alloys.

The essential questions, summarized from the literature review, are listed as follows:

1. While investigating the passive alloys, the widely used conventional electrochemical techniques are unable to detect the real metal oxidation rate for specific element, especially in the potential domain that the cathodic current is not negligible. This will result in the inaccurate interpretation of the polarization curve, due to the nature of the measured current being the sum of the anodic and cathodic current.
2. So far, the characterization on the composition and thickness of the passive are mainly carried out by the surface sensitive techniques, such as XPS and AES, as

reviewed in this chapter. However, these techniques are conducted ex situ with the risk of altering the composition and thickness of the film. An in situ investigation of the passivation is needed.

3. Contradictions exist on the presence of Mo in the passive film, according to the literature review in chapter 2.4.4, probably because different electrolyte/passive potential/passivation time were used in the studies. The influence of the techniques on the results, as mentioned in point 2, cannot be ruled out.

This dissertation attempts to address the questions raised above, with the help of the in situ AESEC, on a series of Ni-based alloys. The elemental dissolution rates were measured in real-time, which enables the direct measurement of the passive film formation and dissolution. The passivation of Ni-Cr alloy, Ni-Cr-Mo alloys, and a novel Ni-Cr-Fe-Ru-Mo-W HEA was studied using such methodology. The role of Mo was emphasized.

3. EXPERIMENTATION

In this chapter, the AESEC technique will be introduced in detail firstly, as it has been used as the principal tool in this dissertation. Then, some other techniques used in this dissertation will be introduced shortly.

3.1 ATOMIC EMISSION SPECTROELECTROCHEMISTRY (AESEC)

3.1.1 OVERVIEW

AESEC is a relatively new technique developed by Dr. Kevin Ogle in the early 90s[150] based on a prototype designed using a non-electrochemical dissolution cell developed by Pierre[151]. AESEC can measure in real time the species released from the specimen in contact with the electrolyte on an element by element basis either during a spontaneous open-circuit reaction or under electrochemical polarization. This ability has proven useful for the investigation of elemental dissolution kinetics for many types of corrosion reactions involving multi-element materials such as the dealloying phenomenon[152-154], pretreatment of Al alloys[155, 156], and the passivation of Cr-containing alloys[39, 40, 43, 45] etc.

AESEC consists of three main parts: 1) an electrochemical flow cell; 2) an inductively coupled plasma-atomic emission spectroscopy (ICP-AES); 3) a data acquisition system. **Fig. 3.1** shows the schematic diagram for AESEC. The following sections will introduce these three parts and related content.

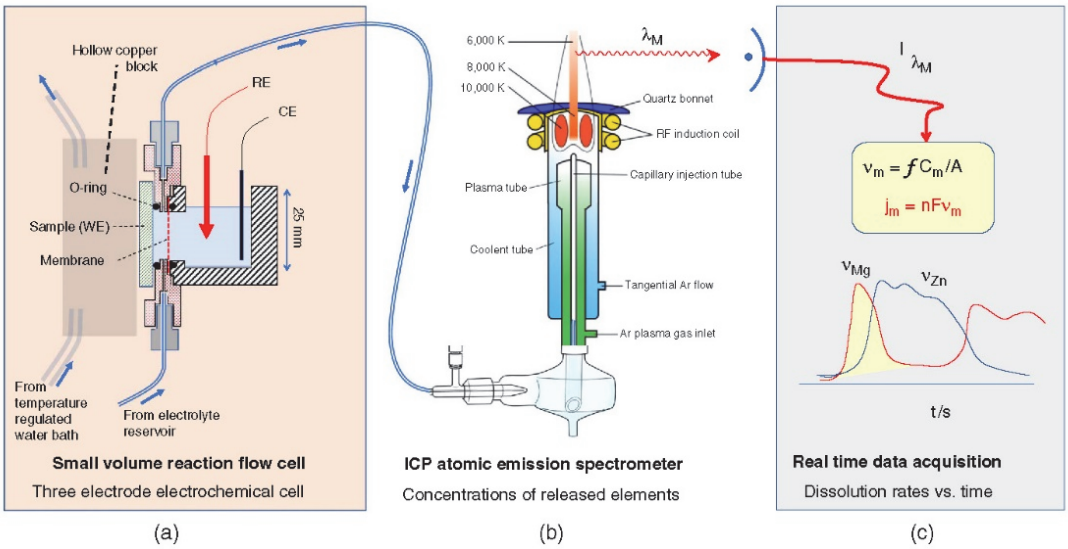

Figure 3.1 The schematic diagram of AESEC[151].

3.1.2 THE ELECTROCHEMICAL FLOW CELL

3.1.2.1 The structure of the flow cell

To realize the real time measurement of the dissolved species from a particular material, a customized electrochemical flow cell was designed for AESEC. As shown in **Fig. 3.1 (a)**, the flow cell consists of two compartments that are separated by a cellulose membrane (Zellu Trans/Roth). The membrane allows ionic conduction but prevented the bulk mixing of the electrolytes. The reaction compartment has a volume of ca. 0.3 ml, with the continuous flowing electrolyte introduced by a capillary from the bottom and leaving from the top. The electrolyte is introduced by a peristaltic pump at a fixed flow rate. The flow rate is normally determined by measuring the time of consuming 5 ml deionized water. Specimen as the working electrode is placed against the reaction compartment with an area of 1 cm^2 or 0.5 cm^2 exposed to the electrolyte defined by the O-ring. Reference and counter electrodes are placed in the other compartment filled with the same electrolyte. In the situation when temperature control is needed, a hollow copper block may be placed behind the specimen with water from a temperature regulated water bath flowing inside.

3.1.2.2 The residence time distribution (RTD) of the flow cell

The use of the flow cell affords the ability to collect the dissolved species and

transport them into ICP-AES for elemental analysis and thereby correlate concentration transient in the electrolyte with electrochemical measurements. In this way, the contribution of individual elements to the electrochemical measurements may be obtained, i. e. elementally resolved electrochemistry. However, the concentration and electrochemical transients do not have the same time resolution due to the hydrodynamics inside the flow cell. The elemental dissolution transients, which are formed instantaneously, will be broadened due to the hydrodynamics in the flow cell. The current transient is recorded instantaneously by the potentiostat. This difference makes it impossible to directly compare one to the other, which is essential for determining the rate of oxide film formation when the cathodic current is negligible[45, 157-160] or the determination of the cathodic current when oxide formation is negligible[161, 162]. To this end, Ogle and Weber[150] proposed a numerical convolution method that could broaden the current transient to correlate it with the elemental dissolution transient. The relationship between the interfacial dissolution rate $D_M(t)$ and the measured elemental concentration transient $\nu_M(t)$ obeys the following function

$$\nu_M(t) = \int_0^t D_M(t)h(t-\tau)d\tau \tag{3.1}$$

where h(t) is the residence time distribution (RTD) of the flow cell, τ is simply a variable for integration. The optimal situation is to solve the above equation to get $D_M(t)$ so that the measured dissolution transient $\nu_M(t)$ can be converted back to the interfacial dissolution rate. A method of deconvolution was developed and published by Shkirskiy et al.[162] However, due to the large error that might occur during the calculation of deconvolution, it is not done routinely. Instead, the current density transient $j_e(t)$ is usually convoluted to make a comparison between external current and the measured elemental current (converted from the elemental dissolution transient). The convolution is realized by determining the RTD for the currently used flow cell. It was proposed and experimentally demonstrated by using Cu in HCl solution[163] (**Fig. 3.2**) that the RTD closely follows a log-normal distribution. The function was shown below.

$$h(t) = \begin{cases} \sqrt{\frac{\beta}{\pi\tau^2}} \cdot e^{-\frac{1}{4\beta}} \cdot e^{-\beta\left(\ln\frac{t}{\tau}\right)^2} & if\ t > 0 \\ 0 & if\ t = 0 \end{cases} \quad (3.2)$$

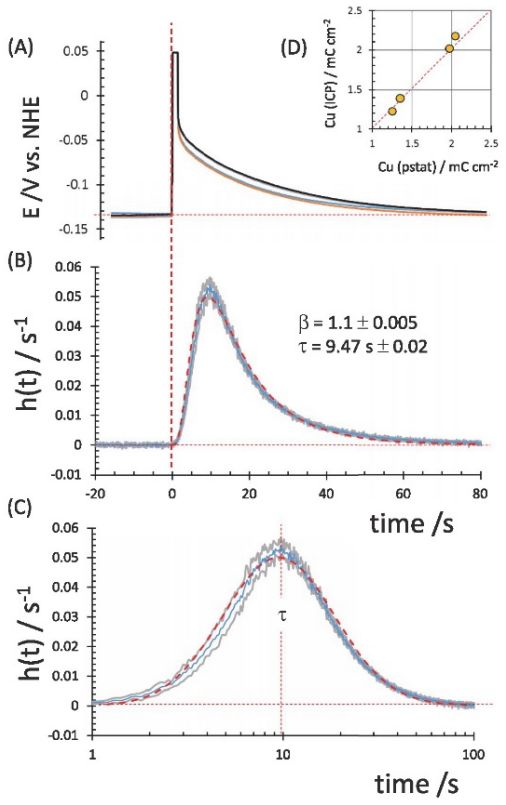

Figure 3.2 Galvanostatic experiment of Cu in 1 M HCl[163]. A 1 mA pulse (1.5 s) was applied to the sample and (A) potential (B) the dissolution transient in linear time scale and (C) log time scale were recorded downstream from the electrochemical flow cell. The dashed curve represents a non-linear least square fit to Eq. 3 with the fitting parameters given in the figure. (D) Integral of the Cu ICP transient (expressed as charge assuming n = 1) versus the integral of the electrochemical current transient. This result confirms the n = 1 dissolution mechanism.

3.1.3 ICP-AES

3.1.3.1 Overview

The ICP operating at atmospheric pressure was first introduced by Reed in 1961 as a technique for growing crystals under high temperature conditions. Afterwards, Greenfield et al.[164] and Wendt and Fassel[165] developed ICP into an analytical technique, in which the tail flame above the plasma was used as the spectroscopy source. By the end of the 1960s, the ICP was established as a viable analytical method, with numerous publications describing diverse uses of the method in practical analytical applications. Ultimately, the modern ICP systems used nowadays were finalized in the mid-1970s.

In the current configuration of the AESEC employed in our lab, an Ultima 2C

ICP-AES (Horiba Jobin-Yvon, France) was used for elemental analysis. In principle, the ICP-AES can be divided into two parts 1): the excitation source, e.g., the inductively coupled plasma; 2): the optical spectrometer that detects the spectra. Each part will be introduced in the following sections.

3.1.3.2 Inductively coupled plasma

A plasma is an ionized gas that is macroscopically neutral (i.e., with the same number of positive particles (ions) and negative particles (electrons)). Though many gases could be used for creating plasma, the most commonly used is argon due to the following reasons[166]:

1. a simple spectrum is emitted by argon in contrast to a flame where primarily molecular spectrum are observed;
2. argon has the capability to excite and ionize most of the elements of the Periodic Table;
3. no stable compounds are formed between argon and the analytes.

Plasmas may be classified according to the kind of electrical field that is used to create and sustain the plasma[166]:

1. direct current plasma (DCP) is obtained when a direct current field is established across electrodes;
2. ICP is obtained when a high-frequency field is applied through a coil;
3. microwave-induced plasma (MIP) is obtained when a microwave field is applied to a cavity.

ICP is currently the most used plasma because of some unique properties. **Fig. 3.3** gives a schematic diagram of the ICP. The radiofrequency (RF) coil, usually made of copper, is the component that provides the power for the generation and sustainment of the plasma. The power normally ranges from 1000 W to 1500 W, and is transferred to the plasma gas through a load coil. In this dissertation, the power used was mainly 1000 W, with the exception of the experiments carried out in sodium chloride, in which a power of 1200 W was used due to the high concentration of the salt. The torch assembly consists

of a set of three concentric coaxial tubes made of refractory material. In the current setup in our lab, two the outer tube and inner tube are made of quartz, and the injector tube is made of alumina. Each concentric tube has an entry point, with the inner (plasma) and outer (coolant) tubes having tangentially arranged entry points and the injector tube consisting of a capillary tube through which the aerosol is introduced from the nebulization/spray chamber.

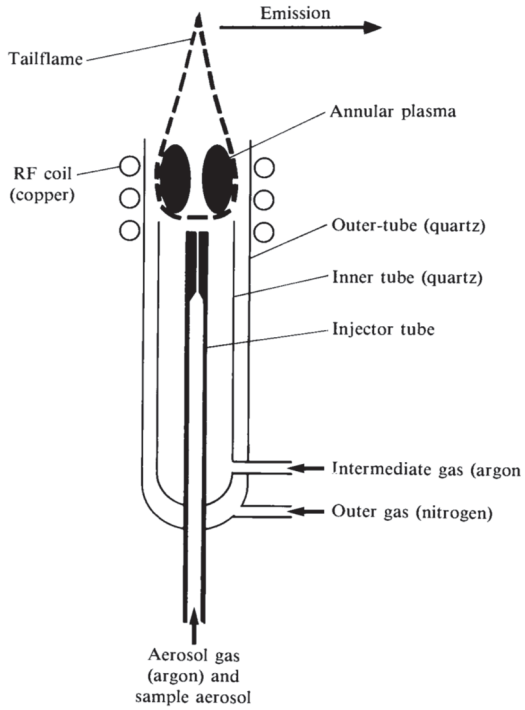

Figure 3.3 Schematic diagram of the ICP[167].

The plasma forms above the inner tube within the outer tube. Its location is largely determined by the position of the induction coil (RF coil). The input power from the RF coil causes the induction of an oscillating magnetic field whose lines of force are axially orientated inside the plasma torch and follow elliptical paths outside the induction coil as shown in **Fig. 3.4**. If the field is oscillating rapidly, the particles generate eddy currents within the field. These eddy currents flow in circular paths that run concentrically inside the torch. The fluctuating magnetic field couples with the plasma. The plasma contains charged particles (ions and electrons). These charged particles are accelerated, and energy is transferred from the particles to the gas atoms by collision. Since the plasma is at atmospheric pressure and the mean free path of the particles is small, the rate of collision is high, causing a high degree of excitation and ionization. A highly ionized high-

temperature plasma is then formed inside the inner tube of the torch, which is surrounded by the induction coil.

To ignite the plasma, "seed" electrons must be introduced to cause the ionization of the argon gas, usually the spark created by a Tesla coil. Electrons and argon ions are then formed which absorb energy from the alternating field. Collisions between the accelerating argon ions and electrons yield a large quantity of charged particles in sufficient numbers to absorb the energy from the RF field.

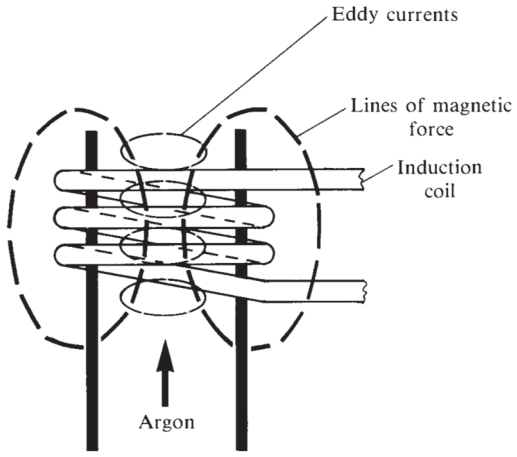

Figure 3.4 The eddy currents the magnetic fields created by the RF coil[167].

The sample of interest to analyze is introduced into the base of the plasma by the aerosol gas, usually argon, as shown in **Fig. 3.3**. This punches a hole in the center of the plasma, thus creating the characteristic "doughnut" or toroidal shape of the ICP. The aerosol gas, along with the sample aerosol, passes through the center of the hot plasma, creating a tunnel in which it is heated by the extremely hot, inert argon plasma.

When the sample aerosol enters the plasma, various fundamental processes take place that allows the ultimate visualization of the information via AES. These processes are summarized in **Fig. 3.5**. The mechanisms for excitation and ionization in the ICP have been widely discussed, and it is believed that they take place because of collisions between analyte atoms with energetic electrons.

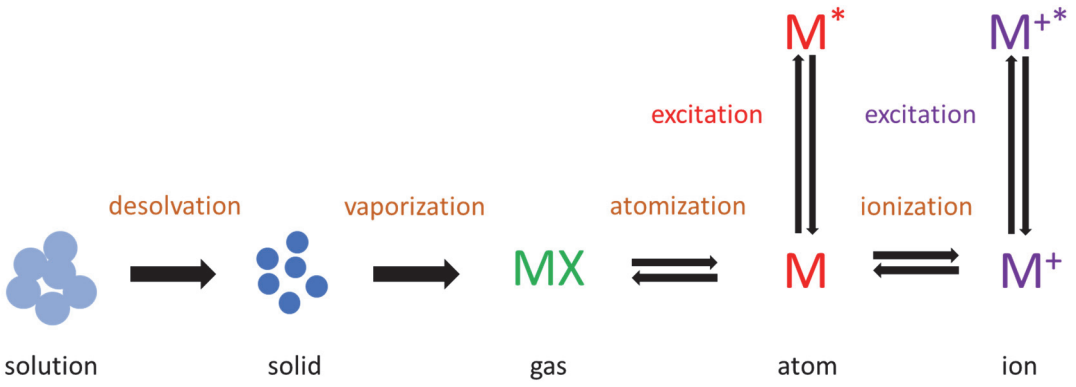

Figure 3.5 Processes that occur when sample droplets enter the plasma.

3.1.3.3 Sample introduction—nebulizer

To analyze the solution of interest, a sample aerosol must be created first from the solution. This is usually done by pneumatic nebulization or ultrasonic nebulization. Within the work of this dissertation, only pneumatic nebulization was used. Therefore, only pneumatic nebulization will be discussed in this part.

A typical pneumatic nebulizer for ICP spectrometry operates at 0.6-1.2 L min^{-1} gas flow with a liquid flow rate of 0.5-1.5 ml min^{-1}. Whereas, in our case, taking the RTD and other factors into account, the nebulizer operated at ~0.59 l min^{-1} gas flow, and the liquid flow rate used was either ~1.5 ml min^{-1} or ~3 ml min^{-1} depending on the situation.

A wide variety of pneumatic nebulizer designs have been described[168, 169], but here the focus is on devices that were used in this dissertation work. **Fig. 3.6** gives the schematic diagrams of two types of pneumatic nebulizers that were used in this dissertation work. These two types of nebulizers have different design strategies with the former has a concentric gas flow with the liquid and the latter a parallelly gas flow with the liquid. Concentric nebulizers are usually constructed of one-piece, fused glass. They come in the standard format, recessed tip variant for high solids, micro-flow, high pressure operation, and direct injection. The Enhanced Parallel Path Method nebulizer used in the dissertation work was to deal with solutions with high total dissolved solids. It works on the basic principle that anybody of liquid can be used to produce a fine mist with a gas stream if they are in close proximity to each other. It is not necessary to have a critical alignment of the gas stream and the liquid. In view of the above understanding, the

Enhanced Parallel Path Method nebulizer is designed with a very large opening for the liquid path, preventing the common problem of tiny particles in the liquid from plugging the sample path.

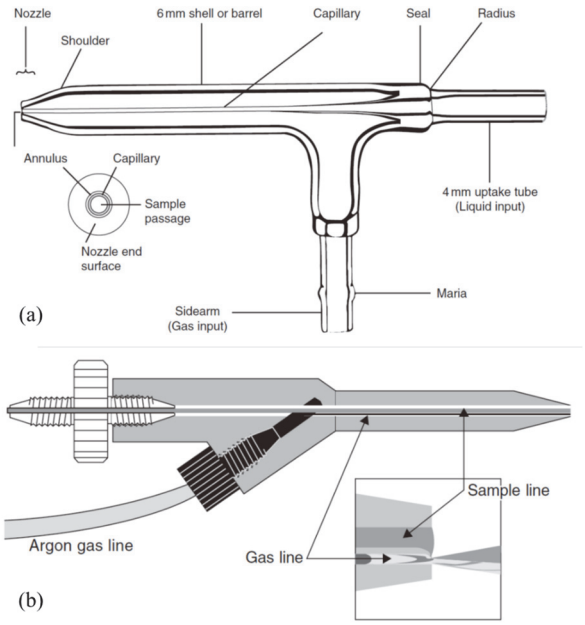

Figure 3.6 The schematic diagrams of two types of nebulizer used in this dissertation work. (a) A Meinhard® glass concentric nebulizer. (b) An Enhanced Parallel Path nebulizer (PEEK Mira Mist)[166].

3.1.3.4 Sample introduction—spray chamber

The sample aerosol created by the nebulizer is called the primary aerosol, and that enters the plasma is called the tertiary aerosol. These two are different, mainly because that even though the ICP is a robust ionization source, it is known that once the size of the particles processed by the plasma exceeds a certain maximum value, it is difficult to maintain a homogeneous vapor, representative of the bulk sample composition, inside the plasma. The exact particle size is not well known and may vary depending on the composition. Some describe as 10 μm[166] while the other describes as 20 μm[170]. Nevertheless, the range of dozens of microns is generally accepted to be the limitation. The aerosol produced by the nebulizer is coarse. Thus it cannot be loaded directly into the plasma otherwise it will reduce the robustness leading to a greater propensity for matrix interferences and ultimately instability and extinction of the discharge[171]. Thus, a spray chamber is introduced to refine the primary aerosol. The benefits of having a spray chamber can be concluded as follows:

1. reduce the amount of aerosol reaching the plasma;
2. decrease the turbulence associated with the nebulization process;
3. reduce the aerosol particle size.

The combination of the nebulizer and the spray chamber can produce the particle size of around 10 μm, which is ideal for the plasma to fully process.

There are many different kinds of designs available for the spray chamber. **Fig. 3.7** gives two designs that are currently used for the AESEC. The cyclonic spray chamber (**Fig. 3.7 a**) is used for the routine experiment with high sensitivity. However, when the precision becomes the priority, the twister spray chamber may be used. The Twister cyclonic spray chamber features a central transfer tube that acts as a secondary particle separator helping separate larger aerosol particles from the sample. This reduces solvent load in the plasma and thus increases the precision.

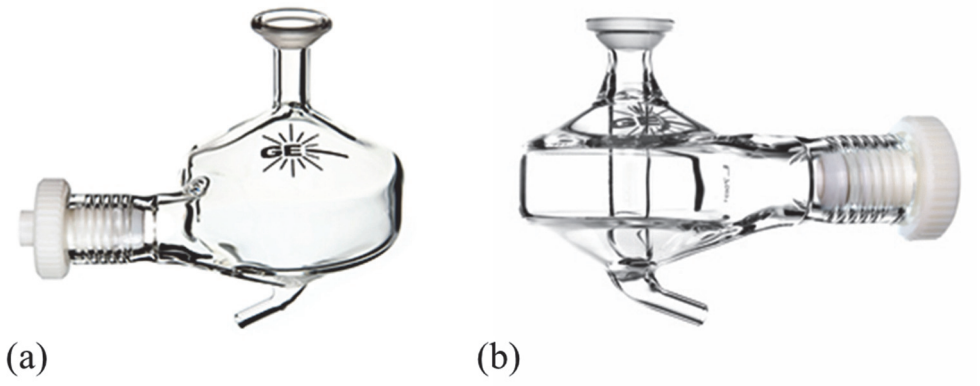

Figure 3.7 The glass cyclonic spray chamber (a) and twister cyclonic spray chamber (b), courtesy of Glass Expansion Inc.

In the cyclonic spray chamber (**Fig. 3.7 a**), the aerosol is introduced tangentially (from the nebulizer) to induce swirling. The initial process involves the aerosol swirling downwards close to the spray chamber wall. At the bottom of the spray chamber, a second inner spiral carries the aerosol to the exit point. The combination of the induced tangential flow and subsequent aerosol swirling leads to a reduction in aerosol particle size.

3.1.3.5 Atomic emission spectroscopy

It has been mentioned in the former section that the sample aerosol in the plasma

will be atomized and ionized to get the free analyte atoms or ions. At this moment, they are at their low energy level, e.g. ground state. When an atom or ion absorbs sufficient energy from the RF field, the electron will raise from ground state to a higher energy level, e.g. excited state. This is so called absorption or excitation. The excited electron is unstable (the lifetime of an excited electron is typically 10^{-8} seconds), it will return to its ground state. This process is accompanied by the emission of a photon of radiation. The energy of the photon is only decided by the difference of the energy between the excited state and the ground state, as described by the following equation:

$$E_2 - E_1 = h\nu \tag{3.3}$$

where E_2 and E_1 are the energy of the excited state and the ground state, respectively. h is the Plank constant. ν is the frequency of the radiation. Since ν can be described according to the following equation:

$$\nu = \frac{c}{\lambda} \tag{3.4}$$

where c is the velocity of light, and λ is the wavelength of the radiation. Thus, the excitation and emission process of the atoms and ions can be characterized by the emission of light with different wavelengths. These wavelengths are only decided by the energy difference between the excited state and the ground state. The electronic configuration of each element is different from that of other elements, and consequently its emission spectrum is also unique. **Fig 3.8** gives a diagram of the possible emission for the 3s electron of sodium. In a hot environment (i.e., the ICP), the sodium atoms are capable of absorbing radiation, such that electronic transitions from the 3s level to higher excited states can occur. These electronic transitions occur at specific wavelengths. Experimental observation of sodium identifies absorption peaks at 589.0, 589.6, 330.2, and 330.3 nm. By considering the energy-level diagram in **Fig. 3.8** for sodium, it is possible to identify that these wavelength doublets correspond to electronic transitions from the 3s level to either the 3p or 4p levels for 589.0/589.6 and 330.2/330.3 nm, respectively. The atomic spectra of all the elements in a sample comprise the sample spectrum. Analysis of the emission spectrum obtained from an unknown sample can determine the elements present in the sample.

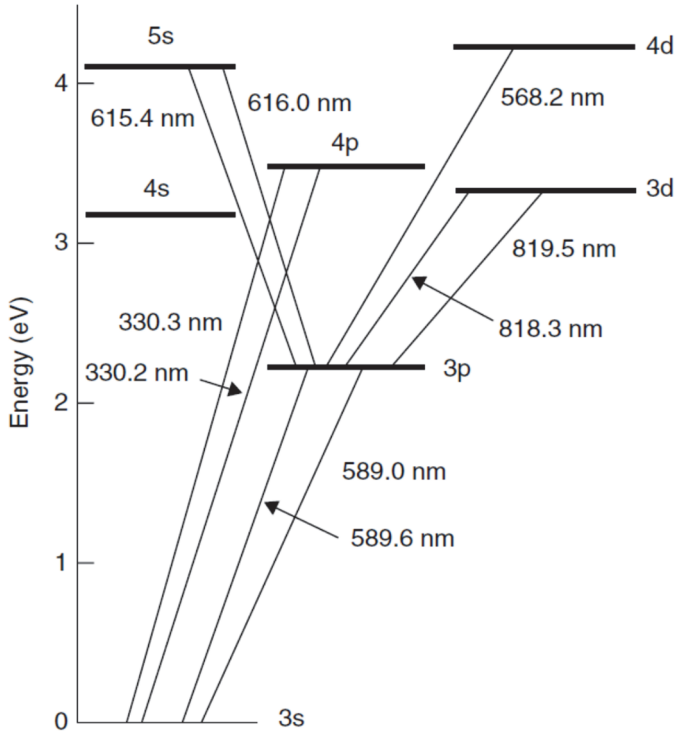

Figure 3.8 The possible emission wavelengths for a 3s electron of sodium[170].

While the identification of the wavelengths presents in an atomic emission spectrum permits the qualitative analysis of a sample, the intensity of the spectral lines is related to the amount of each element present in the sample. This allows the quantity of each element present to be calculated, thus achieve the quantitative analysis by AES.

3.1.3.6 Spectrometers

To isolate the analytical wavelengths of interest from the light emitted from the plasma emitted by the sample in the plasma, the spectrometer is required. Most of these wavelengths lie in the region of 160-860 nm and therefore a spectrometer should ideally be capable of determining all wavelengths in this region. Sensitivity may be enhanced at wavelengths below 200 nm by flushing the spectrometer with argon or nitrogen (our case) or by using a pump to evacuate it. This helps reduce the ingress of oxygen, which may otherwise absorb the light emitted in this region of the spectrum.

The realization of isolating the wavelength is normally through a blazed grating. **Fig. 3.9** gives the schematic diagram of a blazed grating. The blazed grating consists of a series of equidistant parallel grooves cut at an angle into the surface of a mirror. The angle of the blaze determines the performance of the grating by reducing the problems

associated with the wavelengths of different orders overlapping. Light striking the grating will be diffracted to a degree that is dependent on its wavelength.

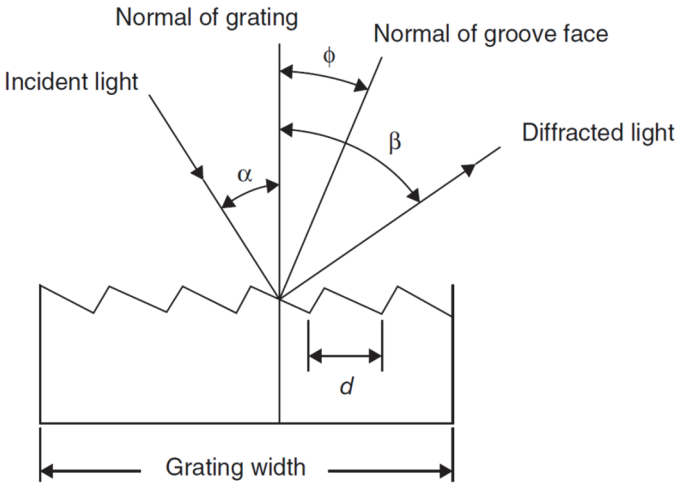

Figure 3.9 Schematic diagram of a blazed grating: d, distance between grooves; ϕ, angle of a groove (blaze angle); α, angle of incidence and β, angle of reflection.

Two available setups of spectrometers are usually used in practice. The first way is to measure one wavelength at a time while the second allows multi-wavelength measurement at the same time. The former is so called monochromator, and the latter is a polychromator. The schematic diagrams of both setups are shown in **Fig. 3.10**. Note that for each setup, different designs are available. What shown in the figure are the designs currently used in AESEC, e.g., the Czerny-Turner monochromator and the Paschen-Runge polychromator.

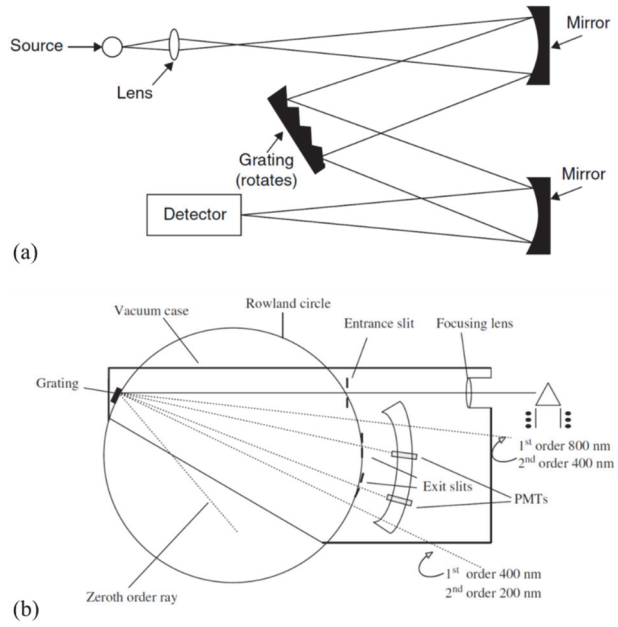

Figure 3.10 The schematic diagram of the Czerny-Turner monochromator[170] and the Paschen-Runge polychromator[166].

3.1.3.7 Detectors

Detectors are devices that could "view" the spectral information offered by the spectrometers. Two types of detectors are commonly used for modern ICP-AES systems. They are photomultiplier tubes (PMTs) and solid-state detectors (charge-transfer device, CTD). The former is used for AESEC. The latter refers to several semiconductor detectors such as charge-coupled device (CCD) and charge injection device (CID) and is largely used for an alternative polychromator configuration called echelle style spectrometers.

The PMT is a device that converts incident light into a current[172]. The electrical current that is measured at the anode of the PMT is proportional to the amount of light that struck the photocathode. This current is then converted into a voltage signal that is then transformed via an analog-to-digital (A/D) converter to a suitable computer for processing purposes.

As for the CTDs, they are semiconductor devices consisting of a series of cells or pixels that accumulate charge when exposed to light. The amount of stored (accumulated) charge is then a measure of the amount of light to which a pixel has been exposed.

3.1.4 DATA TREATMENT

The analog signals received by the photo-multiplier (PMT) from mono and polychromator were digitized by three 16 bit A/D converters operating at a frequency of 250 kHz such that all signals were truly simultaneous. The digital data was monitored by the QuantumTM software (Horiba Jobin Yvon SAS) in real time. The intensity of the radiation emission signals from the elements can be quantified by a standard ICP-AES calibration method as described in **Fig. 3.11**. The 0.1, 0.2 and 0.3 ppm solutions of Ni, Cr, and Mo were prepared using standard solutions (SCP ScienceTM). A clear linear relationship can be seen between the emission intensity and the solution concentration in all three elements.

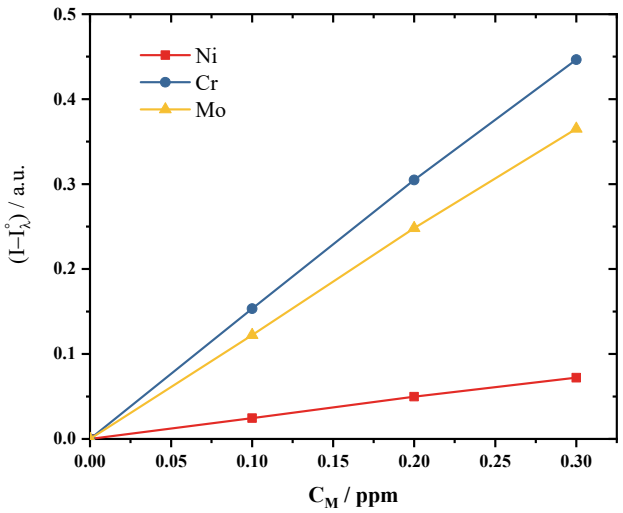

Figure 3.11 Standard ICP calibration curve showing normalized emission intensities of Ni, Cr, and Mo at the characteristic wavelength of 231.60, 267.72, and 202.03 nm, respectively

The emission intensity of a specific element at its own wavelength is proportional to the concentration of the element in the plasma, which in turn is proportional to its concentration in the electrolyte, which enters the plasma at a constant rate. The elemental concentration in the electrolyte, C_M (μg ml^{-1}), has a relationship with the elemental intensity values (I_M) as:

$$C_M = (I_M - I_M^\circ)\kappa_\lambda \tag{3.5}$$

where I_M° is the background intensity signal, and κ_λ is the sensitivity factor for a given wavelength. From **Fig. 3.11**, κ_λ can be obtained experimentally with the slope of each line. The C_M may be converted to elemental dissolution rate ν_M (μg s^{-1} cm^{-2}) with the flow rate f (ml min^{-1}) and the exposed reaction area A (cm^2) as:

$$\nu_M = fC_M/A \tag{3.6}$$

The specific data treatment processes are given in detail in each results chapter. Such as the conversion of ν_M to j_M and the convolution of j_e etc.

3.2 OTHER TECHNIQUES

3.2.1 X-RAY DIFFRACTION

X-ray diffraction is a powerful nondestructive technique for characterizing crystalline materials. It provides information on structures, phases, preferred crystal

orientations (texture), and other structural parameters, such as average grain size, crystallinity, strain, and crystal defects. The principle of XRD can be described using **Fig. 3.12**. When a monochromatic beam of X-rays is incident on a sample, the reflected X-rays follow Bragg's law ($n\lambda = 2d\sin\theta$). The X-ray diffraction pattern is a characteristic of the substance under investigation.

In this dissertation, it was used to characterize the phase structure of the alloys. A PANanalytical X'Pert Pro diffractometer was used with Cu(Kα1) radiation (λ = 1.5418 Å) directly on the specimen with the size of 20 mm × 20 mm. the angular resolution was 0.02° over the angular range of 5-80° (2θ) with 0.5 seconds acquisition time.

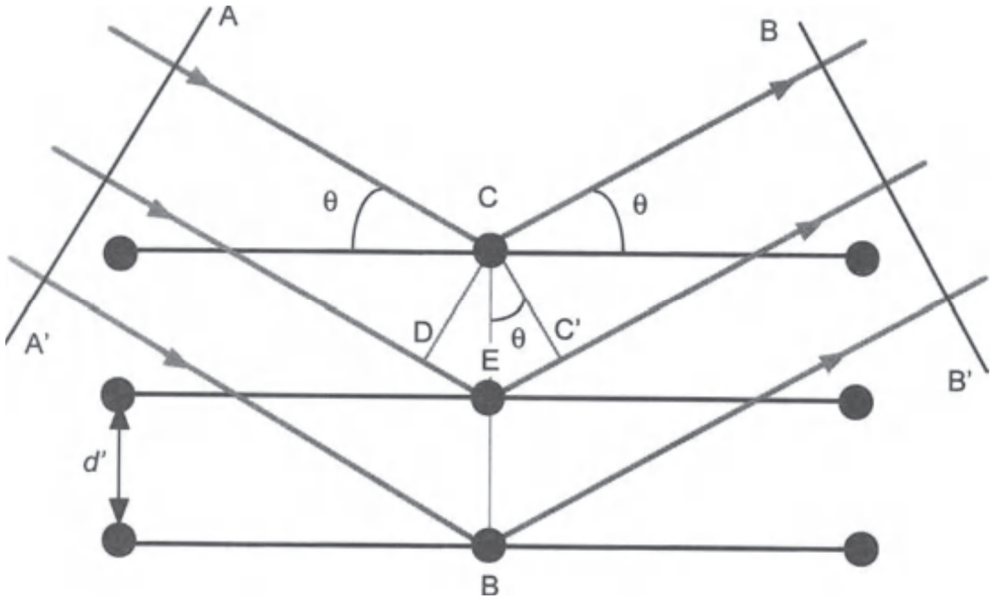

Figure 3.12 The schematic diagram of X-ray diffraction.

3.2.2 X-RAY PHOTOELECTRON SPECTROSCOPY

X-ray photoelectron spectroscopy (XPS) is a surface characterization technique that can analyze a sample to a depth of ~10 nanometers (nm)[173, 174]. Information that can be obtained from analyzing XPS results includes elemental composition, empirical formula, chemical state, and electronic state of the elements that exist within a material[173].

XPS measures the kinetic energy (K.E.) of the photoelectron, which is an electron

ejected by a photon. The photon interacts with a core level electron transferring its energy and causing the electron emission by the photoelectric effect. In practice, soft X-rays (Mg Kα = 1253.6 eV and Al Kα = 1486.6 eV) are usually used as the excited photon source. The K.E. measured by XPS is a function of the electron binding energy (B.E.) according to the following equation

$$K.E. = h\upsilon - B.E. - \theta_s \tag{3.7}$$

Where h is the Plank's constant, υ is the X-ray frequency, and θ_s is the instrument's spectrometer work function. Since B.E. of an electron in a particular shell of an atom is unique to each element, thus, identification of the elements present on a material's surface can be realized.

Fig. 3.13 gives the schematic diagram of an XPS instrument. The key components of a commercial XPS system include a source of X-rays, an ultra-high vacuum (UHV) stainless steel chamber with UHV pumps, an electron collection lens, an electron energy analyzer, Mu-metal magnetic field shielding, an electron detector system, a moderate vacuum sample introduction chamber, sample mounts, a sample stage, and a set of stage manipulators[175].

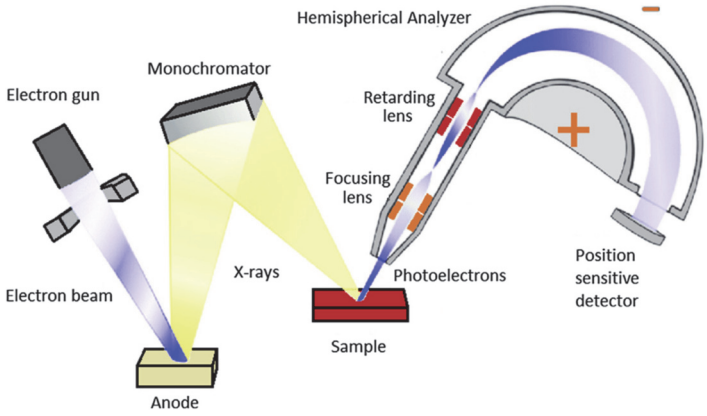

Figure 3.13 Schematic diagram of an XPS instrument[175]

.

4. THE PASSIVATION OF Ni-Cr-Mo ALLOYS: TIME RESOLVED SURFACE ACCUMULATION AND DISSOLUTION OF CR AND MO DURING PASSIVE-ACTIVE CYCLES[1]

In this chapter, the first attempt to investigate the passivation of Ni-Cr-Mo alloys with elemental-resolved AESEC was made on a commercial C-22 alloy.

ABSTRACT

The surface accumulation and dissolution of Cr and Mo were monitored as a function of time during potentiostatic active-passive cycles and during the spontaneous passivation of a Ni-Cr-Mo alloy (Hastelloy C-22) in 2 M H_2SO_4. Atomic emission spectroelectrochemistry was used to directly measure the elemental dissolution rates of the alloy components in real time and combined with a mass balance, the Cr and Mo surface accumulations were determined. Cr accumulation occurred during the passivation treatment either at an applied potential or spontaneously at open circuit. Mo accumulation occurred during spontaneous passivation and partially redissolved during polarization in the passive domain. The dissolution behavior of Mo corresponded well with the elemental polarization curves and thermodynamic calculations.

[1] This chapter repeats the article "X. Li, K. Ogle, The Passivation of Ni-Cr-Mo Alloys: Time Resolved Enrichment and Dissolution of Cr and Mo during Passive-Active Cycles, Journal of The Electrochemical Society, 166 (2019) C3179-C3185." with minor modification.

4.1 INTRODUCTION

The outstanding corrosion resistance of Ni-Cr alloys is due to the spontaneous formation of a "passive" film, in this case, a nanoscale Cr enriched oxide. This name passive film is however somewhat misleading as the film is actually very dynamic, forming and dissolving as a material interacts with its environment. Hugh Issacs[17] observed and discussed this dynamic behavior for a stainless steel in chloride electrolyte in his pioneering work with the scanning vibrating electrode. This work, likewise, seeks to observe in real time the formation and dissolution of the dynamic passive film by directly measuring the time resolved Cr, Ni and Mo surface accumulations via atomic emission spectroelectrochemistry (AESEC).

The passivation of Ni-Cr binary alloys was first investigated by Bond and Uhlig[108] and then in more detail by Myers, Beck and Fontana[109] who demonstrated that the addition of Cr to 20 to 30% greatly reduced the passive current density in H_2SO_4 by at least two orders of magnitude. The nature and composition of the film was only determined much later by ex situ surface analysis. In acidic sulfate solutions, the electrolyte of interest in this work, a nanometric duplex film of essentially pure Cr(III) oxides and hydroxides has been observed[111, 112]. For a pure Ni-Cr binary alloy in 0.5 M H_2SO_4, Jabs et al.[112] identified a Cr_2O_3 inner layer and $Cr(OH)_3$ outer layer. Marcus and Grimal[176] observed a 1.1 nm thick oxide film, consisting of an inner 96% Cr_2O_3 and 4% Fe_2O_3 and an outer layer of 100% $Cr(OH)_3$ film following a 300 s potentiostatic passivation of an Ni-Cr-Fe alloy in 0.05 M H_2SO_4. Oxidized Ni was conspicuously absent from the film although it has been detected for films formed in neutral and alkaline solution[11, 112].

The addition of Mo to the alloy results in a more corrosion resistant material, especially as concerns pitting and crevice corrosion[21, 177]. However, the results are contradictory regarding its presence in the passive film. G. Lorang et al.[11] studied a Ni-Cr-Mo alloy (Hastelloy C4) in neutral 5 M NaCl using Auger electron spectroscopy (AES) and ion sputtering. They found that the Mo concentration was just above the detection limit in the passive film and did not consider it further. Lloyd et al.[50], in their study of a series of Ni alloys in 1 M NaCl with 0.1 M H_2SO_4, including Hastelloy C4, showed that

Mo oxides were consistently present in the passive films despite the segregation of the film into a duplex structure for high Cr-content alloys. In this case, Mo was uniquely in the outer layer. The differences in alloy composition and electrolyte may play a role in the different observations but in summary, the role of Mo remains unclear.

Lutton et al.[178] applied inductively coupled plasma mass spectroscopy (ICP-MS) to measure current and dissolution rate for a chloride free, Na_2SO_4 of pH 5.5, for the passivation of Ni-Cr alloys at an applied potential of 0.2 V vs. SCE. In this near neutral solution, no Mo accumulation was observed. They interpreted their results in terms of a hydroxylated NiO was believed to build on the surface instead of more stable Cr_2O_3 due to the fast growth kinetics and slow dissolution rate of Ni^{2+} oxides.

In previous research, the direct measurement of elemental dissolution rates by AESEC during passivation has proven useful to understand selective dissolution and passivation for Cr containing alloys[39, 150, 179-182]. In particular, by applying a mass balance to the elemental dissolution rates, it was possible to monitor the time resolved elemental accumulations on the surface during electrochemical experiments. The formation and dissolution of the passive film on stainless steel was followed by monitoring the Cr accumulation as a function of time[150], and was extended to measure simultaneous Cr and Si accumulations for a Si rich stainless steel[39]. This article presents, for the first time, the extension of this technique to measure Cr and Mo accumulation and dissolution during the passivation of Ni alloys.

4.2 EXPERIMENTAL

4.2.1 MATERIALS

The Ni-Cr-Mo alloy used in this work was a single phase commercial Hastelloy C22 nickel alloy. **Table 4.1** gives the typical composition as published by the manufacturer (Haynes Intl.) and the composition of the specific sample used here. The nominally pure Ni sample was prepared from 99.99% Ni cylinders. They were arc melted into nickel lump under argon atmosphere and then cold-rolled into Ni sheet. Before each electrochemical experiment, the specimen was ground to 2000 silicon carbide paper, cleaned by deionized water and subsequently ethanol, then dried by nitrogen. All solutions used for

electrochemical experiments are 2 M H_2SO_4 prepared by using deionized water (18.2 MΩ cm, Millipore) and 95% sulfuric acid (Sigma Aldrich).

Table 4.1 Nominal composition of Hastelloy C-22, and the composition of the specific alloy used in this work obtained by determined by Cambridge Materials Testing Limited using ASTM E1019-18, ASTM E1097-12 and ASTM E1479-16. b = balance, M = maximum.

Alloy	Ni	Cr	Mo	Fe	W	Co	Mn	Si	C	V	Cu
Nominal	56[b]	22	13	3	3	2.5[M]	0.5[M]	0.08[M]	0.01[M]	0.35[M]	0.5[M]
ASTM	57.6	20.7	12.97	3.74	2.8	--	0.27	<0.01	0.012	--	0.06

4.2.2 INSTRUMENTATION

The AESEC system was used to measure elemental dissolution rates. It consists of an electrochemical flow cell coupled to an inductively coupled plasma atomic emission spectroscopy (ICP-AES) unit. The structure of the equipment has been described in detail elsewhere[150, 183]. A peristaltic pump was used to pump solution into flow cell and then into ICP-AES. Potential dynamic polarization curves were performed at a flow rate of approx. 1.5 ml/min to obtain better detection of elements in flowing solution. Transient potentiostatic experiments were performed at approx. 3 ml/min to optimize the time resolution of the experiment[163].

The wavelengths used for ICP-AES chosen for Ni, Cr, Mo, Fe and Mn, the detection limit of each element and the oxidation states used for calculating equivalent elemental current are shown in **Table 4.2**. The wavelength selectors in ICP-AES contains a polychromator and a monochromator. Normally the element detected by monochromator has lower detection limit. Cr was detected always with polychromator. Monochromator were used to detect either Ni or Mo, depending on requirement.

Conventional electrochemical methods were performed using a Gamry Reference 600. A saturated calomel electrode (SCE) and a Pt foil were used as reference and counter electrode respectively. All potentials are reported relative to SCE unless otherwise stated. Polarization curves were performed from the cathodic to anodic direction at 0.5 mV/s. The details of other experiments are described in the results section.

Table 4.2 ICP-AES parameters and assumed oxidation states for the calculation of effective dissolution current densities, **eq. (4.4)**.

Element	Ni	Cr	Mo	Fe	Mn
Wavelength (nm)	231.604	267.716	202.032	259.940	257.610
Detect limitation (ppb) at 3 ml/min	15.8 (poly)/4.7 (mono)	6.4(poly)	12.3(poly)/2.0 (mono)	3.8(poly)	0.7(poly)
Oxidation state	II	III	VI	III	II

4.2.3 DATA TREATMENT

The dissolution rate of each element, ν_M, may be determined from the emission intensity of that element at a specific wavelength I_λ as follows:

$$\nu_M = \frac{f\left(I_\lambda - I_\lambda^\circ\right)}{\kappa_\lambda A} \tag{4.1}$$

Where I_λ° is the background intensity, $\varkappa_\lambda$ is the sensitivity factor of this element at a certain wavelength. These values are determined by conventional ICP-AES calibration methods. The flow rate, *f*, is measured to 1% accuracy for each experiment. The surface area, A, is the geometric surface exposed to the electrolyte, defined by the O-ring of the electrochemical flow cell.

The total quantity of dissolved M at any time, $Q_M(t)$, may be calculated by integrating the dissolution rate of M:

$$Q_M(t) = \int_0^t \nu_M(t)dt \tag{4.2}$$

The total quantity of excess M accumulated at the surface, Θ_M, relative to Ni (or any other element) may be determined by mass balance as:

$$\Theta_M(t) = \left(\frac{X_M}{X_{Ni}}\right) \times Q_{Ni}(t) - Q_M(t) \tag{4.3}$$

where X_M is the mass fraction of element M determined from **Table 4.1**. The first term of **eq. (4.3)** gives the hypothetical dissolution rate assuming M dissolves congruently with

Ni. The difference between this term and the measured dissolution rate of M is a measure of surface accumulation of M. This assumes that the reference element (Ni in this case) completely dissolves in the oxidized state.

In order to compare the elemental dissolution rate with the external electrical current density, dissolution rate, ν_M was then transformed to elemental current density, j_M, by assuming z electron(s) are lost during the electrochemical process using **eq. (4.4)**

$$j_M = {(z_M F \nu_M)}/{m_M} \tag{4.4}$$

where z_M is the valence of the ion ejected into solution, m_M is the atomic mass of M, and F is the Faraday constant.

The faradaic yield of anodic dissolution may be determined by comparing the sum of the dissolution current densities, j_Σ, with the electrochemical current density measured with the potentiostat, j_e. Frequently it is interesting to normalize the elemental currents to the bulk alloy composition referencing them to Ni:

$$j'_e = \left(\frac{z_{Ni}\chi_{Ni}}{z_M\chi_M}\right) j_M \tag{4.5}$$

where χ represents the mole fraction, determined from **Table 4.1**.

During transient experiments, the comparison of j_e with dissolution rates requires a correction of the residence time distribution, h(t), of dissolved elements in the flow cell and capillaries of the system[163]. It has been demonstrated that h(t) follows a log-normal function:

$$h(t) = \begin{cases} \sqrt{\frac{\beta}{\pi\tau^2}} \cdot e^{-\frac{1}{4\beta}} \cdot e^{-\beta\left(ln\frac{t}{\tau}\right)^2} & if\ t > 0 \\ 0 & if\ t = 0 \end{cases} \tag{4.6}$$

where value of τ and β are empirically determined parameters, 0.99 and 10.23 respectively, obtained by applying a short anodic pulse to Cu in HCl solution[150].

4.3 RESULTS

4.3.1 OVERVIEW OF ELECTROCHEMICAL BEHAVIOR

An overview of the various electrochemical phenomena associated with Ni and the Ni-Cr alloy in 2 M H_2SO_4 may be deduced from the polarization curves shown in **Fig. 4.1**. Both materials exhibit passive behavior. Pure Ni (a) shows a broad active peak, followed by a passive domain ($0.2 < E < 0.8$ V), and finally a transpassive domain ($E > 0.8$ V). The C-22 alloy (b) shows the same basic phenomena but the passive current is reduced by nearly an order of magnitude, from 20 μA cm^{-2} to 4 μA $cm^{-2,}$ and the i_{crit} is reduced by three orders of magnitude, from 10 mA cm^{-2} to 13 μA cm^{-2}. This result demonstrates the contribution of the alloying elements to the formation of the passive film. The results of **Fig. 4.1** are in good qualitative agreement with the polarization curves of pure Ni and 77Ni-23Cr binary alloy in 1 M H_2SO_4 presented by Myers et al[109]. Note that the alloy also shows a second, very broad peak in the passive domain, the origin of which we will discuss shortly.

The passive film forms spontaneously for the C-22 alloy on contact with this electrolyte. This is demonstrated in **Fig. 4.1c** where the polarization sweep was begun only slightly below the open circuit potential. No active peak was observed, and the passive current was identical to that of the **Fig. 4.1b**. This further demonstrates that the more cathodic potentials used for **Fig. 4.1b** at least partially remove the passive film which reforms during the anodic sweep.

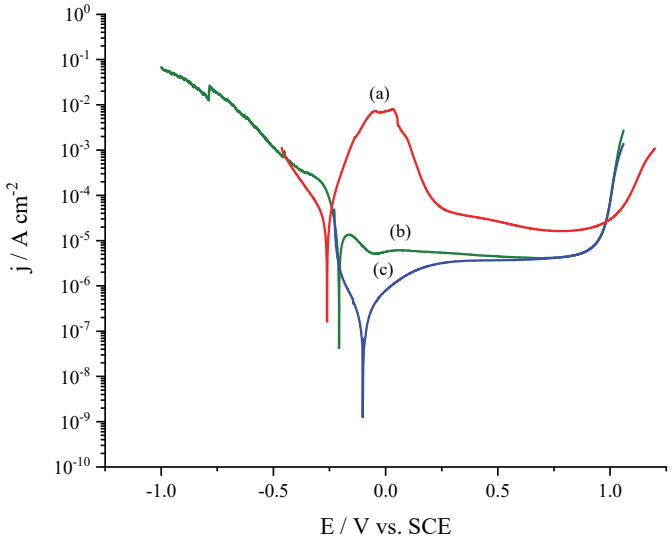

Figure 4.1 *Polarization curves of pure Ni (a) and C-22 Ni-Cr-Mo alloys (b, c) in 2 M H_2SO_4 with a starting potential at −1 V vs. SCE (b) and −0.2 V vs. OCP (c) at 0.5 mV/s and ambient temperature.*

Deeper insight into the electrochemical reactions occurring in each potential domain of **Fig. 4.1** may be obtained by considering the elemental dissolution rates. **Fig. 4.2** through **4** gives the AESEC polarization curves comparing the convoluted electrical current, j_e^*, overlaid with the apparent elemental currents, j_M from **Eq. (4.4)**. For nominally pure Ni (**Fig. 4.2**), j_e^* mirrors rather closely the nickel dissolution current showing two well-resolved anodic peaks as previously discussed in the literature[184], although $j_e^* > j_{Ni}$ throughout except in the final period. The difference between the two reflects the formation of insoluble oxidation products. A mass-charge balance indicates that 0.218 C cm^{-2} of excess charge is unaccounted for by the ICP-AES. Assuming a uniform thickness of $Ni(OH)_2$ on the surface of 4.1 g cm^{-3}, this would approximately correspond to a 162 nm film. The partial current due to oxide formation, j_{ox}, may be determined by mass-charge balance as $j_{ox} = j_e^* - j_{Ni}$. This is also shown in **Fig. 4.2**. It is seen that oxide growth ($j_{ox} > 0$) occurs throughout the active peak until the second maximum in current density (≈ 0.05 V), and beyond this, in the passive domain, oxide dissolution occurs ($j_{ox} < 0$). This result demonstrates that Ni oxide dissolution is kinetically slow, even in acidic electrolyte. Lutton et al.[178] explained the elemental dissolution rates of a Ni-Cr-Mo alloy measured by ICP-MS by a slow Ni oxide dissolution in a pH 5.5 chloride-free solution.

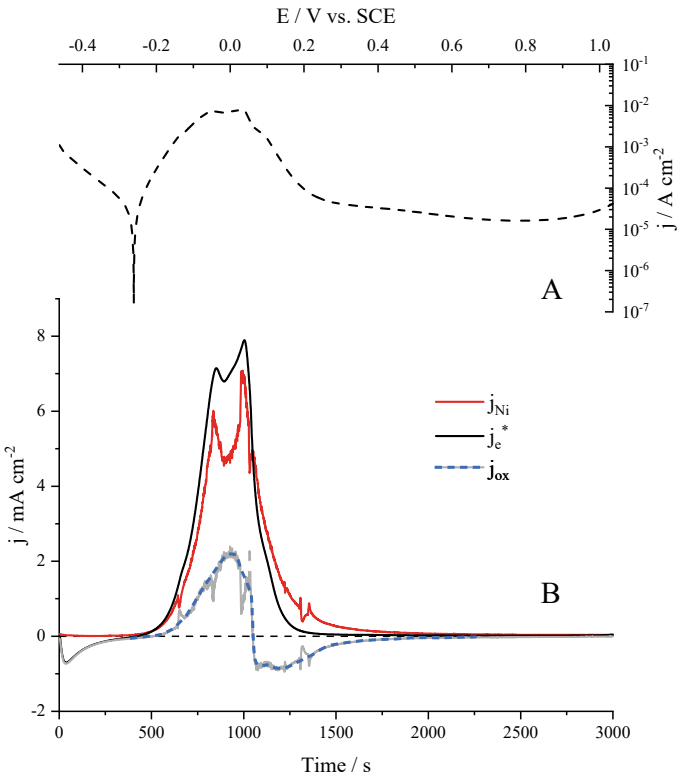

Figure 4.2 (A) Polarization curve of pure Ni at 0.5 mV/s and ambient temperature. (B) Convoluted electrical current density, j_e^* overlaid with AESEC elemental current, j_{Ni}, as a function of time. The partial current density, j_{ox}, associated with oxide formation and dissolution is shown as a dashed line.

For the C22 alloy, the elemental dissolution currents of Ni, Cr, Mo, Fe, Mn and their sum, j_Σ, are shown. Other alloying elements, W, Co, Si, V, and Cu were below the detection limit and are not shown and will not be discussed in this work. Unlike the case for pure Ni, the elemental dissolution does not mirror j_e (**Fig. 4.3**). A peak of elemental dissolution (a1), occurs just below the active peak in j_e (a2). Curiously, elemental dissolution is minimal during a2 demonstrating that most of the anodic current leads to the formation of insoluble oxides. This contrasts markedly with the Fe-Cr-Ni systems investigated previously in the same electrolyte[183] where elemental dissolution and electrical current were in very good agreement indicative of faradaic and congruent dissolution. This is an interesting result in light of the hypothesis of Marcus[185], discussed the role of alloying elements in terms of the metal-metal and metal-oxide bond strength. They concluded that Mo and W would favor oxide stability without dissolution while Cr and Ni favor metal dissolution, in qualitative agreement with our results.

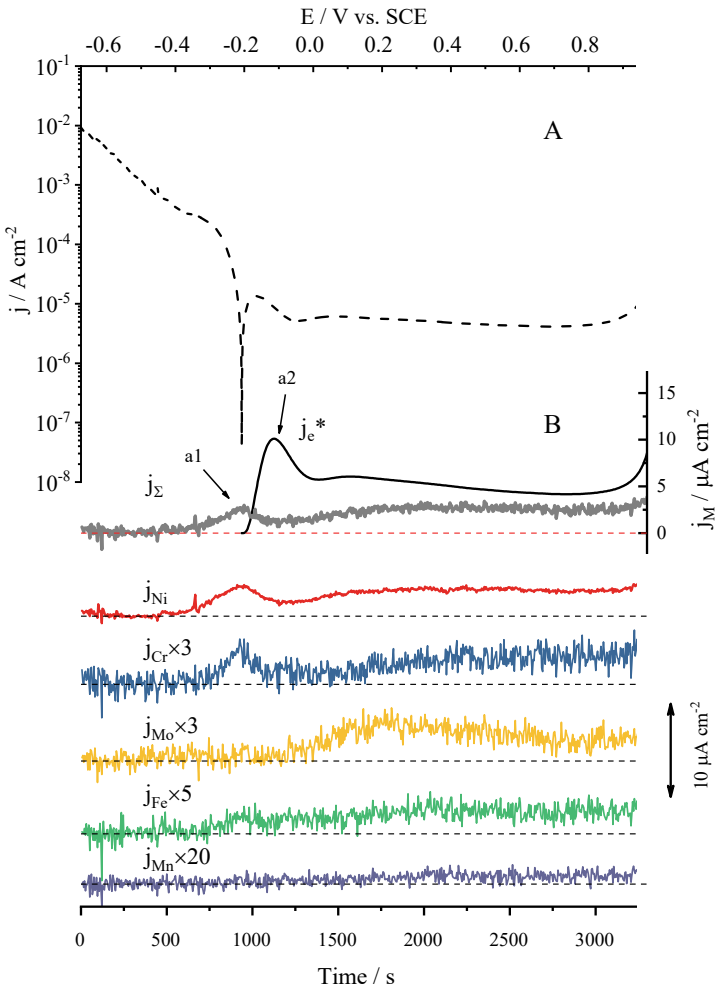

Figure 4.3 (A) Polarization curve of C-22 alloy in 2 M H_2SO_4 alloy started from −1 V vs. SCE at 0.5 mV/s and ambient temperature. (B) Convoluted electrical current, j_e^*, overlaid with the sum of the AESEC elemental currents, j_Σ. Single elemental current, j_M, is showed below with offset on different color. The dotted line below each elemental current indicates zero value. Some elemental currents were multiplied by a constant for clarity.

Of special interest for this work is the unique behavior of Mo. The elemental dissolution of Ni, Cr, and Fe all contribute to a1, while Mo does not rise above the detection limit, suggesting that Mo is retained on the surface during the first steps of passive film formation. As the potential increases above 0 V, Mo dissolution rate increases progressively, passes through a maximum, and is finally nearly congruent with Ni.

The mass charge balance during the active peak, a2, yields approximately 2.5 mC cm^{-2} of undetected oxidation, a factor of 100 less than for pure Ni and suggesting the formation of a nanometric film on the order of 2-3 nm. The mass-charge balance may be considered as a lower limit as the simultaneous cathodic reaction may mask some anodic current.

The polarization curve after spontaneous passivation in the electrolyte (**Fig. 4.4**, and **1c**) shows no active peak, and the current rises steadily from the $E_{j=0}$ to a steady-state passive current. The elemental dissolution rates of Cr, Mo, and Fe are above the detection limit but do not vary with potential. Only Ni contributes to the evolution of the passive current. For E > +0.2 V, it is observed that $j_e > j_\Sigma$ demonstrating that a significant quantity of oxidation did not dissolve in the electrolyte. This demonstrates that film growth continued after passivation.

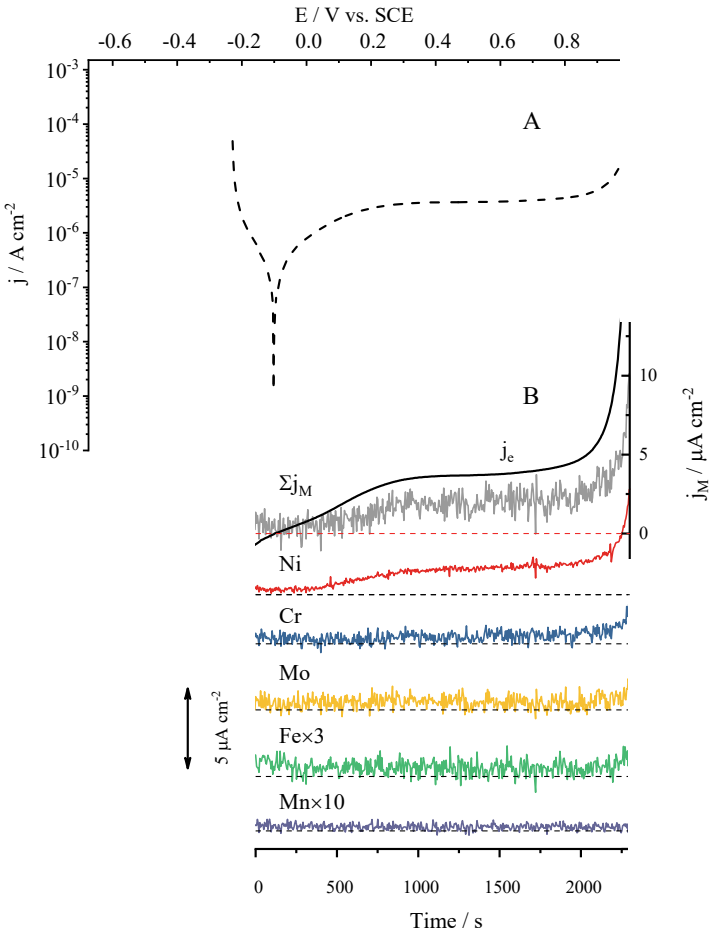

Figure 4.4 (A) Polarization curve of C-22 alloy in 2 M H_2SO_4 alloy started from −0.2 V vs. OCP at the scan rate of 0.5 mV/s and ambient temperature (B) Convoluted electrical current, j_e^*, overlaid with the sum of the AESEC elemental currents, j_Σ. Single elemental current, j_M, is showed below with offset on different color. The dotted line below each elemental current indicates zero value. Some elemental currents were multiplied by a constant for clarity.

4.3.2 PASSIVATION AT AN APPLIED POTENTIAL

To gain further insight into the passivation mechanism and kinetics, a potential step experiment was performed from the open circuit potential (≈ −0.2 V) into the passive domain (E_{ap} = +0.3 V). The open circuit potential was obtained after an activation step at −0.8 V followed by an open circuit exposure for 300 s described in detail in 4.3.3. The results of a typical passivation experiment are shown in **Fig. 4.5**. Note that the elemental current densities of Cr and Mo were normalized relative to Ni using **eq. (4.5)**. A significant quantity of Ni and Mo dissolve during the anodic transient. The Cr dissolution rate, however, does not significantly rise above the detection limit, clearly demonstrating that Cr is retained on the surface.

We attribute the Cr retention to the formation of the Cr oxide/hydroxide passive film. Once the potential was released after 120 s at +0.3 V, it dropped sharply to a stable 0.02 V, clearly in the passive state showing that the Cr oxide film is stable. The dissolution

of Mo at +0.3 V agrees with the elemental polarization curve (**Fig. 4.3**), where Mo dissolution was observed in this potential range.

Also shown is the electrical current density before (j_e) and after (j_e^*) numerical convolution. The unconvoluted current density shows a very sharp peak, rising to ≈ 220 mA cm^{-2} when E_{ap} is first applied, and then quickly drops towards zero. The current transient is consistent with a pulse of electrochemical dissolution and therefore, the dissolution transients resemble the log-normal distribution of residence times, h(t), associated with dissolved species in the flow cell[163]. This is demonstrated by the convoluted form of the current density (j_e^*) which shows a similar shape as the dissolution transients. The area of the j_e^* transient is only slightly larger than the dissolution transient, although it is somewhat broader again indicative of oxide formation.

The quantity of excess Cr, calculated from mass balance, is extremely small, estimated to be 0.128 μg cm^{-2} assuming 20.7% Cr. This would correspond to only 0.245 nm of a uniformly distributed Cr_2O_3 film with the usual density of 5.22 g cm^{-2}. The small thickness value may be attributed to the fact that the surface was already passive prior to the potential step. A mass-charge balance gives 377 μC cm^{-2} of charge, which would correspond to 0.38 nm, the same order of magnitude as determined by mass-balance.

These results are comparable to the Cr content of the passive film measured by AESEC for stainless steel in H_2SO_4[39]. The mass-charge balance was attempted in the former but required a complex calculation due to a high spontaneous corrosion rate prior to the step into the passive potential domain.

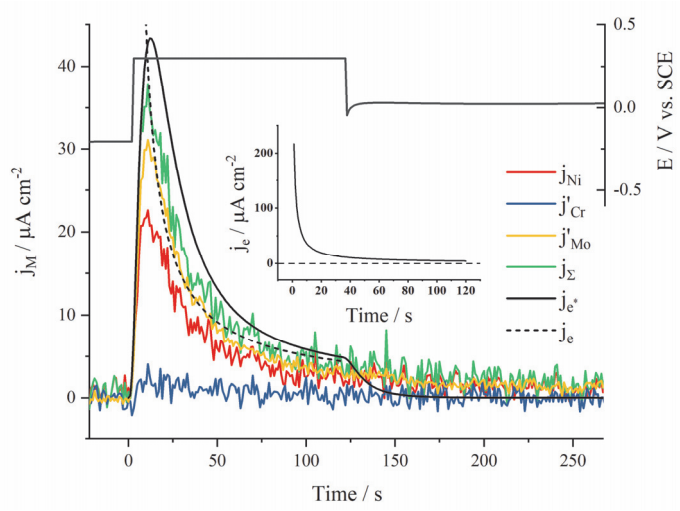

Figure 4.5 Potentiostatic passivation at +0.3 V. Shown are E, j_{Ni} and the normalized, j'_{Cr} and j'_{Mo}, during a potentiostatic sequence at +0.3 V vs. SCE in 2 M H_2SO_4 in ambient temperature. The sum of the elemental current, j_Σ, the convoluted electrical current, j_e^*, and the unconvoluted electrical current, j_e, are superimposed. The Inset shows the full amplitude of j_e.

4.3.3 ACTIVATION AND SPONTANEOUS PASSIVATION AT OPEN CIRCUIT

The Ni alloy undergoes spontaneous passivation when immersed in this electrolyte. The spontaneous passivation reaction may be monitored by following the elemental dissolution rate of Ni, however, it is first necessary to remove the preexisting passive film. This may be done by applying a cathodic pulse to the surface. We refer to this process as "cathodic activation". An example of this experiment is given in **Fig. 4.6** showing the applied potential and the elemental dissolution curves for Ni, Cr, and Mo. Activation involved a 120 s pulse to −0.8 V, during which period the dissolution of Cr, Ni, and Mo are observed, which we attribute to the dissolution of the passive film and perhaps a brief active dissolution of the alloy.

The precise mechanisms of activation are not clear, and the choice of −0.8 V was based upon a series of dissolution experiments at different potentials. Note that the intense cathodic current in this potential domain, not shown, was on the order of −25 mA cm^{-2} and dominated by hydrogen formation as indicated by the appearance of hydrogen bubbles in the electrolyte flow. This intense cathodic current would completely mask any anodic processes that might contribute to j_e making a mass charge balance during activation quite impossible. We attribute the elemental dissolution of Cr to the dissolution of the passive film by the reaction of

$$\mathrm{Cr(III)(oxide-hydroxide)} + e^- \rightarrow \mathrm{Cr^{2+}(aq)} \qquad (4.7)$$

which occurs simultaneously with the active dissolution of the alloy. The latter is indicated by the dissolution of Ni during this period. The reduction potential of Ni^{2+}/Ni ($E° = -0.58$ V vs. SCE) is more positive than the applied potential, $E = -0.8$ V. The intense cathodic current will lead to an uncompensated ohmic potential drop such that active Ni dissolution may occur, facilitated by the formation of hydrogen bubbles.

Following this step, the potential was released as shown in **Fig. 4.6**. It increased rapidly to approximately −0.2 V, coupled with the selective dissolution of Ni indicative of spontaneous passivation. Only a small peak of Cr, well below the congruent dissolution limit, was observed during this period and no detectable Mo. Considering the bulk composition of the alloy, the quantity of Ni dissolved at open circuit in **Fig. 4.6** corresponds to a Cr accumulation of 0.05 μg cm^{-2}, or 0.09 nm Cr_2O_3. Again, the value may only be considered as relative because it is based on the same assumptions of a congruent stoichiometry between Ni dissolution and Cr oxide formation, a uniform film, and the hypothesis that the cathodic activation step completely removes the passive film.

There is an important difference between the spontaneous passivation reaction and that which occurs at +0.3 V as concerns Mo dissolution. Nearly congruent Mo dissolution was observed at +0.3 V but is absent during spontaneous passivation. This is consistent with the polarization curve of **Fig. 4.3** as well, where no Mo dissolution is observed near $E_{j=0}$.

Also shown in **Fig. 4.6** is the dissolution rate of Ni obtained from a similar experiment conducted with pure Ni. The activation step leads to an intense dissolution of Ni, which dropped slowly. When released to the open circuit, the Ni dissolution rate increased progressively to about 40 μA cm^{-2}, consistent with the passive current observed in the polarization curve of **Fig. 4.1a**. Unlike the situation for the C-22 alloy, no dissolution maximum was observed.

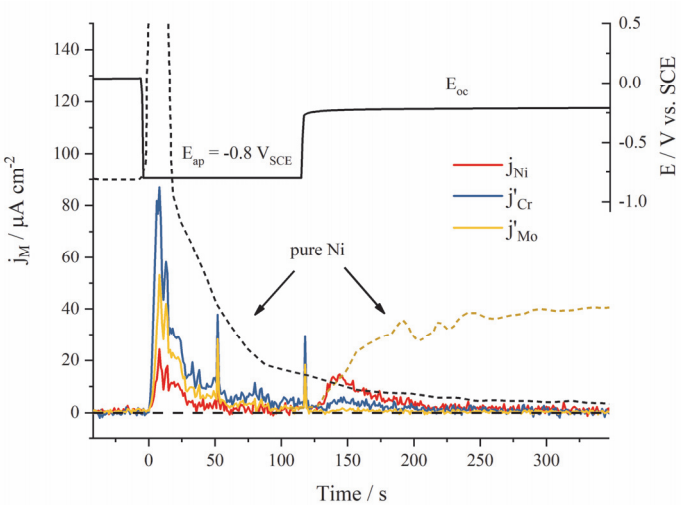

Figure 4.6 Cathodic activation at −0.8 V and spontaneous passivation. Shown are E, j_{Ni} and the normalized, j'_{Cr} and j'_{Mo}, during a potentiostatic sequence at −0.8 V vs. SCE in 2 M H_2SO_4 in ambient temperature. Also shown is j_{Ni} for a similar experiment for a nominally pure Ni sample. The E-t profile for pure Ni is not shown.

4.3.4 ELEMENTAL ACCUMULATIONS DURING ACTIVE-PASSIVE CYCLES

A series of active-passive cycles were applied to the sample following the protocol of previous work[39, 40]. The variation of excess Cr and Mo was determined from a mass balance by **eq. (4.3)**. An example is shown in **Fig. 4.7** for a period of three cycles. The first cathodic activation period (CA0, for t < 0) corresponds to the dissolution of the air formed passive film. Following this, the spontaneous passivation (SP1) leads to a sharp increase in Θ_{Cr} of approximately +0.08 µg cm^{-2} followed by a slow but readily detectable rise. The anodic passivation step at +0.3 V (AP1) leads to a second sharp jump in Θ_{Cr} and again followed by a slow progressive increase. The following cathodic activation step (CA1) results in a large decrease in Θ_{Cr} consistent with the dissolution of the passive film. The mass loss at CA1 is less than the growth during SP1 and AP1, which may be due to an incomplete removal of the passive film in the activation step. The figure shows that Θ_{Cr} is steadily decreasing when the potential is suddenly released and the Θ_{Cr} starts to increase. Also, hydrogen bubble formation during the activation step may partially block the surface so that less material is dissolved than is formed in the passivation step. Finally, the mass balance assumes that the alloy undergoing oxidation has the bulk composition given in **Table 4.1**. Relatively small variations in the bulk composition will affect the Θ_{Cr} calculated from selective Ni dissolution.

As the system evolves through the second and third cycles, the film growth/film dissolution ratio approaches unity (≈ 0.89), suggesting that it may have been approaching a steady state. Identical continuous curves are shown indicating the evolution of the

baseline and demonstrating that the difference between minimum and maximum is relatively constant. The variation of Mo was more complex. Mo accumulation occurred exclusively during spontaneous passivation, partially dissolved during the high potential step, and then dissolved completely during the activation step.

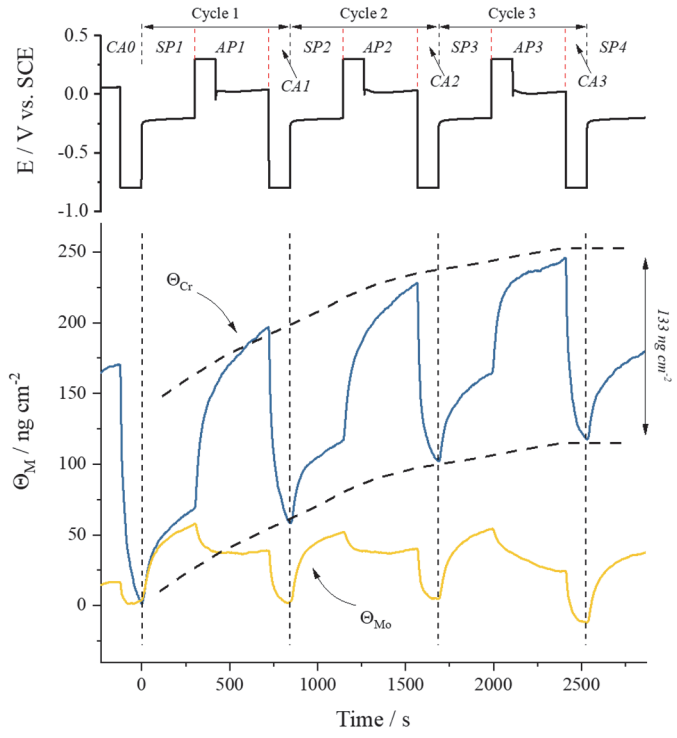

Figure 4.7 The accumulation of Cr and Mo as a function of time for a series of three potentiostatic passivation (+0.3 V vs. SCE)-activation cycles (−0.8 V vs. SCE).

A similar cyclic experiment was performed for the simple case of the spontaneous passivation shown for Cr and Mo in **Fig 4.8**. In this case, the Cr accumulation formed during spontaneous passivation was mostly dissolved during cathodic activation, with accumulation and dissolution following each other fairly closely, although the quantity of Cr decreased slightly with each cycle. Mo showed a very different behavior as accumulation occurred only during the spontaneous passivation and was only slightly dissolved during activation. The net result was that the quantity of Mo grew steadily on the surface.

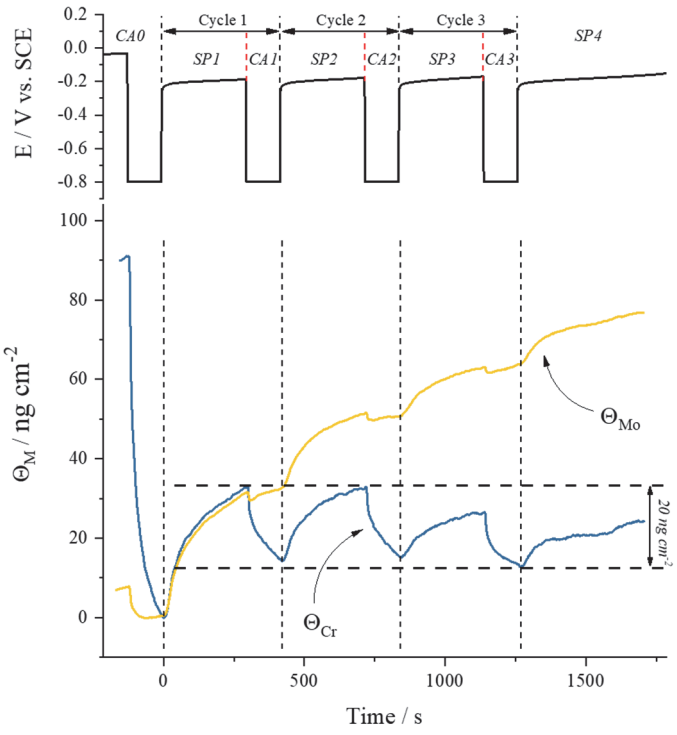

Figure 4.8 The accumulation of Cr and Mo as a function of time for spontaneous passivation (E_{oc} ≈ −0.2 V)-activation cycles (E_{ap} = −0.8 V vs. SCE).

4.4 DISCUSSION

The kinetics of Cr and Mo accumulation presented here yield new insights into the role of Mo and Cr during the passivation of the Ni-Cr-Mo alloys. It is observed that the two elements show a contrasting behavior during electrochemical experiments. As a point of reference, it is useful to consider the most thermodynamically stable species of the different alloying components, while keeping in mind the limitations of this approach. The predominant species of the different alloying elements is shown in **Fig. 4.9** as a function of potential for pH = 0 as determined with the Hydra-Medusa software and associated database[186]. Also shown is the calculated saturation concentration of dissolved Mo species. Note that the diagram for Fe and W are given below as references.

The interpretation of the accumulation and dissolution of Cr during the cyclic experiments of these experiments are fairly straight forward. The Cr(III) species that make up the passive film are stable at both the spontaneous passivation and the potentiostatic passivation potentials. Applying the activation potential leads to the formation of the soluble Cr(II) species with nearly complete dissolution of the film. This result is entirely consistent with previous work on stainless steel[39, 40], although the observation of Cr

accumulation during spontaneous passivation is a new result. The limits of the thermodynamic calculations are also clearly illustrated by this interpretation however, as Cr(III) is predicted to be completely soluble at this pH.

The variations of the Mo accumulation are more difficult to interpret. Most significant perhaps, is that whether or not Mo accumulation will occur depends on the potential at which passivation occurs. In this work, Mo accumulation occurred only during the spontaneous passivation step, consistent with the elemental polarization curves of **Fig. 4.3** in which no Mo dissolution was observed below 0 V. Therefore, whether or not Mo is accumulated in the passive film would depend on the history of the material and the specific conditions of passivation perhaps explaining some of the controversy on this issue.

Based on the predictions of **Fig. 4.9**, the accumulation of Mo during spontaneous passivation might be attributed to the formation of a Mo(IV) species, the most stable being MoO_2(s). Apparently, the following activation step did not lead to a significant removal of the excess Mo.

When the potential is stepped to 0.3 V, Mo dissolution did occur both in the polarization curve and during potentiostatic experiments. From the predominant species calculations, this might be associated with the Mo(IV) to Mo(VI) species, the most stable being the slightly soluble H_2MoO_4.

$$MoO_2 \rightarrow H_2MoO_4 + 2e^- \qquad (4.8)$$

This species, in turn, apparently dissolves during the activation step rather than undergo a transformation to MoO_2(s).

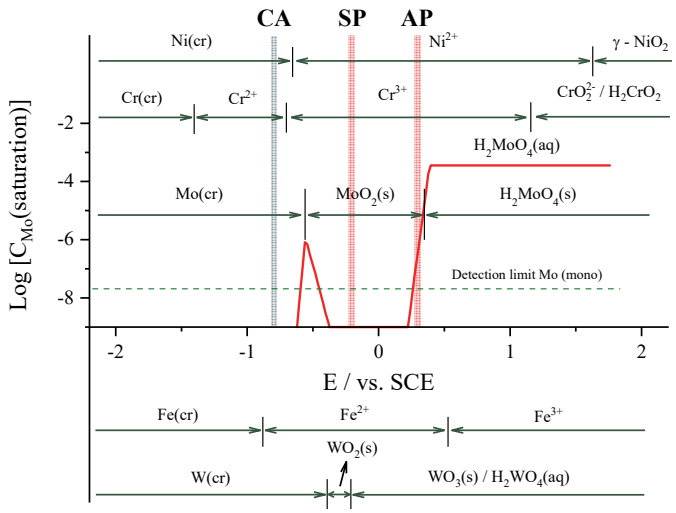

Figure 4.9 Predominant species for Ni, Cr, Mo, Fe, and W as a function of potential for pH = 0 as determined by Hydra-Medusa and the associated database. Also shown is the predicted saturation concentration of total dissolved Mo species.

These results are consistent with Maurice et al.[132] who demonstrated on stainless steel in 0.05 M H_2SO_4, that Mo was mostly present as Mo(IV) in the Cr-rich inner layer prior to anodic polarization, and became increasingly enriched (up to 16% of cations) as Mo(VI) in the outer layer of the passive film. Again this would indicate the change in state between the Mo(IV) and Mo(VI) species, the latter being relatively more soluble and prone to dissolution. Also, for stainless steel, the accumulation of Mo in the inner layer was demonstrated by Olsson et al[187]. Our results complement these studies demonstrating that Mo retention and dissolution may depend on the history of the sample, varying with potential and pH.

These results may also be compared with another recent AESEC study for the same alloy, among several others, which showed that, in an initially neutral chloride solution, Mo accumulation occurred in the transpassive domain and dissolved in the passive domain[182]. In that work, unbuffered solutions were used, and it was postulated that Mo retention was associated with local pH changes, the acid pH favoring the formation of the less soluble Mo species.

4.5 CONCLUSIONS

This work has demonstrated the use of AESEC to monitor the formation and dissolution of surface accumulations of Cr and Mo during active-passive cycles and during spontaneous passivation of a Ni-Cr-Mo alloy. The active peak of the polarization curve for C-22 was not associated with a significant elemental dissolution, indicting an important

difference as compared to the previously investigated austenitic stainless steel (Fe-Cr-Ni alloys) in the same electrolyte. Rather elemental dissolution occurred before the active peak and during the passive domain.

The formation and dissolution of a Cr accumulation were observed during cyclic potentiostatic passivation (+0.3 V) and activation (−0.8 V), respectively, and during spontaneous passivation at the open circuit potential. This accumulation was attributed to the formation and dissolution of the passive film. Mo accumulation was only observed during spontaneous passivation (≈ −0.2 V). Under anodic polarization, partial Mo dissolution was observed, which then dissolved completely during the activation cycle from high potential. When cycling between spontaneous passivation (≈ −0.2 V) and the activation potential, very little Mo dissolution was observed, suggesting that the nature of the surface Mo species was altered by the application of an anodic passivation potential. These results are consistent with thermodynamic considerations that indicate the predominant formation of a very weakly soluble MoO_2 during spontaneous passivation (≈ −0.2 V) and a more soluble H_2MoO_4 at the anodic passivation potential (+0.3 V).

5. THE CONTRIBUTION OF Cr AND Mo TO THE PASSIVATION OF Ni22Cr AND Ni22Cr10Mo ALLOYS IN SULFURIC ACID[2]

Continuing the work in **chapter 4**, to further clarify the role of Cr and Mo on passivation of Ni-Cr-Mo alloys, synthetic Ni-Cr and Ni-Cr-Mo alloys were studied with in situ AESEC coupled with ex situ XPS in this chapter.

ABSTRACT

The beneficial effects of Mo on passive film formation were investigated for Ni22Cr10Mo with in situ AESEC and XPS by comparison with Ni22Cr and pure Ni and Mo. Both spontaneous ($E \approx -0.2\ V_{SCE}$) and anodic passivation ($E = +0.3\ V_{SCE}$) showed Cr accumulation, while significant Mo accumulation (as Mo(IV)) only occurred during spontaneous passivation with a markedly reduced open circuit corrosion rate as a consequence. Mo facilitated the active to passive transition in the low potential domain probably by favoring the oxidation of Cr to Cr_2O_3 over $Cr(OH)_3$. At higher potential, Mo dissolved as Mo(VI) and did not accumulate on the surface.

[2] This chapter repeats the article "X. Li, J. D. Henderson, F. P. Filice, D. Zagidulin, M. C. Biesinger, F. Sun, B. Qian, D. W. Shoesmith, J. J. Noël, K. Ogle, The contribution of Cr and Mo to the passivation of Ni22Cr and Ni22Cr10Mo alloys in sulfuric acid, Corrosion Science, in press" with minor modification.

5.1 INTRODUCTION

Ni-Cr-Mo alloys are a class of corrosion resistant alloys commonly used in the petrochemical, nuclear, and chemical processing industries and have been suggested as one of the corrosion resistant engineering barriers in the proposed Yucca Mountain spent nuclear fuel repository[188]. The alloying elements, Cr and Mo, play an important role in establishing the corrosion resistance of the alloy. Cr is known to promote the formation of a corrosion resistant surface oxide, known also as a passive film. That Cr is the majority species in the passive film has been confirmed by various techniques[29, 40, 111]. Additions of Mo to the alloy have been shown to stabilize the passive film, especially when there is a risk of localized corrosion[24, 126, 127]. The benefits of alloyed Mo are empirically known, yet the underlying mechanisms are not well understood[189]. Many studies have been carried out to clarify the role of Mo and yet even the conditions under which Mo may be accumulate in the passive film remain uncertain. Some studies suggest Mo enriches in the film[30, 132, 139] while some others suggest the opposite[8, 60, 145, 146]. The proposed mechanisms by which Mo may promote passivation include a beneficial influence on repassivation, in which case Mo may have only a transitory existence in the film[126, 190, 191], and/or the formation of an ion-selective layer of Mo species, reinforcing the protectiveness of the Cr-based film[50, 62].

Zhang et al.[192] recently proposed a theory that the accumulation or depletion of Mo in the passive film is strongly correlated with the nature of the solution, based on their aberration-corrected transmission electron microscopy results. Solutions containing Cl^- induced the accumulation of Mo. They proposed that Cl^- ions could extract Mo from the matrix into the electrolyte solution by forming a soluble $MoCl_x$ complex, then the $MoCl_x$ could be further oxidized to Mo oxide and enriched in the outer region of the passive film. However, other researchers have reported Mo depletion in the passive film in solutions containing Cl^-[60, 193]. Inline ICP-MS, coupled with other in situ and ex situ techniques, was recently employed by Cwalina et al.[46] to investigate the kinetics of oxide formation and growth on Ni22Cr and Ni22Cr6Mo (wt.%) alloys in 0.1 M NaCl solutions with the pH adjusted to 4 and 10. It was found that the addition of Mo to the Ni22Cr alloy resulted in the increased accumulation of Cr in the surface film.

We have recently demonstrated that the accumulation of Cr and Mo could be monitored quantitatively as a function of time during electrochemical experiments with a commercial Ni22Cr10Mo alloy, Hastelloy C-22, in sulfuric acid, using atomic emission spectroelectrochemistry (AESEC)[45]. Besides having the ability to passivate in sulfuric acid when an anodic polarization was applied, it also spontaneously passivated at the open-circuit (or corrosion) potential, E_{oc}. We demonstrated that the accumulation of surface Cr occurred during both spontaneous passivation and anodic passivation, attributed to the build-up of Cr oxides as a passive film. The film was removed by a subsequent cathodic activation. By contrast, Mo accumulation only occurred during spontaneous passivation at open circuit following cathodic activation. This excess Mo partially dissolved during a subsequent anodic passivation step ($E = 0.3\ V_{SCE}$) and almost completely dissolved during the following cathodic activation ($E = -0.8\ V_{SCE}$). Therefore, it was proposed that Mo accumulation in the oxide film was strongly influenced by the history of the material and the specific conditions of passivation. Based on thermodynamic considerations, the accumulation of Mo in the film during spontaneous passivation at lower potential was attributed to the formation of insoluble Mo(IV) oxides; their subsequent dissolution at higher potential was attributed to the oxidation of these oxides to the more soluble Mo(VI) species.

The goal of this work is to further clarify the role of Mo on the kinetics of passive film formation and dissolution. To this end we present new results with a simplified ternary alloy (Ni22Cr10Mo). To highlight the role of Mo, we compare the behavior of this material with the binary alloy (Ni22Cr) and with pure Mo and Ni using a combination of in situ AESEC and ex situ XPS for the alloys.

5.2 EXPERIMENTAL

5.2.1 SAMPLE PREPARATION

The Ni22Cr and Ni22Cr10Mo (wt.%) alloy ingots were fabricated using an Edmund Bühler MIM1 arc-melting system operated under an Ar atmosphere. Pure Ni (99.99%), Cr (99.99%), and Mo (99.99%) metals were used to obtain the desired compositions. The melting process was repeated at least three times for each alloy, with ingots turned over after each melting process. The as-fabricated ingots were annealed at

1000°C for 24 h under vacuum (10^{-5} mbar). The annealed ingots were then cold rolled into sheets. The as-rolled sheets were solution-treated at 1000°C under vacuum (10^{-5} mbar) for 24 hours and then quenched in water. The as-quenched samples were confirmed to be single fcc phase using X-ray diffraction (XRD), not shown. Samples used for AESEC and XPS experiments were cut from the sheet, mechanically ground by a series of SiC papers up to P4000 then polished to a mirror finish using 1 μm diamond suspension. Before each experiment, samples were rinsed with deionized (DI) water.

5.2.2 ATOMIC EMISSION SPECTROELECTROCHEMISTRY

Atomic emission spectroelectrochemistry (AESEC) is based on the combination of an electrochemistry flow cell with an inductively coupled plasma atomic emission spectrometer (ICP-AES). The AESEC technique has been comprehensively reviewed in the recently published article by Ogle[151]. The principle of AESEC is to collect and analyze species released from a sample surface in real-time while conducting electrochemical measurements. To achieve this, a specially designed flow cell is used to carry out the electrochemistry. Meanwhile, the ICP-AES is used to detect the dissolved species downstream. As a result, the dissolution rate of each element as a function of time can be obtained. Additionally, by assuming the oxidation state of each element, the dissolution rates can be converted into elemental currents to compare with the external electrical current measured by the potentiostat. The emission wavelengths selected for analysis of Ni, Cr, and Mo are shown in **Table 5.1**, as well as the detection limits defined as ($C_{3\sigma} = 3\sigma/\varkappa$) where σ is the standard deviation of background intensity in the absence of the element and $\varkappa$ is the sensitivity (i.e. slope) of the intensity vs. concentration curve. Note that detection limits may vary considerably from one experiment to the next depending on plasma conditions. In all cases, the polychromator of the ICP-AES spectrometer was used for both Ni and Cr, and the monochromator was used for Mo. Additionally, the equivalent detection limits expressed in dissolution rates and electrical current densities are shown. The calculation of ν_M and j_M are described in the data treatment section.

Table 5.1 Wavelengths and typical experimental detection limits for Ni and Cr (polychromator), and Mo (monochromator). Equivalent dissolution rates and current densities at the flow rate of 1.5 ml/min are also shown. The latter were calculated with the oxidation states of Ni(II), Cr(III), and Mo(VI).

Element	Ni	Cr	Mo
Wavelength / nm	231.604	267.716	202.032
Detection limit / ng cm^{-3}	12	6.2	1.4
ν_M / ng cm^{-2} s^{-1}	0.30	0.16	0.035
j_M / μA cm^{-2}	0.99	0.89	0.21

5.2.3 ELECTROCHEMICAL SETUP

Immediately after surface preparation, samples were assembled with the homemade electrochemical flow cell, exposing either 0.5 or 1 cm^2 of the surface to the electrolyte. A typical three electrode system was used during all electrochemical measurements. Electrochemical experiments were performed using a Gamry Instruments Reference 600 for AESEC experiments or a Solartron 1287 potentiostat for XPS sample preparation. The sample served as the working electrode (W.E.). A Pt foil serving as the counter electrode (C.E.) and a saturated calomel electrode (SCE) as the reference electrode (R.E.) were placed in a second compartment separated from the W.E. by a conductive membrane. Solutions of 2 M H_2SO_4 were made by mixing DI water and 95% H_2SO_4. The electrolyte was pumped into the cell at a speed of ~3 ml per minute (cyclic potentiostatic experiments) or ~1.5 ml per minute (potentiodynamic polarization). Deaeration was achieved by sparging Ar gas into the solution for 30 mins before the experiment and continuously until the experiment finished. Aerated solution refers to the solution exposed to air.

5.2.4 DATA TREATMENT

The emission intensity of the element M at the specific wavelength (I_λ) obtained from ICP-AES (Horiba, Ultima 2C) was converted into a dissolution rate (ν_M) according to **eq. (5.1)**.

$$\nu_M = \frac{f\left(I_\lambda - I_\lambda^\circ\right)}{\kappa_\lambda A} \tag{5.1}$$

where I_λ° is the background intensity, and $\varkappa_\lambda$ is the sensitivity factor of element M at the chosen wavelength, determined by conventional ICP-AES calibration methods using commercially available element standards (PlasmaCAL, SCP Science). The flow rate, f, was measured to a relative error of ≤ 1% for each experiment. The surface area, A, is the geometric surface of the W.E. exposed to the electrolyte, defined by the O-ring of the electrochemical flow cell.

The dissolution rate of element M (ν_M) may be normalized to the bulk composition relative to a chosen element (N) by **eq. (5.2)**.

$$\nu'_M = \left(\frac{X_N}{X_M}\right) \nu_M \tag{5.2}$$

where X_M and X_N are the mass fractions of elements M and N, respectively.

The surface excess (relative to Ni) of an element M, Θ_M, from time A to time B, may be determined by **eq. (5.3)**

$$\Theta_M = \int_A^B \left(\frac{X_M}{X_{Ni}} \nu_{Ni} - \nu_M\right) \tag{5.3}$$

An increase of Θ_M indicates M is accumulating on the surface while a decrease of Θ_M indicates excess dissolution of M.

To compare the elemental dissolution rate (ν_M) with the external electrical current density (j_e) measured by the potentiostat, ν_M may be converted to an equivalent elemental current density, j_M, by **eq. (5.4)**:

$$j_M = {(n_M F \nu_M)}/{m_M} \tag{5.4}$$

where n is the presumed number of electron(s) involved in the electrochemical dissolution reaction, m_M is the atomic mass of M, and F is the Faraday constant.

During transient experiments at short times, the comparison of j_e with the sum of the elemental currents (Σj_M) requires a correction of the residence time distribution, h(t),

of dissolved elements in the flow cell and capillaries of the system[163]. It has been demonstrated that h(t) follows a log-normal function:

$$h(t) = \begin{cases} \sqrt{\frac{\beta}{\pi\tau^2}} \cdot e^{-\frac{1}{4\beta}} \cdot e^{-\beta\left(\ln\frac{t}{\tau}\right)^2} & \text{if } t > 0 \\ 0 & \text{if } t = 0 \end{cases} \quad (5.5)$$

where the values of τ and β are empirically determined parameters, 0.99 and 10.23 respectively, obtained by applying a short anodic pulse to Cu in HCl solution[150, 163]. It was demonstrated that the correction of the current density may be realized by convoluting j_e using **eq. (5.6)**[150].

$$j_e^*(t) = \int_0^t j_e(\tau)h(t-\tau)d\tau \quad (5.6)$$

5.2.5 XPS CHARACTERIZATION

Specimens considered for XPS characterization were prepared using the identical electrochemical flow cell setup enclosed in a N_2-filled glove box to minimize the influence of oxygen exposure. The oxygen level in the glovebox was controlled in the range of 50 ppm to 100 ppm. After treatment, each sample was rinsed with DI water, dried, and stored in a separate Ar-filled glove box with oxygen levels continuously maintained at 0.1 ppm until XPS analysis.

XPS measurements were carried out using a Kratos AXIS Supra spectrometer. All spectra were collected using the monochromatic Al Kα X-ray source (photon energy = 1486.6 eV) operating at 12 mA and 15 kV (180 W). During analysis, pressures inside the analysis chamber were maintained at, or below, 10^{-8} Torr. Calibration of the instrument work function was done using the binding energy (B.E.) of a standard metallic Au sample ($4f_{7/2}$ at 83.95 eV). In all spectra, photoelectrons were collected from an area of 700 μm × 400 μm. For all samples, spectra were collected at multiple take-off angles including 90, 50, 30, and 15°; however, only the 90° data set is described here due to the high noise level associated with the lower angles.

Survey spectra were recorded over a B.E. of 0-1200 eV using a pass energy of 160

eV at a step size of 1 eV. High-resolution spectra of the C 1s, O 1s, Ni 2p, Cr 2p, Mo 3d, and S 2p lines were collected using a pass energy of 20 eV at a step size of 0.1 eV. All spectra were charge-corrected by setting the aliphatic (C-C) adventitious carbon signal to 284.8 eV. All signal processing and deconvolution were performed with CasaXPS software (v2.3.19) using a Shirley background subtraction. The deconvolution of high-resolution spectra was done using previously determined fitting parameters and constraints collected from standard metallic and oxide samples of Ni[68, 194], Cr[68, 195], and Mo[196].

5.3 RESULTS

5.3.1 OVERVIEW OF ELECTROCHEMICAL BEHAVIOR

Fig. 5.1 shows conventional polarization curves for Ni22Cr and Ni22Cr10Mo alloys in aerated and deaerated 2 M H_2SO_4. Both alloys showed an anodic peak denoting the active to passive transition and a well-defined passive domain. For convenience, these two anodic domains will be labelled A1 ($\sim -0.25\ V_{SCE} < E < \sim 0.1\ V_{SCE}$) and A2 ($E > \sim 0.1\ V_{SCE}$) respectively as indicated. For Ni22Cr10Mo, current densities were lower in magnitude in both the cathodic domain (C, $E < -0.25\ V_{SCE}$) and the active to passive transition (A1) as compared to Ni22Cr. The effect was particularly marked for the critical current (maximum of A1) for which approximately an order of magnitude decrease was observed. Within the passive domain (A2), current densities were comparable for both Ni22Cr and Ni22Cr10Mo. By comparing the potentiodynamic polarization curves, we conclude that Mo promotes the formation of the passive film during the active to passive transition in the low potential domain (A1) but does not seem to alter the protective nature of the film once formed in the high potential domain (A2). This is consistent with what has been previously reported on Ni alloys[48, 50, 197] and for stainless steel[140].

Deaeration of the electrolyte had little influence on the electrochemistry (**Fig. 5.1**) for either alloy. The slight increase in the critical current density after deaeration may be attributed to the elimination of oxygen reduction, which also occurs in this potential range, the total current being the sum of the cathodic and anodic partial reactions. This same effect also accounts for the slight shift of the peak position and E_{corr} to a lower potential in both cases. Although the effect was minimal, deaeration was important for this study so as to have the maximum resolution of the anodic reactions in the domain A1, where the

effect of Mo is most clearly visible.

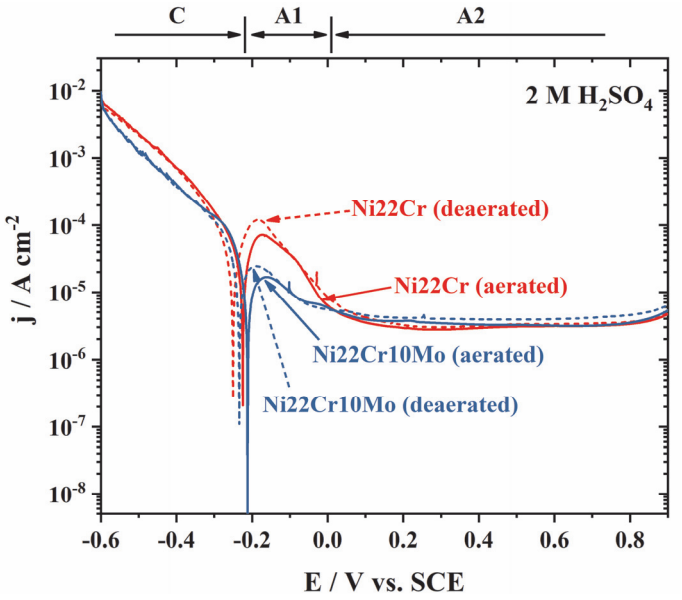

Figure 5.1 The potentiodynamic polarization curves of Ni22Cr (red) and Ni22Cr10Mo (blue) alloys in aerated (solid line) and deaerated (dotted lines) 2 M H_2SO_4, at ambient temperature, from −0.6 V_{SCE} to 0.9 V_{SCE} at 0.5 mV s^{-1}.

5.3.2 ELEMENTAL ELECTROCHEMISTRY OF Ni22Cr AND Ni22Cr10Mo

Elementally resolved polarization curves in aerated and deaerated 2 M H_2SO_4 solutions are shown in **Fig. 5.2** and **Fig. 5.3** for alloys Ni22Cr and Ni22Cr10Mo, respectively. The conventional polarization curve, identical to **Fig. 5.1**, is shown in the upper part of each figure. The lower part shows the elemental currents for Ni (j_{Ni}), Cr (j_{Cr}), and Mo (j_{Mo}). Elemental currents were calculated from the elemental dissolution rate according to **eq. (5.4)** assuming $n_{Ni} = 2$, $n_{Cr} = 3$ and $n_{Mo} = 6$. The green dashed lines overlaid with j_{Cr} and j_{Mo} are the expected elemental currents, j_{Cr° and j_{Mo°, assuming congruent dissolution with Ni, based on the following equation:

$$j_{M^\circ} = \left(\frac{\chi_M}{\chi_{Ni}}\frac{n_M}{n_{Ni}}\right) j_{Ni} \qquad (5.7)$$

where χ_M is the mole ratio of element M (Cr or Mo). The sum of the elemental dissolution currents, Σj_M, is also compared with the total electrical current, j_e.

During all polarization measurements in **Fig. 5.2** and **Fig. 5.3**, an excess dissolution of Cr ($j_{Cr} >> j_{Cr^\circ}$) was seen at the onset of the cathodic polarization (−0.6 V_{SCE}). For Ni22Cr10Mo, excess Mo dissolution ($j_{Mo} >> j_{Mo^\circ}$) was also observed. This may be

attributed to the dissolution of the air-formed oxide. As the applied potential was increased, elemental currents stabilized at low values, around the detection limit. This continued until the active to passive transition, where both j_{Ni} and j_{Cr} showed a peak. Deaeration had little to no effect on the elemental dissolution rates.

Unlike the case for a 304 stainless steel[183], anodic dissolution of Ni22Cr was not faradaic. Considering the active peak for the deaerated solution, a faradaic dissolution yield of 56.7% was obtained based on the assumption of $n_{Ni} = 2$ and $n_{Cr} = 3$. The electrical current that did not lead to dissolution ($j_\Delta = j_e - \Sigma j_M$, shown as the blue dotted line in **Fig. 5.2b**) may be attributed to the formation of insoluble oxides for the deaerated solution, as the cathodic current is negligible. Integration of j_Δ yielded 14 mC cm^{-2} corresponding to a film thickness of 7 nm if only the formation of Cr_2O_3 is considered.

The accumulation of Cr in the film was observed in the active to passive transition domain (A1) for the Ni22Cr alloy. This is indicated by calculating the partial rate of Cr accumulation, $j_{\Delta Cr} = j_{Cr^\circ} - j_{Cr}$, shown in the insets of **Fig. 5.2a** and **b**. A broad, secondary dissolution peak (labelled "α") was detected during the descending edge of the active dissolution peak, ($\Sigma j_M > j_e$) implying that non-faradaic dissolution occurred. This supports the idea that excess oxide formation occurred in the active domain, and this excess oxide subsequently dissolved to leave the final passive film. Lutton et al. also observed a delayed dissolution of excess oxide during potentiostatic passivation experiments on Ni22Cr and Ni22Cr6Mo alloys[178].

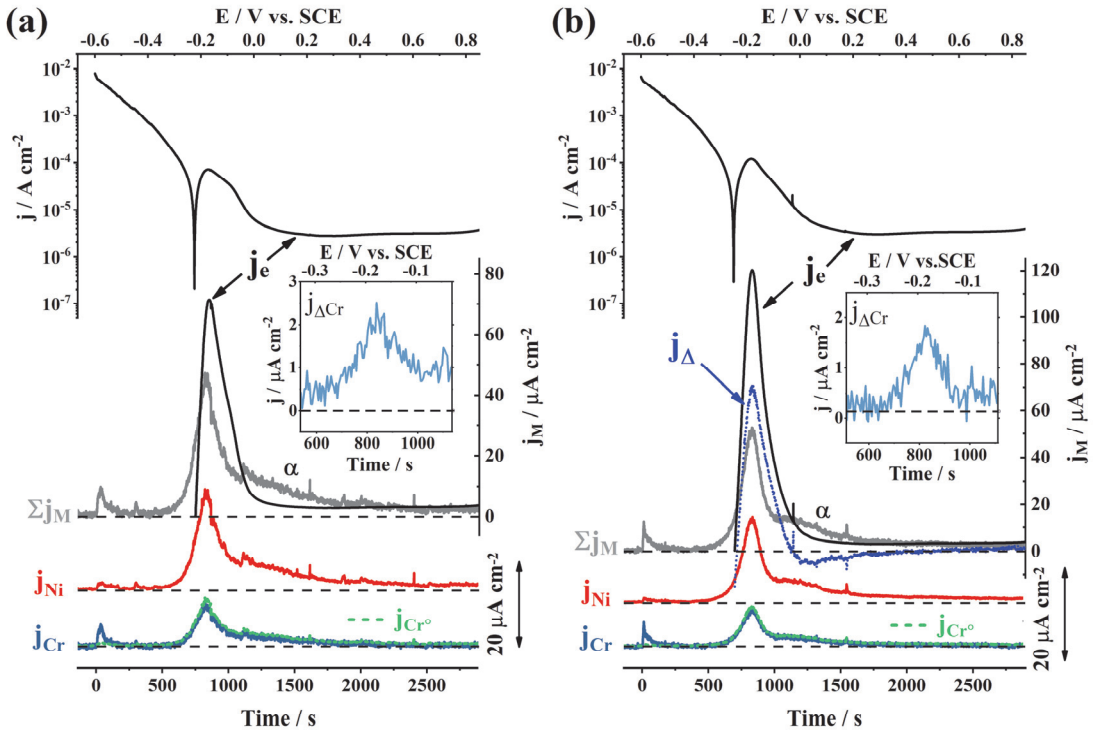

Figure 5.2. Elemental resolved potentiodynamic polarization curve for Ni22Cr recorded in aerated (a) and deaerated (b) 2 M H_2SO_4. For j_e in the bottom panels, only positive values are shown. Σj_M indicates the sum of the elemental currents. Elemental currents of Ni(II) and Cr(III) are offset for clarity. The green dashed lines are assumed congruent elemental currents for Cr (relative to Ni). Shown in insets are $j_{\Delta Cr} = j_{Cr^\circ} - j_{Cr}$, showing the accumulation of Cr during the active to passive transition.

For Ni22Cr10Mo (**Fig. 5.3**), $j_e > \Sigma j_M$ in the active to passive transition domain (A1) and the passive domain (A2), indicating the formation of insoluble species. However, the contributions of Cr and Mo changed markedly with potential. During the active to passive transition, a significant Mo accumulation ($j_{Ni} >> j_{Mo} \approx 0$) and a less significant Cr accumulation were observed. In the passive domain, Mo dissolution approached a congruent level and Cr dissolution was below the detection limit.

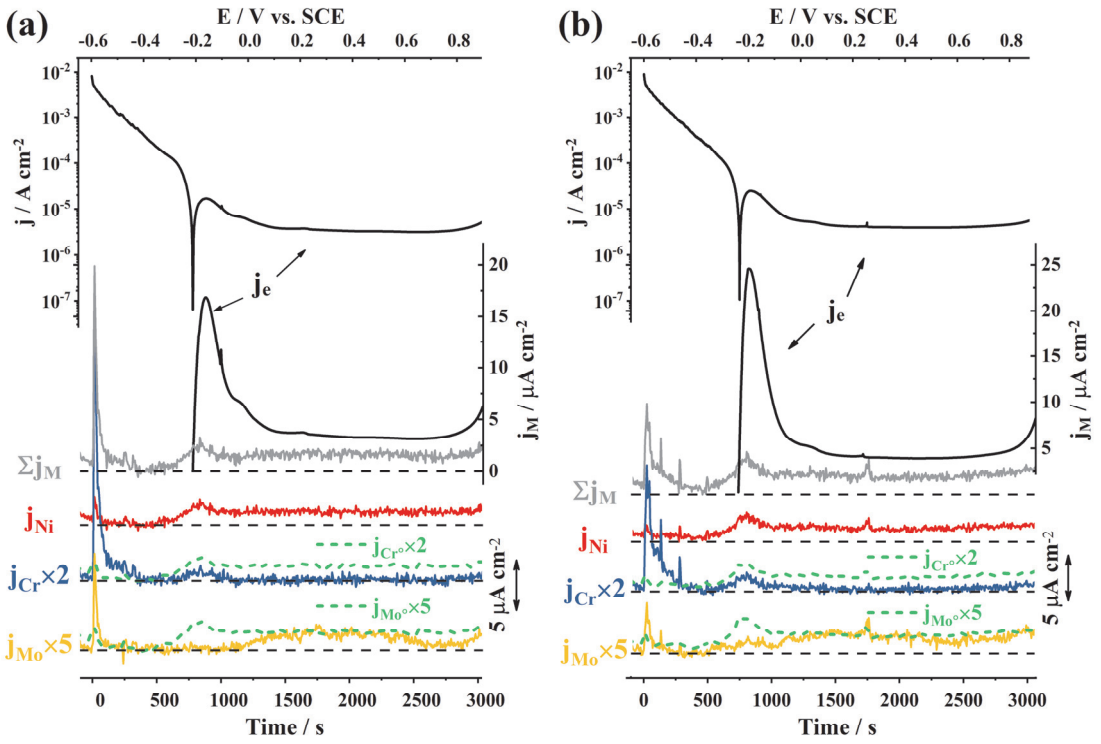

Figure 5.3 Elemental resolved potentiodynamic polarization curve for Ni22Cr10Mo in aerated (a) and deaerated (b) 2 M H_2SO_4. For j_e in the bottom panels, only positive values are shown. Σj_M indicates the sum of the elemental currents. Elemental currents of Ni(II), Cr(III), and Mo(VI) are offset for clarity. The green dashed lines are the assumed congruent elemental currents for Cr and Mo.

5.3.3 ELECTROCHEMISTRY OF PURE MO AND NI

To further clarify the behavior of Mo as a function of potential, the polarization curve of nominally pure Mo was obtained, **Fig. 5.4**. Also shown for comparison is a similar curve for nominally pure Ni, replotted from reference[45]. It is observed that the onsets of Ni and Mo oxidation occur at nearly the same potential (≈ −0.25 V_{SCE}) however the dissolution of Mo does not occur until a more positive potential (≈ 0 to 0.1 V_{SCE}) most likely associated with the oxidation of Mo(IV) species to the more soluble Mo(VI) species. This is accompanied by a transition in the polarization curve from a passive plateau to an increasing current-potential curve, characteristic of transpassive behavior. This confirms the hypothesis that the oxides of Mo formed in the potential range of the active to passive transition are not soluble while oxidized Ni is soluble. Thus, we would expect a Ni-Mo alloy to exhibit selective Ni dissolution in this potential domain, leaving behind a residual Mo oxide film. For E > 0 V_{SCE}, Mo dissolution is significantly enhanced.

The potential range in which Mo oxidation occurs without measurable dissolution corresponds well with the domain of the active to passive transition (A1) of the ternary alloy. It is therefore reasonable to attribute the lower critical current measured for the ternary alloy in this domain to the build-up of Mo oxides. These results suggest that Mo oxides formed during active to passive transition facilitates the nucleation and growth of the passive film.

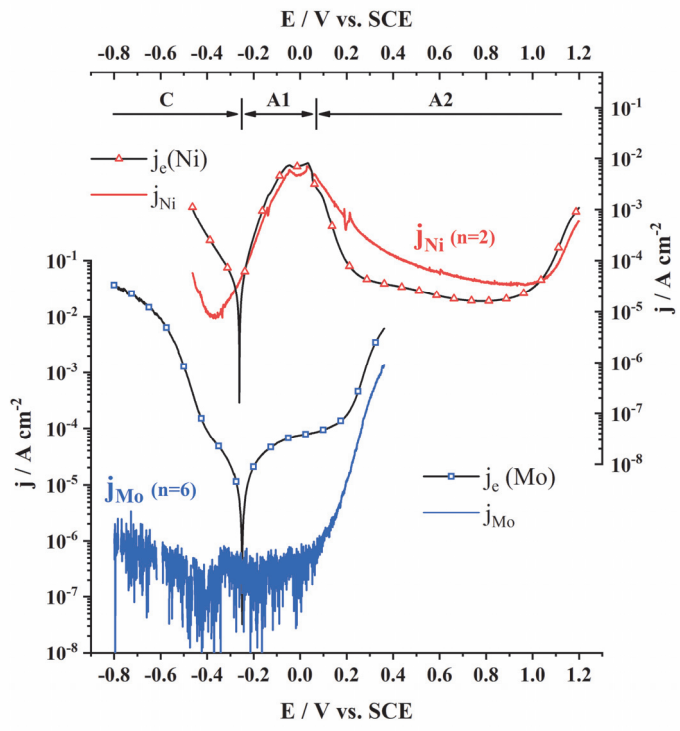

Figure 5.4 The elemental resolved polarization curves of pure Ni and Mo in 2 M H2SO4. The Ni data are replotted from reference[45].

5.3.4 PASSIVE FILM FORMATION AND DISSOLUTION

5.3.4.1 Spontaneous Passivation (Potential Domain A1)

The growth of the oxide film in the potential domain A1, where the effect of Mo was most significant, was further investigated. The spontaneous passivation of the alloys was monitored as a function of time via a cycle of cathodic activation-open circuit potential, referred to as an SP cycle, shown in **Fig. 5.5a** and **b** for Ni22Cr and Ni22Cr10Mo, respectively. Cathodic activation (CA) was achieved by polarizing the alloy to −0.8 V_{SCE} for 200 s. This resulted in a sharp dissolution peak involving all the alloying elements. The excess dissolution of Cr was indicated for both alloys ($\nu'_{Cr} >> \nu_{Ni}$) and excess Mo for the Ni22Cr10Mo alloy ($\nu'_{Mo} >> \nu_{Ni}$). We refer to this as cathodic activation, as it corresponds to the dissolution of the passive film. Spontaneous passivation was then observed on the

release of the potential to E_{oc} (see inset). This is indicated by the excess Ni dissolution ($\nu_{Ni} > \nu'_{Cr}$) observed during this period, and the increase in E_{oc}, which quickly stabilized at ~ −0.2 V_{SCE} for both alloys. Mo accumulation was also indicated for the Ni22Cr10Mo alloy where $\nu_{Ni} > \nu'_{Mo}$.

Spontaneous passivation, **Fig. 5.5**, showed not only the accumulation of Cr and Mo in the oxide film, but also indicated the effect of this oxide film on the corrosion rate. For the Ni22Cr alloy, the Ni dissolution rate reached a steady-state value (ν_{Ni} = 3 ng cm^{-2} s^{-1}, E_{oc} = −0.24 V_{SCE}) with Cr dissolving congruently ($\nu'_{Cr} = \nu_{Ni}$). This is a factor of 4 lower than the dissolution rate observed for pure Ni under nominally identical conditions[45] (ν_{Ni} = 12 ng cm^{-2} s^{-1}, E_{oc} = −0.31 V_{SCE}) and illustrates the effect of Cr on spontaneous passivation. However, this was still a 10-fold increase relative to the open circuit dissolution rate before cathodic activation (ν_{Ni} = 0.3 ng cm^{-2} s^{-1}, E_{oc} = 0 V_{SCE}), when the material was protected by the air-formed oxide film. This demonstrates that the air-formed passive film on Ni22Cr was more efficient at lowering the corrosion rate than the film formed spontaneously in H_2SO_4.

For the Ni22Cr10Mo alloy, the spontaneous dissolution rate decreased to nearly the detection limit ($\nu_{Ni} \approx$ 0.4 ng cm^{-2} s^{-1}, E_{oc} = −0.22 V_{SCE}) following spontaneous passivation, comparable to the open circuit dissolution rate before cathodic activation. This demonstrated the effect of Mo on reinforcing spontaneous passivation of Ni22Cr10Mo alloy as compared to the binary alloy.

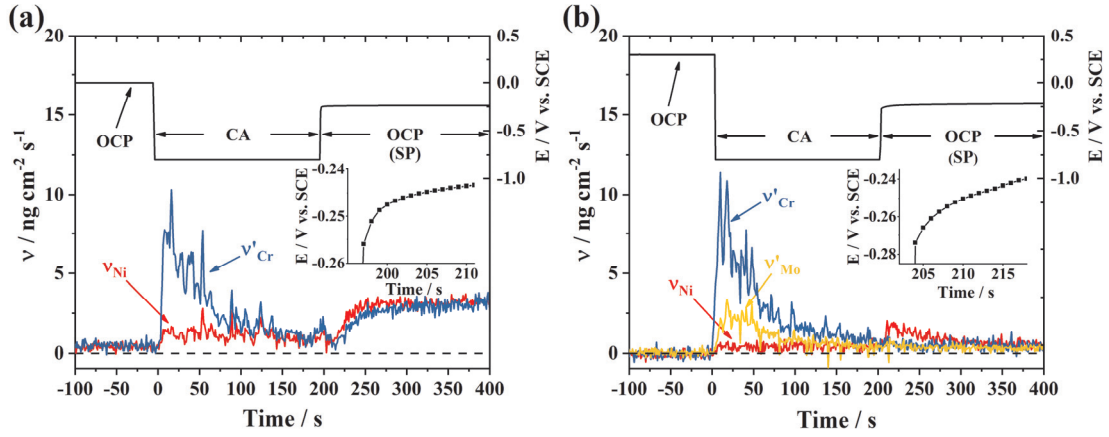

Figure 5.5 Normalized elemental dissolution rates (ν'_{Cr} and ν'_{Mo}) recorded during cathodic activation for Ni22Cr (a) and Ni22Cr10Mo (b) in deaerated 2 M H_2SO. Insets show the first 15 seconds of the open circuit potential after cathodic activation.

The surface excess of Cr (Θ_{Cr}) and Mo (Θ_{Mo}) during spontaneous passivation of Ni22Cr10Mo (**Fig. 5.5b**) may be calculated according to **eq. (5.3)**, assuming Ni completely dissolved into the solution. The calculation yielded $\Theta_{Cr} \approx 25$ ng cm^{-2} and $\Theta_{Mo} \approx 16$ ng cm^{-2}, while for the Ni22Cr alloy, $\Theta_{Cr} \approx 40$ ng cm^{-2}, although the error was large.

5.3.4.2 Anodic Passivation

Passivation at higher potential in the passive domain[3] (A2) was investigated for both alloys by stepping to a more positive potential, E = 0.3 V_{SCE}, (**Fig. 5.1**) following the SP cycle. The resulting dissolution profiles for the anodic passivation are shown in **Fig. 5.6a** and **b** for Ni22Cr and Ni22Cr10Mo, respectively. The anodic step occurs at t = 0 as indicated. Prior to this, the alloy was allowed to corrode freely at open circuit. Again, the efficiency of the spontaneously formed passive film on the ternary alloy is indicated by the decreased open circuit dissolution rate for t < 0.

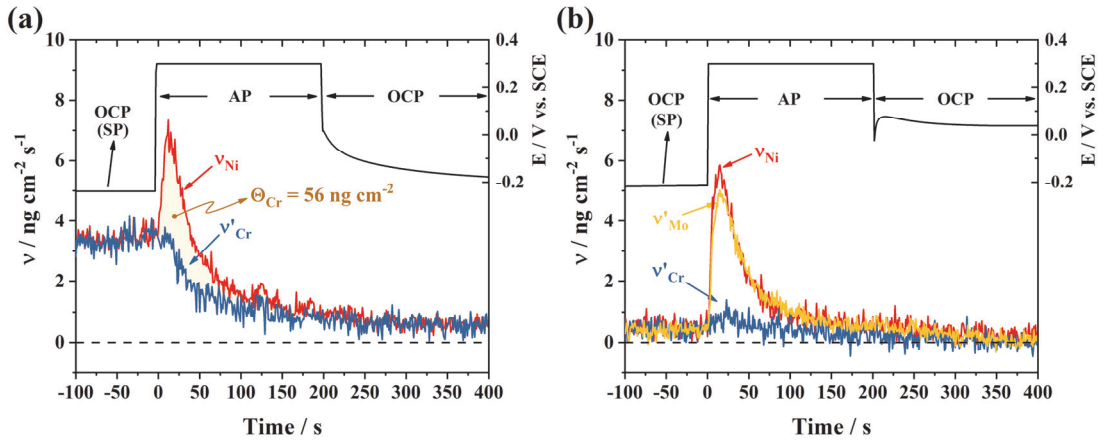

Figure 5.6 Normalized elemental dissolution rates (ν'_{Cr} and ν'_{Mo}) recorded during anodic passivation (0.3 V_{SCE}) for Ni22Cr (a) and Ni22Cr10Mo (b) in deaerated 2 M H_2SO_4. Surface accumulations were determined by integration and mass balance, exemplified in yellow for Θ_{Cr} in **Fig. 5.6a**.

During the anodic potential step, Ni was selectively removed from the surface ($\nu_{Ni} >> \nu'_{Cr}$) for both Ni22Cr and Ni22Cr10Mo alloys. This is consistent with the growth

[3] We use the term " passive " as referring to the potential domain were the current is relatively independent of potential in the polarization curve. As spontaneous passivation was demonstrated to occur at potentials below the passive domain, the term is used simply as a convention.

of the Cr-dominant passive film. A Mo dissolution peak was observed for Ni22Cr10Mo which is nearly congruent with Ni dissolution (see below) and may be attributed to the formation of slightly soluble Mo(VI). The following open circuit corrosion rate for t > 200 s was somewhat higher for the binary alloy as compared to the ternary alloy but the difference was less marked than following spontaneous passivation (t < 0). That the post-AP corrosion rate of the ternary alloy was similar to that of the binary alloy is not surprising since Cr accumulation occurred simultaneously with Mo dissolution, partially eliminating the Mo-oxides formed during spontaneous passivation.

By mass balance, the surface accumulation of Cr was Θ_{Cr} = 56 ng cm^{-2} and Θ_{Cr} = 81 ng cm^{-2} for Ni22Cr and Ni22Cr10Mo, respectively, corresponding to estimated film thicknesses of 0.16 nm and 0.23 nm, assuming a uniform Cr_2O_3 layer with the usual density of 5.22 g cm^{-3}. These extremely low values suggest that passivation may not be uniform on the surface and/or the oxides formed are much less dense than the standard densities used in the calculation. Similarly low values have been determined in previous studies for stainless steel[39, 40], C-22 Ni alloy[45], and a Ni-based high entropy alloy[43].

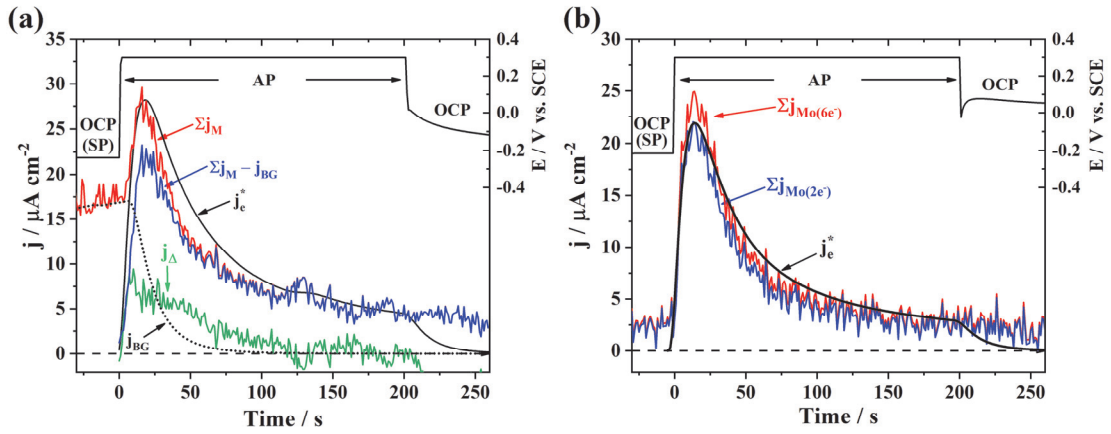

Figure 5.7 Comparison of the convoluted electrical current, j_e^*, and the sum of the elemental currents, Σj_M, for (a) Ni22Cr and (b) Ni22Cr10Mo alloys. Mo(6e$^-$) and Mo(2e$^-$) indicate the number of electrons contributed by Mo is chosen as 6 and 2, respectively.

The faradaic yield of dissolution during anodic passivation can be determined by comparing the sum of the elemental current, Σj_M, with the convoluted external electrical current, j_e^*. This comparison for Ni22Cr and Ni22Cr10Mo is shown in **Fig. 5.7**. For the

binary alloy, the decreasing background dissolution from the open circuit corrosion (j_{BG}) preceding the polarization was calculated and subtracted[40]. The resulting difference between Σj_M and j_{BG} was compared with j_e^*, and a faradaic yield of 80% was obtained. The quantity of excess charge calculated by integrating $j_\Delta = j_e^* - \Sigma j_M - j_{BG}$ was 450 μC cm^{-2}, corresponding to an estimated uniform Cr_2O_3 film thickness of ≈ 0.23 nm. Again, the low value suggests that the film is not uniform but the good agreement between the coulometric analysis and the elemental mass balance indicates the quantitative nature of the approach.

The faradaic yield of dissolution for Ni22Cr10Mo is shown in **Fig. 5.7b**. Two separate curves are shown in which n = 2 (lower) and n = 6 (upper) were assumed for Mo dissolution, as there is some ambiguity as to the precise dissolution reaction, Mo(IV) → Mo(VI) or Mo(0) → Mo(VI). In either case, with only 10% Mo, the assumption of the Mo oxidation state did not significantly affect the calculated faradaic yield which was near 100%. The quantity of excess charge, Θ_e, was obtained by integrating the difference, $j_\Delta = j_e^* - \Sigma j_{Mo(2e^-)}$. The value of Θ_e = 269 μC cm^{-2}, similar in magnitude to the value obtained by mass balance. This result confirms the hypothesis that the oxidation of Mo in the high potential domain results in a predominately soluble form of Mo oxide.

5.3.4.3 Potentiostatic Cycles

The interplay between the different elements may be apprehended by their behavior over several active-passive cycles. The surface excess of Cr and Mo, Θ_{Cr} and Θ_{Mo}, were determined as a function of time during a sequence of activation-passivation cycles as shown in **Fig. 5.8**. The cycles consisted of cathodic activation (200 s at E = −0.8 V_{SCE}), OCP (300 s), anodic passivation (200 s at E = 0.3 V_{SCE}), and OCP (300 s) referred to as an AP cycle. For both alloys, the formation of the passive film was demonstrated by the increase of Θ_{Cr} during spontaneous passivation and more significantly during anodic passivation. The removal of the passive film was detected by the rapid decrease of Θ_{Cr} during cathodic activation. The cycles demonstrate that the passive film was formed and removed, however, the slow increase in the background may suggest some non-reversibility in the process and/or changes in the near-surface alloy composition. The Mo surface excess, Θ_{Mo}, for the Ni22Cr10Mo alloy showed a similar trend, increasing during

spontaneous passivation, decreasing slightly during anodic passivation, and decreasing during cathodic activation. Overall, the results indicate that, for AP cycles, passivation and activation were reasonably reversible within experimental error.

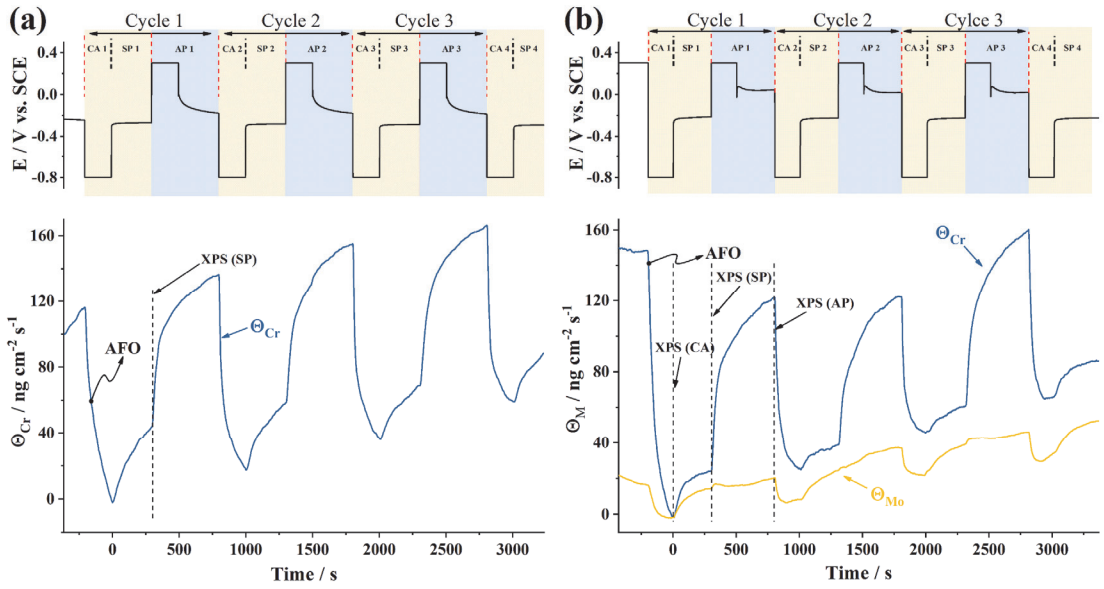

Figure 5.8 The surface excess of Cr (and Mo) for Ni22Cr (a) and Ni22Cr10Mo (b) during AP cycles in deaerated 2 M H_2SO_4. The upper part of the figure shows the corresponding potential. The activation cycle with spontaneous passivation is highlighted in light yellow, the anodic passivation in light blue. AFO: air-formed oxide.

The reversibility of spontaneous passivation during repeated SP cycles was investigated for Ni22Cr10Mo in **Fig. 5.9**, where the surface excess of Cr and Mo, Θ_{Cr} and Θ_{Mo} during four SP cycles are shown. The accumulation and subsequent dissolution of surface Cr oxide was clear in the variation of Θ_{Cr} with time, however, Θ_{Mo} increased steadily, indicating that Mo accumulated more in the spontaneous passivation (SP) period than was removed during the cathodic activation period, resulting in a net increase in Mo accumulation with every cycle. The maximum amount of Cr decreased with successive cycles such that by the fourth cycle Cr accumulation and dissolution were considerably attenuated. This result suggests a cumulative action of the Mo build-up: as the Mo content of the surface was enhanced during successive SP cycles, the formation of Cr oxide was hindered.

These results for both Cr and Mo are very similar to previous results for alloy C-

22, a commercial Ni-Cr-Mo alloy[45]. The maximum accumulation of Cr throughout the AP cycles, Θ_{Cr}(max), was approximately 114 ng cm^{-2}, similar to that of the C-22 alloy, Θ_{Cr}(max) = 133 ng cm^{-2}. During spontaneous passivation, Θ_{Cr} from the first spontaneous passivation was around 15 ng cm^{-2}, similar to that of the commercial alloy.

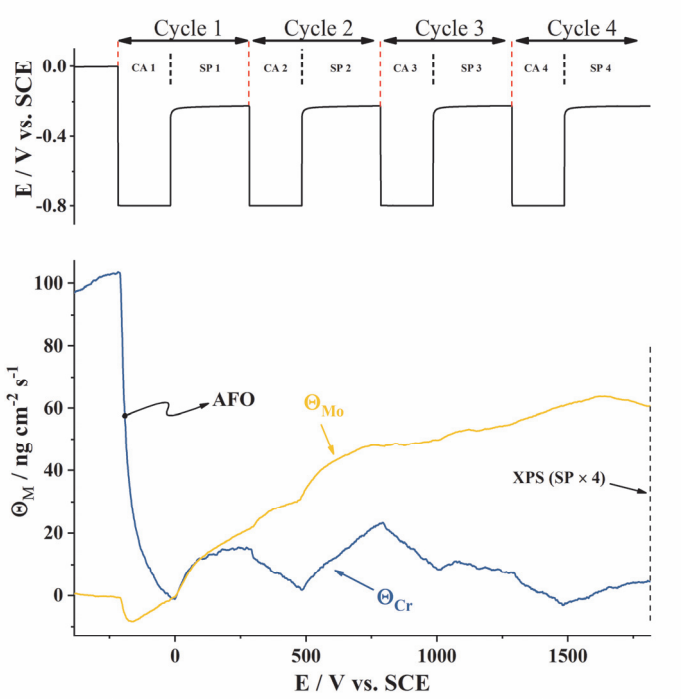

Figure 5.9 The surface excess of Cr (Θ_{Cr}) and Mo (Θ_{Mo}) during SP cycles for Ni22Cr10Mo in deaerated 2 M H_2SO_4. The upper part of the figure shows the corresponding potential. AFO: air-formed oxide.

5.3.5 XPS CHARACTERIZATION

To gain further insight into the chemical nature of Cr and Mo in the oxide film, as observed by AESEC, XPS was performed at various stages in the cyclic experiments. To avoid atmospheric contamination, the electrochemical experiments were performed in an inert atmosphere glovebox and the specimens transferred into the XPS vacuum system without exposure to the ambient atmosphere. The parameters for deconvoluting the high-resolution spectra were described in the experimental section. The fitting of the Mo 3d signal for samples exposed to H_2SO_4 required the consideration of sulfate and sulfide signals, due to the overlap of S 2s and Mo 3d bands. The presence of sulfate and sulfide was confirmed by the S 2p band in the survey spectrum, and their ratio was obtained from the high-resolution spectrum of the S 2p region (neither shown here). The ratio of different Mo species was then calculated after subtracting the contribution of sulfate and sulfide signals (S 2s).

XPS results for the air-formed oxide on Ni22Cr10Mo alloy are given in **Fig. 5.10** and may be considered a reference for the electrochemical experiments. For Ni and Mo, the metallic peak dominated the spectra. Small quantities of Mo and Ni oxide were detected with 8% NiO and 14% $Ni(OH)_2$ and 15% Mo(IV) and 20%Mo(VI). The Cr spectrum showed oxide as the predominate species, with Cr(III) oxide and hydroxide accounting for 25% and 28% respectively with no detectable Cr(VI).

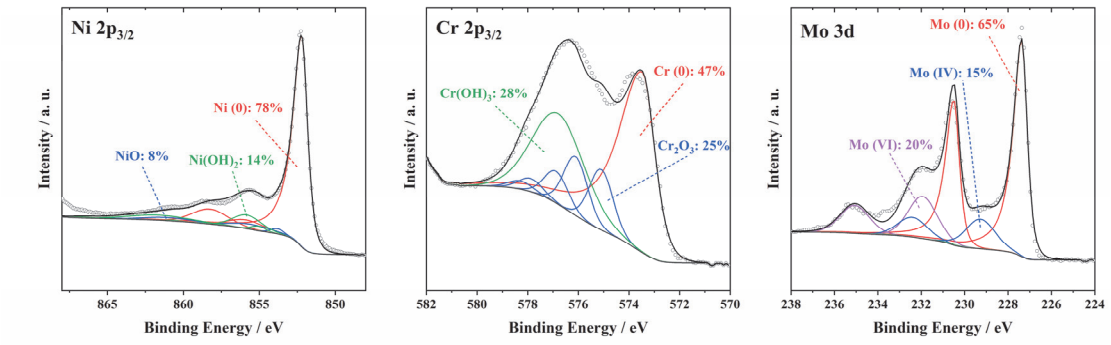

Figure 5.10 Deconvoluted XPS high-resolution spectrum of Ni($2p_{3/2}$), Cr($2p_{3/2}$), and Mo(3d) regions recorded for the air-formed oxide on Ni22Cr10Mo alloy.

XPS spectra obtained at different points within a single anodic passivation (AP) cycle for Ni22Cr10Mo are shown in **Fig. 5.11**. The spectra represent the surfaces obtained after cathodic activation (CA), spontaneous passivation (SP), and anodic passivation (AP) as indicated in **Fig. 5.8**. **Fig. 5.12** shows the spectra obtained after four cycles of spontaneous passivation (SP) as indicated in **Fig. 5.9**. The relative intensities of the integrated peaks for the different species of each element for each phase of the cycles are presented in **Fig. 5.13**.

Cathodic activation (**Fig. 5.11a**) led to an increase in the fraction of Cr(0) (76%) as compared to the same material with air-formed oxides (48%), consistent with the partial removal of the passive film by cathodic activation. The Ni(0) and Mo(0) showed only a slight increase (9% and 3%, respectively). This is consistent with the intense Cr dissolution peaks observed in **Fig. 5.5b**. It should be noted that even under the nitrogen atmosphere in the glove box, it is impossible to obtain spectra of the surface immediately after cathodic activation, as the surface is exposed to the electrolyte for several seconds, and some degree of reoxidation most certainly occurs during this period.

Spontaneous passivation occurred during the open circuit exposure following the

cathodic activation. The corresponding XPS spectra are shown in **Fig. 5.11b**. A decrease of ~10% was observed in Ni(0), Cr(0) and Mo(0) fractions and an increase of the respective oxidized species, as shown in **Fig. 5.12**. The passivating effect of this film on the corrosion rate was indicated in **Fig. 5.5b** where the elemental dissolution rates were reduced to around the detection limit after film formation.

Anodic passivation was investigated in **Fig. 5.11c** after a single complete AP cycle. The ratio of Cr(III)/Cr(0) was further enhanced, consistent with the AESEC results shown in **Fig. 5.6b**. The relative amount of Mo(VI) increased while that of Mo(IV) decreased. These trends are also indicated in **Fig. 5.12**. This implies that the passive potential (0.3 V_{SCE}) favored the formation of Mo(VI), in agreement with thermodynamic considerations[45]. The enhanced Mo dissolution observed in the anodic domain of the polarization curve (**Fig. 5.3**) and the anodic passivation (**Fig. 5.6b**) can, therefore, be attributed to the formation of Mo(VI) in the passive domain which, in an acid solution, is more soluble than the Mo(IV) species.

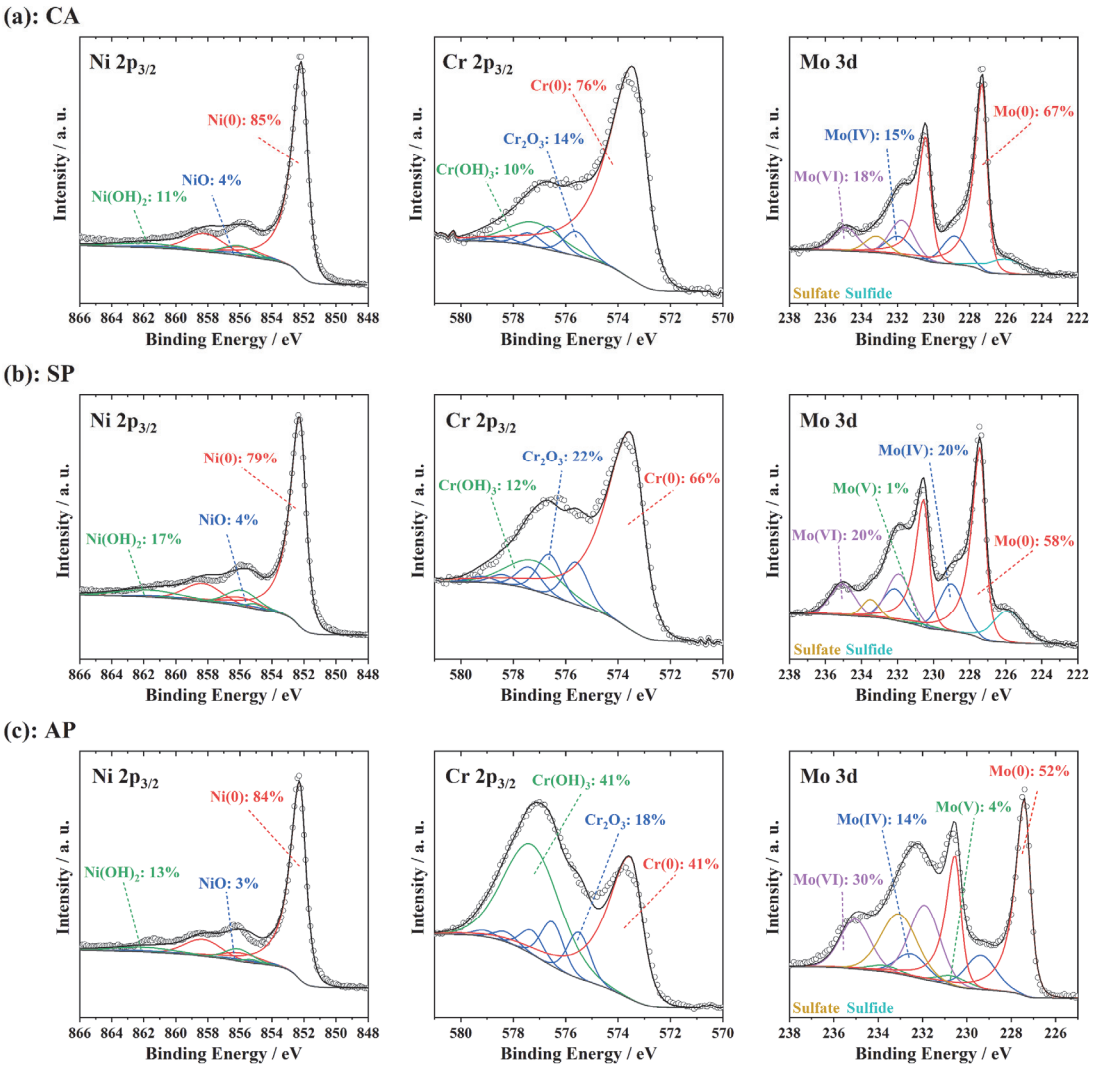

Figure 5.11 Deconvoluted XPS high-resolution spectrum of Ni($2p_{3/2}$), Cr($2p_{3/2}$), and Mo(3d) recorded at various steps within the AP cycle. (a): cathodic activation. (b): spontaneous passivation. (c): anodic passivation.

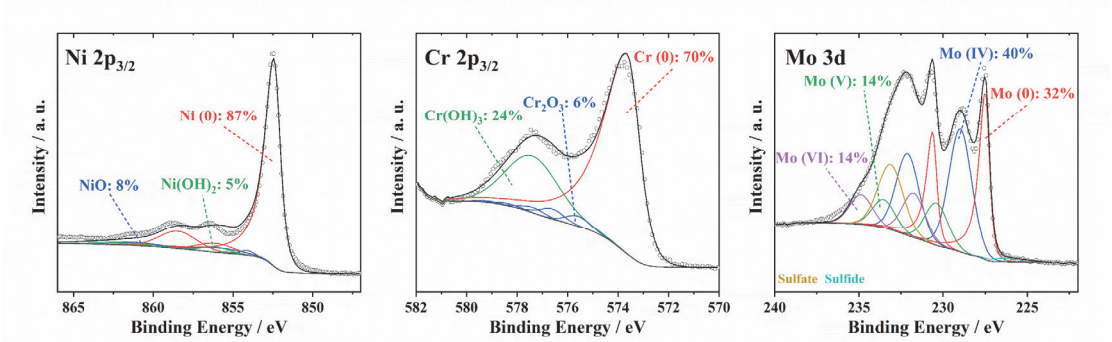

Figure 5.12 Deconvoluted XPS high-resolution spectrum of Ni($2p_{3/2}$), Cr($2p_{3/2}$) and Mo(3d) recorded after a sequence of four SP cycles.

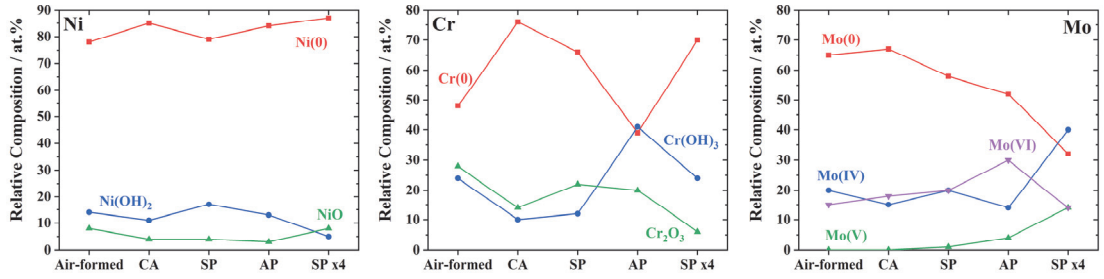

Figure 5.13 Comparison of relative composition for Ni, Cr, and Mo species obtained at various stages of the experiment cycle.

The accumulation of Mo was observed to increase with successive SP cycles in the AESEC profiles of **Fig. 5.9**. To confirm this result and identify the oxidations states of Mo present in the passive film, XPS spectra (**Fig. 5.12**) were obtained after a series of four SP cycles. The Mo(0) contribution decreased by nearly 50% while Cr(0) actually increased slightly by 6% (**Fig. 5.12**). These results are qualitatively consistent with the AESEC results of **Fig. 5.9**.

The total elemental analysis was determined by combining the elemental analysis from the survey with the oxidation state analysis from the high-resolution spectra. The total composition is shown in **Fig. 5.14a** which includes the metallic species. As previously mentioned, the M(0) oxidation states will decrease in percentage as the oxide film thickens because the metallic substrate is masked by the oxide film. These results demonstrate that the oxide film increased in thickness CA < SP < AP as we would expect. The SPx4 was intermediate between CA and SP.

The relative composition of the surface oxides, **Fig. 5.14b**, was determined by removing the metallic states from the analysis and normalizing to 100%. CA and SP have similar composition, although the results of **Fig. 5.14a** indicate that the passive film thickness had increased following SP. Although cathodic activation should remove much of the passive film, some degree of spontaneous passivation may happen, due to the inevitable contact with the electrolyte before the sample was taken out of the flow cell, resulting in the re-formation of the oxide. The spontaneously passivated film showed a Cr/Mo oxide ratio of 1.5. This value increased to 4.2 following anodic passivation. Again, this result demonstrates the significant accumulation of Cr during anodic passivation. The

ratio of Mo(IV)/Mo(VI) increased from 1.0 (SP) to 2.1 (AP) with a slight appearance of Mo(V) species. A series of four SP cycles led to a marked enhancement of Mo (Mo/Cr = 1.3) and a Mo(VI)/Mo(IV) ratio = 0.36.

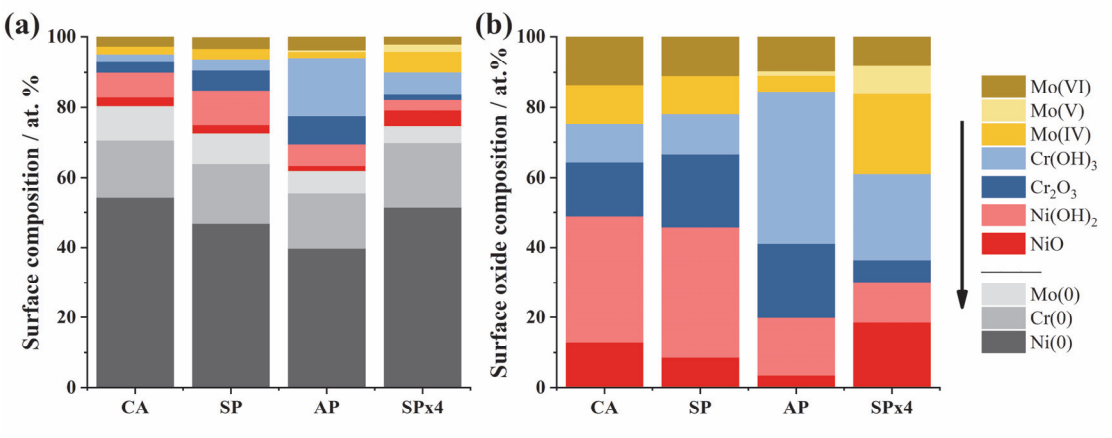

Figure 5.14 (a) Total XPS elemental analysis including the zero oxidation state elements and (b) Normalized surface composition of the oxides on Ni22Cr10Mo following CA, SP, AP, and SP x4 (fractions given in at.%). Legends are arranged in the same order (indicated by the arrow) as the species shown in the bar graph.

There is consistency between the XPS results (**Fig. 5.14**) and the surface excess profiles from AESEC (**Fig. 5.8b** and **Fig. 5.9**). The ratio of Mo/Cr in the surface oxides following spontaneous passivation was determined to be 1.2 by XPS compared with 1.4 by AESEC. After anodic passivation, this ratio decreased to 0.4 for XPS and 0.2 for AESEC. The results were less consistent after four SP cycles with a Mo/Cr ratio of 2.4 for XPS as compared to 12 for AESEC although the trend of Mo accumulating on the surface was consistent in both experiments.

The origin of the discrepancies in quantification between XPS and AESEC is difficult to assess. A major difference is the local nature of XPS analysis compared to the global nature of AESEC. For XPS, only a small surface area (0.028 mm^2) in the center of the dissolution crater is measured while AESEC gives an average value over the entire working electrode area. Further, the active-passive cycle experiment may be difficult to reproduce after several cycles and the problem is exacerbated due to the transfer to XPS.

The Ni22Cr10Mo alloy showed a significantly lower spontaneous dissolution rate after open circuit passivation than did the Ni22Cr alloy. To gain insight into the origin of

this difference, the spontaneously formed passive film on Ni22Cr was also analyzed by XPS, as shown in **Fig. 5.15**. The sample was cathodically activated and then released to OCP for 300 seconds. Both NiO and Cr_2O_3 fitting parameters were included in the deconvolution; however, they were not required to model the experimental spectra, suggesting the absence of these species at the surface. Instead, both spectra were dominated by signals of the metallic state, with small amounts of hydrated oxides (i.e. $Ni(OH)_2$ and $Cr(OH)_3$). Taking the AESEC results into account, we can attribute the accumulated Cr observed during spontaneous passivation to the formation of $Cr(OH)_3$. This is in contrast to the Ni22Cr10Mo alloy where the Cr 2p spectra showed a $Cr_2O_3/Cr(OH)_3$ ratio of 1.8 (**Fig. 5.11**).

These results suggest that Mo oxides formed in the A1 potential domain facilitate the oxidation of Cr to Cr_2O_3 rather than $Cr(OH)_3$ which may be considered a step in the nucleation of the passive film as a high $Cr_2O_3/Cr(OH)_3$ ratio has been associated with a more protective oxide, at least for one alloy C2000 (Ni23Cr16Mo1.6Cu)[29].

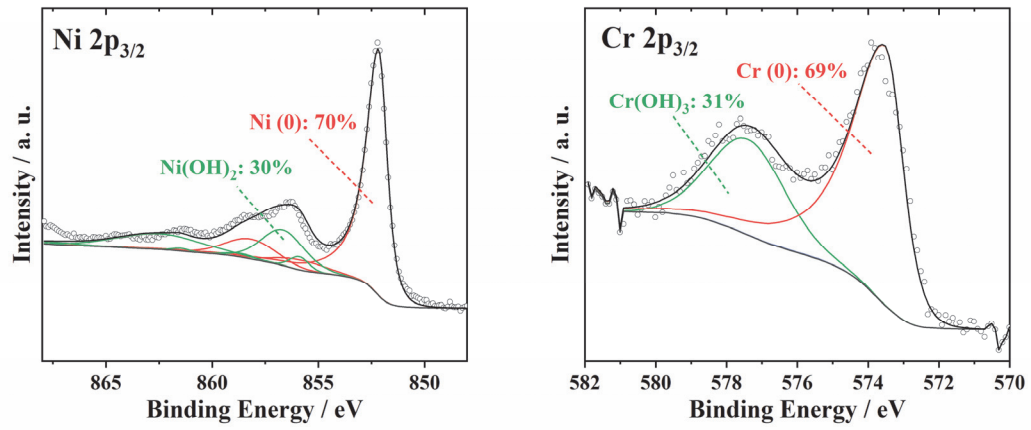

Figure 5.15 Spontaneous passivation: Deconvoluted XPS high-resolution spectra of Ni($2p_{3/2}$) and Cr($2p_{3/2}$) from the Ni22Cr alloy after a CA-OCP cycle.

5.4 DISCUSSION

For the majority of Cr containing alloys (Fe-Cr, Ni-Cr), Cr is the major element enriched in the passive film. This occurs via a mechanism of selective dissolution of Ni or Fe, leaving behind a residual Cr(III) oxide/hydroxide film, i.e.

$$2Ni_xCr + 3H_2O \rightarrow 2xNi^{2+}(aq) + Cr_2O_3(s) + 6H^+ + (6 + 4x)e^- \quad (5.8)$$

$$Ni_xCr + 3H_2O \rightarrow xNi^{2+}(aq) + Cr(OH)_3(s) + 3H^+ + (3 + 2x)e^- \quad (5.9)$$

It is well known that in sulfuric acid, the critical current for passivation decreases markedly with increasing %Cr, as less Ni dissolution is necessary to produce an equivalent Cr(III) film[109].

How are these reactions affected by Mo alloying? In the experimental conditions of this work, it appears that Mo will affect the film when passivation occurs at low potentials (A1) because, unlike Ni and Cr, Mo oxidation yields completely insoluble oxidation products in this potential domain. Therefore Mo(IV)-oxides build-up on the surface. This Mo oxide accumulation apparently promotes **eq. (5.8)** over **eq. (5.9)** thereby enhancing the ratio of $Cr_2O_3/Cr(OH)_3$ resulting in a film with improved barrier properties.

As the potential increases, the excess Mo will dissolve such that the high potential passive film shows a similar composition and corrosion resistance properties for both alloys. The spontaneously formed passive film probably does not correspond to the stable film formed at longer times and/or higher potential which has been the object of most ex situ spectroscopic studies to date. More likely it represents a "pre-passive" film[198] that may be considered as an unstable film during the early stages of growth.

The low-potential accumulation of Mo during spontaneous passivation was previously attributed to the oxidation of Mo(0) to MoO_2 (**eq. (5.10)**) in the low potential domain, based on thermodynamic considerations[45]. Its subsequent dissolution at higher potential was attributed to the oxidation of Mo and partial oxidation of preformed MoO_2 to MoO_4^{2-}, **eq. (5.11)**. In acid solution, molybdate exists in equilibrium with precipitated molybdates, indicated as $MoO_3 \cdot H_2O(s)$ (**eq. (5.12)**), which would explain the partial dissolution of Mo observed at high potential. The solid molybdate species may also be linked to the series of polymeric species such as $Mo_7O_{24}^{6-}$ and $Mo_8O_{26}^{4-}$ known to form under these conditions[199].

$$Mo + 2H_2O \rightarrow MoO_2 + 4H^+ + 4e^- \quad (5.10)$$

$$MoO_2 + 2H_2O \rightarrow MoO_3 \cdot H_2O(s) + 2H^+ + 2e^- \quad (5.11)$$

$$MoO_3 \cdot H_2O(s) \rightarrow MoO_4^{2-} + 2H^+ \quad (5.12)$$

The dissolution of molybdic acid (**eq. (5.12)**) is known to be slow and the kinetics and mechanism of this reaction have been investigated in sulfuric acid in the framework of Mo extraction from ores[200].

Alloys containing Mo have frequently been associated with an enhanced self-healing ability of the passive film[48, 132]. A defect in the passive film results in the underlying alloy being exposed to the electrolyte, followed by the re-formation of the passive film. The formation of a defect is to some extent simulated in this paper by the removal of the passive film by cathodic activation, and its subsequent re-formation initiated by the spontaneous passivation. Similar ideas have been proposed previously[201]. Newman[138] investigated repassivation of Fe-19Cr and Fe-19Cr-2.5Mo (wt.%) in 1 M HCl using a scratching electrode device. During repassivation, Mo significantly inhibited dissolution after the removal of 1-2 atom layers of Fe-Cr alloy. Thus, he concluded that Mo took effect at a sub-monolayer level, e.g. the Mo accumulated at kink or step sites. Scanning tunneling microscopy results given by Maurice et al.[132] suggest that, for an austenitic stainless steel single crystal surface in 0.05 M H_2SO_4, Mo nanostructures would form selectively in local defects in the passive film. In this work, the accumulation of Mo measured from mass balance during spontaneous passivation yielded an extremely low value (16 ng cm^{-2}, less than a monolayer), which would suggest that Mo was not homogeneously distributed but accumulated at local sites.

Spontaneous passivation was also observed for the binary Ni22Cr alloy; however, the spontaneously formed passive film on Ni22Cr was less efficient than the film formed on Ni22Cr10Mo under identical conditions. The XPS results suggested that the formation of Mo(IV)-oxides on the surface favored the formation of Cr_2O_3 during spontaneous passivation. Recent publications have suggested similar effects. A first-principles investigation by Samin et al.[202] showed that the addition of Mo to the alloy stabilized oxygen adsorption, thus making the oxide more favorable. Yu et al.[203] reported that the addition of 6 wt.% Mo inhibited Kirkendall void formation by promoting the nucleation

of a metastable $Ni_{2-x}Cr_xO_3$ corundum structure.

There have been some discussions recently regarding the role of $NiCr_2O_3$ in the passivation of Ni-Cr and Ni-Cr-Mo alloys[46]. In the data presented here, the mass balance calculations assume that oxidized Ni is nearly 100% soluble. Therefore, it is impossible to detect the formation of Ni oxide independent of the other alloying components. The near 100% faradaic efficiency for anodic passivation (**Fig. 5.7**) suggests that it makes a very small contribution at best. At higher pH however, Ni(II)-oxides are much less soluble than in 2M H_2SO_4, and very different results might be expected[46].

The relatively complex chemistry of Mo and its transitory existence in the passive film may explain some of the disagreement in the literature concerning its presence and nature in the passive film. It has been reported for stainless steels in HCl solutions that during active dissolution, the oxidation state of Mo was Mo(IV) according to Olefjord et al.[136, 139]; however, it was Mo(VI) according to Hashimoto et al.[60] Our results would support the Mo(IV) theory, though both oxidation states were present after spontaneous passivation. Passivation at 0.3 V_{SCE} resulted in the increase of Mo(VI) (the thermodynamically predominant oxidation state of Mo[24] at 0.3 V_{SCE}) and the decrease of Mo(IV). To our knowledge, there are no data in the literature concerning Ni22Cr10Mo alloys in this electrolyte to confirm this attribution. In acidic chloride solution, Olefjord et al.[139] also reported that Mo was significantly enriched as Mo(VI) in the passive film in a Mo-alloyed austenitic stainless steel during anodic passivation.

The effect of Mo for anodic passivation was less obvious in this work, however the low pH may have masked the effect. Local breakdown of the passive film in Cl^- containing solutions may be due in part to the recombination of metal cation vacancies, e.g. V''_{Ni} and V'''_{Cr}, expressed in the conventional Kröger-Vink notation[203-205]. It has been proposed that doping Ni and Cr oxides with Mo(VI) may create defects in the film by replacing Ni or Cr in the oxide lattice (e.g. $Mo^{4\cdot}_{Ni}$ and $Mo^{3\cdot}_{Cr}$) thereby eliminating the metal cation vacancies and thereby hindering local film breakdown.

These results confirm the mechanisms proposed in the previous AESEC study of commercial alloy C-22, which also contained Fe (3.7 wt.%), W (2.8 wt.%), and Mn (0.3 wt.%). The critical and passive current densities were quasi-identical in this work and the

previous study, indicating that the other alloying elements did not play a significant role in the passivation mechanisms. Therefore, we may generalize the results obtained with a ternary Ni-Cr-Mo alloy to similar commercial systems.

5.5 CONCLUSIONS

The electrochemical behaviors of Ni22Cr and Ni22Cr10Mo alloys and pure Mo were investigated by elemental resolved polarization curves in aerated and deaerated sulfuric acid solutions. Alloying with Mo improved the active to passive transition probably by favoring the nucleation and growth of Cr_2O_3 with respect to $Cr(OH)_3$ by a factor of 10 less decrease in the critical current density. This was associated with a significant Mo accumulation. In the passive domain, the current density was not significantly different between the two alloys suggesting that the passive film formed in the high potential domain ($E > 0\ V_{SCE}$) was independent of Mo.

These results were consistent with the electrochemistry of pure Mo which oxidized to form insoluble Mo oxides in the low potential domain (A1, $E < \sim 0\ V_{SCE}$) but formed soluble Mo species at higher potential. A similar behavior was observed for Mo in the alloys with preferential Ni and Cr dissolution in the low potential domain and the accumulation oxidized Mo in the oxide film.

The accumulation of Cr (on Ni22Cr) or Cr and Mo (on Ni22Cr10Mo) were observed in real-time during spontaneous passivation in the low potential domain ($E \approx -0.2\ V_{SCE}$) under free corrosion conditions. The Mo accumulated passive film formed on the ternary alloy showed a markedly reduced free corrosion rate as compared to the binary alloy and a higher $Cr_2O_3/Cr(OH)_3$ ratio. It is reasonable to infer that the Mo accumulation in this potential domain favors the nucleation and growth of Cr_2O_3 thereby improving the corrosion resistance of the film. Repeated spontaneous passivation-cathodic activation cycles showed a continuous accumulation of Mo in the oxide and a decrease in the quantity of Cr.

Anodic passivation resulted in a further increase of Cr on the surfaces of both Ni22Cr and Ni22Cr10Mo. However, Mo dissolved nearly congruently with Ni at this step for the ternary alloy and the resulting passive film was depleted in Mo as compared to the

film formed spontaneously at lower potential. The ratio of Mo(VI)/Mo(IV) increased demonstrating that Mo dissolution was due to the formation of partly soluble Mo(VI) species.

6. INVESTIGATING THE ROLE OF Mo AND Cr DURING THE BREAKDOWN AND REPASSIVATION OF OXIDE FILMS FORMED ON NI-BASED ALLOYS IN HYDROCHLORIC ACID

The theory of potential-dependent Mo behavior has been established according to the results obtained from **chapter 4 and chapter 5**. This chapter studied three commercial Ni alloys with different combinations of Cr and Mo contents in concentrated HCl solution. The use of HCl solution simulates the environment inside a crevice, as the crevice corrosion is one of the major practical issues for these types of alloys.

ABSTRACT

In this work, the elemental dissolution behavior of commercially available Ni-based alloys (BC-1, C-22, and G-35) was presented in the context of cathodic activation, spontaneous passivation, and anodic passivation in hydrochloric acid solution. When the passive film was removed by cathodic activation, the spontaneous passivation of surface oxides was found to proceed by the accumulation of mainly Mo, but also Cr oxides. An alloy's ability to recover from oxide film damage was found to improve with increased Mo content. For the lowest Mo-content alloy considered here, approximately 8 wt.% Mo, repassivation was unsuccessful and active dissolution was observed. For higher Mo-containing alloys, repassivation occurred quickly, and dissolution rates stabilized at values comparable to the original passive surface. The surface species responsible for successful repassivation were found to be dominated by Mo(IV) oxides by ex situ XPS. When electrochemically passivated by the application of an anodic potential, a portion of the previously accumulated Mo species were removed. However, Mo maintained a significant role during the reformation of the Cr-rich oxide film.

6.1 INTRODUCTION

Ni-based alloys containing various alloying elements, including both Cr and Mo, have become important industrial materials due to their corrosion resistance in aggressive environments. Serving as the alloy matrix, Ni can accommodate high concentrations of alloying elements while maintaining a single-phase (fcc) structure[206]. While Cr content promotes the formation of a Cr-rich barrier oxide, which is primarily responsible for protecting the underlying metallic substrate[83, 207], additions of Mo into Cr-containing alloys have been shown to result in the enrichment of oxidized Mo species on the outside of the Cr-rich oxide[50]. By itself, the Cr-rich oxide provides excellent protection in oxidizing environments; however, the presence of Mo becomes increasingly important at low pH and high chloride concentration[127, 208]. These conditions are commonly associated with localized corrosion processes, including both pitting and crevice corrosion[209-211]. Resistance to localized corrosion is influenced by the Mo content, which increases both film stability and repassivation behavior[50, 127, 190].

While alloyed Cr and Mo are recognized to act synergistically in improving corrosion resistance, many mechanistic features remain unclear. In a recent review by Lutton Cwalina et al., the benefits of alloyed Mo in Cr containing alloys were revisited[189]. First-principles calculations by Samin et al. demonstrated that additions of Mo enhance the adsorption of oxygen on the surface of Ni-Cr alloys[202]. Using in situ transmission electron microscopy, Yu et al. showed that during early-stage gas phase oxidation, Mo additions reduce the formation of voids in the oxide layer formed on Ni-Cr alloys[203]. Using scanning tunneling microscopy, Maurice et al. observed nanoscale surface defects in passivated Fe-Cr alloys[132]. When Mo was added to the alloy, defects were found to generate a nanostructured "plug", which appeared to act as a healing phenomenon for the defects. Based on the observations in these studies, the influence of Mo can be generally summarized in terms of two main outcomes: an increase oxide stability and an improvement in the ability of the oxide film to repair the breakdown.

Currently, limited information has been published regarding the in situ (or in-operando) dissolution behavior of Ni-based alloys. This hinders efforts to optimize alloy composition, which requires a thorough understanding of how composition affects

corrosion performance in a range of exposure conditions. Atomic emission spectroelectrochemistry (AESEC) and other similar techniques have proven valuable in studying the in situ dissolution behavior of corroding systems, including both active and passive systems[150, 178, 183]. In our previous study, the AESEC technique was used to reveal a previously unreported dynamic behavior of alloyed Mo during the transpassive film breakdown on several Ni-Cr-Mo alloys in 1 M NaCl[182], and to trace the surface accumulation of Cr and Mo during potentiostatic active-passive cycles on C-22 Ni-Cr-Mo alloy[45]. Here, the elemental dissolution behavior of three commercial Ni-based alloys was investigated during film breakdown, spontaneous passivation (SP), and anodic passivation (AP) processes in 1 M HCl. Results obtained by AESEC were compared to ex situ surface analyses performed by X-ray photoelectron spectroscopy (XPS).

6.2 EXPERIMENTAL

6.2.1 MATERIALS

Materials used in this study were provided by Haynes International in the form of mill-annealed sheets. To conform to the dimensions of the electrochemical flow cell used for AESEC measurements, samples were machined to an appropriate dimension for the flow cell, 25 mm × 10 mm. The thickness of individual samples varied depending on the thickness of the original as-received sheet. Nominal alloy compositions, as reported by Haynes International, have been summarized in **Table 6.1**. Alloy compositions, determined according to ASTM E1019-18, ASTM E1097-12, and ASTM E1479-16 procedures, are included in **Table 6.2**. These more accurate compositions were used in the quantification of AESEC measurements and will be referenced throughout the text.

Table 6.1 As reported by Haynes International, the nominal composition of Hastelloy samples are summarized. Values are given in wt.% where M indicates the maximum concentration of an individual alloying element, while Bal. indicates the alloying element making up the balance due to fluctuations in composition.

Alloy	Ni	Cr	Mo	Fe	W	Cu	Co	Mn	V	Al	Si	C
BC-1	Bal.	15	22	2M	-	-	1M	0.25	-	0.5M	0.08M	0.01M
C-22	Bal.	22	13	3	3	0.5M	2.5M	0.5M	0.35M	-	0.08M	0.01M
G-35	Bal.	33.2	8.1	2M	0.6M	0.3M	1M	0.5M	-	0.4M	0.6M	0.05M

Table 6.2 Summary of the empirically determined compositions for alloy BC-1, C-22, and G-35. Values are given in wt.%. Analysis carried out by Cambridge Materials Testing Limited according to ASTM E1019-18, ASTM E1097-12, and ASTM E1479-16.

Alloy	Ni	Cr	Mo	Fe	W	Cu	Co	Mn	V	Al	Si	C
BC-1	60.9	14.4	22.10	0.85	0.01	0.03	--	0.25	--	0.18	<0.01	0.011
C-22	57.6	20.7	12.97	3.74	2.80	0.06	--	0.27	--	0.28	<0.01	0.012
G-35	56.3	33.4	7.98	0.54	0.07	0.02	--	0.45	--	0.24	<0.01	<0.010

Before experiments, sample surfaces were prepared using wet silicon carbide (SiC) paper. Samples to be used in electrochemical measurements were ground using P600, P800, P1000, and P1200 grit SiC paper. Samples intended for surface analyses were further ground using P2500 and P4000 SiC paper, followed by polishing with a 1-μm diamond suspension. Following surface preparation, samples were rinsed with Type-1 water, followed by ethanol, and then dried in a stream of high purity N_2 or Ar gas.

Experimental solutions were prepared with reagent grade HCl and Type-1 water. Quantification of inductively coupled plasma atomic emission spectroscopy (ICP-AES) data involved the use of standard solutions. These standards were prepared using aliquots of metal standards (SCP Science) directly in the experimental electrolyte (1 M HCl).

6.2.2 ELECTROCHEMICAL METHODS

Electrochemical experiments were carried out using either a Reference 600 (Gamry Instruments, Warminster, PA, USA) or a Solartron Analytical model 1287 (Solartron Analytical, Hampshire, UK) potentiostat. Experiments were conducted in a custom-built PTFE flow cell designed for AESEC measurements. A brief description of this flow cell is provided below, an extensive description having been published elsewhere[150, 151, 212].

The exposed area of a working electrode (W.E.) was limited to 1 cm^2. The flow rate in the W.E. compartment was maintained at ~2.75 ml min^{-1} using a peristaltic pump. The counter (C.E.) and reference electrodes (R.E.) were housed in a second compartment, separated from the flow cell by an ionically conductive membrane. A saturated Ag/AgCl electrode (−0.197 V vs. SHE) and a Pt flag served as the R.E. and C.E., respectively. All electrochemical measurements were repeated at least twice.

The temperature during electrochemical measurements was maintained at 75°C by pre-heating the electrolyte and directly heating the W.E. affixed to the flow cell. Electrolyte temperatures were maintained by placing the solution reservoir in either an isothermal bath or on a hot plate. The W.E. temperature was maintained by placing a heating element directly on the surface opposite to the flow cell. Here, the heating element was either a hollowed Cu heating disk connected to an isothermal bath or an electric heating assembly containing thermistors connected to a digital temperature controller allowing for closed-loop temperature regulation. Together, these controls maintained experimental temperatures close to 75°C during all experiments. All experiments were performed in naturally aerated solutions except for experiments done for XPS analysis, which were conducted in an N_2-purged glove box.

Both dynamic- and static-polarization experiments were conducted using the described experimental setup. Dynamic polarization experiments were initiated at −0.4 V (vs. Ag/AgCl) and scanned positively at a scan rate of 0.5 mV s^{-1}, until a final potential of 1 V (vs. Ag/AgCl). Static polarization experiments involved several potential steps. Initially, samples were equilibrated under open-circuit conditions and then subjected to an applied potential of −0.8 V (vs. Ag/AgCl) for 60 s, followed by a 300 s period on open circuit to facilitate relaxation. Samples were then subjected to an applied potential of 0.6 V (vs. Ag/AgCl) for 60 s before again being released to open circuit to facilitate relaxation. These two steps, cathodic and anodic polarization followed by OCP measurements, were repeated up to four times each.

6.2.3 AESEC MEASUREMENTS AND DATA TREATMENT

The AESEC setup has been described in detail previously[150, 151]. Briefly, situated downstream of the electrochemical flow cell is an ICP-AES instrument (Ultima

2C spectrometer, Horiba Jobin-Yvon, France). Species released during electrochemical experiments were carried from the W.E. surface by the flow of fresh electrolyte and injected into the plasma of the spectrometer. The emission intensity at wavelengths specific to each element was measured and used to quantify the instantaneous elemental dissolution rates of the alloy components. Correlation with the instantaneous electrochemical current was made possible by correcting for a short residency time in the flow cell and through the intermediate capillaries.

The solution exiting the flow cell was introduced to the ICP using a Burgener PEEK Mira Mist® Nebulizer (Horiba Jobin-Yvon, France). Operating at 1 kW and 40.68 MHz, species exposed to the plasma undergo atomization and excitation, with the subsequent relaxation processes generating emission lines characteristic for the atom of origin. Independent mono- and polychromator optics allow the simultaneous monitoring of several emission lines. Since Mo was the alloying element present in the lowest concentrations, it was detected using the monochromator to provide increased spectra resolution. For experiments involving low dissolution rates, emission intensities exhibited poor signal-to-noise. When necessary, data were treated with a boxcar average (n = 5) as used and discussed previously[162]. Unless otherwise stated, data were not subjected to smoothing (or averaging).

For the elements studied, emission lines and their detection limits are summarized in **Table 6.3**. Experimental detection limits ($C_{3\sigma}$) were calculated using **eq. (6.1)**, where σ_B is the standard deviation of the background signal and α is the sensitivity factor determined from the calibration standards.

Table 6.3 Experimental emission lines and limits of detection.

Element	Wavelength/nm	Detection Limit, $C_{3\sigma}$/ppb
Ni	231.60	10.8 ± 0.3
Cr	267.72	4.8 ± 0.2
Mo	202.03	1.4 ± 0.1

$$C_{3\sigma} = 3\frac{\sigma_B}{\alpha} \tag{6.1}$$

Standard calibration was used to convert emission line intensities into instantaneous concentrations (C_M). Values of C_M were then converted into instantaneous dissolution rates (ν_M) according to **eq. (6.2)**, where f was the flow rate and A the surface area of the W.E.

$$\nu_M = f\frac{C_M}{A} \tag{6.2}$$

Congruent and incongruent dissolution behaviors were distinguished by comparing the composition of the electrolyte to that of the bulk material. This was done by normalizing individual dissolution rates against the bulk alloying element, Ni, according to **eq. (6.3)**, where $X_{M.}$ is the mass fraction of alloying element M. Values used for mass fractions were determined from the empirical data in **Table. 6.2** to ensure accuracy.

$$\nu'_M = \left({}^{X_{Ni}}/_{X_M}\right)\nu_M \tag{6.3}$$

Features of increased, decreased, and congruent dissolution was identified relative to the bulk composition by considering normalized dissolution rates. For instance, congruent dissolution was observed when ν'_M was approximately equal to ν_{Ni}, i.e., alloying element M was dissolving at a rate proportional to its bulk alloy composition. When ν'_M exceeded values of ν_{Ni}, alloying element M was selectively removed from the alloy matrix; i.e., the dissolution rate of M was higher than expected based on its bulk alloy composition. On the other hand, when ν'_M was less than ν_{Ni}, alloying element M was being accumulated on the surface of the alloy, i.e., its dissolution rate was less than expected based on its bulk alloy composition. The quantity of excess M, Θ_M, at the time, t, was calculated using **eq. (6.4)**.

$$\Theta_M = \int_0^t \left((X_M/X_{Ni})\nu_{Ni} - \nu_M\right)dt \tag{6.4}$$

Instantaneous dissolution rates were also converted into elemental current densities (j_M) according to **eq. (6.5)**, where F is Faraday's constant, m_M is the molar mass of metal M and, n is the number of electrons transferred in the oxidation reaction. Comparison of the sum of all elemental currents (j_Σ) relative to the electrochemical current measured by the potentiostat (j_e) provides the opportunity to separate anodic current contributions leading to dissolution, oxide growth, gas evolution, etc.

$$j_M = \frac{\nu_M\, F\, n}{m_M} \tag{6.5}$$

6.2.4 XPS MEASUREMENTS

Samples prepared for surface analysis underwent the identical electrochemical treatment used when making ICP-AES measurements but inside an N_2-purged glove box with the atmospheric O_2 content maintained at ~50 ppm to minimize further oxidation following the electrochemical experiment. Samples were then transferred and stored in an Ar-purged glove box with an O_2-content maintained at < 0.1 ppm O_2 to avoid oxidation between preparation and XPS analysis. When required, samples were then introduced into the XPS instrument using a custom-built Ar-filled glove box connected directly to the spectrometer.

XPS measurements were carried out using a Kratos AXIS Supra spectrometer. All spectra were collected using a monochromatic Al Kα X-ray source (photon energy = 1486.6 eV) operating at 12 mA and 15 kV (180 W). During analysis, the pressure inside the analysis chamber was maintained at ≤ 10^{-8} Torr. Calibration of the instrument work function was done using the binding energy (B.E.) of a standard metallic Au sample ($4f_{7/2}$ at 83.95 eV). In all spectra, photoelectrons were collected at a take-off angle of 90° from a 700 μm × 400 μm area. Survey spectra were recorded in a B.E. window from 0 to 1200 eV using a pass energy of 160 eV and a step size of 1 eV. High-resolution spectra of the C 1s, O 1s, Ni 2p, Cr 2p, Mo 3d, and S 2p lines were collected using a pass energy of 20 eV and a step size of 0.1 eV. All spectra were charge corrected against the aliphatic (C-C)

adventitious carbon signal set to 284.8 eV. All signal processing and deconvolution were performed with CasaXPS software (ver. 2.3.19) using a Shirley background subtraction. Deconvolution of high-resolution spectra was done using previously detailed fitting parameters and constraints collected from high-quality standard reference samples (Ni[68, 194], Cr[68, 195], Mo[196]).

6.3 RESULTS AND DISCUSSION

6.3.1 POTENTIODYNAMIC POLARIZATION BEHAVIOR

Polarization curves of these three alloys in aerated 1 M HCl (75°C) are presented in **Fig. 6.1**. As previously observed, the behavior changed with Mo content[208, 213] with alloy G-35 (7.98 wt.% Mo) displaying the most pronounced active-passive transition, while alloy BC-1 (22.10 wt.% Mo) showed no such transition. The E_{corr} was in the order of BC-1 > C-22 > G-35, due to the suppression of active dissolution, as revealed in **Fig. 6.2**. The active peaks of those alloys are not representative of the anodic reactions due to the high cathodic current densities, thus are not discussed here. The true anodic reaction rates may be decomposed by AESEC, shown and discussed in the following section.

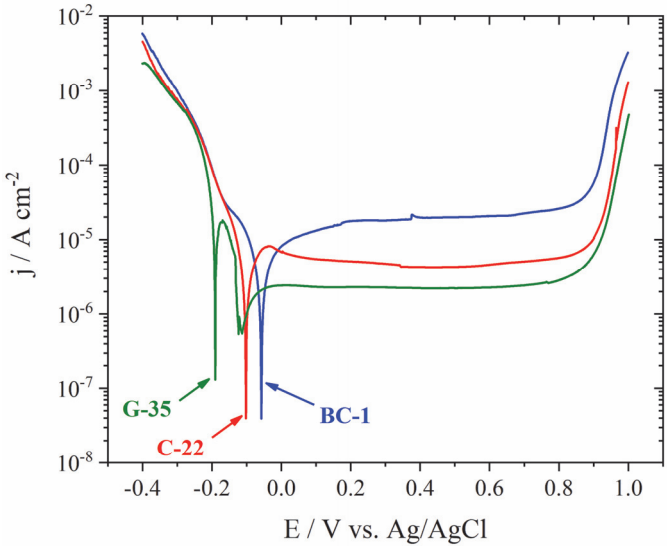

Figure 6.1 Polarization behavior of alloys BC-1, C-22, and G-35 in 1 M HCl at 75°C.

At more positive applied potentials, i.e., in the passive domain, all three alloys exhibited a potential-independent current density indicating passivity up to ~0.85 V. At applied potentials ≥ 0.85 V, the exponential increase of the current density indicating the transpassive conversion of Cr(III) into soluble Cr(VI) species[39, 214, 215]. As expected,

alloys containing larger Cr contents exhibited lower passive current densities, **Fig. 6.1**. Following the active-passive transition for alloy G-35, the measured current density switched from net anodic to net cathodic between ~−0.13 and −0.11 V, as previously observed for this alloy (not published), due to the reduction of dissolved O_2.

The electrochemical current densities (j_e) shown in **Fig. 6.1** were decomposed into the elemental current densities using AESEC measurements. The results obtained during the polarization of alloys (A) BC-1, (B) C-22, and (C) G-35, are shown in **Fig. 6.2**. j_e obtained from the potentiostat was also compared to values of j_M, the sum of the elemental currents, providing information on the faradaic yield of the anodic reactions. In measurements presented here, species released from the alloy and detected by ICP-AES were assumed to have dissolved as Ni(II), Cr(III), and Mo(IV). Oxidation states were assigned based on both ex situ surface analyses, presented later in this study, and thermodynamic data[216].

For the BC-1 alloy, immediately following the application of −0.4 V (or t = 0), increases in j_{Ni}, j_{Cr}, and j_{Mo} were observed, which quickly stabilized at low values within the cathodic domain, **Fig. 6.2(A)**. These features were the result of oxide film damage, discussed in greater detail during potentiostatic experiments (below). At applied potentials < E_{corr}, j_Σ stabilized at ~ 5 μA cm^{-2}. As the applied potential was increased to > E_{corr}, j_Σ initially remained low, confirming the absence of an active domain, before increasing to a maximum value of ~ 10 μA cm^{-2}, which then persisted throughout the passive domain. A minor current transient was observed at ~1500 s for alloy BC-1. Comparing j_e with j_Σ confirmed that a portion of the current measured by the potentiostat could not be accounted for by dissolution. In this case, differences between j_e and j_Σ are the result of oxidation reactions unrelated to dissolution, i.e., the formation of oxidized surface species not detected by ICP-AES. This discrepancy, $j_\Sigma < j_e$, which persisted through the passive domain, can be attributed to film growth[29]. The difference between j_e and j_Σ increased with increased applied potential throughout the passive domain, indicating an increased contribution of film growth at higher applied potentials.

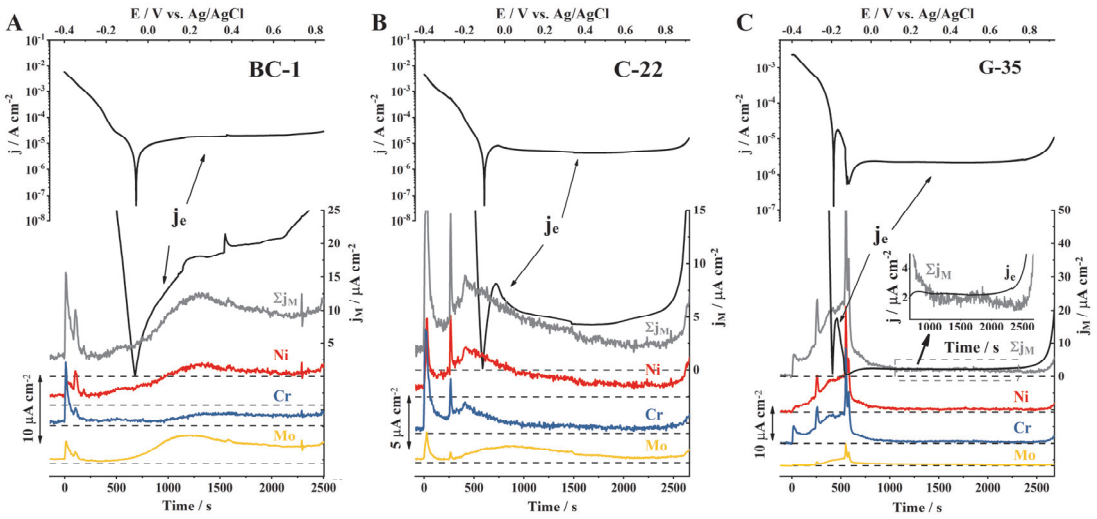

Figure 6.2 Comparison of the external current density (j_e) with the elemental (j_M) and sum current densities (j_Σ) for dynamic polarization experiments conducted in naturally aerated 1 M HCl at 75°C. The location of j = 0 for j_Σ (and j_e), j_{Ni}, j_{Cr}, and j_{Mo} are indicated but the dashed lines. Values of j_M were treated with a boxcar average (n=5) to reduce noise resulting from relatively low dissolution rates. Inset in (C) shows the enlarged area in the passive domain.

Comparing the measurements made on alloy BC-1, **Fig. 6.2(A)**, to those made on alloys C-22 and G-35, **Fig. 6.2(B)** and **2(C)**, revealed several similarities. Like BC-1, the application of −0.4 V (t = 0) resulted in momentary increases in j_{Ni}, j_{Cr} and j_{Mo}. Consistent with the role of Mo in suppressing active dissolution, the maximum value of j_Σ was lower for alloy C-22 (12.97 wt.% Mo) than for alloy G-35 (7.98 wt.% Mo). For alloy G-35, values of j_Σ exceeded values of j_e during active dissolution, suggesting a contribution from cathodic reactions in this region. At higher applied potentials, where film formation occurred, values of j_Σ were less than values of j_e for both alloys, as observed for alloy BC-1. This indicated an anodic contribution to film growth. Based on this discrepancy, film growth appeared highest for BC-1, followed by C-22, and lastly, G-35 (shown in the inset in **Fig. 6.2(C)**). Nonetheless, in all cases, the difference between j_Σ and j_e increased as the applied potential increased.

Dissolution behavior was further investigated by excess dissolution rate as a function of applied potential, **Fig. 6.3**. In this way, the potential domains of accumulation, excess dissolution, and congruent dissolution were identified. In the representation shown in **Fig. 6.3**, a positive value ($\nu_{M^\circ} - \nu_M > 0$) indicates that the dissolution rate of element M (either Cr or Mo) was less than expected based on its bulk composition in the alloy,

indicating its accumulation at the surface. On the other hand, a negative value ($\nu_{M^\circ} - \nu_M < 0$) indicates the dissolution rate of element M exceeded the amount expected based on the alloy bulk composition, i.e., M was selectively removed from the surface. The separations between depletion (or excess dissolution) and accumulation are indicated along the y-axes, **Fig. 6.3**.

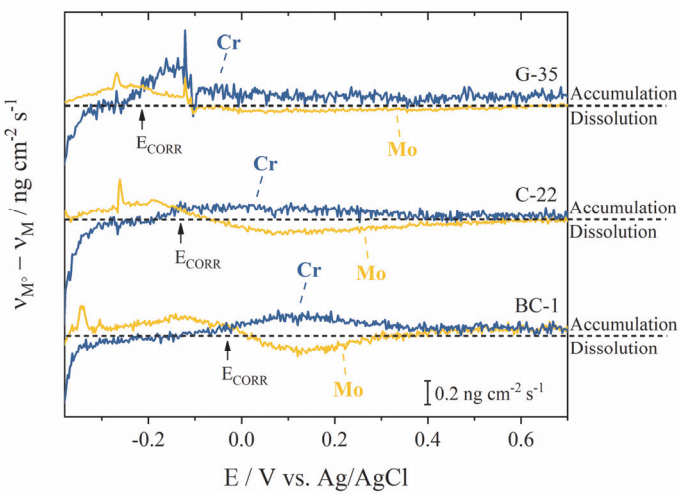

Figure 6.3 Trends in Cr and Mo accumulation and excess dissolution during dynamic polarization experiments, **Fig. 6.1**. Shown is the difference between the assumed dissolution rate of element M, ν_{M°, and its measured dissolution rate, ν_M. For each alloy, values of congruent dissolution (y = 0) are indicated by the dotted line.

For all alloys, a transition between two distinct dissolution behaviors was found near the E_{corr}. Below the E_{corr}, Cr was the dominant cation released from the electrode, while Mo was accumulated to some extent. However, at applied potentials higher than E_{corr}, this trend was found to reverse, suggesting that the previously accumulated Mo became the dominant species released while Cr was accumulated at the surface. As the applied potential increased through the region where film formation occurred, this opposing effect between Cr accumulation and Mo dissolution disappeared for BC-1 and C-22, indicating the formation of a film with a stable composition. This occurred at a lower potential for the high Mo alloy (BC-1) than for alloy C-22 with a lower Mo content. For the high Cr alloy G-35 the difference was maintained over the full potential range, with a slight but continuous Cr accumulation effectively preventing further Mo dissolution.

While AESEC data collected during potentiodynamic polarization experiments highlighted changes in dissolution behavior as a function of applied potential, data was somewhat difficult to interpret. This was especially true in the context of film breakdown and repassivation behavior, where both the applied potential as well as time play an important role[217]. To further investigate the transition between active and passive states,

static polarization measurements were employed.

6.3.2 POTENTIOSTATIC POLARIZATION BEHAVIOR

A potentiostatic approach was adopted in which negative and positive applied potentials were used to force surface activation and passivation, respectively. Between the applied potentials, free corrosion at E_{corr} was monitored. During both the applied and open-circuit potential measurements, dissolution behavior was recorded and will be discussed below. For all the alloys, the potential measurements made during cyclic activation-passivation experiments are presented in **Fig. 6.4**, where activation and passivation processes are indicated by the red and blue regions, respectively. Furthermore, locations considered for subsequent surface analysis are marked (*) in **Fig. 6.4** and will be further discussed below.

Surface activation was initiated by the application of −0.8 V, an applied potential at which high cathodic current densities were observed. During cathodic activation, H_2 evolution occurred at a high rate, experimentally observed as bubbles exiting the flow cell. Similar activation procedures have been employed previously[39, 45, 218]. The resulting damage to the oxide film, observed by AESEC, may be explained by reducing the species in the oxide into their soluble forms or by the physical removal of the surface oxide due to the rapid formation of gas bubbles at the surface. Following surface activations and a period of open circuit relaxation, passivation was promoted by the application of 0.6 V, a potential selected from the range of potentials where film formation was found to occur (see **Fig. 6.1**). Experimentally, activation and passivation procedures were cycled to investigate the effect of the repeated breakdown in the surface oxide and each alloy's ability to recover.

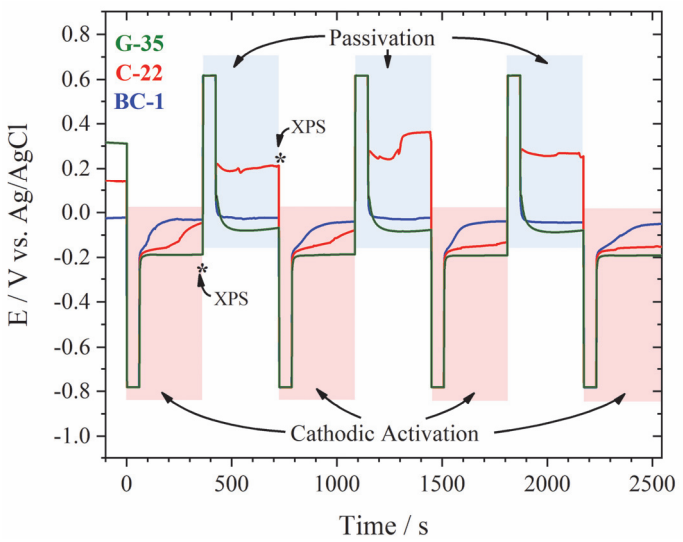

Figure 6.4 Measured potentials during cyclic potentiostatic experiments. Red areas indicate cathodic activation process (−0.8 V + 300 s OCP). Blue areas indicate passivation processes (0.6 V + 300 s OCP). Surface analysis by XPS was conducted at the indicated locations (*).

6.3.2.1 Cathodic Activation

Potentials measured during the cathodic activation processes are indicated as red regions in **Fig. 6.4**. Before the first cathodic activation, i.e., $t < 0$, the values of E_{corr} were related to the Cr-content of each alloy. Alloy G-35 (33.4 wt.% Cr) had the highest measured E_{corr}, followed by C-22 (20.7 wt.% Cr), and lastly BC-1 (14.4 wt.% Cr). This was consistent with the influence of Cr-content on oxide films formed in relatively non-aggressive environments, in this case, an air formed oxide[125]. After cathodic activation, i.e., the application of −0.8 V, this trend was found to reverse. Once activated, the alloy's ability to re-establish an oxidized surface condition, i.e., show increases in E_{corr}, was related to the alloy's Mo-content. In our previous work, we demonstrated that Mo-content was important to the stability of the oxide film as well as in stifling active dissolution behavior in acidic conditions[67, 131]. Other studies have also highlighted the ability of alloyed Mo to improve corrosion resistance in acidic conditions[140, 208]. In the data presented here, alloys BC-1 (22.10 wt.% Mo) and C-22 (12.97 wt.% Mo) demonstrate increases in E_{corr} after being activated, while the E_{corr} of alloy G-35 (7.98 wt.% Mo) stabilized at relatively low values. For alloy BC-1, E_{corr} values rapidly increased and stabilized at approximately −0.03 V, comparable to values measured before activation, i.e., $t < 0$. For alloy C-22, E_{corr} values increased more slowly and stabilized at −0.05 V after the first activation, approximately 0.2 V below the E_{corr} measured at $t < 0$. In the case of alloy G-35, E_{corr} values stabilized quickly and did not increase with time. Instead, E_{corr} values measured for alloy G-35 stabilized at −0.18 V, approximately 0.5 V below values measured at $t < 0$. While

the behavior of E_{corr} remained consistent for repeated activation processes, shown in **Fig. 6.4**, alloys BC-1 and C-22 both demonstrated a weakened ability to recover with repeated active-passive cycles. In the case of alloy BC-1, consecutive activation processes required longer times to achieve a steady-state condition. In the case of alloy C-22, E_{corr} values measured after activations were found to stabilize at lower values as the number of cycles increased.

Presented in **Fig. 6.5** are the normalized dissolution rates, ν'_M, measured during the first cathodic activation process followed by the subsequent open circuit behavior. Since similar dissolution patterns were observed during repeated activation processes, only the first activation is discussed. However, the complete active-passive dissolution behavior has also been included in the supporting information (**Fig. S6.1**). Before the first cathodic activation, i.e., $t < 0$, dissolution rates were below the equivalent limits of detection by ICP-AES, consistent with the presence of a protective air-formed oxide film. However, during the application of −0.8 V, a surge of metal dissolution was observed, confirming damage to the oxide film. During this activation process, labeled in **Fig. 6.5**, measurements of both $\nu'_{Cr,}$ and ν'_{Mo} were found to be greater than that of ν_{Ni}, suggesting their excess dissolution from the electrode surface. For all the alloys, Cr was found to be the dominant species released from the surface, followed by Mo. This suggests that cathodically induced damage released mainly Cr but also Mo, consistent with the composition of oxides formed on Cr/Mo containing alloys[29, 219, 220].

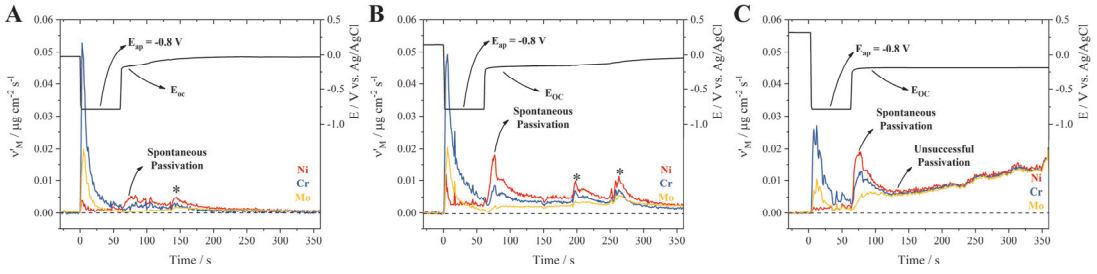

Figure 6.5 Normalized dissolution rates obtained during the first cathodic activation (−0.8 V vs. Ag/AgCl) and subsequent open circuit measurement for alloy (A) BC-1, (B) C-22, and (C) G-35. All dissolution rates are normalized to Ni, **eq. (6.3)**. For clarity, dissolution transients observed during the spontaneous repassivation process are indicated (*).

Upon release to open-circuit, again labeled in **Fig. 6.5**, alloys showed dissolution

behavior consistent with the spontaneous passivation of the surface. Both Cr and Mo were found to accumulate at the surface to some extent (i.e., ν'_{Mo}, $\nu'_{Cr} < \nu_{Ni}$), while Mo accumulation dominated this process. This was consistent with observations made during dynamic-polarization experiments (see **Fig. 6.3**), where Mo was found to be the dominant species accumulated at potentials below the apparent E_{corr}. Unsurprisingly, the surface repassivate ability of the alloy could be related to the Mo-content. Shown in **Fig. 6.5(A)**, alloy BC-1 (22.10 wt.% Mo) showed an immediate accumulation of Mo (and Cr), while quickly trending toward congruent dissolution (i.e., $\nu'_{Mo} = \nu'_{Cr} = \nu_{Ni}$) at a low overall dissolution rate. The comparison of the dissolution rate of the air formed oxide (i.e., $t < 0$) with that of the repassivated oxide demonstrates the excellent ability of this alloy to recover from damage to the surface oxide. This was consistent with the discussion of E_{corr} values following activation, **Fig. 6.4**, which suggested alloy BC-1 was able to rapidly return to a condition similar to the air formed oxide (i.e., $t < 0$). For alloy BC-1, regardless of whether the surface had an air formed oxide, was activated by cathodic polarization, or even electrochemically passivated (discussed below), measured potentials were approximately −0.02 V. The ability of alloy BC-1 to resist localized damage to the oxide film has been reported and is attributed to its high-Mo content[131, 221].

As suggested in the discussion of E_{corr} values, alloy C-22 showed increases in E_{corr} following activation, **Fig. 6.4**, toward a plateau value, suggesting the re-establishment of an oxidizing surface condition. This was, however, significantly slower than the repassivation behavior found for alloy BC-1, again suggested by E_{corr} measurements. The dissolution behavior shown in **Fig. 6.5(B)** confirmed these observations, showing that alloy C-22 required a longer time than alloy BC-1 to successfully repassivate and restore low dissolution rates. Following the release to open-circuit, the accumulation of both Cr and Mo occurred, as observed for alloy BC-1. Elemental dissolution rates trended toward congruent behavior and stabilized at low total dissolution rates, confirming the successful repassivation of alloy C-22, but to a slightly lesser degree than for alloy BC-1.

Momentary increases in elemental dissolution rates were occasionally observed for both alloy BC-1 and alloy C-22, indicated (*) in **Fig. 6.5(A)** and **(B)**, although they are of greater amplitude for the lower-Mo-containing alloy C-22. These dissolution transients are the result of film breakdown events during the early stages of repassivation.

Corresponding features were not observed during E_{corr} measurements when negative-going potential transients would be typical. When dissolution rates were converted into values of j_M and j_Σ, transients were found to correspond to current increases of between 9 and 31 μA cm^{-2}. An example of the converted currents can be found in the supporting information (**Fig. S6.2**). According to previously reported polarization resistance (R_P) values, these current transients are commonly accompanied by potential transients ≤ 3 mV (not published). During repeated cathodic activation cycles, momentary increases in dissolution rates were consistently observed during the spontaneous passivation process of alloy C-22 and, to a lesser extent alloy BC-1. It is worth mentioning that with each dissolution transient, the separation between ν'_{Mo} (and ν'_{Cr}) and ν_{Ni} increased, suggesting an increased Mo accumulation following an "event" which then slowly reapproached congruent behavior. When another event occurred, the separation (or accumulation), again increased, but not as markedly, before approaching congruent behavior. This behavior is consistent with the two roles attributed to alloyed Mo: stabilization of the oxide film and repair of localized breakdown events.

As shown in **Fig. 6.5(C)**, the dissolution behavior observed after the activation of alloy G-35 differed from that of BC-1 and C-22. While initially Mo and Cr accumulation was observed following the release to open circuit after approximately 50 s, dissolution became congruent and gradually increased with time. The occurrence of congruent dissolution, together with the continued increase in dissolution rate, demonstrated unsuccessful repassivation of this alloy. This is consistent with expectations for G-series alloys, which are not noted for their corrosion resistance in HCl solution as a result of their relatively low Mo-content[222, 223]. While alloy G-35 does contain a considerable amount of Mo, 7.98 wt.%, these differences in corrosion behavior suggest some critical concentration (or ratio) between alloyed Cr and Mo must exist to promote film stability in HCl environments.

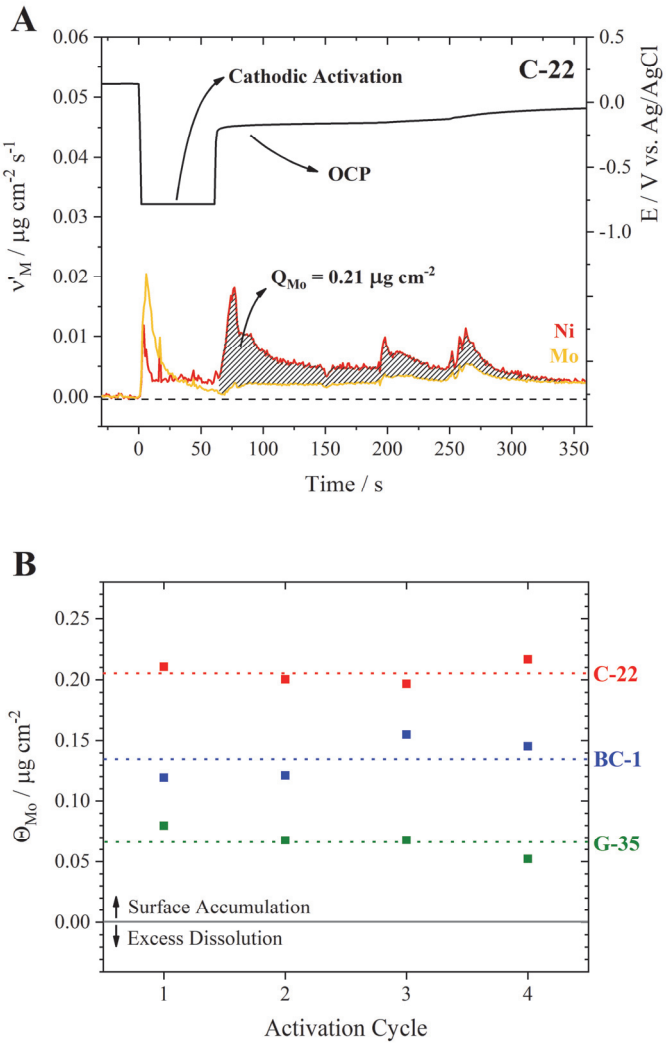

Figure 6.6 Quantification of the Mo accumulation (Θ_{Mo}) occurring during spontaneous passivation. (A) Graphical depiction of the area considered as accumulation during the 1st activation process on alloy C-22. (B) Values of Θ_{Mo} for repeated activation cycles for all alloys. Dotted lines indicate calculated averages.

The extent of Mo accumulation (Θ_{Mo}) was quantified during the spontaneous passivation processes using **eq. (6.4)**. A graphical representation of the area corresponding to Mo accumulation was highlighted in **Fig. 6.6(A)**, while the values obtained over repeated activation processes are shown in **Fig. 6.6(B)**. While Mo-accumulation would be expected to scale with an alloy's Mo-content, the experimentally determined values of Θ_{Mo} show that accumulation increased according to: G-35 (7.98 wt.% Mo) < BC-1 (22.10 wt.% Mo) < C-22 (12.97 wt.% Mo). Furthermore, comparing values obtained over repeated activation cycles, alloy C-22 was found to consistently demonstrate the largest value of Θ_{Mo}.

An explanation for this behavior was based on the observations of the dissolution transients observed during the spontaneous passivation of alloy C-22 (**Fig. 6.5(B)**). While

the mechanisms by which Mo increases corrosion resistance remains an ongoing area of research[189], two main benefits are largely agreed upon. First, Mo content is beneficial in establishing a stable oxide film, especially in acidic chloride media[208]. Here, during the repassivation process observed for alloys BC-1 and C-22, Mo accumulation was found to be dominant, as dissolution rates stabilized at low values. Second, Mo content is vital in the repair of localized breakdown events[138]. While BC-1 was able to quickly form a stable oxide film, and exhibited only small breakdown events, alloy C-22 displayed much larger breakdown events. During these events, the increased separation between ν'_{Mo} and ν_{Ni} indicated increased Mo accumulation following each event, consistent with breakdown behavior. Alloyed Mo is well known to promote the deposition of polymeric molybdate species at the breakdown site to stifle or block further dissolution[199, 224]. If events are both frequent and severe, as for alloy C-22, one would expect the accumulation of Mo at the surface to be greater than that at the surface of an alloy, BC-1, experiencing only minor breakdown events and more rapidly establishing a stable passivating oxide.

6.3.2.2 Anodic Passivation

While the ability of each alloy to recover from damage experienced by the oxide film was of primary interest, the electrochemically assisted passivation processes are also worth mentioning. Indicated as blue regions in **Fig. 6.4**, after the application of 0.6 V, E_{corr} values were found to increase relative to the values measured after activation. This increase was most significant for alloy C-22, followed by G-35, and lastly BC-1. The normalized dissolution behavior recorded during the passivation process was similar for all alloys, **Fig. 6.7**. During the application of 0.6 V, all alloys experienced the selective dissolution of Mo from the surface (i.e. $\nu'_{Mo} > \nu_{Ni}$), while Cr was accumulated to some extent ($\nu'_{Cr} < \nu_{Ni}$). While passive oxide films formed on Cr/Mo containing alloys are known to be enriched in both Cr and Mo, the selective removal of Mo species observed here was believed to be the consequence of the previous spontaneous passivation process. As discussed above, during spontaneous passivation, all alloys were found to accumulate Mo at the surface. Additionally, this was consistent with the dynamic experiments (**Fig. 6.3**) which highlighted the excess dissolution of Mo and the accumulation of Cr at applied potentials higher than the apparent value of E_{corr}. Previously, we demonstrated the dynamic nature of Mo-species to concentration at the surface in the event of film breakdown and partially released during

the reformation of Cr oxides[182].

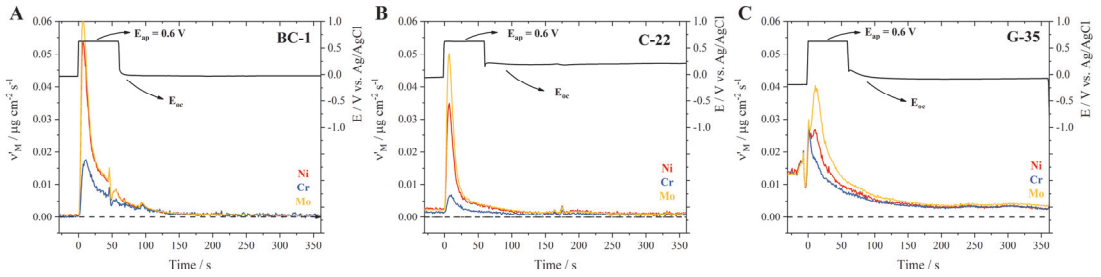

Figure 6.7 Normalized dissolution rates obtained during the 1st passivation (0.6 V vs. Ag/AgCl) and subsequent open circuit measurement for alloy (A) BC-1, (B) C-22, and (C) G-35. All dissolution rates are normalized to the Ni-content in the alloy, **eq. (6.3)**.

While the dissolution behavior of all alloys suggested the reformation of a Cr-rich surface film, differences in film quality were observed. In the case of alloys BC-1 and C-22, dissolution rates were found to quickly approach the limits of detection once released to open-circuit, implying the excellent protection afforded by these passive oxides. In contrast, alloy G-35 showed a significantly slower decrease in dissolution rate when released to open-circuit with steady-state congruent dissolution eventually occurring. These differences suggest some critical film composition is important in obtaining stability in HCl solutions.

6.3.3 SURFACE ANALYSIS

Surface compositions were determined using XPS after both spontaneous and anodic passivation. The times on the activation/passivation cycle when surface analyses were performed are indicated (*) in **Fig. 6.4**. Since similar dissolution patterns were observed for repeated activation/passivation cycles, only the surface compositions following the first SP and AP were analyzed. Survey spectra obtained after both SP and AP for the three alloys are compared in **Fig. 6.8**. Subtle differences were found in the intensities of the Ni 2p, Cr 2p, and Mo 3d signals. For all alloys, the intensity of the Mo 3d signal was found to increase following SP when compared to AP condition. In contrast, the Cr 2p signal was found to increase following AP compared to SP condition. These changes, quantified using the Ni $2p_{3/2}$, Cr 2p, and Mo 3d signals, are summarized in **Table 6.4**.

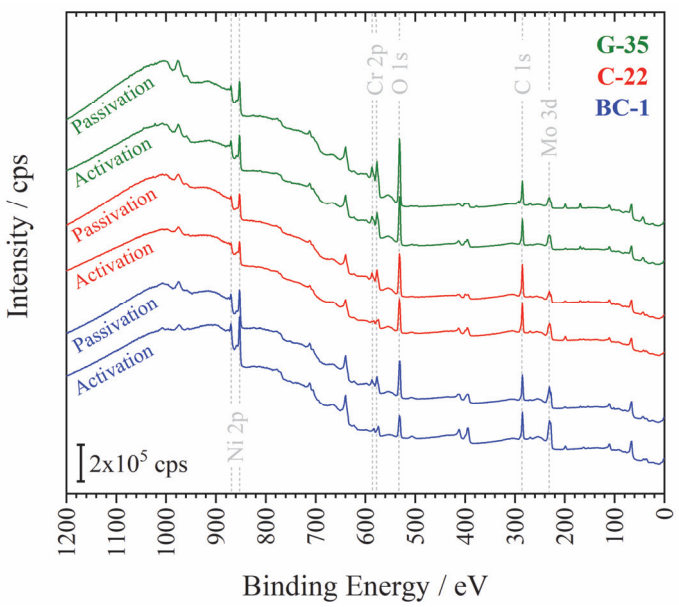

Figure 6.8 Comparison of survey spectra collected for G-35, C-22, and BC-1 in following SP and AP. Quantification of the $Ni2p_{3/2}$, Cr 2p, Mo 3d, and O 1s is given in **Table 6.4**.

Table 6.4 Surface composition (at.%) of G-35, C-22, and BC-1 following SP and AP considering the $Ni2p_{3/2}$, Cr 2p, and Mo 3d signals.

Alloy	Stage	Ni $2p_{3/2}$	Cr 2p	Mo 3d
G-35	Activation	36.8	46.3	16.9
	Passivation	33.8	56.2	10.0
C-22	Activation	45.7	24.2	30.1
	Passivation	38.1	46.1	15.8
BC-1	Activation	52.5	14.8	32.7
	Passivation	42.4	32.3	25.3

Since the oxidized alloy surface species were of primary interest here, the O 1s signal was not considered in the surface compositions listed in **Table 6.4**. Oxide films formed on various Cr-containing alloys in a variety of exposure conditions are known to be on the order of a few nm thick[178, 219, 225]. With an effective analysis depth of 5-10 nm, the relative compositions of Ni, Cr, and Mo, obtained from survey spectra are expected to comprise both metallic and oxidized components. Information on oxide compositions was extracted by deconvolution of chemical state information present in high-resolution spectra.

High-resolution spectra obtained for the Ni $2p_{3/2}$, Cr $2p_{3/2}$, and Mo 3d photoelectrons, as well as the deconvoluted chemical states, after both SP and AP, are

presented in **Fig. 6.9**. For both surface conditions, the Ni $2p_{3/2}$ signal was dominated by metallic Ni. This was true for all alloys, as shown in **Fig. 6.9(A)**, **(D)**, and **(G)**. The contributions from NiO and $Ni(OH)_2$ were found not to exceed a total contribution of 13.6 at.%. In all cases, the metallic Ni contribution dominated the signal, ranging from 86.4 to 100 at.%.

The high-resolution Cr $2p_{3/2}$ spectra recorded on alloys (B) BC-1, (E) C-22, and (H) G-35, **Fig. 6.9**, display mixtures of Cr_2O_3, $Cr(OH)_3$, and metallic Cr. This was true for both the SP and AP surfaces. For SP, the contribution from oxidized Cr species was relatively low compared to that of the metallic species, especially for the low Cr-containing alloy BC-1. The concentration of oxidized Cr species after SP was found to increase with the Cr-content of the alloy with BC-1 (14.4 wt.% Cr) < C-22 (20.7 wt.% Cr) < G-35 (33.4 wt.% Cr). Following AP, the contributions from oxidized Cr species were found to increase for all alloys compared to those observed for SP.

Deconvolution of high-resolution Mo 3d spectra collected on the three alloys, **Fig. 6.9** (C) BC-1, (F) C-22, and (I) G-35, after SP and AP, exhibited a complex mixture of metallic and oxidized Mo species (Mo(IV), Mo(V), and Mo(VI)). In some analyses, a small amount of S contamination was observed. The S 2s signal, which overlapped with the Mo 3d signal, was subtracted using the chemical state information provided by analyzing the S 2p peak. The relative amount of oxidized Mo species was found to decrease for AP as compared to SP. This was consistent with AESEC information, which demonstrated a tendency of Mo-species to accumulate during SP and be removed during AP. The spectra in **Fig. 6.9** indicate a clear preference for Mo(IV) surface species during SP, while Mo(VI) species dominate after AP. Thermodynamics supports the formation of higher valence state Mo species such as MoO_3 or MoO_4^{2-}[216], with the latter being known to undergo complex polymerization reactions at low pH[103, 199, 224].

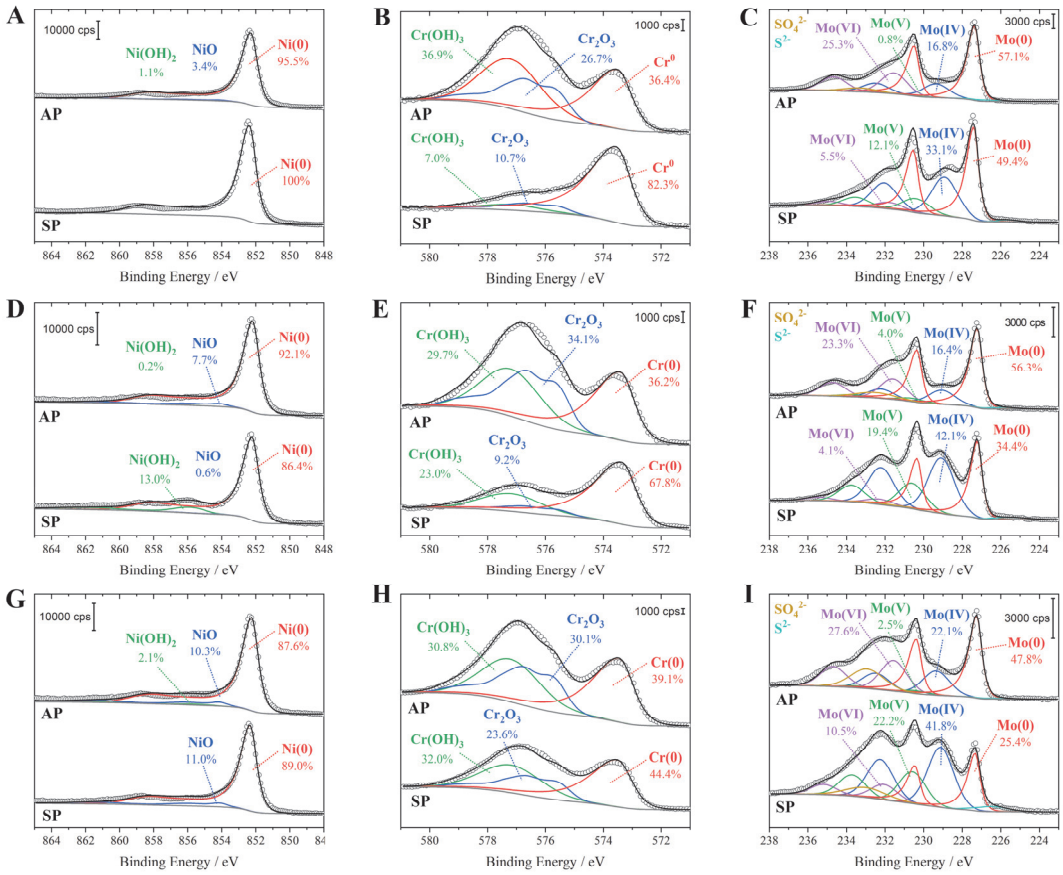

Figure 6.9 High-resolution Ni $2p_{3/2}$, Cr $2p_{3/2}$, and Mo 3d spectra collected for alloys (A-C) BC-1, (D-F) C-22, and (H-I) G-35. Surface analysis was conducted after spontaneous passivation (SP) and anodic passivation (AP) steps, as discussed for potentiostatic polarization data. Experimental data (solid black) is presented along with the resultant fit (dotted black) and individual components considered in the deconvolution (various solid colours).

While deconvoluted high-resolution spectra provide information on the ratios of oxides to metal and the distribution of various oxidized species, they do not provide a true representation of what is on the surface. For instance, the ratio of oxide to metal may increase for a given element, while the total signal intensity in the survey spectra decreases relative to other species. A more representative analysis of surface composition can be obtained by coupling the information provided by the survey spectra (i.e., the average surface composition) and the deconvoluted high-resolution spectra (i.e., the relative speciation concentrations). Shown in **Fig. 6.10** are the relative surface compositions expressed in terms of the metallic (Ni, Cr, and Mo) and oxide contributions ($Ni(OH)_2$, NiO, Cr_2O_3, $Cr(OH)_3$, Mo(IV), Mo(V), and Mo(VI)).

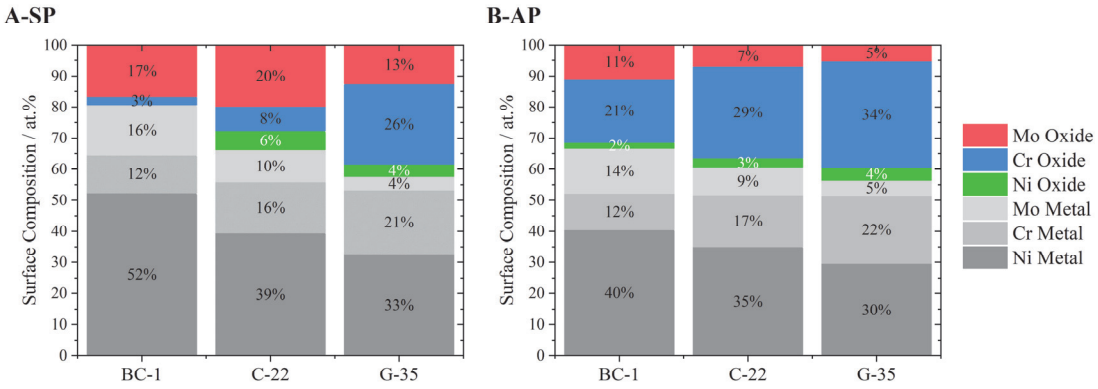

Figure 6.10 Surface composition of BC-1, C-22, and G-35 after surface (A) SP and (B) AP.

After SP, **Fig. 6.10(A)**, the amount of oxidized Mo surface species increased in the order of G-35 < BC-1 < C-22, consistent with the trends observed by AESEC, as expressed by the values of Θ_{Mo}, **Fig. 6.6(B)**. Both the AESEC and XPS data, **Fig. 6.10(A)**, show alloy C-22 exhibited the largest amount of Mo-rich surface species following SP. On surfaces analyzed after AP, all alloys demonstrated a decrease in oxidized Mo content and an increase in oxidized Cr content, **Fig. 6.10(B)**. This change was consistent with the observations made by AESEC, which showed a tendency of Mo accumulation during SP and the subsequent release during AP.

6.4 CONCLUSIONS

Using the in situ measurements afforded by AESEC, kinetic information regarding the dissolution behavior of Hastelloy BC-1, C-22, and G-35, was reported. Dissolution was investigated during surface activation, spontaneous passivation, and anodic passivation in HCl solutions. Following activation, Mo-accumulation processes were found to dominate the spontaneous passivation behavior, while Cr accumulation was also an important factor. In the event of damage to the oxide films formed on high Mo-containing alloys, BC-1 (22.10 wt.% Mo) and C-22 (12.97 wt.% Mo), oxide films were found to be rapidly repaired. However, alloy C-22 required a slightly longer time and exhibited momentary breakdown behavior. Since both film formation and breakdown events involved the accumulation of Mo-species, alloy C-22 was found to accumulate a larger amount of Mo-species compared to BC-1. In the case of alloy G-35 (7.98 wt.% Mo), while

an initial attempt to repassivate the damaged oxide was apparent, elemental dissolution rates were found to increase with congruent behavior rapidly, suggesting active dissolution. During anodic passivation processes, previously accumulated Mo species were partially removed while Cr-accumulation dominated the film formation. The concept of Mo accumulation and subsequent dissolution is consistent with previous studies conducted on film breakdown/repair. Data acquired by AESEC was also compared to ex situ XPS surface analysis. Both relative surface composition and oxidation state information were discussed with connections made to the AESEC data. Most notably, the observation suggesting the large Mo-accumulation for the moderate Mo-containing alloy (C-22) was consistent between AESEC and XPS measurements. These findings suggest the dual role of alloy Mo in stabilizing and repairing the oxide film.

6.5 SUPPLEMENTARY INFORMATION

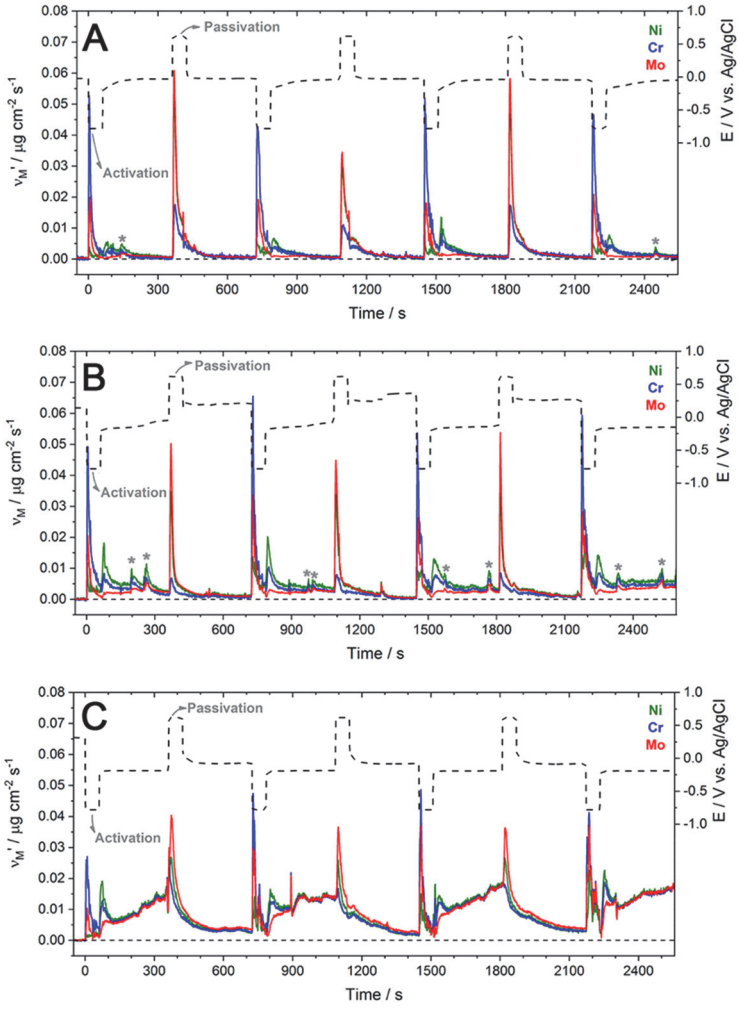

Figure S6.1 Normalized dissolution rates obtained during the repeated cathodic activation (−0.8 V vs. Ag/AgCl) and passivation (0.6 V vs. Ag/AgCl) procedures for alloys (A) BC-1, (B) C-22, and (C) G-35. Between activation and passivation, the open-circuit relaxation process was monitored. All dissolution rates are normalized to the Ni-content in the alloy, **eq. (6.3)**.

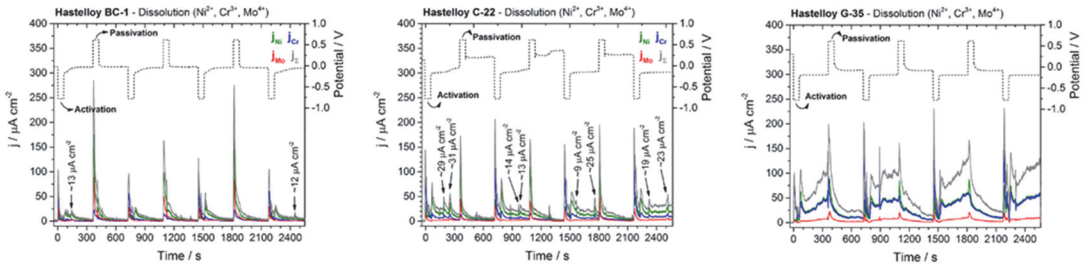

Figure S6.2 Instantaneous elemental (j_M) and sum current densities (j_Σ) for potentiostatic polarization experiments. At maximum current increase corresponding to transients (or breakdowns) are indicated.

7. MOLYBDENUM SURFACE ACCUMULATION AND RELEASE DURING TRANSPASSIVE DISSOLUTION OF Ni-BASED ALLOYS[4]

The previous chapters mainly focused on the role of Cr and Mo in the passive domain. In this chapter, Mo was found to have an interesting behavior in the transpassive domain.

ABSTRACT

The role of alloyed Mo during transpassive dissolution of four commercially available Ni-based alloys, BC-1, C-22, G-30, and G-35, was investigated by atomic emission spectroelectrochemistry. In the transpassive potential domain, Ni was the dominant cations released, while Cr, Mo, and Fe were found to concentrate, at least partially, on the surface. Namely, Mo, was found to dissolve at a relative rate significantly below its bulk concentration. This was particularly pronounced for alloy G-30, which contained a higher Fe content. When the applied potentials returned to the passive region, the surface-accumulated Mo was released. These results suggest a mechanism of Mo accumulation and release that could play a significant role in repassivation in initially neutral electrolytes such as occurs during crevice corrosion.

[4] This chapter repeats the article "J.D. Henderson, X. Li, D.W. Shoesmith, J.J. Noël, K. Ogle, Molybdenum surface enrichment and release during transpassive dissolution of Ni-based alloys, Corrosion Science, 147 (2019) 32-40." with minor modification.

7.1 INTRODUCTION

Ni-based alloys are frequently used to replace conventional steels when service conditions become aggressive and high corrosion rates ensue. Applications include, but are not limited to, the nuclear, petrochemical, and chemical processing industries. These alloys, which differ mainly in composition, are continuously being modified to improve corrosion and/or mechanical properties[226, 227]. However, successfully tailoring composition to a given application requires the thorough understanding of how individual alloying elements affect behavior. Chromium is, of course, the most significant constituent as concerns corrosion resistance, and its role in passivity has been thoroughly documented[178, 208]. The significance of the other alloying elements, such as Fe and Mo, on corrosion resistance is less well understood. These elements may be of critical importance in the transpassive potential domain, where the electrochemical conversion of the Cr(III) oxide into soluble Cr(VI) species occurs[48, 127, 208], making the Cr(III) based passive film less stable. This may be problematic for some industrial applications in which the Ni alloy is exposed to electrolytes containing large amounts of oxidizing impurities, resulting in high corrosion potentials[181, 228].

Molybdenum, in particular, remains an interesting alloying component, as it is well known to enhance corrosion resistance. For example, in the empirically defined PREN for both Ni-based alloys and stainless steels, the %Mo counts 3.3 times the %Cr[127, 227, 229]. Nevertheless, the exact mechanisms by which Mo increases the corrosion resistance remain elusive. Benefits of Mo addition include the suppression of active dissolution and increased resistance to localized corrosion[23, 208]. Among the proposed mechanisms, two concepts are frequently discussed. First, Mo has been suggested to concentrate at defect sites of the oxide film, acting as a reinforcement or filler at defect locations in the oxide[132, 138]. Second, Mo oxides, found in the outer portion of Cr-dominated oxide films, are believed to provide a cation-selective nature to the oxide film, preventing the ingress of aggressive Cl^- ions[22, 57].

The mechanism of passivation for Fe-Cr and Ni-Cr alloys involves a selective dissolution of Fe and Ni, leaving behind a Cr(III) oxide film[40, 41, 69]. For austenitic stainless steel, it has been suggested that when the passive film is breached, Mo oxides

form a temporary protective film which slows down active dissolution sufficiently to allow the Cr(III) passive film to reform[60]. This is important in the mechanism of pitting and crevice corrosion in that the local electrolyte conditions may not favor the spontaneous formation of a Cr(III) oxide film and this temporary protection could be a determining factor in the corrosion resistance.

This temporary protection hypothesis suggests that the release mechanism of Mo could therefore play a critical role in the corrosion resistance of Cr-Mo alloys of Ni or Fe. At present, studies of the effect of Mo have been limited to conventional electrochemistry and ex situ surface analysis. While these studies demonstrated a tendency of Mo to concentrate at the oxide/solution interface, no kinetic information concerning its release and its build-up on the surface have been presented, to our knowledge[29, 47, 50].

In this work, atomic emission spectroelectrochemistry (AESEC) was used to expose, for the first time, a quantitative observation of Mo retention and release during the transpassive dissolution of commercial Ni-Cr-Mo alloys. Findings demonstrate that Mo is accumulated at the surface during the onset of transpassive dissolution. During repassivation, the surface-accumulated Mo was selectively removed. Notably, the degree of Mo accumulation and subsequent dissolution at the surface were found to increase with increasing Fe content of the alloy. This was attributed to the rapid hydrolysis of Fe(III) compared to Ni(II), leading to increased local acidification, which is known to promote the deposition of Mo-species.

7.2 EXPERIMENTAL

7.2.1 MATERIALS

Alloys used in this study were provided by Haynes International (Kokomo, IN, USA) in the form of mill-annealed sheets. Coupons were cut to dimensions of 25×10 mm^2 to fit in the requirements of the flow cell. Coupon thickness varied between 5 and 10 mm, based on the thickness of the original sheet. The nominal composition of each alloy, as reported by Haynes International, is provided in **Table 7.1**.

Table 7.1 Nominal compositions (wt.%) as reported by Haynes International. M indicates the maximum concentration of an individual alloying element, while Bal. indicates the alloying element making up the balance due to fluctuations in composition.

Alloy	Ni	Cr	Mo	Fe	W	Cu	Nb	Co	Mn	V	Al	Si	C
BC-1	Bal.	15	22	2^{M}	-	-	-	-	0.25	-	0.5^{M}	0.08^{M}	0.01^{M}
C-22	Bal.	22	13	3	3	0.5^{M}	-	2.5^{M}	0.5^{M}	0.35^{M}	-	0.08^{M}	0.01^{M}
G-35	Bal.	33.2	8.1	2^{M}	0.6	0.3^{M}	-	1^{M}	0.5^{M}	-	0.4^{M}	0.6^{M}	0.05^{M}
G-30	Bal.	30	5.5	15	2.5	2	0.8	5	1.5	-	-	0.8^{M}	0.03^{M}

Since the analysis of AESEC data relies heavily on the use of accurate compositions, i.e., for normalization purposes, the exact composition of each alloy, determined by glow discharge optical emission spectroscopy (GD-OES), is also included in **Table 7.2**. For discussion purposes, both compositions (**Table 7.1 & 2**) are included here.

Table 7.2 Alloy composition (wt.%) as obtained by GD-OES compositional analysis.

Alloy	Ni	Cr	Mo	Fe	W	Cu	Nb	Co	Mn	V	Al	Si	C
BC-1	59.7	16.53	22.28	0.76	0.01	0.007	0.03	0.17	0.27	0.02	0.19	<0.01	<0.01
C-22	52.7	25.14	13.8	3.79	3.09	0.04	0.03	0.65	0.25	0.20	0.20	0.02	0.01
G-35	52.7	36.53	8.52	0.78	0.04	0.01	0.051	0.38	0.45	0.04	0.23	0.22	0.05
G-30	38.03	31.4	5.46	15.89	2.78	1.77	0.81	2.1	1.21	0.06	0.16	0.24	0.014

Prior to each measurement, coupons were ground using wet SiC paper, with the final surface preparation using P1200 grit. Coupons were then rinsed with deionized (DI) water (18.2 MΩ cm), followed by ethanol, and dried in a stream of N_2 gas. Careful surface preparation produced reproducible surface conditions and ensured a proper seal between the coupon and flow cell.

Solutions were prepared using reagent grade NaCl (Carl Roth GmbH) and DI water. Standard solutions, used to quantify atomic emission spectrometry (AES) data, were prepared using aliquots of metal standards (SCP Science) in the experimental electrolyte (1 M NaCl). Standard solutions were run through the inductively coupled plasma atomic emission spectrometer (ICP-AES) immediately following each experiment.

7.2.2 ELECTROCHEMICAL MEASUREMENTS

Electrochemical measurements were made using either a Gamry Reference 600

(for AESEC) or a Biologic VSP potentiostat (conventional electrochemistry). All electrochemical measurements were carried out in a custom-built PTFE flow cell designed for use with the AESEC setup. The flow cell, briefly summarized below, has been extensively detailed elsewhere[150, 212]. The working electrode (W.E.) was affixed to the flow cell with an exposed surface area of 1 cm^2 by the application of a fixed pneumatic pressure against an O-ring. A second compartment, isolated from the flow cell compartment by a porous membrane, housed the reference (R.E.) and counter electrodes (C.E.). A saturated Ag/AgCl electrode (−0.197 V vs. SHE) served as the R.E. against which all potentials were measured. A platinum flag was used as the C.E. All electrochemical experiments described herein were repeated at least twice.

The temperature was maintained at approximately 75°C by placing the experimental electrolyte in an isothermal circulating bath. During the experimental procedure, electrolyte introduced to the flow cell was drawn directly from the reservoir housed within the isothermal bath. Additionally, a hollowed Cu heating disk, connected to the circulating component of the isothermal bath, was fixed behind the W.E. Together, this maintained the temperature of the W.E. and electrolyte at approximately 75°C during all measurements. The flow rate was controlled using the built-in peristaltic pump of the ICP-AES instrument. Prior to each experiment the flow rate was calibrated to be approximately 2.75 ml min^{-1}.

Cyclic polarization experiments were initiated 0.1 V vs. Ag/AgCl below the corrosion potential and scanned positively at a scan rate of 0.5 mV s^{-1}, until a potential of 1 V vs. Ag/AgCl was reached. The scan was then reversed, and the potential scanned negatively until it reached the initial $E_{j=0}$. Separate potentiostatic experiments were conducted using three potential steps. Initially, samples were held in the passive region 0.3 V vs. Ag/AgCl for 5 min. Subsequently, samples were brought into the transpassive domain 1 V vs. Ag/AgCl for a period of 1, 2, or 4 min, indicated for each experiment. Finally, the return to the initial applied potential 0.3 V vs. Ag/AgCl caused the sample to repassivate.

7.2.3 AESEC MEASUREMENTS AND DATA TREATMENT

Details regarding the data acquisition and treatment have been described by Ogle

et al.[150]. Briefly, the downstream positioning of the ICP-AES instrument, an Ultima 2C spectrometer (Horiba Jobin-Yvon, France), allows for the detection of cations released from the WE in real-time. A Burgener PEEK Mira Mist® Nebulizer (Horiba Jobin-Yvon, France) was used to introduce the electrolyte leaving the flow cell into the ICP. The resultant aerosol enters a 40.68 MHz inductively coupled Ar plasma, operating at 1.2 kW. Independent monochromator and polychromator optics were used to monitor emission lines from the ICP torch. The monochromator was used for a single element with high spectral resolution, in this case Mo, while the polychromator was used to simultaneously detect other elements of interest. Emission lines used for the elements of interest and their respective limits of detection are summarized in **Table 7.3**. The detection limit ($C_{3\sigma}$) was calculated according to **eq. (7.1)**, where σ_B is the standard deviation of the background signal and α the sensitivity factor determined from the calibration standards.

Table 7.3 Experimental emission lines and limits of detection.

Element	Wavelength /nm	Detection Limit, $C_{3\sigma}$ /ppb	Equivalent, j_M /µA
Ni	231.60	22.8	1.9
Cr	267.72	10.0	0.93
Mo	202.03	4.61	0.23
Fe	259.94	9.40	0.81

$$C_{3\sigma} = 3\frac{\sigma_B}{\alpha} \tag{7.1}$$

Upon completion of AESEC experiments, instantaneous emission intensities for each metal were converted into instantaneous concentrations (C_M) by standard calibration. C_M values were then converted into instantaneous dissolution rates (ν_M) according to **eq. (7.2)**, where *f* is the flow rate and A the surface area:

$$\nu_M = f\frac{C_M}{A} \tag{7.2}$$

Congruent and incongruent dissolution behavior were distinguished by comparing the composition of the electrolyte to that of the bulk material. This was done by normalizing individual dissolution rates against that of the bulk alloying element, Ni, according to **eq. (7.3)**.

$$v'_M = \left({}^{X_{Ni}}/_{X_M}\right) v_M \tag{7.3}$$

where X_M is the mass fraction of element M as determined by GD-OES (**Table 7.1**). Perfect congruent dissolution occurs when $\nu'_M = \nu_{Ni}$, i.e., the two are dissolving at equal rates relative to the bulk composition. If $\nu'_M > \nu_{Ni}$, it implies the selective dissolution of alloying element M in comparison to the bulk alloying element, Ni. In contrast, $\nu'_M < \nu_{Ni}$ implies that excess M is concentrating at the surface. The quantity of excess M, Θ_M, may be determined by mass balance as:

$$\Theta_M = \int_0^t \left(\left({}^{X_M}/_{X_{Ni}}\right) v_{Ni} - v_M \right) dt \tag{7.4}$$

The elemental current density or metal M, j_M, was determined by conversion of the corresponding instantaneous dissolution rate (ν_M) according to **eq. (7.5)**:

$$j_M = \frac{v_M F n}{m} \tag{7.5}$$

where F is Faraday's constant, m the molar mass of metal M and n the number of electrons transferred in the oxidation reaction of metal M. The later assumes that the oxidation state of the dissolved M is known or may be surmised from equilibrium calculations. This is a formal definition only, as dissolution may occur via non-faradaic processes such as the dissolution of oxide films.

7.3 RESULTS

7.3.1 CYCLIC POLARIZATION

The polarization behavior of BC-1, C-22, and G-35 is shown in **Fig. 7.1A** and that of G-30, in **Fig. 7.1B**. All four alloys exhibited passive behavior, with the alloys of higher Cr content having higher potentials of zero current, $E_{j=0}$, and lower passive current densities, j_{pass}, consistent with previous studies[48]. **Table 7.4** summarizes the values of $E_{j=0}$ and j_{pass} for the different alloys. The anodic branch of the polarization curves may be divided into three potential domains: (1) a passive domain from $E_{j=0}$ to approximately 0.3 V vs. Ag/AgCl, (2) a second passive domain starting near 0.3 V vs. Ag/AgCl, indicated by

an increase in the anodic current followed by a current plateau; and (3) the transpassive domain, indicated by a steady increase in the current, beginning at approximately 0.6 V for alloys BC-1, C -22, and G-35, and at 0.8 V vs. Ag/AgCl for alloy G-30. The extended passive region of G-30 is believed to be the result of Fe(III) oxide stability at high potentials[230].

Return scans showed a ready repassivation for alloys BC-1, C-22, and G-35, without significant hysteresis. This was indicated by the current density retracing the forward scan until ultimately achieving values lower than those recorded during the forward scan. In all cases, $E_{j=0}$ was shifted positive relative to its value on the forward scan. Interestingly, all three alloys exhibited approximately the same $E_{j=0}$ values on the reverse scan. The decreased current densities observed on the reverse scan have been attributed to the repair of the Cr(III) barrier layer[191].

Table 7.4 Approximate potential of zero current on the forward scan, $E_{j=0}$, and passive current density, j_{pass}, estimated at 0.2 V vs. Ag/AgCl. Values are averaged over repeat experiments.

	$E_{j=0}$ / V	j_{pass} / A cm^{-2}
BC-1	−0.090	3.4 x 10^{-6}
C-22	0.019	1.9 x 10^{-6}
G-35	0.066	9.7 x 10^{-7}
G-30	0.076	8.6 x 10^{-6}

The reverse scan on alloy G-30 (**Fig. 7.1B**) showed an interesting irreproducibility: It was frequently found to have hysteresis or a complete loss of I-E relationship, as shown by the solid and dotted curves, respectively. Both behaviors suggest the onset of localized corrosion processes, with one eventually repassivating (solid line) and the other becoming self-sustaining (dotted line). The process occurring during the self-sustaining localized process was confirmed to be crevice corrosion by optical observations of damage along the impression of the O-ring. Since crevice corrosion itself is not the focus of the present work, only AESEC data in which active crevice corrosion was not observed are discussed.

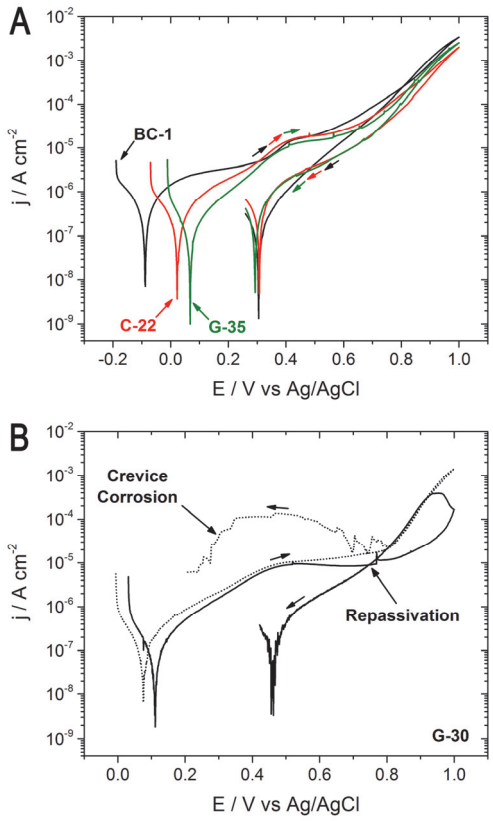

Figure 7.1 (A) Cyclic polarization behavior of alloy (A) BC-1, C-22, G-35, and (B) G-30 in 1 M NaCl at 75°C.

Within the passive region, no metal cations were detected by ICP-AES. This was attributed to the low corrosion rates afforded by the Cr-rich oxide film present in this region. Only at transpassive potentials (i.e. the breakdown of the secondary passive region) were cations detected, approximately 0.6 V for alloys BC-1, C-22, and G-35, and 0.8 V vs. Ag/AgCl for alloy G-30. Polarization in the transpassive domain led to an exponential increase in dissolution rates as a function of potential. The resultant AESEC data for cyclic polarization experiments is shown in **Fig. 7.2**. All alloys demonstrate patterns of incongruent dissolution, indicated by $\nu'_M \neq \nu_{Ni}$. Comparison of normalized rates reveals the decreased dissolution rate of Cr, Mo, and Fe, relative to Ni, suggesting the accumulation of these elements at the electrode surface. In other words, Ni was selectively removed from the oxide during transpassive dissolution while other alloying elements were accumulated, at least to some extent.

Of particular interest in **Fig. 7.2** and the focus of this article, is the unusual behavior of Mo during the reverse scan. Interestingly, repassivation resulted in ν'_{Mo} becoming larger than ν_{Ni}, suggesting the selective dissolution of Mo. While repassivation

resulted in receding values of ν_{Ni}, ν'_{Cr}, and ν'_{Fe}, the elevated rates of Mo dissolution persisted for some time following repassivation. While Mo appears to be initially retained at the surface during transpassive dissolution, it is subsequently released during repassivation. This feature is particularly pronounced for alloy G-30, and a thorough discussion of normalized data is conducted below for potentiostatic experiments.

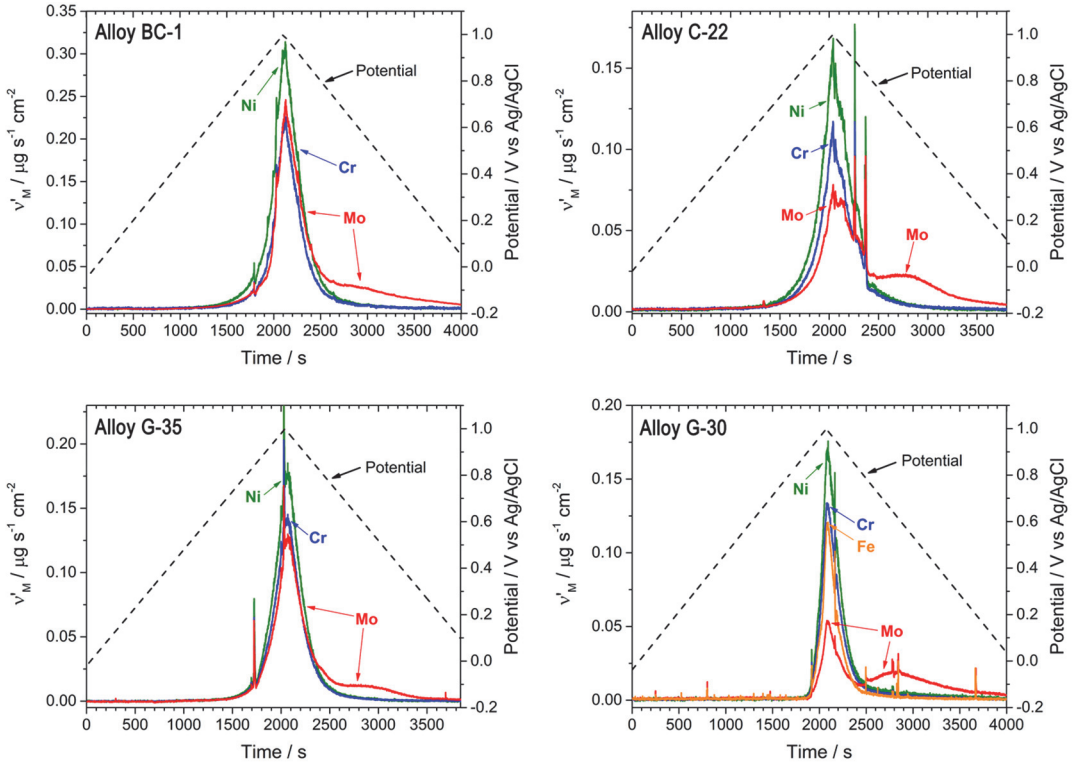

Figure 7.2 Normalized dissolution rates of alloys BC-1, C-22, G-35, and G-30, during cyclic polarization experiments in 1 M NaCl at 75°C. All dissolution rates are normalized against Ni.

7.3.2 POTENTIOSTATIC POLARIZATION

To better quantify the kinetics and mechanism of Mo retention and dissolution, a four-step potentiostatic experiment was performed: (1) the WE was held in the passive region (0.3 V vs. Ag/AgCl) for 300 s to obtain a steady-state passive film; (2) the potential was then stepped to the transpassive domain (1 V vs. Ag/AgCl) for 120 s; (3) the WE was returned to the passive region, and (4) finally released to open-circuit. The resulting data, expressed as normalized dissolution rates and elemental currents, are presented in **Fig. 7.3** and **4**, respectively.

In the analysis of the normalized dissolution data, the observations are similar to those made during cyclic experiments. Notably, potentiostatic experiments avoided complications arising from localized processes apparent in potentiodynamic experiments. While samples were held in the passive region, step 1, no metal cations were detected by ICP-AES. Following the application of the transpassive potential, step 2, all alloys demonstrated a surge of metal dissolution. The relative intensities of the normalized dissolution rates were similar to those found during cyclic experiments. In all cases, Ni was found to be the dominant cation released from the WE, while Cr, Mo, and Fe were apparently retained, to some extent, at the surface.Of the alloying elements monitored, Mo showed the greatest tendency of surface accumulation. Shown in **Fig. 7.3**, during repassivation all alloys exhibited the selective dissolution of Mo species, interpreted as a subsequent release of surface accumulated Mo. The extent of Mo retention and release was greatest for alloy G-30 and quite significant for C-22. Interestingly, this process did not correlate directly with the Mo content of the alloy.

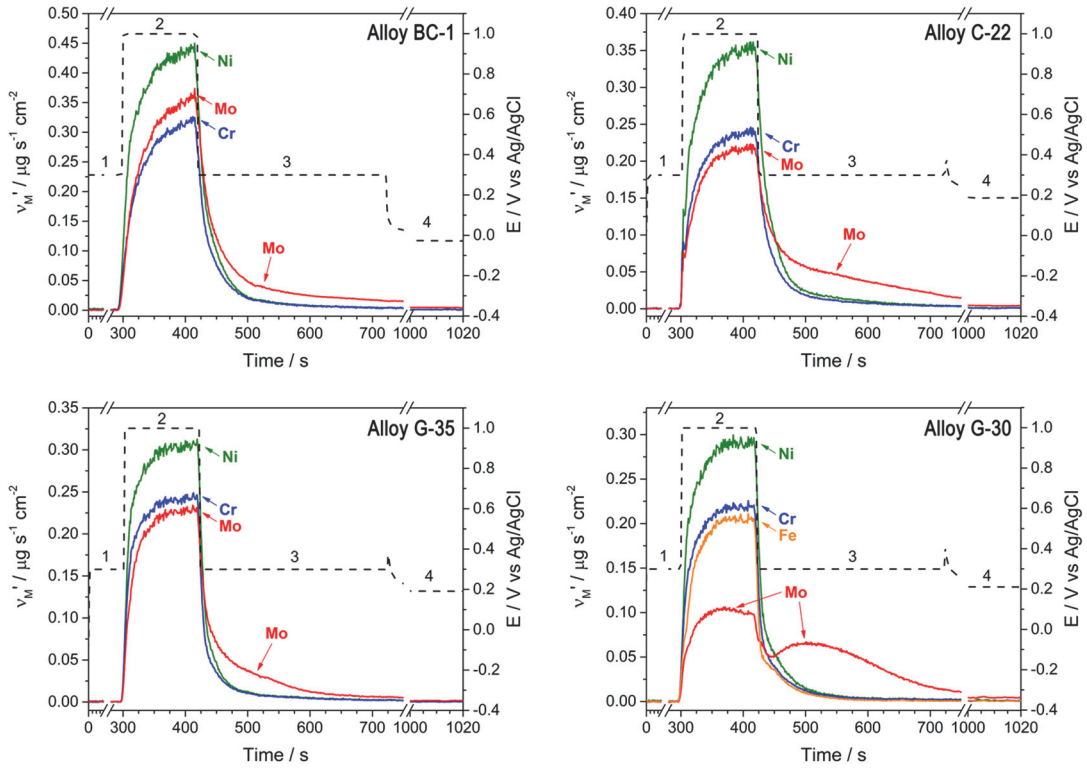

Figure 7.3 Normalized dissolution rates of alloys BC-1, C-22, G-35, and G-30, during potentiostatic polarization experiments in 1 M NaCl at 75°C. All dissolution rates are normalized Ni.

Additionally, the stoichiometry of dissolution was monitored with ICP-AES during potentiostatic experiments. To directly compare the elemental current densities, j_M, to the electrical current density, j_e, a convolution procedure was carried out. Details of this convolution have been published previously[150]. Briefly, convolution involves correcting the instantaneous current density, j_e, for the distribution of residence times in the flow cell. In this way, the elemental current densities, j_M, may be compared directly with the convoluted electrical current density, j_e^*. As shown in **Fig. 7.4**, significant currents were detected only after the application of the transpassive potential. The convoluted current density recorded by the potentiostat, j_e^*, the current contributed by individual alloying elements, j_M, and the sum current from all elemental currents, j_Σ, are compared in **Fig. 7.4**. Values of j_M were calculated according to the following oxidation states: Ni(II), Cr(VI), Mo(VI), and Fe(III). Oxidation state information was based on both thermodynamics as well as findings in the literature[29, 230]. Since dissolution prior to the transpassive domain was negligible, oxidation states were selected based on the environment for transpassive dissolution.

Using the dissolution rates and elemental currents obtained during potentiostatic experiments, information on alloy composition and faradaic yield was extracted. A summary of this information is detailed in **Table 7.5**. Using elemental dissolution rates, the total dissolved metal was used to determine a relative alloy composition for comparison to the compositions provided by Haynes International and GD-OES analysis, **Tables 7.1 & 2** respectively. Since in the ICP-AES data, only Ni, Cr, Mo, and Fe were quantified, the compositions provided by Haynes International and by GD-OES analysis were reweighted for a valid comparison. As shown in **Table 7.5**, the reweighted compositions are in agreeance with only minor discrepancies. Since AESEC data shows dissolution occurs incongruently, the alloy composition determined by ICP-AES is expected to be affected by surface accumulation processes. For example, the surface accumulation of Cr- species, highlighted in AESEC data above, leads to a consistently lower Cr content in ICP-AES analysis. Important for the upcoming discussion section is the low amount of Fe detected for alloys BC-1 and G-35 by both GD-OES and ICP-AES. As reported by Haynes, these alloys are expected to contain a maximum concentration of 2% Fe, however, based on both GD-OES and ICP-AES data presented here, the Fe content is in fact much lower, approximately 0.6%.

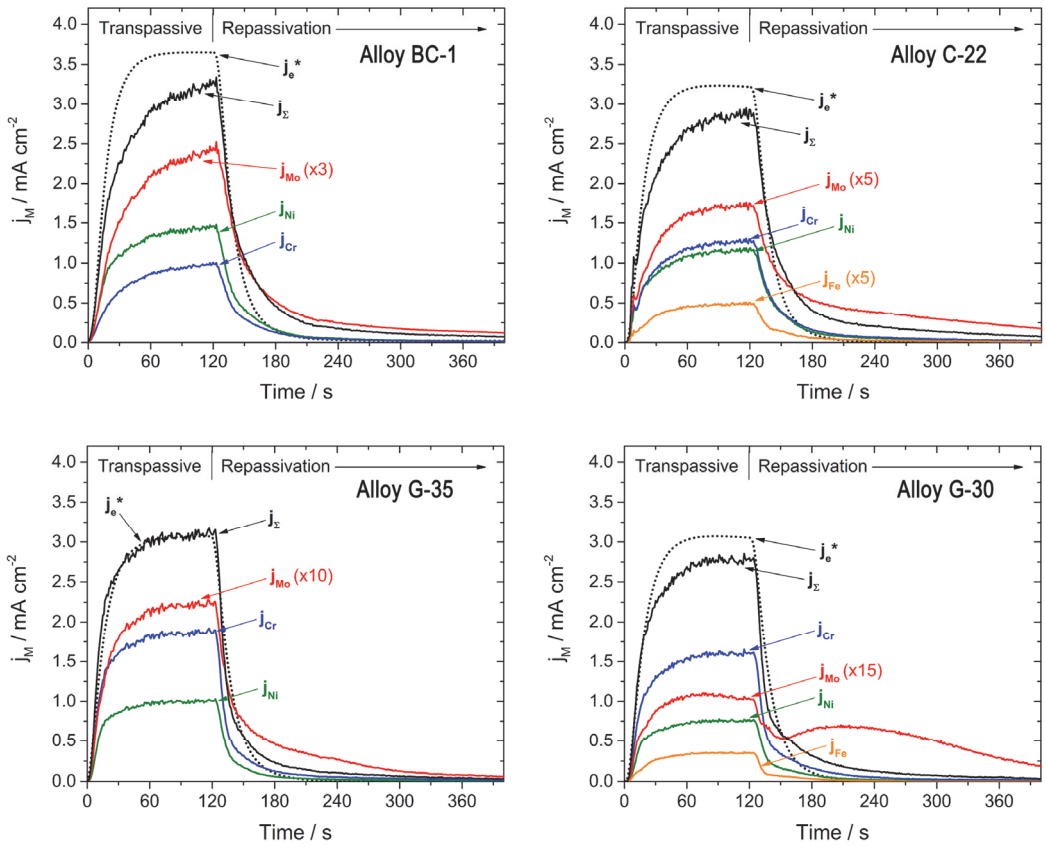

Figure 7.4 Instantaneous elemental, j_M, sum, j_Σ, and convoluted electrochemical current, j_e^*, for potentiostatic polarization experiments in 1 M NaCl at 75°C.

In addition to comparing the re-weighted alloy compositions, faradaic yields were determined by the direct comparison of j_e^* and j_Σ from **Fig. 7.4**. The values obtained for alloys BC-1, C-22, G-35, and G-30 are shown in **Table 7.5**. The average faradaic yield, 98.0%, implies that the metallic dissolution measured by ICP-AES is in good agreement with the instantaneous current densities recorded by the potentiostat. However, minor discrepancies in faradaic yields may be the result of additional anodic processes undetected by the ICP-AES, e.g., O_2 evolution or oxide formation.

Table 7.5 Reweighted alloy compositions, considering Ni, Cr, Mo, and Fe, and faradaic yields determined for potentiostatic experiments shown in **Fig. 7.3 & 4**.

Alloy	Source	Ni /%	Cr /%	Mo /%	Fe /%	faradaic Yield /%
	Haynes Int.	62.6	15.2	22.2	--	
BC-1	GD-OES	60.1	16.7	22.4	0.7	92.2
	ICP-AES	64.6	12.7	22.6	0.5	
	Haynes Int.	59.6	23.4	13.8	3.2	
C-22	GD-OES	55.2	26.3	14.5	3.9	98.4
	ICP-AES	62.7	20.3	13.7	3.3	
	Haynes Int.	58.4	33.4	8.2	--	
G-35	GD-OES	53.2	37.1	8.6	0.8	95.8
	ICP-AES	59.1	32.5	8.4	0.6	
	Haynes Int.	46	32.1	5.9	16.0	
G-30	GD-OES	41.9	34.6	6.0	17.5	105.6
	ICP-AES	49.9	31.2	5.2	13.8	

7.3.3 MO ACCUMULATION

As detailed in the discussion of **Fig. 7.3**, the high degree of Mo-accumulation observed for alloy G-30, made this alloy ideal for the further study of accumulation/dissolution phenomenon. Additional experiments were conducted as a function of time spent in the transpassive domain, shown in **Fig. 7.5**. Generally, as time spent in the transpassive domain increased, so did the signal corresponding to Mo dissolution during repassivation.

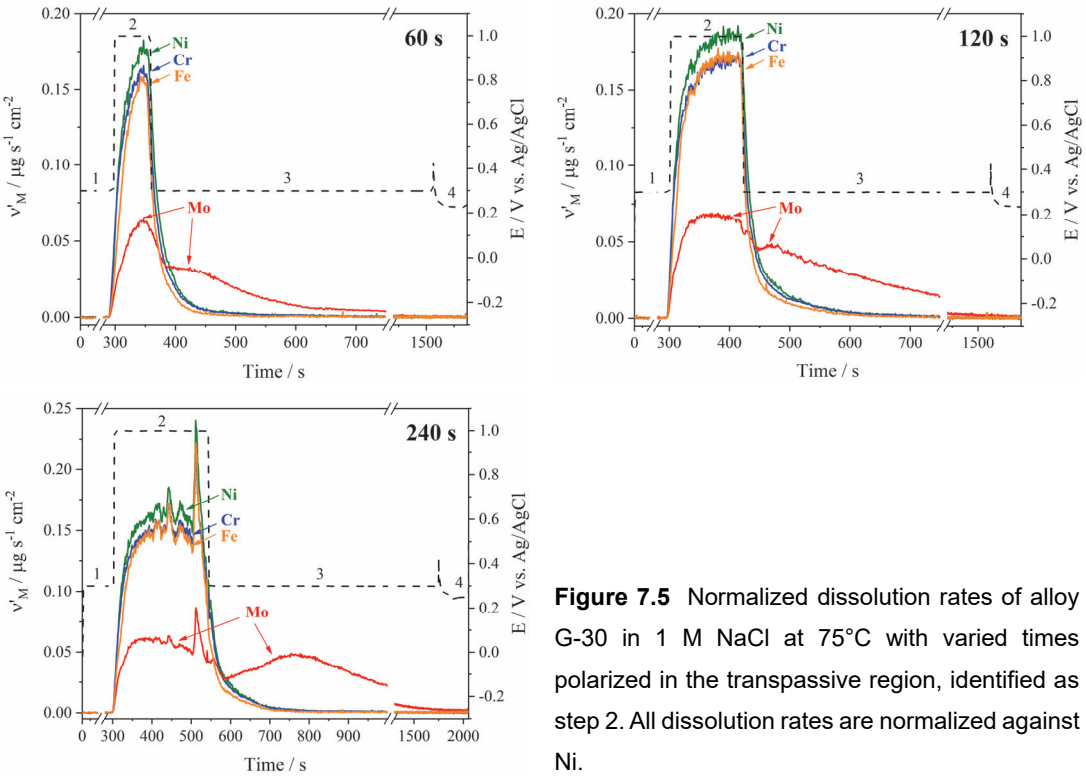

Figure 7.5 Normalized dissolution rates of alloy G-30 in 1 M NaCl at 75°C with varied times polarized in the transpassive region, identified as step 2. All dissolution rates are normalized against Ni.

Direct comparison of the accumulation and dissolution of Mo is possible by considering the excess Mo, Θ_{Mo}, during steps 2 and 3, accumulation and dissolution, respectively. The calculation of excess Mo was made according to **eq. (7.4)**. In step 2, the degree of accumulation is visualized as the difference between the integrals of Ni and Mo dissolution rates. In step 3, the dissolution of surface-accumulated Mo is the difference between Mo and Ni dissolution rates. For clarity, the regions considered as accumulation and dissolution are graphically depicted in **Fig. 7.6A**.

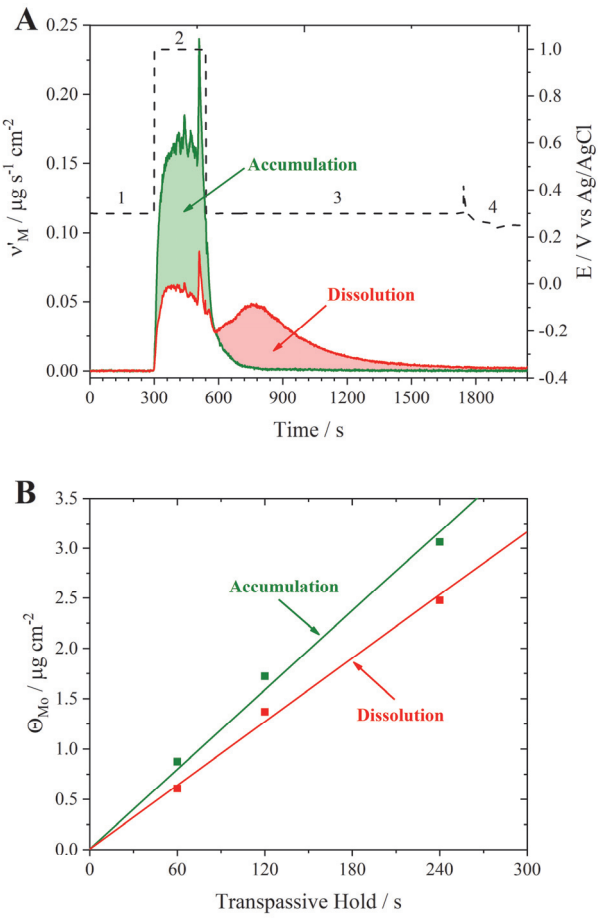

Figure 7.6 Comparison of the accumulation and dissolution of Mo species during transpassive dissolution and repassivation of alloy G-30, respectively. (A) graphical depiction of areas considered as accumulation/dissolution of molybdenum species. (B) Comparison of accumulation and dissolution as a function of time polarized in the transpassive region.

Values corresponding to accumulation and dissolution are compared in **Fig. 7.6B** as a function of time polarized in the transpassive region. The amount of Mo-accumulation was found to be proportional to the time spent in the transpassive region. The dissolution process followed a similar relationship; however, it was consistently lower than the degree of accumulation. Comparison of the two values of Θ_{Mo} yields a percent difference of between 40.2 and 56.8%.

Discrepancy between these values suggests that the surface-accumulated Mo species are not completely removed during repassivation. This implies that previous studies, which demonstrated accumulation of Mo in the oxide following transpassive polarization, have likely underestimated the extent of Mo-accumulation during transpassive dissolution. In such experiments, immediately following the application of a transpassive potential, the relaxation of the W.E. to a passive potential and subsequent repassivation can be expected to initiate the release of Mo species. This process is anticipated to occur rapidly prior to the removal of the W.E. from solution.

7.4 DISCUSSION

These results represent the first real-time quantitative measurement of the Mo accumulation during transpassive dissolution and its release during the return to the passive state. Obviously, this observation would lend support to the temporary protection hypothesis described in the introduction. When an oxide is compromised, either due to transpassive dissolution or modification in solution chemistry (i.e., pit or crevice), Mo oxides should precipitate on the surface. As the exposed material repassivates, these Mo-rich oxides would dissolve.

It is reasonable to suppose that the accumulation/release mechanism is triggered by changes in the local pH. It is well known that Mo oxides precipitate at low pH, as shown in the equilibrium calculations of **Fig. 7.7**, and a significant decrease in pH may be associated with the high rate of metal dissolution anticipated during transpassive dissolution. Highlighted in **Fig. 7.7** are the experimentally determined pH values for the initial solution (~7.4) and the solution expelled during transpassive dissolution. Since in situ pH measurements were not available in the current flow cell design, downstream collection of transpassive solution was subject to diffusion processes and therefore, experimentally measured values (~3-4) are expected to over-estimate the true pH at the corroding surface. The idea that this process is pH dependent is supported by the fact that the largest Mo retention was associated with the alloy with the highest Fe-content. In particular, Fe(III) cations are expected to undergo a more extensive hydrolysis as compared to Ni(II)[230, 231], resulting in a lower pH. The role of Fe content on this behavior is further supported by the fact that C-22, containing 3% Fe, has larger amounts of retained Mo, compared to BC-1 and G-35, which contain at most ~0.6% Fe, based on both GD-OES and ICP-AES analysis. Nevertheless, the data presented here are only suggestive as to the role of Fe.

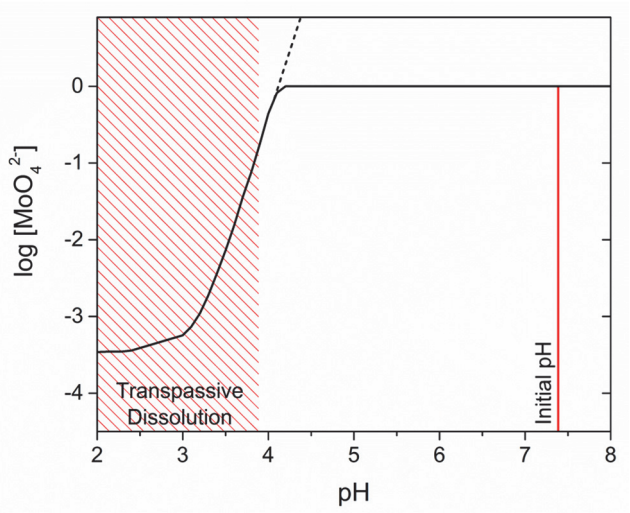

Figure 7.7 Solubility of Mo(VI), MoO_4^{2-}, as a function of pH. Calculation done for 1 mol L^{-1} MoO_4^{2-}, however, the dotted line indicates how solubility is anticipated to change as concentration increases. Data reproduced from Hydra-Medusa software.

In summary of the AESEC results, a graphical illustration of the accumulation/release process is presented in **Fig. 7.8**. While the potential is in the passive region, a passive oxide, known to be rich in Cr(III)[208], covers the surface and limits the dissolution of the underlying substrate. However, as the system is brought into the transpassive domain, the electrochemical conversion of Cr(III) to Cr(VI) results in the destruction of this protective oxide. As a result, cations begin to be released from the metallic substrate into solution. The ensuing hydrolysis reactions lead to a drop in local pH and the deposition of Mo-rich corrosion products, which are insoluble under acidic conditions (**Fig. 7.7**). When the system is returned to the passive region, the reestablishment of the protective oxide, again, limits dissolution and allows the previously developed pH gradient at the surface to dissipate. The return to the initial pH (~7) results in the increased solubility of the Mo-rich products and therefore their release from the surface.

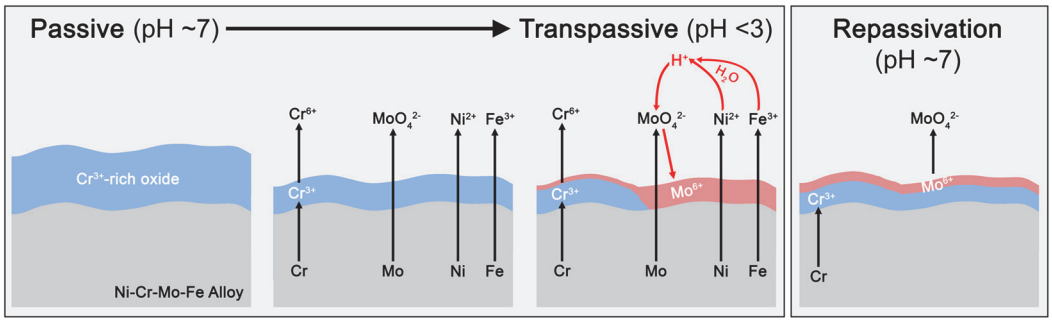

Figure 7.8 Graphical representation of the surface accumulation during the onset of transpassive dissolution and subsequent release of Mo species during the repassivation of Ni-based alloys.

This accumulation may play an important role in the repassivation of the material. While the work presented here measures only the degree of accumulation/release and does not attempt to assess its effect on passivity, it is the first account of this dynamic process. Other investigations have shown that under transpassive conditions Mo concentrates in the outer portion of the oxide film[29, 47, 232]. However, as in the cyclic polarization experiments, repassivation resulted in a release of at least a portion of the surface-accumulated Mo. The ex situ methodology employed in previous investigations has prevented the observation of this dynamic process.

The process of Mo deposition at low pH has been extensively studied in the context of crevice corrosion[21, 103, 130, 182, 199, 221, 224]. Shan and Payer demonstrated that Mo-rich corrosion products deposit as solid species within the acidified crevice, while species of Ni, Cr, and Fe are transported outside of the acidified environment before depositing[224]. The Mo-rich corrosion products found to deposit within the crevice were later characterized by Jakupi et al. by energy dispersive X-ray spectroscopy (EDX) and Raman spectroscopy[199]. While thermodynamics would suggest the formation of MoO_3, their findings suggest the formation of polymeric molybdates, including $Mo_7O_{24}^{6-}$ and $Mo_8O_{26}^{4-}$, under the acidic conditions present during crevice corrosion.

The occasional observation of crevice corrosion on the G-30 alloy is interesting, and the ability to observe this may represent another line of research for the future. Unfortunately, we were not able to identify the reasons why crevice corrosion was observed in some circumstances and not in others. Previous work has demonstrated that, compared to C-22 and BC-1, alloy G-30 is particularly susceptible to crevice corrosion in hot concentrated chloride solutions[131]. In general, the initiation of crevice corrosion is random and depends on many variables including solution chemistry, crevice geometry, and the ensuing damage morphology. An extensive discussion on the factors involved during the crevice corrosion of Ni-Cr-Mo alloys can be found in a recent review by Carranza and Rodríguez[188].

7.5 CONCLUSIONS

For the first time, the dynamic behavior of Mo during the transpassive dissolution of Ni-Cr-Mo alloys has been explored using the operando measurement afforded by AESEC. Alloying additions of Cr, Mo, and Fe appear to be retained on the alloy surface, compared to Ni, during transpassive dissolution. Immediately following repassivation, the Mo species accumulated during transpassive dissolution were released from the surface, while the accumulated Cr and Fe were not. As the time spent in the transpassive region increased, so did the accumulation in Mo surface species.

The dual phenomena of transpassive Mo-accumulation and dissolution were found to be particularly pronounced on the high Fe-containing alloy, Hastelloy G-30. This was attributed to the increased local acidification due to the release of rapidly hydrolyzed Fe(III). Decreased pH has been extensively linked to the deposition of Mo-rich corrosion product, especially in the context of crevice corrosion.

8. DISSOLUTION AND PASSIVATION OF A Ni-Cr-Fe-Ru-Mo-W HIGH ENTROPY ALLOY BY ELEMENTALLY RESOLVED ELECTROCHEMISTRY[5]

In this chapter, a novel HEA containing Cr and Mo was investigated. Mo behaved differently from the Ni-Cr-Mo alloys

ABSTRACT

The formation and dissolution of the passive film on a novel NiCrFeRuMoW high entropy alloy in H_2SO_4 were measured with atomic emission spectroelectrochemistry. Passivation involved Cr and Ru enrichment, whether passivation was achieved spontaneously at the open circuit or by potentiostatic step into the passive domain. The other elements, Ni, Fe, Mo, and W dissolved at rates approximately proportional to their bulk concentrations. The air formed film showed only a Cr enrichment. Excellent corrosion resistance properties were indicated by spontaneous passivation, the low passive current in the polarization curve, and the absence of detectable elemental dissolution during the active peak.

[5] This chapter repeats the article "X. Li, J. Han, P. Lu, J.E. Saal, G.B. Olson, G.S. Frankel, J.R. Scully, K. Ogle, Communication—Dissolution and Passivation of a Ni-Cr-Fe-Ru-Mo-W High Entropy Alloy by Elementally Resolved Electrochemistry, Journal of The Electrochemical Society, 167 (2020)." with minor modification.

8.1 INTRODUCTION

High-entropy alloys (HEAs) are a new class of materials consisting of five or more principal elements. They have demonstrated a combination of exceptional properties such as high strength and ductility, improved fatigue resistance, fracture toughness, and thermal stability and have great potential for use in extreme environments[233-236]. Progress to date also suggests the possibility of enhanced corrosion resistance[4, 235]. Their vast compositional design space creates new opportunities for material development, however the difficulty of navigating this space remains a formidable obstacle[237]. To progress in the development of corrosion resistant HEA materials, we would like to better understand how each element contributes to the passivation, corrosion, and dissolution of such an alloy. To achieve this, atomic emission spectroelectrochemistry (AESEC) was used to obtain real time observations of passive film formation and dissolution on an element by element basis.

8.2 EXPERIMENTATION

The alloy used in this work was a highly corrosion resistant HEA with elemental composition of 38Ni21Cr20Fe13Ru6Mo2W at.%. This alloy was originally proposed based upon a computational design approach exploiting many of the attributes desired in alloys resistant to Cl^- and reducing acids[89, 238]. Its preparation and metallurgical characterization have been previously described[100]. Following heat treatment at 1250 °C for 120 h and water quenching, it was found to be a homogeneous single-phase structure[100]. Passive film formation[44, 89] and localized corrosion behavior of this HEA have been described previously[100].

The AESEC technique directly measures simultaneously the elemental dissolution rate of each individual alloying element by coupling an inductively coupled plasma atomic emission spectrometer downstream from an electrochemical flow cell. A review of the principles and instrumentation of AESEC is available elsewhere[151] including all of the calculations used in this work. The sample preparation, experimental conditions, and calculations were identical to those recently published by Li and Ogle[45] for the Ni-Cr-Mo system unless otherwise stated. Elemental dissolution rates were determined as a

function of time for Ni, Cr, Fe, Ru, Mo, and W. The use of the monochromator was required for W and Ru, and, as only one element could be measured with the monochromator in a single experiment, W dissolution was measured in separate experiments. Due to its low concentration in the alloy and corrosion characteristics, W dissolution was always very low and near the detection limit of ≈ 7 ppb (1 pmol s^{-1} cm^{-2}).

8.3 RESULTS AND DISCUSSION

An overview of the HEA reactivity in Ar purged 2 M H_2SO_4 was obtained by considering its linear sweep polarization curve (**Fig. 8.1A**). The upper trace gives the conventional polarization curve of electrochemical current density (j_e) vs. potential. Five domains are apparent: the cathodic domain (c1), an active peak (a1), followed by a cathodic loop (c2). The latter may be due to the accumulation of elements such as Ru, which are catalytically active to hydrogen reduction. This was followed by a stable passive (a2), and a transpassive (a3) domain. The elemental dissolution rates, ν_M, (lower curves) were detected only during the cathodic activation step (120 s at −1 V vs. SCE) and during the transpassive domain. Both are shown on an expanded scale in 1B and 1C, respectively, with the dissolution rates normalized to the bulk Ni composition as normalized rate $\nu'_M = (\chi_{Ni}/\chi_M)$ ν_M, where χ_M is the atomic fraction of element M. Excellent corrosion resistance properties of the alloy in this electrolyte were indicated by the low passive current in the polarization curve and the absence of detectable elemental dissolution during the active peak, which suggests immediate incorporation into the surface film.

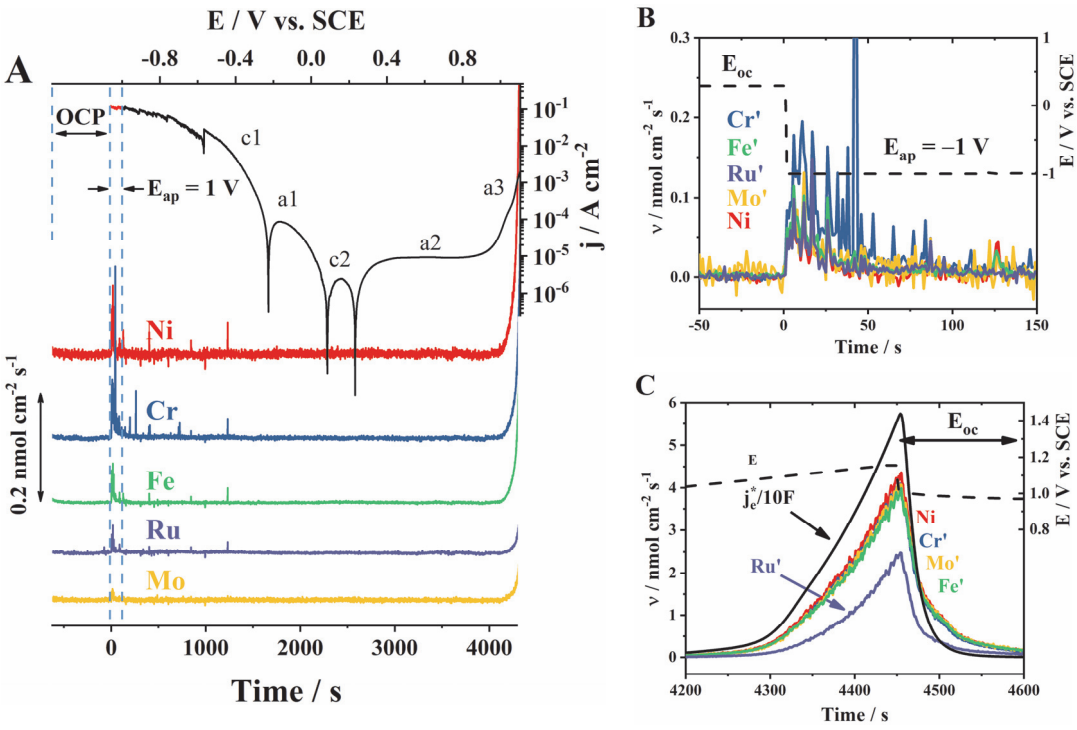

Figure 8.1 A: Elementally resolved polarization curve of the HEA in Ar purged 2 M H_2SO_4, ambient temperature, from −1 V to +1.1 V vs. SCE at 0.5 mV/s following a 120 s cathodic activation at −1 V vs. SCE. Inset B: magnification of the normalized elemental dissolution rates during cathodic activation. C: normalized elemental dissolution rate during transpassivation.

The cathodic activation (**Fig. 8.1B**) resulted in the release of all six elements (W not shown). The intense cathodic current density ($j_e < -100$ mA cm^{-2}) led to the formation of significant hydrogen gas which may explain the sharp perturbations. The normalized Cr dissolution rate was higher than the other elemental dissolution rates suggesting the dissolution of a Cr enriched film formed by exposure to air and/or water during the preparation process. This is consistent with previous XPS results in which only Cr accumulation was observed in the air-formed oxide[44].

The transpassive domain (**Fig. 8.1C**) showed congruent elemental dissolution for all elements except Ru, which may be enriched in the surface layers. At higher potentials (not shown), the Ru dissolution increased well above that of the other elements. The electrical current, j_e, followed the form of j_M, however the faradaic yield of dissolution (not including W) was only about 50%, suggesting a significant contribution of anodic processes such as oxide and/or oxygen formation, which could not be not directly detected by ICP-AES.

Elemental dissolution transients recorded during a potentiostatic passivation step are shown in **Fig. 8.2A** and **B**, compared with the expected congruent dissolution rate based on the Ni dissolution rate, $\nu_{M^\circ} = (\chi_M/\chi_{Ni})\nu_{Ni}$, shown as a dashed curve. The oxide film was first removed by a 120 s cathodic activation at −1.0 V vs. SCE followed by 300 s stabilization period at open circuit. Then the potential was stepped to +0.6 V vs. SCE. Significant accumulation of Ru and Cr occurred during the potentiostatic passivation as their dissolutions rates were nearly undetectable (**Fig. 8.2B**), consistent with previous studies[44]. Mo dissolved at rates very close to its hypothetical congruent values ($\nu_{Mo} \approx \nu_{Mo^\circ}$) and the Fe dissolution rate was slightly below the expected congruent value (**Fig. 8.2A**). In a separate experiment (not shown), W was found to be nearly congruent with Ni although the noisy W signal made a strict analysis of this element difficult.

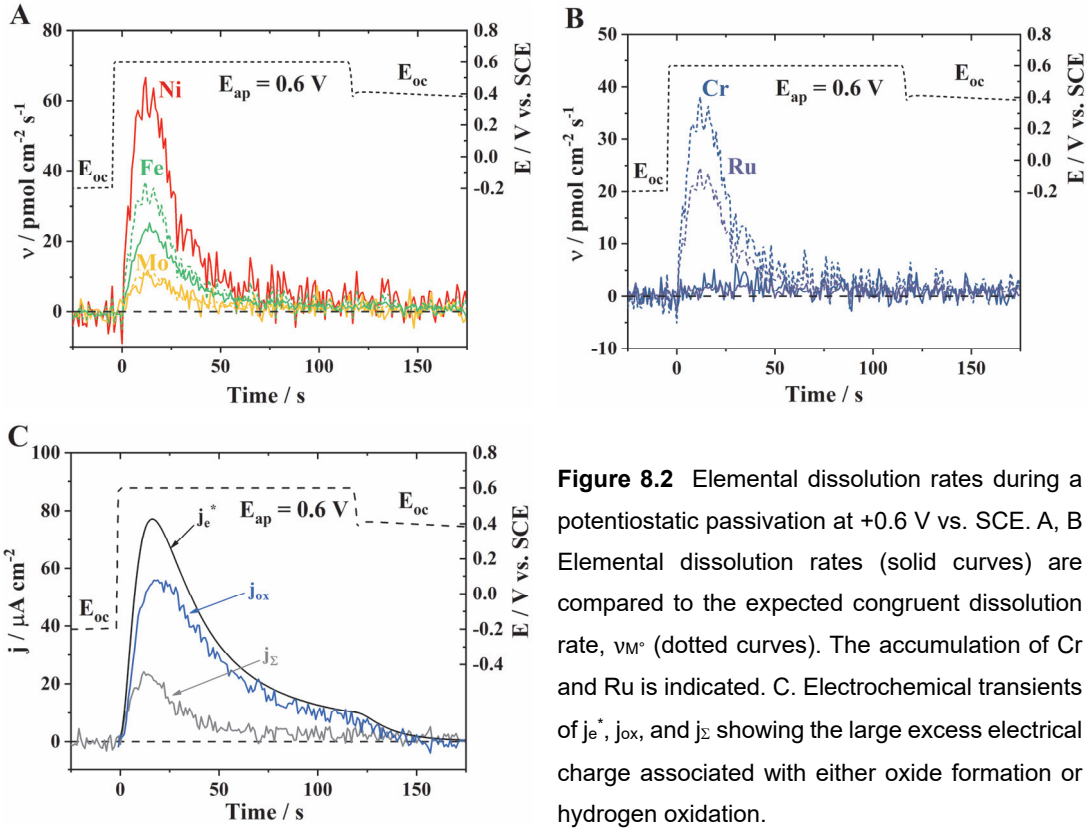

Figure 8.2 Elemental dissolution rates during a potentiostatic passivation at +0.6 V vs. SCE. A, B Elemental dissolution rates (solid curves) are compared to the expected congruent dissolution rate, ν_{M° (dotted curves). The accumulation of Cr and Ru is indicated. C. Electrochemical transients of j_e^*, j_{ox}, and j_Σ showing the large excess electrical charge associated with either oxide formation or hydrogen oxidation.

The dissolution rates of Cr and Ru increased slightly following passivation and became congruent within experimental error. Integration of the Ni dissolution transient gives the quantity, Q_M, dissolved: Q_{Ni} = 2.0 nmol cm^{-2}. Assuming that all or most of the oxidized Ni goes into solution, the surface accumulation Θ_M of other elements may be

estimated from mass-balance as $\Theta_M = (\chi_M/\chi_{Ni})Q_{Ni} - Q_M$. In this way, the Ru and Cr composition of the accumulations may be estimated as: Θ_{Cr} = 1.0 nmol cm^{-2}, Θ_{Ru} = 0.51 nmol cm^{-2} and Θ_{Fe} = 0.34 nmol cm^{-2}. Considering only Θ_{Cr}, this would correspond to ≈ 0.16 nm of Cr_2O_3 assuming a uniform film of the usual density. This low value is consistent with previous experiments for stainless steel[39, 40] and Ni-Cr-Mo alloys[45].

The current density transient, j_e^*, was significantly more intense than the elemental dissolution as indicated in **Fig. 8.2B** which compares j_e^* with the sum of the elemental dissolution rates expressed as current, j_Σ. (Note that the * indicates that the current data has been convoluted so as to have a similar time scale as the spectroscopic emission data[151]). For reference, the unconvoluted current transient is also shown. The oxidation state of each element for calculating elemental current was chosen as follows: Ni(II), Cr(III), Fe(II), Ru(IV) and Mo(VI). Comparison of j_e^* and j_Σ gives a faradaic dissolution yield of approximately 25%. In previous work with Ni-Cr-Mo alloys[45], the faradaic yield of dissolution was much higher, approximately 65% with the excess current very nearly accounted for by oxide formation. From **Fig. 8.2C**, the difference between j_e^* and j_Σ was integrated to give an excess charge density of Θ_e/F = 32 nmol cm^{-2} corresponding to 1.6 nm if considered as a uniform film of Cr_2O_3. This demonstrates that the formation of insoluble oxides is favored for the HEA in the passive domain.

The difference between the thicknesses estimated by mass-balance and mass-charge balance is surprising. Our previous work with Ni-Cr-Mo, the two estimations gave similar values, 0.25 nm and 0.38 nm respectively. The assumption that only Ru and Cr oxides formed during this experiment would not explain the difference. This is demonstrated by consideration of total oxidation current, j_{ox}, in **Fig. 8.2C** which is estimated by assuming all oxidized Ni was soluble and the other elements were oxidized congruently. Even with this estimation, the large excess of anodic current is evident and suggests that elements other than Cr and Ru contributed to the oxide film. However, the oxidation of adsorbed hydrogen may also contribute to the j_e transient as the cathodic current during the activation step was on the order of −100 mA, 100 times that of the Ni-Cr-Mo alloy.

Spontaneous passivation was observed following activation (**Fig. 8.3**). After being

released, the potential rose slowly from E_{oc} = −400 mV vs. SCE to −150 mV vs. SCE over an approximately 300 s period, and then suddenly jumped to +300 mV vs. SCE in about 50 s. The potential jump occurred simultaneously with a peak of Ni, Fe, and Mo dissolution.

W dissolution was also observed as shown from a separate experiment. Again, Cr and Ru were not observed, and we may presume they were accumulated on the surface as the passive film reformed. The calculation based on the transient dissolution of Ni during spontaneous passivation gives accumulations of 0.48 nmol cm^{-2} of Cr and 0.34 nmol cm^{-2} of Ru on the surface. When potentiostatic passivation was performed after spontaneous passivation, the Ni dissolution was reduced to 15% of that observed in **Fig. 8.2**.

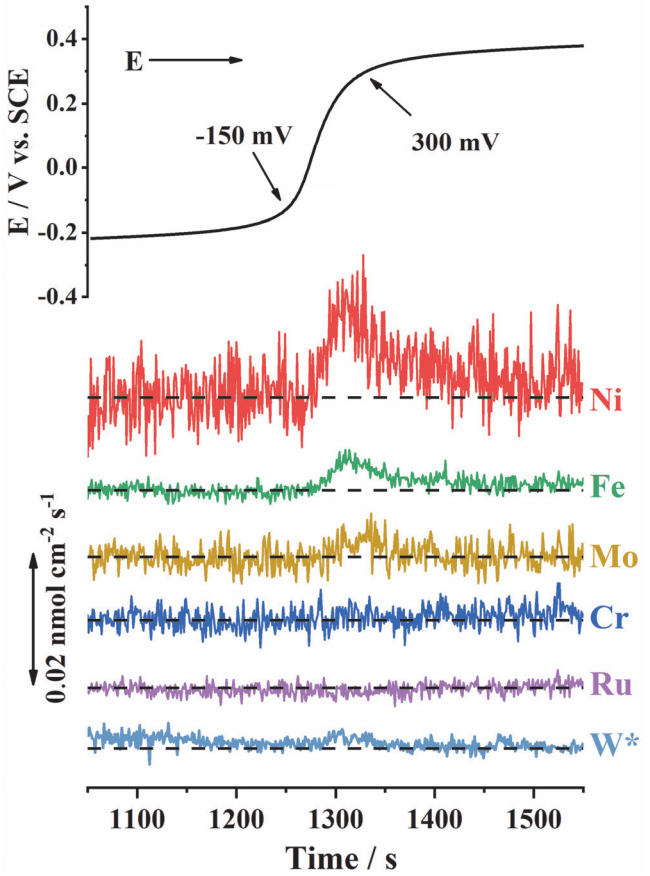

Figure 8.3 Elemental dissolution rates during spontaneous passivation at open circuit after cathodic activation (−1 V vs. SCE). Dashed line indicates zero. Dissolution rates of Cr, Fe, Ru, Mo, and W are offset.

*W was measured in a separate experiment.

The Cr and Ru surface accumulations were formed during the passivation steps and dissolved during the activation step. The excess Cr and Ru were clearly visible in the dissolution transients (**Fig. 8.4**), although significant amounts of Ni, Fe, and Mo were also observed. The mechanism of cathodic dissolution is complex and probably involves not

only the reduction of the oxides but also their physical removal by hydrogen gas. The true interfacial potential in this domain is probably much more positive than the −1 V vs. SCE imposed due to ohmic potential drops associated with the large cathodic current (≈ −100 mA cm^{-2}) coupled with the finite electrolyte resistance that is further enhanced by intense hydrogen bubble formation.

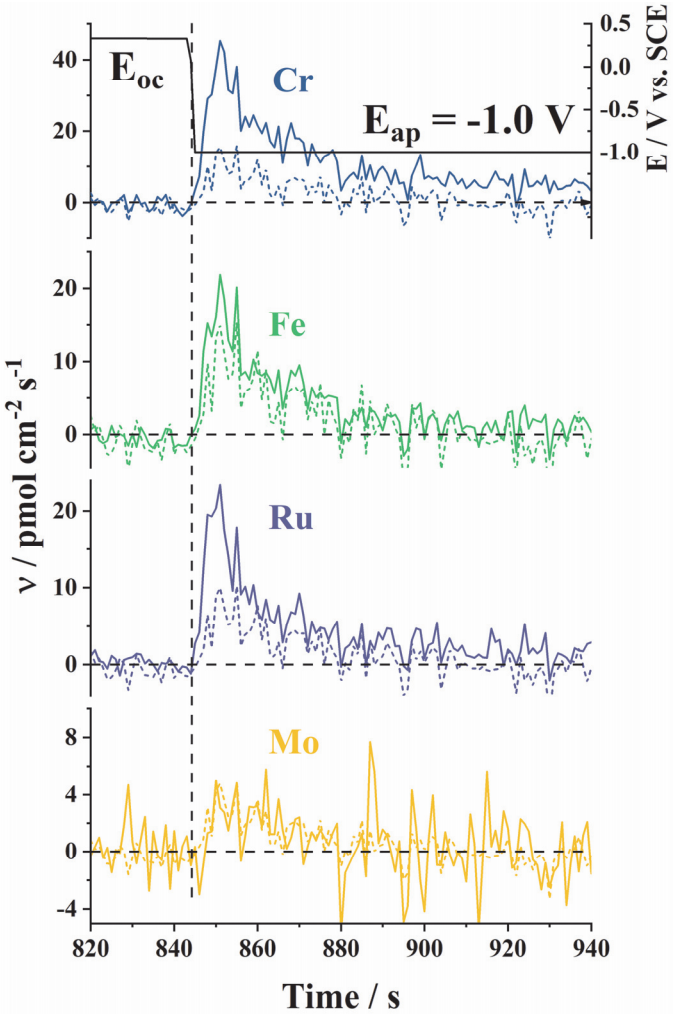

Figure 8.4 Elemental dissolution rates during a potentiostatic activation at −1 V vs. SCE. Elemental dissolution rates (solid curves) are compared to the expected congruent dissolution rate, ν_{M° (dotted curves). Excess dissolution of Cr and Ru is indicated.

Two unique features of the NiCrFeRuMoW HEA investigated here, as compared with Ni-Cr and Ni-Cr-Mo previously studied[45], was the accumulation of Ru and Cr observed during passivation and the absence of a Mo accumulation during spontaneous passivation. For stainless steel and Ni-Cr alloys, Cr is usually the major element enriched in the passive film[30, 220]. The presence of Cr as a major alloying element in HEAs, however, does not guarantee the formation of the Cr-enriched passivation film[236]. For

example, previous work[98] with the equiatomic CoCrFeMnNi HEA in 0.1 M H_2SO_4, using on-line ICP-MS combined with electrochemistry, suggested that the film was enriched in Fe and Mn but depleted in Cr as compared to a 304 stainless steel. Likewise, an on-line ICP-MS investigation of the compositionally complex alloy Al1.5TiVCr in 0.5 M NaCl demonstrated that the repassivation of the alloy occurred by the formation of an Al-rich oxide film[64]. These diverse mechanisms illustrate the interest of elementally resolved electrochemical measurements.

8.4 CONCLUSIONS

This work has demonstrated the use of AESEC to measure the contribution of the alloy components to the formation and dissolution of the passive film on a novel, corrosion resistant, non-equiatomic NiCrFeRuMoW high entropy alloy. Passivation involved the accumulation of Cr and Ru, whether passivation was achieved spontaneously at open circuit, or by a potentiostatic step into the passive domain. The other elements, Ni, Mo, and W dissolved at rates approximately proportional to their bulk concentrations while a slight accumulation of Fe was indicated. The accumulation of Ru was significant in that apparently it enhanced the catalytic properties of the material to hydrogen reduction. Excellent corrosion resistance properties of this alloy in this electrolyte were indicated by spontaneous passivation, the low passive current in the polarization curve and the absence of detectable elemental dissolution during the active peak. Potentiostatic passivation showed a significant excess of charge (low faradaic yield of dissolution), implying that oxide formation and/or the oxidation of adsorbed hydrogen contributed significantly to the total anodic reactions.

9. CONCLUSIONS AND PERSPECTIVES

In this dissertation, the passivation behavior of a series of Ni-based alloys was investigated. Elemental dissolution was monitored in situ by AESEC during electrochemical processes. Surface accumulation and excess dissolution of alloying elements such as Cr and Mo were obtained by applying mass-balance to the dissolution rate data. The oxidation states of Mo were predicted by thermodynamic calculations and experimentally determined by XPS. These results illustrated the role of the alloying elements in passivation. The major conclusions and perspectives are given below.

9.1 ENRICHMENT OF Cr DURING PASSIVATION

The role of Cr is clear and straightforward. Cr was observed to accumulate on the surface during passivation (anodically and spontaneously) for Ni-Cr, Ni-Cr-Mo alloys (**chapters 4, 5, 6**), and the NiCrFeRuMoW HEA (**chapter 8**). This Cr accumulation correlated directly with a decrease in elemental dissolution rates for all elements, consistent with the theory of a Cr-enriched passive film. The enriched Cr may be removed by cathodic activation accompanied by a return to the initial corrosion rate. When the alloy was switched from the active state to the passive state by repeated potentiostatic cycles, Cr could be built up and removed from the surface reversibly.

The quantity of accumulated Cr during anodic and spontaneous passivation was tiny, i.e., less than one monolayer of Cr_2O_3. This indicates that only a fraction of the surface was involved in the sequence of potentiostatic cycles.

9.2 THE ROLE OF Mo

The role of Mo was investigated for commercial C-22 alloy in **chapter 4**, **chapter 5** for synthetic Ni-Cr-Mo alloy in H_2SO_4 solution, and **chapter 6** for commercial Ni-Cr-Mo alloys in HCl solution. It was found that Mo lowered the i_{crit} and improved the spontaneous passivation of Ni-Cr-Mo alloys with a potential-dependent behavior in both H_2SO_4 and HCl solutions. In the neutral NaCl solution, the accumulation of Mo was observed in the transpassive domain (**chapter 7**), probably associated with the local pH

change.

9.2.1 POTENTIAL-DEPENDENT Mo ENRICHMENT AND DISSOLUTION

Results obtained from the synthetic Ni-Cr-Mo in H_2SO_4 (**chapter 5**) and commercial Ni-Cr-Mo alloys in H_2SO_4 (**chapter 4**) and HCl (**chapter 6**) showed that the role of Mo was potential-dependent. In the low potential domain (active-passive transition domain), Mo accumulated on the surface and promoted the formation of the passive film. The accumulation of Mo is associated with a decrease of i_{crit} for Ni-Cr-Mo alloys compared to Ni-Cr alloy (**chapter 5**). In the high potential domain (passive domain), Mo was, in contrast, active. The dissolution of Mo in the passive domain is above congruent for Ni-Cr-Mo alloys (**chapters 4, 5, 6**).

Mo also enhanced the spontaneous passivation ability. When the passive film was removed by cathodic activation, Ni-Cr-Mo alloys formed a passive film spontaneously. The quality of this film, in terms of the resistance to dissolution, was closely related to the Mo content in the alloy. In H_2SO_4, after spontaneous passivation, Ni22Cr alloy showed ~7 times higher elemental dissolution during E_{oc} as compared to Ni22Cr10Mo alloy. In HCl, alloy G-35 with ~8 wt.% Mo and ~33 wt.% Cr showed unsuccessful spontaneous passivation, indicated by the continuously increasing elemental dissolution rate during E_{oc}. In contrast, alloy BC-1 (~14 wt.% Cr, ~22 wt.% Mo) and alloy C-22 (~21 wt.% Cr, 13 wt.% Mo) showed successful spontaneous passivation, with elemental dissolution rate reduced to near the detection limit.

The oxidation state of Mo during spontaneous passivation was identified as mainly insoluble Mo(IV) by XPS. Accumulated Mo was very likely to promote the formation of Cr_2O_3 since it was not found on the surface for Ni-Cr alloy under the identical situation.

When the Ni-Cr-Mo alloys were passivated at the high potential domain, Mo(IV) was oxidized to more soluble Mo(VI) and released from the passive film. This mechanism is illustrated in **Fig. 9.1**.

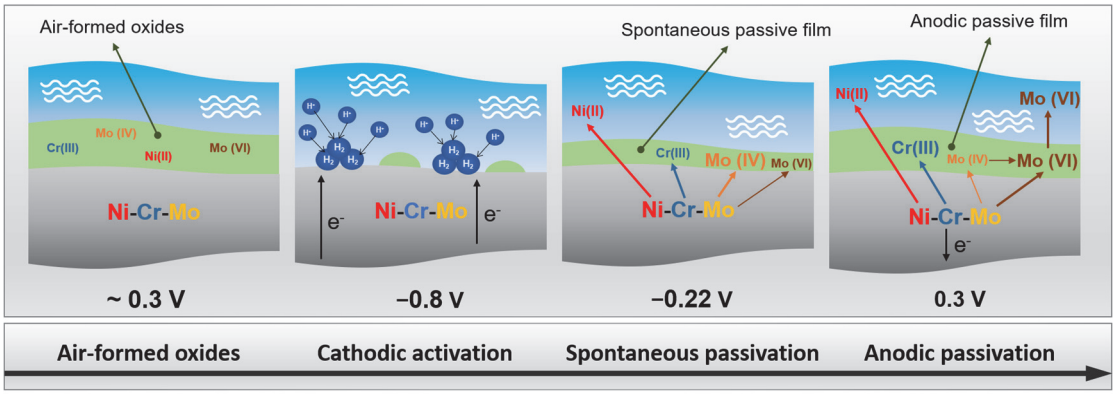

Figure 9.1 Schematic diagram showing the role of Mo in spontaneous passivation and anodic passivation.

9.2.2 MO ENRICHMENT AND DISSOLUTION DURING TRANSPASSIVE DOMAIN

The effect of Mo during transpassive dissolution was investigated in **chapter 7**. Mo accumulated on the surface during the transpassive dissolution of Ni-Cr-Mo alloys in a neutral NaCl solution. The Mo enrichment is probably caused by the change of local pH, as the solubility of Mo(VI) species, which was the dominant Mo species in the transpassive domain, becomes lower as the pH decreases. Enriched Mo redissolved when the surface was repassivated by an anodic potential. This suggests the temporary protective effect of Mo during the transpassive domain, illustrated by **Fig. 9.2**.

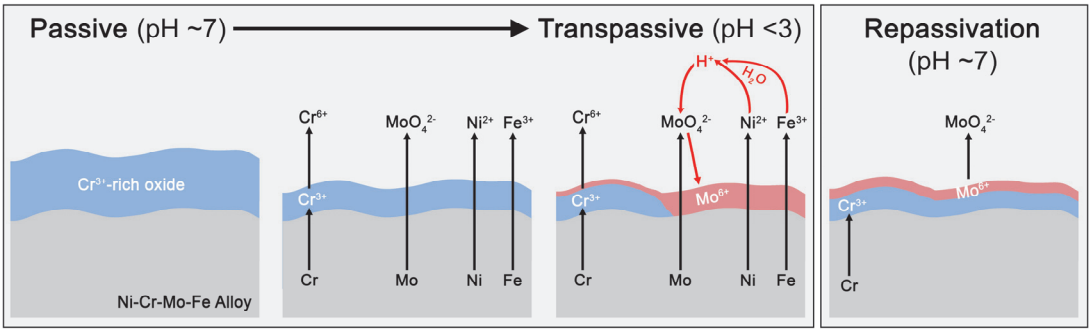

Figure 9.2 The mechanism of Mo enrichment during transpassive dissolution and its release during repassivation.

9.3 PASSIVATION OF A NOVEL NiCrFeRuMoW HEA.

The passivation of the novel NiCrFeRuMoW HEA investigated in **chapter 8** showed unique features as compared to the convention Ni-Cr-Mo alloys. The elemental

resolved polarization curve of the HEA in 2 M H_2SO_4 showed no dissolution until the transpassive domain. The air-formed oxide of HEA was enriched in Cr, while the anodic formed passive film showed enrichments of Cr as well as Ru. When the passive film was removed by cathodic activation, the HEA remained an inert surface showing no apparent elemental dissolution. Spontaneous passivation of the HEA involved the enrichments of Cr and Ru and occurred at ~−150 mV_{SCE}.

The alloying element Mo in this HEA showed different behavior compared to the Ni-Cr-Mo alloy investigated in this dissertation. Spontaneous passivation for Ni-Cr-Mo alloys involved mainly Mo. However, for the HEA, during spontaneous passivation, Mo dissolved congruently with Ni. It has to be noted that the spontaneous passivation occurred at different E_{oc} for the HEA and the Ni-Cr-Mo alloys.

9.4 PERSPECTIVES

9.4.1 MECHANISMS

9.4.1.1 The relationship between active-passive transition, spontaneous passivation, and pitting corrosion resistance.

It has been demonstrated in this work that Mo reduced i_{crit} and improved the spontaneous passivation for Ni-Cr-Mo alloys. In appendix B, an equimolar NiCrFeMnCo HEA and its variant, (NiCrFeMnCo)N HEA with 0.13 wt.% N were studied in 0.1 M H_2SO_4. The addition of N showed a similar effect as Mo: 1) the active peak was significantly reduced by alloying with N; 2) the (NiCrFeMnCo)N alloy showed spontaneous passivation while the NiCrFeMnCo did not. This implies that i_{crit} is closely related to spontaneous passivation. Interestingly, the alloying element Mo and N, according to the well-known PREN, all benefit for improving the resistance to pitting corrosion. Therefore, the correlation between spontaneous passivation and pitting corrosion resistance is of interest to further study.

9.4.1.2 The role of Ru in the HEA

For the HEA investigated in this dissertation, Ru showed interesting behavior that merits further study. Ru dissolved congruently with Ni while removing the air-formed oxide but showed extensive excess dissolution while removing the anodic passive film

formed at +0.6 V_{SCE}. Ru may be enriched on the surface during anodic passivation, serve as a catalyst for hydrogen reduction reaction, indicated by the massive difference between j_{Σ} and j_e.

Moreover, in the transpassive domain, Ru accumulated on the surface at the beginning of the transpassive dissolution. However, its dissolution increased rapidly and switched to excess dissolution as compared to other elements. The role of Ru during transpassive dissolution and its possible catalytic effect on oxygen evolution reaction is of interest to study.

9.4.1.3 The dynamic passivation

Passivity is considered as a state where the ion release on the surface of the material is remarkably hindered by the formation of the passive film. However, shown in our results, the alloying element Mo was instead active when the matrix was in the passive state. When the matrix was in the active state, in contrast, Mo was passive, i.e., existed as insoluble oxide. Recently, Han et al. also reported similar elemental behavior between Al and Zn on Al-Zn alloys[239]. Choudhary et al. showed that, in an AlTiVCr multi-principle element alloy, V was active, i.e., dissolved above the congruence, in the passive domain[240].

The concept of passivity, based on the above discussion, is therefore needed to be refined, especially as the new materials with multi principle elements are merging nowadays, whose corrosion behavior is considerably different from the conventional alloys[241].

9.4.2 THE FUTURE OF THE AESEC TECHNIQUE

Recent decades have seen an emergence of multi principle element alloys (MPEAs), including HEAs and compositional complex alloys (CCAs). These new type of alloys possesses unique properties such as excellent corrosion resistance[235, 236]. Corrosion study of such alloys using conventional electrochemical measurements may be challenging since these methods only give information on the overall behavior of the alloy. The multi principle element nature of the MPEAs makes the proper interpretation of the electrochemistry results demanding.

AESEC offers an ideal solution that has been demonstrated in this dissertation and

many publications[64, 98, 240, 242]. The ability to monitor multiple element dissolution while applying electrochemistry helps to reveal the fate of the elements that constitute the alloy during passivation and dissolution. The methodology used in the current work can be applied to other MPEAs, which will give precious information for developing new corrosion-resistant alloys.

The development of new coupled techniques will lead to more remarkable progress for AESEC. For example, AESEC-EIS[239] allows direct measurement of passive film properties; or a mechanical scratch cell will allow greater insight into repassivation phenomena[243].

APPENDIX A. THE EFFECT OF N ON THE PASSIVATION OF THE CANTOR ALLOY INVESTIGATED BY ELEMENTALALLY RESOLVED ELECTROCHEMISTRY.

A1. INTRODUCTION

The CoCrFeMnNi equimolar HEA, also known as the Cantor alloy, is one of the first developed HEAs and probably one of the most extensively studied HEAs[93, 236, 244]. Its corrosion behaviors in various electrolytes have been examined[42, 98, 99, 245-247]. It was found that in sulfuric acid solution, the Cantor alloy possesses passivation behavior[42, 98, 99]. However, regarding the composition of the passive film, contradictions exist between different studies. Luo et al. studied the Cantor alloy and compared it with 304 stainless steel in 0.1 M H_2SO_4. They found that the passive film formed on the Cantor alloy was enriched in Fe and Mn but depleted in Cr, according to the XPS results[98]. Meanwhile, online ICP-MS results showed no obvious selective dissolution during the passivation of the Cantor alloy. While in a recent study by Want et al., XPS results showed that the passive films of the Cantor alloy formed in 0.05 M H_2SO_4 were found to be dominated by Cr oxide[42].

Nitrogen as an alloying element has been used for decades in the stainless-steel industry. Its effect in terms of the corrosion behavior is to increase the resistance to localized corrosion. According to the well-known pitting resistance equivalent number (PREN), %N (wt. %) counts 16 while %Cr and %Mo count 1 and 3.3, respectively, which indicates the remarkable impact of N on the pitting corrosion resistance. The exact mechanism of how N take effect is still unclear. It was found by Baba et al. that N dissolved as NH_4^+ during crevice corrosion of nitrogen-bearing austenitic stainless (SUS316L) steel in 0.1 and 0.5 M Na_2SO_4 solutions and a 3.5% NaCl solution. They proposed that NH_4^+ consumed H^+ in the pit, thus controlled the local pH and promoted the repassivation[248].

In this work, AESEC was employed to measure the elemental dissolution during the passivation of the Cantor alloy and its variant, a Cantor-N alloy with 0.13 wt.% N. Though N itself as an element cannot be measured by the inductively coupled plasma - atomic emission spectroscopy (ICP-AES), the influence of N on the passivation may be

obtained by comparing the elemental dissolution between the Cantor and the Cantor-N alloys. Furthermore, the elemental dissolution results obtained in this work may help to clarify some contradictions existed in the literature.

A2. EXPERIMENTATION

The Cantor and Cantor-N HEAs were produced using a pressurized induction furnace as described elsewhere[249]. All the samples were homogenized at 1200 °C for 12 h, followed by water quenching. The chemical composition of the HEAs was shown in **Table A1**.

Table A1. The chemical composition of the HEAs used in this work, determined by the energy dispersive spectrometer (EDS).

Composition / wt.%	Ni	Cr	Fe	Mn	Co	N
Cantor	20.63	18.64	20.43	20.30	19.99	\
Cantor-N	20.78	18.89	20.23	19.92	20.07	0.13

A3. RESULTS AND DISCUSSION

Polarization curves for the Cantor and the Cantor-N HEAs are compared in **Fig. A1**. Hydrogen evolution occurred with nearly identical kinetics for both materials with a Tafel slope of ≈230 mV decade^{-1}. The anodic reaction, however, differed significantly between the two alloys. The Cantor alloy showed an intense anodic peak (**a1**) corresponding to the active to passive transition. For the Cantor-N alloy, the anodic peak was a factor of 500 times less intense and barely detectable, masked by the hydrogen evolution reaction (HER). Nevertheless, the passive current was approximately a factor of two more intense for the Cantor-N alloy. The low passive current for the Cantor alloy caused the anodic reaction rate to drop below that of HER immediately after **a1**, leading to a cathodic loop, labeled c, in **Fig. A1**. Interestingly, the transpassive behavior (E > 0.8 V) was nearly identical for the two alloys.

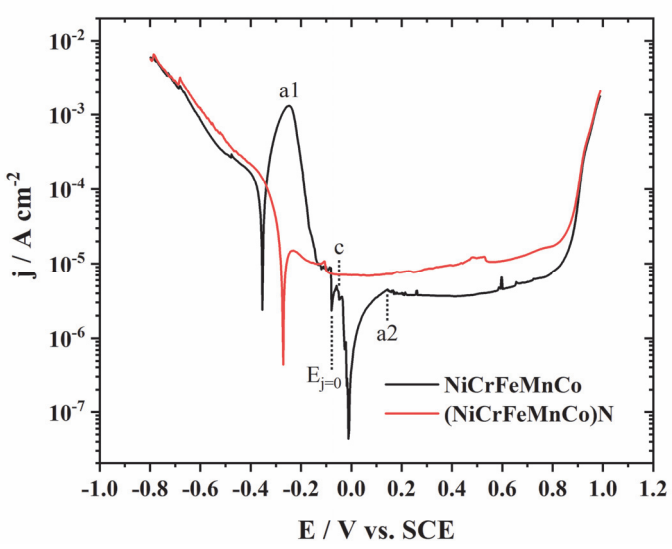

Figure A1. The polarization curves of Cantor and Cantor-N in aerated 0.1 M H_2SO_4. Scan rate 0.5 mV/s.

Further insight into the anodic reactions may be gained by considering the elemental dissolution rates, **Fig. A2**. For the Cantor alloy, j_e and j_Σ are in close correlation during the anodic peak, **a1**, indicating that the dissolution reaction is nearly faradaic during this potential domain. For the Cantor-N alloy, the anodic dissolution peak is shifted into the cathodic branch and could not be correlated directly with the j_e profile. This demonstrates the utility of elemental dissolution rate analysis for this type of alloy since the active-passive transition for Cantor-N could not be detected otherwise. For the Cantor-N alloy, the onset of the elemental dissolution was shifted by ≈ +0.1 V, from ≈ −0.5 V to ≈ −0.4 V for the Cantor and the Cantor-N alloy, respectively. The situation is similar to the stainless steel nitric acid system investigated by Laurent et al[180].

Throughout the anodic peak, dissolution was nearly congruent. Dissolution in the passive domain was very low and hardly detectable. For the Cantor-N alloy, $j_e > j_\Sigma$ which suggests continued film formation throughout this potential domain. Transpassive dissolution was also congruent.

The influence of alloying with N was mostly shown in the active-passive transition domain: 1) The onset of the elemental dissolution was shifted by ≈ +0.1 V, from ≈ −0.5 V to ≈ −0.4 V for the Cantor and the Cantor-N alloys. 2) The maximum j_Σ of the Cantor alloy was ~500 times lower than that of the Cantor alloy; 3) The E_{pp} was lower for the Cantor-N alloy (~−0.31 V) than the Cantor alloy (−0.25 V). These differences imply that the passive film formation for the Cantor-N alloy was promoted by the alloying element

N.

In the passive domain, the Cantor-N alloy showed higher i_{pass} as compared to the Cantor alloy. However, AESEC results revealed that j_{Σ} for the Cantor-N was approximately the same for both alloys, which means that for the Cantor-N alloy, the faradaic yield for forming insoluble species was higher than the Cantor alloy.

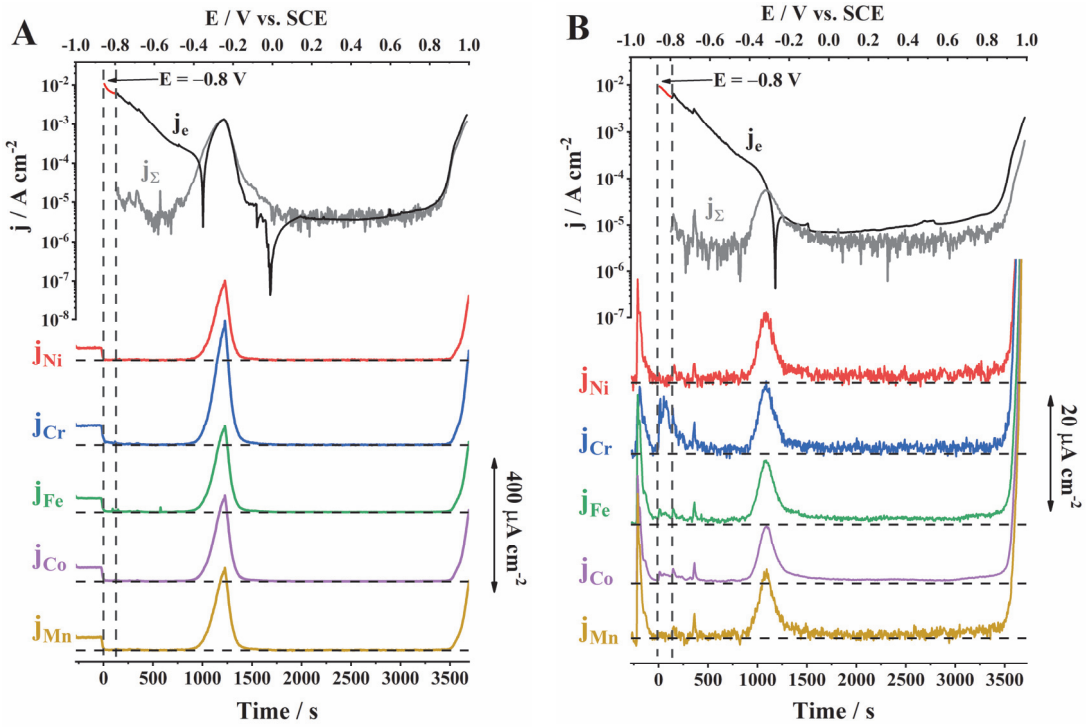

Figure A2. The AESEC polarization curves of the Cantor (A) and the Cantor-N (B) in aerated 0.1 M H_2SO_4. Scan rate 0.5 mV/s.

Spontaneous passivation of the Cantor and the Cantor-N alloys was investigated by AESEC potentiostatic experiments. The specimens were first exposed to the electrolyte under open-circuit conditions, followed by cathodic activation (−0.8 V) for 120 s to remove the passive film if it was formed. At last, the potential was released to open-circuit again. **Fig. A2** shows the elemental dissolution rates measured during this process for both alloys. Note that the dissolution rats of Cr, Fe, Mn, and Co were normalized relative to Ni.

After contact with the electrolyte, the Cantor alloy showed an excess dissolution of Fe, Mn, and Co as compared to Ni and Cr. These elemental dissolution peaks appeared at ~15 s, similar to the time of the peak occurred in a galvanostatic pulse experiment for

simulating the residence time distribution of the flow cell used in the current work[163]. This indicates that the elemental dissolution peaks observed were instantaneously on the time scale of the experiment released from the alloy once exposed to the electrolyte. These results can be compared with the recently published work by Wang et al[42]. They studied the oxide film of the cantor alloy with XPS in 0.05 M H_2SO_4 at different conditions. Their results, which are related to the current work, were summarized in **Table A2**. Ni oxide was not detected in all the cases. The XPS results show that after 1 min open-circuit exposure, Cr enrichment was enhanced, mainly due to the dissolution of Fe oxide. This is consistent with the AESEC results. The nonexistence of the Ni dissolution peak is due to its absent in the surface oxide while that for Cr, is due to its enrichment on the surface.

Table A2. The surface oxide composition investigated for the Cantor alloy at different conditions: the air-formed native oxide; the specimen exposed at E_{oc} for 1 min; the sample passivated at +0.4 V vs. SCE. From ref.[42]

Step	Thickness/nm	Oxide composition/at.%				
		$Cr_{(ox)}$	$Cr_{(hyd)}$	$Mn_{(ox)}$	$Fe_{(ox)}$	$Co_{(ox)}$
Air-formed native oxide	1.4	26.5	19.8	15.2	30.3	8.2
OCP 1 min	1.4	30.4	26.0	18.5	13.9	11.2
Passivated at 0.4 V	1.7	53.4	11.8	13.1	16.4	5.4

The elemental dissolution rates were maintained high during the entire E_{oc} for the Cantor. In contrast, the Cantor-N alloy showed a spontaneous passivation behavior, after which the elemental dissolution rates were reduced to near the equivalent detection limits. The spontaneous passivation involved two dissolution peaks. The first one may associate with the instantaneous dissolution of the surface oxide, as the peak position (~20 s) corresponded to the residence time distribution. The second peak, however, had a much broader distribution, which cannot be attributed to the residence time distribution of the flow cell. This may be ascribed to the evolution of the spontaneously formed passive film.

The cathodic activation of both alloys resulted in the excess dissolution of Cr, indicating that during the previous open circuit exposure, a Cr-enriched film formed on the surface. The other elemental dissolution rates were reduced to near zero in this cathodic reaction dominant potential domain. When the potential was released to open-circuit potential again, the elemental dissolution rates of the Cantor alloy returned to a level comparable to that before the cathodic activation. Small enrichments of Cr and Mn were

observed, as indicated in the inset in **Fig. A3(A)**. For the Cantor-N, spontaneous passivation was achieved again, accompanied by the apparent enrichment of Cr and the enrichment of Mn but with a lesser degree. The elemental dissolution rates decreased rapidly to near zero. It is generally recognized that the alloying element Mn is detrimental to the corrosion resistance of the alloy[13, 99], and was considered being absent in the passive film in our previous work on a 304 stainless steel[40]. The results shown here demonstrate the enrichment of Mn during spontaneous passivation. An unpublished work on a similar non-equimolar HEA (Ni38Fe20Cr22Mn10Co10 at.%) also showed the same results with Mn enrichment observed at +0.1 V vs. SCE in 0.1 M NaCl solution at pH 4.

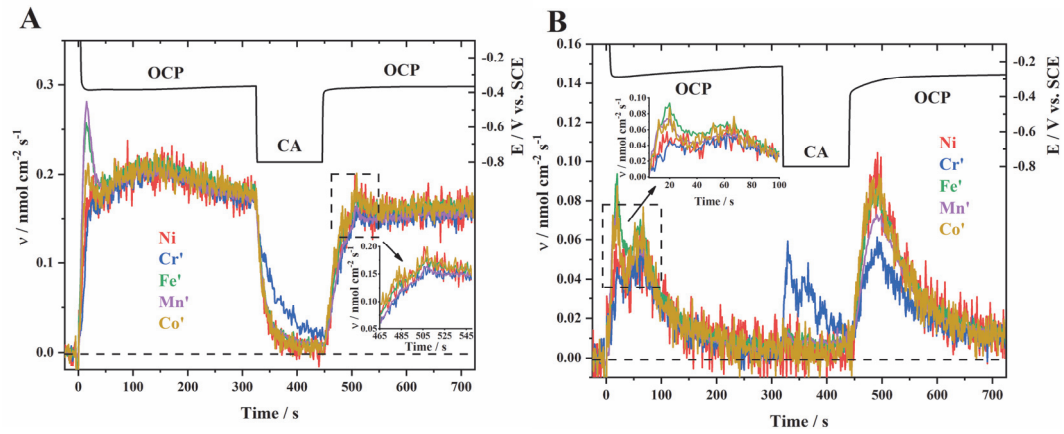

Figure A3. Elemental dissolution recorded during the cathodic activation (−0.8 V) of the Cantor (A) and the Cantor-N (B) alloys.

Following the spontaneous passivation, an anodic potential, +0.4 V, well located in the passive domain for both alloys (see **Fig. A1**), was applied. The normalized elemental dissolution and the comparison between j_{Σ} and j_e^* are shown as **Fig. A4** and **Fig. A5**, respectively. Note that the elemental dissolution background caused by the spontaneous dissolution during E_{oc}, shown as the blue dotted line for j_{Σ} in **Fig. A5**, was artificially subtracted, same as reported before[40]. Passivation was observed with evident enrichment of Cr (**Fig. A4**) and the reduction of j_{Σ} (**Fig. A5**) for both alloys. This indicates the formation of a Cr-enriched passive film. For Fe, Mn, and Co, as shown in the insets, minor accumulation was observed for the Cantor while was not observed for the Cantor-N alloy. This for the Cantor alloy is again consistent with the previous XPS study, as shown in **Table A2**. The passivation at +0.4 V, as revealed by XPS, caused the enhanced Cr enrichment; meanwhile, Ni was not detected in the film.

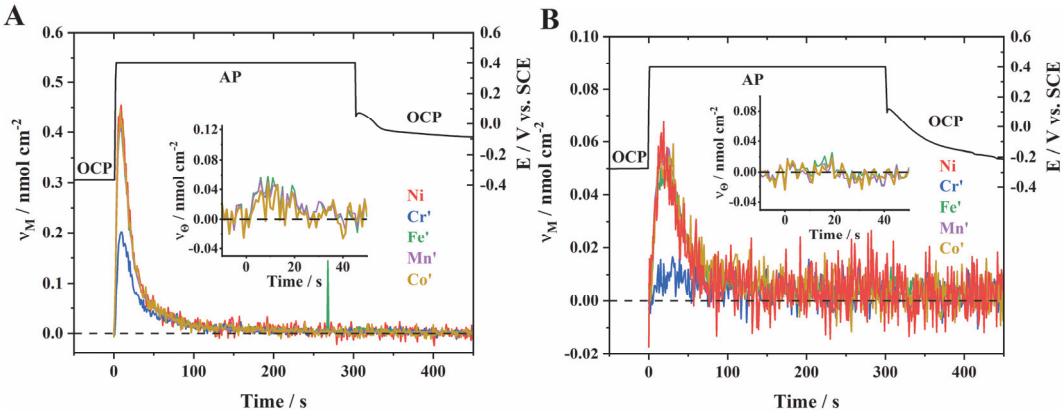

Figure A4. Elemental dissolution rates (in nmol) recorded during the anodic passivation (+0.4 V) of the Cantor (A) and the Cantor-N (B) alloys. Elemental dissolution rates of Cr, Fe, Mn, and Co were normalized relative to Ni. Insets: the enrichments of Fe, Mn, and Co relative to Ni at the beginning of passivation.

j_Σ was compared to the convoluted measured external current, j_e^*, for both alloys. For the Cantor alloy, significant excess elemental current, $j_\Sigma >> j_e^*$, was detected. The same phenomenon was observed for a 304 stainless steel in a previous study[40]. The electrochemical dissolution of metal M during E_{oc} in sulfuric acid may obey the following equation:

$$M + nH^+ \rightarrow M^{n+} + \frac{n}{2}H_2 \quad (1)$$

However, insoluble intermediate may exist before the soluble metal ion was injected into the solution, such as the metal hydroxide:

$$M + nH_2O \rightarrow M(OH)_n + nH^+ \quad (2)$$

Thus, during the spontaneous passivation before anodic passivation, the metal may have a dissolution process as M → $M(OH)_n$→M^{n+}. Therefore, an intermediate hydroxide layer may exist on the surface of the alloy. Considering this layer to be the mixed Ni, Fe, Mn, and Co equimolar hydroxides, and using the excess charge during anodic passivation, $Q_{oc} = \int_0^{300} j_\Sigma - j_e$ = 7 mC, a thickness of ~7 nm was obtained. This value may underestimate the thickness of the film since the charge used to form the passive film was also subtracted from Q_{oc}. In conclusion, an approximate 7 nm thick hydroxide film may exist during E_{oc} as the intermediate layer before the metal ions were injected into the

solution. The formation of the passive film prevented further dissolution from the alloy matrix, resulting in the release of the residual hydroxide layer, thus caused the excess j_{Σ} as compared to j_e.

For the Cantor-N, the elemental dissolution rates before AP were ~10 times lower than that of the Cantor alloy due to spontaneous passivation that forms a Cr and Mn enriched passive film. Thus, the intermediate hydroxide layer is expected to be much thinner, whose subsequent dissolution during AP will add fewer extra values to j_{Σ}. As a result, j_{Σ} was reasonably lower than j_e during AP, though the difference between j_{Σ} and j_e is still not representative of the charge for forming the passive film.

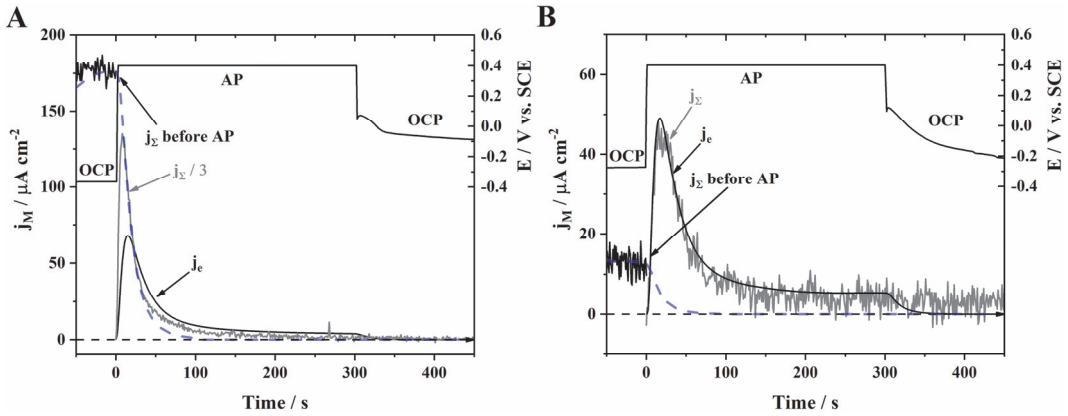

Figure A5. The comparison between j_{Σ} and j_e^* for the Cantor (A) and the Cantor-N (B) alloys.

A4. CONCLUSIONS

In this work, the Cantor and Cantor-N HEAs were studied in the context of the elemental resolved passivation and how it is influenced by alloying with N. It was found that the N addition resulted in the significant reduction of the active-passive transition peak during which the elemental dissolution rates were reduced approximately one order of magnitude. The polarization curve investigation showed higher i_{pass} for Cantor-N alloy. However, the elemental dissolution rates were almost the same for both alloys during the passive domain, indicating a higher insoluble oxide formation rate for Cantor-N alloy.

Another effect of alloying with N found in this work is the remarkably improved spontaneous passivation during E_{oc}. This was observed for Cantor-N by the enrichment

of Cr and Mn with the elemental dissolution rates reduced to near the equivalent detection limits of the ICP-OES. For the Cantor alloy, only slight enrichments of Cr and Mn were observed with no noticeable effect on lowering the dissolution.

Passive film on both the Cantor and the Cantor-N alloys were found to be enriched in Cr. For the Cantor alloy, slight enrichments of Fe, Mn, and Co were also detected.

REFERENCE

[1] ASM Handbook, Volume 13A, Corrosion: Fundamentals, Testing, and Protection, ASM International, United States of America, 2003.
[2] G. Koch, J. Varney, N. Thompson, O. Moghissi, M. Gould, J. Payer, International Measures of Prevention, Application, and Economics of Corrosion Technologies Study, in: G. Jacobson (Ed.), NACE International, United States of America, 2016.
[3] ASM Specialty Handbook: Nickel, Cobalt, and Their Alloys, ASM International, 2000.
[4] Y. Shi, B. Yang, P. Liaw, Corrosion-Resistant High-Entropy Alloys: A Review, Metals, 7 (2017) 43.
[5] J.B. Lumsden, R.W. Staehle, Application of auger electron spectroscopy to the determination of the composition of passive films on type 316 SS, Scripta Metallurgica, 6 (1972) 1205-1208.
[6] G. Okamoto, Passive film of 18-8 stainless steel structure and its function, Corrosion Science, 13 (1973) 471-489.
[7] M. Okuyama, S. Haruyama, Passive film formed on nickel in a neutral solution, Corrosion Science, 14 (1974) 1-14.
[8] A.E. Yaniv, The Composition of Passive Films on Ferritic Stainless Steels, Journal of The Electrochemical Society, 124 (1977).
[9] M. Klimmeck, A study of the kinetics of passive layer formation on Cr Mo alloys, Electrochimica Acta, 25 (1980) 1375-1381.
[10] S.C. Tjong, SIMS / XPS studies of the passive film on nickel, Materials Research Bulletin, 17 (1982) 1297-1304.
[11] G. Lorang, N. Jallerat, K.V. Quang, J.P. Langeron, AES depth profiling of passive overlayers formed on nickel alloys, Surface and Interface Analysis, 16 (1990) 325-330.
[12] B. Stypula, J. Stoch, The characterization of passive films on chromium electrodes by XPS, Corrosion Science, 36 (1994) 2159-2167.
[13] A. Pardo, M.C. Merino, A.E. Coy, F. Viejo, R. Arrabal, E. Matykina, Pitting corrosion behaviour of austenitic stainless steels – combining effects of Mn and Mo additions, Corrosion Science, 50 (2008) 1796-1806.
[14] B. Deng, Y. Jiang, J. Gong, C. Zhong, J. Gao, J. Li, Critical pitting and repassivation temperatures for duplex stainless steel in chloride solutions, Electrochimica Acta, 53 (2008) 5220-5225.
[15] E. McCafferty, Sequence of steps in the pitting of aluminum by chloride ions, Corrosion Science, 45 (2003) 1421-1438.
[16] D.E. Williams, R.C. Newman, Q. Song, R.G. Kelly, Passivity breakdown and pitting corrosion of binary alloys, Nature, 350 (1991) 216-219.
[17] H.S. Isaacs, The localized breakdown and repair of passive surfaces during pitting, Corrosion Science, 29 (1989) 313-323.
[18] G.S. Frankel, L. Stockert, F. Hunkeler, H. Boehni, Metastable Pitting of Stainless Steel, Corrosion, 43 (1987) 429-436.
[19] J. Horvath, H.H. Uhlig, Critical Potentials for Pitting Corrosion of Ni, Cr-Ni, Cr-Fe, and Related Stainless Steels, Journal of The Electrochemical Society, 115 (1968).
[20] A.K. Mishra, X. Zhang, D.W. Shoesmith, The Role of Copper on the Crevice Corrosion Behavior of Nickel-Chromium-Molybdenum Alloys in Aggressive Solutions, Corrosion, 72 (2016) 356-367.
[21] N. Ebrahimi, P. Jakupi, J.J. Noël, D.W. Shoesmith, The Role of Alloying Elements on the Crevice Corrosion Behavior of Ni-Cr-Mo Alloys, Corrosion, 71 (2015) 1441-1451.
[22] A. Tomio, M. Sagara, T. Doi, H. Amaya, N. Otsuka, T. Kudo, Role of alloyed molybdenum on corrosion resistance of austenitic Ni–Cr–Mo–Fe alloys in H 2 S–Cl – environments, Corrosion Science, 98 (2015) 391-398.
[23] K. Hashimoto, K. Asami, A. Kawashima, H. Habazaki, E. Akiyama, The role of corrosion-resistant alloying elements in passivity, Corrosion Science, 49 (2007) 42-52.
[24] G.O. Ilevbare, G.T. Burstein, The role of alloyed molybdenum in the inhibition of pitting corrosion in stainless steels, Corrosion Science, 43 (2001) 485-513.
[25] M.F. Montemor, A.m.p. Simões, M.G.S. Ferreira, M.D.C. Belo, The role of Mo in the chemical composition and semiconductive behaviour of oxide films formed on stainless steels, Corrosion Science, 41 (1999) 17-34.
[26] K. Sugimoto, Y. Sawada, The role of molybdenum additions to austenitic stainless steels in the inhibition of pitting in acid chloride solutions, Corrosion Science, 17 (1977) 425-445.
[27] K. Sugimoto, Y. Sawada, The Role of Alloyed Molybdenum in Austenitic Stainless Steels in the

Inhibition of Pitting in Neutral Halide Solutions, Corrosion, 32 (1976) 347-352.
[28] Q.-T. Song, J. Xu, (TiZrNbTa)90Mo10 high-entropy alloy: Electrochemical behavior and passive film characterization under exposure to Ringer's solution, Corrosion Science, (2020).
[29] X. Zhang, D. Zagidulin, D.W. Shoesmith, Characterization of film properties on the NiCrMo Alloy C-2000, Electrochimica Acta, 89 (2013) 814-822.
[30] D. Zagidulin, X. Zhang, J. Zhou, J.J. Noël, D.W. Shoesmith, Characterization of surface composition on Alloy 22 in neutral chloride solutions, Surface and Interface Analysis, 45 (2013) 1014-1019.
[31] H.-H. Huang, Surface characterization of passive film on NiCr-based dental casting alloys, Biomaterials, 24 (2003) 1575-1582.
[32] R. Cortes, M. Froment, A. Hugot-Le Goff, S. Joiret, Characterization of passive films on Ni and Ni alloys by ReflEXAFS and raman spectroscopy, Corrosion Science, 31 (1990) 121-127.
[33] S.M. Wilhelm, Photoelectrochemical Characterization of the Passive Films on Iron and Nickel, Journal of The Electrochemical Society, 128 (1981).
[34] S. Marcelin, B. Ter-Ovanessian, B. Normand, Electronic properties of passive films from the multi-frequency Mott–Schottky and power-law coupled approach, Electrochemistry Communications, 66 (2016) 62-65.
[35] M.G. Poletti, L. Battezzati, Electronic and thermodynamic criteria for the occurrence of high entropy alloys in metallic systems, Acta Materialia, 75 (2014) 297-306.
[36] B. Ter-Ovanessian, C. Alemany-Dumont, B. Normand, Electronic and transport properties of passive films grown on different Ni-Cr binary alloys in relation to the pitting susceptibility, Electrochimica Acta, 133 (2014) 373-381.
[37] L.A.S. Ries, M. Da Cunha Belo, M.G.S. Ferreira, I.L. Muller, Chemical composition and electronic structure of passive films formed on Alloy 600 in acidic solution, Corrosion Science, 50 (2008) 676-686.
[38] Z. Wang, E.-M. Paschalidou, A. Seyeux, S. Zanna, V. Maurice, P. Marcus, Mechanisms of Cr and Mo Enrichments in the Passive Oxide Film on 316L Austenitic Stainless Steel, Frontiers in Materials, 6 (2019).
[39] B. Laurent, N. Gruet, B. Gwinner, F. Miserque, K. Rousseau, K. Ogle, Dissolution and Passivation of a Silicon-Rich Austenitic Stainless Steel during Active-Passive Cycles in Sulfuric and Nitric Acid, Journal of The Electrochemical Society, 164 (2017) C892-C900.
[40] K. Ogle, M. Mokaddem, P. Volovitch, Atomic emission spectroelectrochemistry applied to dealloying phenomena II. Selective dissolution of iron and chromium during active–passive cycles of an austenitic stainless steel, Electrochimica Acta, 55 (2010) 913-921.
[41] C.O.A. Olsson, D. Landolt, Passive films on stainless steels—chemistry, structure and growth, Electrochimica Acta, 48 (2003) 1093-1104.
[42] L. Wang, D. Mercier, S. Zanna, A. Seyeux, M. Laurent-Brocq, L. Perrière, I. Guillot, P. Marcus, Study of the surface oxides and corrosion behaviour of an equiatomic CoCrFeMnNi high entropy alloy by XPS and ToF-SIMS, Corrosion Science, (2020).
[43] X. Li, J. Han, P. Lu, J.E. Saal, G.B. Olson, G.S. Frankel, J.R. Scully, K. Ogle, Communication—Dissolution and Passivation of a Ni-Cr-Fe-Ru-Mo-W High Entropy Alloy by Elementally Resolved Electrochemistry, Journal of The Electrochemical Society, 167 (2020).
[44] K.F. Quiambao, S.J. McDonnell, D.K. Schreiber, A.Y. Gerard, K.M. Freedy, P. Lu, J.E. Saal, G.S. Frankel, J.R. Scully, Passivation of a corrosion resistant high entropy alloy in non-oxidizing sulfate solutions, Acta Materialia, 164 (2019) 362-376.
[45] X. Li, K. Ogle, The Passivation of Ni-Cr-Mo Alloys: Time Resolved Enrichment and Dissolution of Cr and Mo during Passive-Active Cycles, Journal of The Electrochemical Society, 166 (2019) C3179-C3185.
[46] K.L. Cwalina, H.M. Ha, N. Ott, P. Reinke, N. Birbilis, J.R. Scully, In Operando Analysis of Passive Film Growth on Ni-Cr and Ni-Cr-Mo Alloys in Chloride Solutions, Journal of The Electrochemical Society, 166 (2019) C3241-C3253.
[47] X. Zhang, D.W. Shoesmith, Influence of temperature on passive film properties on Ni–Cr–Mo Alloy C-2000, Corrosion Science, 76 (2013) 424-431.
[48] J.R. Hayes, J.J. Gray, A.W. Szmodis, C.A. Orme, Influence of Chromium and Molybdenum on the Corrosion of Nickel-Based Alloys, Corrosion, 62 (2006) 491-500.
[49] W.J. Tobler, S. Virtanen, Effect of Mo species on metastable pitting of Fe18Cr alloys—A current transient analysis, Corrosion Science, 48 (2006) 1585-1607.
[50] A.C. Lloyd, J.J. Noël, S. McIntyre, D.W. Shoesmith, Cr, Mo and W alloying additions in Ni and

their effect on passivity, Electrochimica Acta, 49 (2004) 3015-3027.
[51] J.M. Bastidas, C.L. Torres, E. Cano, J.L. Polo, Influence of molybdenum on passivation of polarised stainless steels in a chloride environment, Corrosion Science, 44 (2002) 625-633.
[52] R. Qvarfort, Some observations regarding the influence of molybdenum on the pitting corrosion resistance of stainless steels, Corrosion Science, 40 (1998) 215-223.
[53] J.L. Luo, Pit Propagation of Nickel and Nickel Molybdenum Alloys, Journal of The Electrochemical Society, 144 (1997).
[54] S. Maximovitch, G. Barral, F. Le Cras, F. Claudet, The electrochemical incorporation of molybdenum in the passive layer of a 17% Cr ferritic stainless steel. Its influence on film stability in sulphuric acid and on pitting corrosion in chloride media, Corrosion Science, 37 (1995) 271-291.
[55] J. Postlethwaite, R.J. Scoular, M.H. Dobbin, Localized Corrosion of Molybdenum-Bearing Nickel Alloys in Chloride Solutions, Corrosion, 44 (1988) 199-203.
[56] W.C. Moshier, Corrosion Behavior of Aluminum-Molybdenum Alloys in Chloride Solutions, Journal of The Electrochemical Society, 134 (1987).
[57] C.R. Clayton, A Bipolar Model of the Passivity of Stainless Steel: The Role of Mo Addition, Journal of The Electrochemical Society, 133 (1986).
[58] W. Yang, R.-C. Ni, H.-Z. Hua, A. Pourbaix, The behavior of chromium and molybdenum in the propagation process of localized corrosion of steels, Corrosion Science, 24 (1984) 691-707.
[59] J.N. Wanklyn, The role of molybdenum in the crevice corrosion of stainless steels, Corrosion Science, 21 (1981) 211-225.
[60] K. Hashimoto, K. Asami, K. Teramoto, An X-ray photo-electron spectroscopic study on the role of molybdenum in increasing the corrosion resistance of ferritic stainless steels in HC1, Corrosion Science, 19 (1979) 3-14.
[61] T. Kodama, J.R. Ambrose, Effect of Molybdate Ion on the Repassivation Kinetics of Iron in Solutions Containing Chloride Ions, Corrosion, 33 (1977) 155-161.
[62] M. Sakashita, N. Sato, The effect of molybdate anion on the ion-selectivity of hydrous ferric oxide films in chloride solutions, Corrosion Science, 17 (1977) 473-486.
[63] R.J. Brigham, Pitting of Molybdenum Bearing Austenitic Stainless Steel, Corrosion, 28 (1972) 177-179.
[64] Y. Qiu, R. Liu, T. Gengenbach, O. Gharbi, S. Choudhary, S. Thomas, H.L. Fraser, N. Birbilis, Real-time dissolution of a compositionally complex alloy using inline ICP and correlation with XPS, npj Materials Degradation, 4 (2020).
[65] L. Ma, F. Wiame, V. Maurice, P. Marcus, New insight on early oxidation stages of austenitic stainless steel from in situ XPS analysis on single-crystalline Fe–18Cr–13Ni, Corrosion Science, 140 (2018) 205-216.
[66] S. Tougaard, Improved XPS analysis by visual inspection of the survey spectrum, Surface and Interface Analysis, 50 (2018) 657-666.
[67] B. Kobe, M. Badley, J.D. Henderson, S. Anderson, M.C. Biesinger, D. Shoesmith, Application of quantitative X-ray photoelectron spectroscopy (XPS) imaging: investigation of Ni-Cr-Mo alloys exposed to crevice corrosion solution, Surface and Interface Analysis, 49 (2017) 1345-1350.
[68] M.C. Biesinger, B.P. Payne, A.P. Grosvenor, L.W.M. Lau, A.R. Gerson, R.S.C. Smart, Resolving surface chemical states in XPS analysis of first row transition metals, oxides and hydroxides: Cr, Mn, Fe, Co and Ni, Applied Surface Science, 257 (2011) 2717-2730.
[69] A. Machet, A. Galtayries, S. Zanna, L. Klein, V. Maurice, P. Jolivet, M. Foucault, P. Combrade, P. Scott, P. Marcus, XPS and STM study of the growth and structure of passive films in high temperature water on a nickel-base alloy, Electrochimica Acta, 49 (2004) 3957-3964.
[70] L. Zhang, D.D. Macdonald, Segregation of alloying elements in passive systems—I. XPS studies on the Ni–W system, Electrochimica Acta, 43 (1998) 2661-2671.
[71] C. da Fonseca, M.d. Cunha Belo, A Characterisation of Titanium Passivation Films by In-Situ AC Impedance Measurements and XPS Analysis, Materials Science Forum, 192-194 (1995) 177-184.
[72] J.M. Grimai, P. Marcus, XPS study of the segregation of sulphur on Ni-21Cr-8Fe (100) alloy, Surface Science, 249 (1991) 171-179.
[73] Nickel and Nickel alloys, Caxton Press, Inc, U.S.A., 1941.
[74] ASM Handbook Volume 2: Properties and Selection: Nonferrous Alloys and Special-Purpose Materials, ASM International, United States of America, 1990.
[75] Binary Alloys Phase Diagrams, ASM International, 1986.
[76] D. Van Rooyen, Review of the Stress Corrosion Cracking of Inconel 600, Corrosion, 31 (1975) 327-

337.
[77] J.M. Sarver, J.R. Crum, W.L. Mankins, Carbide Precipitation and SCC Behavior of Inconel Alloy 690, Corrosion, 44 (1988) 288-289.
[78] V.B. Singh, A. Gupta, The electrochemical corrosion and passivation behaviour of Monel (400) in concentrated acids and their mixtures, Journal of Materials Science, 36 (2001) 1433-1442.
[79] J. Chen, J. Wang, F. Yan, Q. Zhang, Q.-a. Li, Effect of applied potential on the tribocorrosion behaviors of Monel K500 alloy in artificial seawater, Tribology International, 81 (2015) 1-8.
[80] S. Cao, C.R. Brooks, G. Whittaker, The structure of the heat-affected zone in welds of a Ni-29 wt.% Mo commercial alloy (Hastelloy B2), Materials Characterization, 33 (1994) 21-32.
[81] S.L. Chawla, R.K. Gupta, Materials Selection for Corrosion Control, ASM International, United States of America, 1993.
[82] F.G. Hodge, R.W. Kirchner, An Improved Ni-Cr-Mo Alloy for Corrosion Service, Corrosion, 32 (1976) 332-336.
[83] N. Priyantha, P. Jayaweera, D.D. Macdonald, A. Sun, An electrochemical impedance study of Alloy 22 in NaCl brine at elevated temperature. I. Corrosion behavior, Journal of Electroanalytical Chemistry, 572 (2004) 409-419.
[84] S.D. Day, M.T. Whalen, K.J. King, G.A. Hust, L.L. Wong, J.C. Estill, R.B. Rebak, Corrosion Behavior of Alloy 22 in Oxalic Acid and Sodium Chloride Solutions, Corrosion, 60 (2004) 804-814.
[85] A.C. Lloyd, D.W. Shoesmith, N.S. McIntyre, J.J. Noël, Effects of Temperature and Potential on the Passive Corrosion Properties of Alloys C22 and C276, Journal of The Electrochemical Society, 150 (2003).
[86] B.A. Kehler, G.O. Ilevbare, J.R. Scully, Crevice Corrosion Stabilization and Repassivation Behavior of Alloy 625 and Alloy 22, Corrosion, 57 (2001) 1042-1065.
[87] Z.F. Yin, W.Z. Zhao, W.Y. Lai, X.H. Zhao, Electrochemical behaviour of Ni-base alloys exposed under oil/gas field environments, Corrosion Science, 51 (2009) 1702-1706.
[88] N. Sridhar, G.A. Cragnolino, Applicability of Repassivation Potential for Long-Term Prediction of Localized Corrosion of Alloy 825 and Type 316L Stainless Steel, Corrosion, 49 (1993) 885-894.
[89] P. Lu, J.E. Saal, G.B. Olson, T. Li, O.J. Swanson, G.S. Frankel, A.Y. Gerard, K.F. Quiambao, J.R. Scully, Computational materials design of a corrosion resistant high entropy alloy for harsh environments, Scripta Materialia, 153 (2018) 19-22.
[90] M. Feuerbacher, T. Lienig, C. Thomas, A single-phase bcc high-entropy alloy in the refractory Zr-Nb-Ti-V-Hf system, Scripta Materialia, 152 (2018) 40-43.
[91] Y.J. Zhao, J.W. Qiao, S.G. Ma, M.C. Gao, H.J. Yang, M.W. Chen, Y. Zhang, A hexagonal close-packed high-entropy alloy: The effect of entropy, Materials & Design, 96 (2016) 10-15.
[92] J.W. Yeh, S.K. Chen, S.J. Lin, J.Y. Gan, T.S. Chin, T.T. Shun, C.H. Tsau, S.Y. Chang, Nanostructured High-Entropy Alloys with Multiple Principal Elements: Novel Alloy Design Concepts and Outcomes, Advanced Engineering Materials, 6 (2004) 299-303.
[93] B. Cantor, I.T.H. Chang, P. Knight, A.J.B. Vincent, Microstructural development in equiatomic multicomponent alloys, Materials Science and Engineering: A, 375-377 (2004) 213-218.
[94] T.K. Chen, T.T. Shun, J.W. Yeh, M.S. Wong, Nanostructured nitride films of multi-element high-entropy alloys by reactive DC sputtering, Surface and Coatings Technology, 188-189 (2004) 193-200.
[95] C.-Y. Hsu, J.-W. Yeh, S.-K. Chen, T.-T. Shun, Wear resistance and high-temperature compression strength of Fcc CuCoNiCrAl0.5Fe alloy with boron addition, Metallurgical and Materials Transactions A, 35 (2004) 1465-1469.
[96] P.K. Huang, J.W. Yeh, T.T. Shun, S.K. Chen, Multi-Principal-Element Alloys with Improved Oxidation and Wear Resistance for Thermal Spray Coating, Advanced Engineering Materials, 6 (2004) 74-78.
[97] J.-W. Yeh, S.-J. Lin, T.-S. Chin, J.-Y. Gan, S.-K. Chen, T.-T. Shun, C.-H. Tsau, S.-Y. Chou, Formation of simple crystal structures in Cu-Co-Ni-Cr-Al-Fe-Ti-V alloys with multiprincipal metallic elements, Metallurgical and Materials Transactions A, 35 (2004) 2533-2536.
[98] H. Luo, Z. Li, A.M. Mingers, D. Raabe, Corrosion behavior of an equiatomic CoCrFeMnNi high-entropy alloy compared with 304 stainless steel in sulfuric acid solution, Corrosion Science, 134 (2018) 131-139.
[99] J. Yang, J. Wu, C.Y. Zhang, S.D. Zhang, B.J. Yang, W. Emori, J.Q. Wang, Effects of Mn on the electrochemical corrosion and passivation behavior of CoFeNiMnCr high-entropy alloy system in H2SO4 solution, Journal of Alloys and Compounds, (2019).
[100] T. Li, O.J. Swanson, G.S. Frankel, A.Y. Gerard, P. Lu, J.E. Saal, J.R. Scully, Localized corrosion

behavior of a single-phase non-equimolar high entropy alloy, Electrochimica Acta, 306 (2019) 71-84.
[101] G.C. Palit, K. Elayaperumal, Passivity and pitting of corrosion resistant pure metals Ta, Nb, Ti, Zr, Cr and A1 in chloride solutions, Corrosion Science, 18 (1978) 169-179.
[102] S.J. Mulford, D. Tromans, Crevice Corrosion of Nickel-Based Alloys in Neutral Chloride and Thiosulfate Solutions, Corrosion, 44 (1988) 891-900.
[103] R.S. Lillard, M.P. Jurinski, J.R. Scully, Crevice Corrosion of Alloy 625 in Chlorinated ASTM Artificial Ocean Water, Corrosion, 50 (1994) 251-265.
[104] N.S. Zadorozne, M.C. Giordano, A.E. Ares, R.M. Carranza, R.B. Rebak, Anodic characteristics and stress corrosion cracking behavior of nickel rich alloys in bicarbonate and buffer solutions, Corrosion Science, 108 (2016) 1-10.
[105] E.A. Lizlovs, A.P. Bond, Anodic Polarization of Some Ferritic Stainless Steels in Chloride Media, Journal of The Electrochemical Society, 116 (1969).
[106] A.K. Mishra, S. Ramamurthy, M. Biesinger, D.W. Shoesmith, The activation/depassivation of nickel–chromium–molybdenum alloys in bicarbonate solution: Part I, Electrochimica Acta, 100 (2013) 118-124.
[107] N. Sato, K. Kudo, An ellipsometric study of anodic passivation of nickel in borate buffer solution, Electrochimica Acta, 19 (1974) 461-470.
[108] A.P. Bond, H.H. Uhlig, Corrosion Behavior and Passivity of Nickel-Chromium and Cobalt-Chromium Alloys, Journal of The Electrochemical Society, 107 (1960).
[109] J.R. Myers, F.H. Beck, M.G. Fontana, Anodic Polarization Behavior Of Nickel-Chromium Alloys In Sulfuric Acid Solutions, Corrosion, 21 (1965) 277-287.
[110] F.G. Hodge, B.E. Wilde, Effect of Chloride Ion on the Anodic Dissolution Kinetics of Chromium-Nickel Binary Alloys in Dilute Sulfuric Acid, Corrosion, 26 (1970) 246-250.
[111] S. Boudin, J.L. Vignes, G. Lorang, M. Da Cunha Belo, G. Blondiaux, S.M. Mikhailov, J.P. Jacobs, H.H. Brongersma, Analytical and electrochemical study of passive films formed on nickel—chromium alloys: Influence of the chromium bulk concentration, Surface and Interface Analysis, 22 (1994) 462-466.
[112] T. Jabs, P. Borthen, H.H. Strehblow, X-Ray Photoelectron Spectroscopic Examinations of Electrochemically Formed Passive Layers on Ni-Cr Alloys, Journal of The Electrochemical Society, 144 (1997).
[113] B. Ter-Ovanessian, B. Normand, Passive films growth on different Ni-Cr alloys from the migration of cation vacancies, Journal of Solid State Electrochemistry, 20 (2015) 9-18.
[114] B. Ter-Ovanessian, N. Mary, B. Normand, Passivity Breakdown of Ni-Cr Alloys: From Anions Interactions to Stable Pits Growth, Journal of The Electrochemical Society, 163 (2016) C410-C419.
[115] C.Y. Chao, A Point Defect Model for Anodic Passive Films, Journal of The Electrochemical Society, 128 (1981).
[116] P. Crook, Corrosion-Resistant Nickel Alloys Part 2, in: ADVANCED MATERIALS & PROCESSES, 2007, pp. 32-33.
[117] R.W. Kirchner, F.G. Hodge, New Ni-Cr-Mo alloy demonstrates high-temperature structural stability with resultant increases in corrosion-resistance and mechanical properties, Materials and Corrosion/Werkstoffe und Korrosion, 24 (1973) 1042-1049.
[118] M.A. Streicher, Effect of Composition and Structure on Crevice, Intergranular, and Stress Corrosion of Some Wrought Ni-Cr-Mo Alloys, Corrosion, 32 (1976) 79-93.
[119] F.G. Hodge, Effect of Aging on the Anodic Behavior of Ni-Cr-Mo Alloys, Corrosion, 29 (1973) 375-383.
[120] G.M. Gordon, F.N. Speller Award Lecture:Corrosion Considerations Related to Permanent Disposal of High-Level Radioactive Waste, Corrosion, 58 (2002) 811-825.
[121] D.S. Dunn, Y.M. Pan, L. Yang, G.A. Cragnolino, Localized Corrosion Susceptibility of Alloy 22 in Chloride Solutions: Part 1—Mill-Annealed Condition, Corrosion, 61 (2005) 1078-1085.
[122] K.J. Evans, A. Yilmaz, S.D. Day, L.L. Wong, J.C. Estill, R.B. Rebak, Using electrochemical methods to determine alloy 22's crevice corrosion repassivation potential, Jom, 57 (2005) 56-61.
[123] A. Davydov, K.V. Rybalka, L.A. Beketaeva, G.R. Engelhardt, P. Jayaweera, D.D. Macdonald, The kinetics of hydrogen evolution and oxygen reduction on Alloy 22, Corrosion Science, 47 (2005) 195-215.
[124] D.D. Macdonald, A. Sun, An electrochemical impedance spectroscopic study of the passive state on Alloy-22, Electrochimica Acta, 51 (2006) 1767-1779.
[125] A.C. Lloyd, J.J. Noël, D.W. Shoesmith, N.S. McIntyre, The open-circuit ennoblement of alloy C-

22 and other Ni-Cr-Mo alloys, Jom, 57 (2005) 31-35.
[126] F. Bocher, R. Huang, J.R. Scully, Prediction of Critical Crevice Potentials for Ni-Cr-Mo Alloys in Simulated Crevice Solutions as a Function of Molybdenum Content, Corrosion, 66 (2010) 055002-055002-055015.
[127] N.S. Zadorozne, C.M. Giordano, M.A. Rodríguez, R.M. Carranza, R.B. Rebak, Crevice corrosion kinetics of nickel alloys bearing chromium and molybdenum, Electrochimica Acta, 76 (2012) 94-101.
[128] J.R. Galvele, Transport Processes and the Mechanism of Pitting of Metals, Journal of The Electrochemical Society, 123 (1976).
[129] E.C. Hornus, C.M. Giordano, M.A. Rodriguez, R.M. Carranza, R.B. Rebak, Effect of Temperature on the Crevice Corrosion of Nickel Alloys Containing Chromium and Molybdenum, Journal of the Electrochemical Society, 162 (2014) C105-C113.
[130] A.K. Mishra, D.W. Shoesmith, Effect of Alloying Elements on Crevice Corrosion Inhibition of Nickel-Chromium-Molybdenum-Tungsten Alloys Under Aggressive Conditions: An Electrochemical Study, Corrosion, 70 (2014) 721-730.
[131] J.D. Henderson, N. Ebrahimi, V. Dehnavi, M. Guo, D.W. Shoesmith, J.J. Noël, The role of internal cathodic support during the crevice corrosion of Ni-Cr-Mo alloys, Electrochimica Acta, 283 (2018) 1600-1608.
[132] V. Maurice, H. Peng, L.H. Klein, A. Seyeux, S. Zanna, P. Marcus, Effects of molybdenum on the composition and nanoscale morphology of passivated austenitic stainless steel surfaces, Faraday Discuss, 180 (2015) 151-170.
[133] M. Pourbaix, Atlas of Electrochemical Equilibria in Aqueous Solutions, National Association of Corrosion Engineers, 1974.
[134] E.A. Lizlovs, Effects of Mo, Cu, Si and P on Anodic Behavior of 17 Cr Steels, Corrosion, 22 (1966) 297-308.
[135] M. Bojinov, Influence of molybdenum on the conduction mechanism in passive films on iron–chromium alloys in sulphuric acid solution, Electrochimica Acta, 46 (2001) 1339-1358.
[136] I. Olefjord, Surface Composition of Stainless Steels during Anodic Dissolution and Passivation Studied by ESCA, Journal of The Electrochemical Society, 132 (1985).
[137] R.C. Newman, The dissolution and passivation kinetics of stainless alloys containing molybdenum—II. Dissolution kinetics in artificial pits, Corrosion Science, 25 (1985) 341-350.
[138] R.C. Newman, The dissolution and passivation kinetics of stainless alloys containing molybdenum—1. Coulometric studies of Fe Cr and Fe Cr Mo alloys, Corrosion Science, 25 (1985) 331-339.
[139] I. Olefjord, B.-O. Elfstrom, The Composition of the Surface during Passivation of Stainless Steels, Corrosion, 38 (1982) 46-52.
[140] M. B.Rockel, The Effect of Molybdenum on the Corrosion Behavior of Iron-Chromium Alloys, Corrosion, 29 (1973) 393-396.
[141] I. OLEFJORD, B. BROX, Quantitive ESCA analysis of the passive state of an Fe-Cr alloy and an Fe-Cr-Mo alloy, Passivity of Metals and Semiconductors, (1983).
[142] E.A. Lizlovs, A.P. Bond, Anodic Polarization Behavior of 25% Chromium Ferritic Stainless Steels, Journal of The Electrochemical Society, 118 (1971).
[143] I. Olefjord, L. Wegrelius, Surface analysis of passive state, Corrosion Science, 31 (1990) 89-98.
[144] G.J. Barnes, A.W. Aldag, R.C. Jerner, Surface Concentration of Molybdenum in Types 316 and 304 Stainless Steel by Auger Electron Spectroscopy, Journal of The Electrochemical Society, 119 (1972).
[145] H. Ogawa, H. Omata, I. Itoh, H. Okada, Auger Electron Spectroscopic and Electrochemical Analysis of the Effect of Alloying Elements on the Passivation Behavior of Stainless Steels, Corrosion, 34 (1978) 52-60.
[146] J.R. Cahoon, R. Bandy, Auger Electron Spectroscopic Studies on Oxide Films of Some Austenitic Stainless Steels, Corrosion, 38 (1982) 299-305.
[147] M.d. Cunha Belo, B. Rondot, F. Pons, J. Le Héricy, J. P. Langeron, Study by Auger Spectrometry and Cathodic Reduction of Passive Films Formed on Ferritic Stainless Steels, Journal of The Electrochemical Society, 124 (1977) 1317.
[148] N. Pessall, J.I. Nurminen, Development of Ferritic Stainless Steels for Use in Desalination Plants, Corrosion, 30 (1974) 381-392.
[149] R.J. Brigham, Temperature as a Crevice Corrosion Criterion, Corrosion, 30 (1974) 396-398.
[150] K. Ogle, S. Weber, Anodic Dissolution of 304 Stainless Steel Using Atomic Emission Spectroelectrochemistry, Journal of The Electrochemical Society, 147 (2000).

[151] K. Ogle, Atomic Emission Spectroelectrochemistry: Real-Time Rate Measurements of Dissolution, Corrosion, and Passivation, Corrosion, 75 (2019) 1398-1419.
[152] P. Zhou, J.W. Erning, K. Ogle, Interactions between elemental components during the dealloying of Cu-Zn alloys, Electrochimica Acta, 293 (2019) 290-298.
[153] P. Zhou, M.J. Hutchison, J.W. Erning, J.R. Scully, K. Ogle, An in situ kinetic study of brass dezincification and corrosion, Electrochimica Acta, 229 (2017) 141-154.
[154] P. Zhou, M.J. Hutchison, J.R. Scully, K. Ogle, The anodic dissolution of copper alloys: Pure copper in synthetic tap water, Electrochimica Acta, 191 (2016) 548-557.
[155] O. Gharbi, N. Birbilis, K. Ogle, Li reactivity during the surface pretreatment of Al-Li alloy AA2050-T3, Electrochimica Acta, 243 (2017) 207-219.
[156] O. Gharbi, N. Birbilis, K. Ogle, In-Situ Monitoring of Alloy Dissolution and Residual Film Formation during the Pretreatment of Al-Alloy AA2024-T3, Journal of The Electrochemical Society, 163 (2016) C240-C251.
[157] M. Mokaddem, P. Volovitch, K. Ogle, The anodic dissolution of zinc and zinc alloys in alkaline solution. I. Oxide formation on electrogalvanized steel, Electrochimica Acta, 55 (2010) 7867-7875.
[158] T.N. Vu, M. Mokaddem, P. Volovitch, K. Ogle, The anodic dissolution of zinc and zinc alloys in alkaline solution. II. Al and Zn partial dissolution from 5% Al–Zn coatings, Electrochimica Acta, 74 (2012) 130-138.
[159] S. Lebouil, J. Tardelli, E. Rocca, P. Volovitch, K. Ogle, Dealloying of Al2Cu, Al7Cu2Fe, and Al2CuMg intermetallic phases to form nanoparticulate copper films, Materials and Corrosion, 65 (2014) 416-424.
[160] M. Serdechnova, P. Volovitch, F. Brisset, K. Ogle, On the cathodic dissolution of Al and Al alloys, Electrochimica Acta, 124 (2014) 9-16.
[161] V. Shkirskiy, K. Ogle, A novel coupling of electrochemical impedance spectroscopy with atomic emission spectroelectrochemistry: Application to the open circuit dissolution of zinc, Electrochimica Acta, 168 (2015) 167-172.
[162] V. Shkirskiy, P. Keil, H. Hintze-Bruening, F. Leroux, P. Volovitch, K. Ogle, Observation of l-cysteine enhanced zinc dissolution during cathodic polarization and its consequences for corrosion rate measurements, Electrochimica Acta, 184 (2015) 203-213.
[163] V. Shkirskiy, P. Maciel, J. Deconinck, K. Ogle, On The Time Resolution of the Atomic Emission Spectroelectrochemistry Method, Journal of The Electrochemical Society, 163 (2015) C37-C44.
[164] S. Greenfield, I.L. Jones, C.T. Berry, High-pressure plasmas as spectroscopic emission sources, The Analyst, 89 (1964).
[165] R.H. Wendt, V.A. Fassel, Induction-Coupled Plasma Spectrometric Excitation Source, Analytical Chemistry, 37 (1965) 920-922.
[166] S.J. Hill, Inductively Coupled Plasma Spectrometry and its Applications, Blackwell Publishing Ltd, UK, 2007.
[167] G.L. Moore, Introduction to Inductively Coupled Plasma Atomic Emission Spectrometry, Elsevier Science Publishers B.V., U.S.A., 1989.
[168] V. Hernandis, J.L. Todoli, A. Canals, J.V. Sala, An experimental study of the behaviour of several elements in inductively coupled plasma mass spectrometry using the single-bore high-pressure pneumatic nebulizer, Spectrochimica Acta Part B: Atomic Spectroscopy, 50 (1995) 985-996.
[169] H. Liu, A. Montaser, Phase-Doppler Diagnostic Studies of Primary and Tertiary Aerosols Produced by a High-Efficiency Nebulizer, Analytical Chemistry, 66 (2002) 3233-3242.
[170] J.R. Dean, Practical Inductively Coupled Plasma Spectroscopy, John Wiley & Sons Ltd, England, 2005.
[171] J.-l. Todolí, J.-m. Mermet, Minimization of acid effects at low consumption rates in an axially viewed inductively coupled plasma atomic emission spectrometer by using micronebulizer-based sample introduction systems, J. Anal. At. Spectrom., 13 (1998) 727-734.
[172] H. Iams, B. Salzberg, The Secondary Emission Phototube, Proceedings of the IRE, 23 (1935) 55-64.
[173] X-Ray Photoelectron Spectroscopy, Nova Science Publishers, 2011.
[174] P.V.D. HEIDE, X-RAY PHOTOELECTRON SPECTROSCOPY An Introduction to Principles and Practices, John Wiley & Sons, 2012.
[175] J.T. Kloprogge, B.J. Wood, Handbook of Mineral Spectroscopy Volume 1: X-ray Photoelectron Spectra, Elsevier, 2020.
[176] P. Marcus, J.M. Grimal, The anodic dissolution and passivation of NiCrFe alloys studied by ESCA,

Corrosion Science, 33 (1992) 805-814.
[177] H.H. Huang, Effect of chemical composition on the corrosion behavior of Ni-Cr-Mo dental casting alloys, J Biomed Mater Res, 60 (2002) 458-465.
[178] K. Lutton, K. Gusieva, N. Ott, N. Birbilis, J.R. Scully, Understanding multi-element alloy passivation in acidic solutions using operando methods, Electrochemistry Communications, 80 (2017) 44-47.
[179] D. Hamm, K. Ogle, C.O.A. Olsson, S. Weber, D. Landolt, Passivation of Fe–Cr alloys studied with ICP-AES and EQCM, Corrosion Science, 44 (2002) 1443-1456.
[180] B. Laurent, N. Gruet, B. Gwinner, F. Miserque, M. Tabarant, K. Ogle, A Direct Measurement of the Activation Potential of Stainless Steels in Nitric Acid, Journal of The Electrochemical Society, 164 (2017) C481-C487.
[181] B. Laurent, N. Gruet, B. Gwinner, F. Miserque, K. Rousseau, K. Ogle, The kinetics of transpassive dissolution chemistry of stainless steels in nitric acid: The impact of Si, Electrochimica Acta, 258 (2017) 653-661.
[182] J.D. Henderson, X. Li, D.W. Shoesmith, J.J. Noël, K. Ogle, Molybdenum surface enrichment and release during transpassive dissolution of Ni-based alloys, Corrosion Science, 147 (2019) 32-40.
[183] K. Ogle, J. Baeyens, J. Swiatowska, P. Volovitch, Atomic emission spectroelectrochemistry applied to dealloying phenomena: I. The formation and dissolution of residual copper films on stainless steel, Electrochimica Acta, 54 (2009) 5163-5170.
[184] J. Vilche, A. Arvia, The Electrochemical Response of Nickel Electrodes in Aqueous Sulfuric Acid Solutions, Journal of The Electrochemical Society, 123 (1976) 1061-1063.
[185] P. Marcus, On some fundamental factors in the effect of alloying elements on passivation of alloys, Corrosion Science, 36 (1994) 2155-2158.
[186] I. Puigdomenech, Hydra/Medusa Chemical Equilibrium Database and Plotting Software, in, KTH Royal Institute of Technology (2004), 2009.
[187] J. Högström, W. Fredriksson, K. Edstrom, F. Björefors, L. Nyholm, C.-O.A. Olsson, Cation profiling of passive films on stainless steel formed in sulphuric and acetic acid by deconvolution of angle-resolved X-ray photoelectron spectra, Applied Surface Science, 284 (2013) 700-714.
[188] R.M. Carranza, M.A. Rodríguez, Crevice corrosion of nickel-based alloys considered as engineering barriers of geological repositories, npj Materials Degradation, 1 (2017).
[189] K. Lutton Cwalina, C.R. Demarest, A.Y. Gerard, J.R. Scully, Revisiting the effects of molybdenum and tungsten alloying on corrosion behavior of nickel-chromium alloys in aqueous corrosion, Current Opinion in Solid State and Materials Science, (2019).
[190] K. Gusieva, K.L. Cwalina, W.H. Blades, G. Ramalingam, J.H. Perepezko, P. Reinke, J.R. Scully, Repassivation Behavior of Individual Grain Facets on Dilute Ni–Cr and Ni–Cr–Mo Alloys in Acidified Chloride Solution, The Journal of Physical Chemistry C, 122 (2018) 19499-19513.
[191] N. Ebrahimi, M.C. Biesinger, D.W. Shoesmith, J.J. Noël, The influence of chromium and molybdenum on the repassivation of nickel-chromium-molybdenum alloys in saline solutions, Surface and Interface Analysis, 49 (2017) 1359-1365.
[192] B. Zhang, X.X. Wei, B. Wu, J. Wang, X.H. Shao, L.X. Yang, S.J. Zheng, Y.T. Zhou, Q.Q. Jin, E.E. Oguzie, X.L. Ma, Chloride attack on the passive film of duplex alloy, Corrosion Science, 154 (2019) 123-128.
[193] H. Habazaki, A. Kawashima, K. Asami, K. Hashimoto, The corrosion behavior of amorphous Fe-Cr-Mo-P-C and Fe-Cr-W-P-C alloys in 6 M HCl solution, Corrosion Science, 33 (1992) 225-236.
[194] M.C. Biesinger, B.P. Payne, L.W.M. Lau, A. Gerson, R.S.C. Smart, X-ray photoelectron spectroscopic chemical state quantification of mixed nickel metal, oxide and hydroxide systems, Surface and Interface Analysis, 41 (2009) 324-332.
[195] M.C. Biesinger, C. Brown, J.R. Mycroft, R.D. Davidson, N.S. McIntyre, X-ray photoelectron spectroscopy studies of chromium compounds, Surface and Interface Analysis, 36 (2004) 1550-1563.
[196] P.A. Spevack, N.S. McIntyre, Thermal reduction of molybdenum trioxide, The Journal of Physical Chemistry, 96 (1992) 9029-9035.
[197] A. Mishra, D. Shoesmith, P. Manning, Materials Selection for Use in Concentrated Hydrochloric Acid, Corrosion, 73 (2016) 68-76.
[198] R. Kirchheim, Kinetics of Film Formation on Fe-Cr Alloys, in: P. Marcus, B. Baroux, M. Keddam (Eds.) European Symposium on Modifications of Passive Films, The institute of Materials, Paris, France, 1993, pp. 102-107.
[199] P. Jakupi, F. Wang, J.J. Noël, D.W. Shoesmith, Corrosion product analysis on crevice corroded

Alloy-22 specimens, Corrosion Science, 53 (2011) 1670-1679.
[200] E.Y. Nevskaya, I.G. Gorichev, A.D. Izotov, B.E. Zaitsev, K.M. Al'dieva, A.M. Kutepov, Kinetics of Molybdenum(VI) Oxide Dissolution in Sulfuric Acid Solutions, Theoretical Foundations of Chemical Engineering, 38 (2004) 316-321.
[201] J.D. Henderson, N. Ebrahimi, X. Li, K. Ogle, J.J. Noel, The Complementarity of Cr and Mo in Reinforcing Oxide Protectiveness on Ni-Cr-Mo Alloys, in: 236th ECS Meeting (October 13-17, 2019), ECS, 2019.
[202] A.J. Samin, C.D. Taylor, First-principles investigation of surface properties and adsorption of oxygen on Ni-22Cr and the role of molybdenum, Corrosion Science, 134 (2018) 103-111.
[203] X.-x. Yu, A. Gulec, C.M. Andolina, E.J. Zeitchick, K. Gusieva, J.C. Yang, J.R. Scully, J.H. Perepezko, L.D. Marks, In Situ Observations of Early Stage Oxidation of Ni-Cr and Ni-Cr-Mo Alloys, Corrosion, 74 (2018) 939-946.
[204] X.X. Yu, A. Gulec, Q. Sherman, K.L. Cwalina, J.R. Scully, J.H. Perepezko, P.W. Voorhees, L.D. Marks, Nonequilibrium Solute Capture in Passivating Oxide Films, Phys Rev Lett, 121 (2018) 145701.
[205] M. Urquidi, Solute-Vacancy Interaction Model and the Effect of Minor Alloying Elements on the Initiation of Pitting Corrosion, Journal of The Electrochemical Society, 132 (1985).
[206] J.R. Davis, Nickel, cobalt, and their alloys, ASM international, 2000.
[207] X. Wu, S. Voyshnis, A. Seyeux, Y. Chumlyakov, P. Marcus, ToF-SIMS study of oxide films thermally grown on nickel-base alloys, Corrosion Science, 141 (2018) 175-181.
[208] A. Mishra, D.W. Shoesmith, P. Manning, Materials Selection for Use in Concentrated Hydrochloric Acid, Corrosion, 73 (2017) 68-76.
[209] J.W. Oldfield, W.H. Sutton, Crevice Corrosion of Stainless Steels I. A Mathematical Model, British Corrosion Journal, 13 (1978) 13-22.
[210] J.W. Oldfield, W.H. Sutton, Crevice Corrosion of Stainless Steels II. Experimental studies, British Corrosion Journal, 13 (1978) 104-111.
[211] P. Marcus, Corrosion mechanisms in theory and practice, CRC press, 2011.
[212] V. Shkirskiy, P. Maciel, J. Deconinck, K. Ogle, On The Time Resolution of the Atomic Emission Spectroelectrochemistry Method, Journal of The Electrochemical Society, 163 (2016) C37-C44.
[213] S.Z. Natalia, C.G. Mabel, B.R. Raúl, E.A. Alicia, M.C. Ricardo, Anodic Behavior of Alloy 22 in Bicarbonate Media: Effect of Alloying, Procedia Materials Science, 8 (2015) 510-518.
[214] N.S. Zadorozne, C.M. Giordano, R.B. Rebak, A.E. Ares, R.M. Carranza, Anodic Behavior of Alloy 22 in Bicarbonate Media Effect of Alloying, Procedia Materials Science, 8 (2015) 510-518.
[215] D.D. Macdonald, A. Sun, N. Priyantha, P. Jayaweera, An electrochemical impedance study of Alloy-22 in NaCl brine at elevated temperature: II. Reaction mechanism analysis, Journal of Electroanalytical Chemistry, 572 (2004) 421-431.
[216] M. Pourbaix, Atlas of electrochemical equilibria in aqueous solution, NACE, 307 (1974).
[217] J. Velázquez, J. Van Der Weide, E. Hernández, H.H. Hernández, Statistical modelling of pitting corrosion: extrapolation of the maximum pit depth-growth, Int. J. Electrochem. Sci, 9 (2014) 4129-4143.
[218] C.-M. Lin, H.-L. Tsai, Evolution of microstructure, hardness, and corrosion properties of high-entropy Al0.5CoCrFeNi alloy, Intermetallics, 19 (2011) 288-294.
[219] J.D. Henderson, A. Seyeux, S. Zanna, M.C. Biesinger, D.W. Shoesmith, J.J. Noël, P. Marcus, Investigating the transport mechanisms governing the oxidation of Hastelloy BC-1 by in situ ToF-SIMS, Corrosion Science, 159 (2019).
[220] Z. Wang, F. Di-Franco, A. Seyeux, S. Zanna, V. Maurice, P. Marcus, Passivation-Induced Physicochemical Alterations of the Native Surface Oxide Film on 316L Austenitic Stainless Steel, Journal of The Electrochemical Society, 166 (2019) C3376-C3388.
[221] N. Ebrahimi, J.J. Noël, M.A. Rodríguez, D.W. Shoesmith, The self-sustaining propagation of crevice corrosion on the hybrid BC1 Ni–Cr–Mo alloy in hot saline solutions, Corrosion Science, 105 (2016) 58-67.
[222] R.W. Revie, Uhlig's corrosion handbook, John Wiley & Sons, 2011.
[223] U. Heubner, Nickel alloys, CRC Press, 2000.
[224] X. Shan, J.H. Payer, Characterization of the Corrosion Products of Crevice Corroded Alloy 22, Journal of The Electochemical Society, 156 (2009) C313-C321.
[225] E. Gardin, S. Zanna, A. Seyeux, A. Allion-Maurer, P. Marcus, Comparative study of the surface oxide films on lean duplex and corresponding single phase stainless steels by XPS and ToF-SIMS, Corrosion Science, 143 (2018) 403-413.
[226] D.C. Agarwal, J. Klower, Nickel base alloys: Corrosion challenges in the new millennium, in:

CORROSION 2001, NACE, 2001.
[227] H.S. Klapper, N.S. Zadorozne, R.B. Rebak, Localized Corrosion Characteristics of Nickel Alloys: A Review, Acta Metallurgica Sinica (English Letters), 30 (2017) 296-305.
[228] P. Fauvet, Nuclear corrosion science and engineering, 679, in, Woodhead Publishing, Cambridge, 2012.
[229] M. Lindgren, E. Huttunen-Saarivirta, H. Peltola, J. Romu, T. Sarikka, H. Hänninen, P. Pohjanne, Crevice Corrosion of Stainless Steels 904L, 2205, and 2507 in High-Temperature Sulfuric Acid Solution Containing Chlorides: Influence of Metal Cations, Corrosion, 74 (2018) 225-240.
[230] M. Pourbaix, Atlas of electrochemical equilibria in aqueous solutions, Pergamon Press, Oxford; New York, 1966.
[231] C.F. Baes, Jr., R.E. Mesmer, The hydrolysis of cations, Wiley Interscience Division, New York, 1976.
[232] B. Yang, J. Li, X. Gong, Y. Nie, Y. Li, Effects of Cu addition on the corrosion behavior of NiCoCrMo alloys in neutral chloride solution, RSC Advances, 7 (2017) 40779-40790.
[233] D.B. Miracle, O.N. Senkov, A critical review of high entropy alloys and related concepts, Acta Materialia, 122 (2017) 448-511.
[234] M.-H. Tsai, J.-W. Yeh, High-Entropy Alloys: A Critical Review, Materials Research Letters, 2 (2014) 107-123.
[235] Y. Qiu, M.A. Gibson, H.L. Fraser, N. Birbilis, Corrosion characteristics of high entropy alloys, Materials Science and Technology, 31 (2015) 1235-1243.
[236] Y. Qiu, S. Thomas, M.A. Gibson, H.L. Fraser, N. Birbilis, Corrosion of high entropy alloys, npj Materials Degradation, 1 (2017).
[237] E.J. Amis, Reaching beyond discovery, Nat Mater, 3 (2004) 83-85.
[238] C.D. Taylor, P. Lu, J. Saal, G.S. Frankel, J.R. Scully, Integrated computational materials engineering of corrosion resistant alloys, npj Materials Degradation, 2 (2018).
[239] J. Han, V. Vivier, K. Ogle, Refining anodic and cathodic dissolution mechanisms: combined AESEC-EIS applied to Al-Zn pure phase in alkaline solution, npj Materials Degradation, 4 (2020).
[240] S. Choudhary, Y. Qiu, S. Thomas, N. Birbilis, Element-resolved electrochemical analysis of transpassive dissolution and repassivation behavior of the multi-principle element alloy AlTiVCr, Electrochimica Acta, 362 (2020).
[241] N. Birbilis, Corrosion of emerging materials, in: 71st Annual Meeting of the International Society of Electrochemistry, Belgrade, 2020.
[242] M.J. Duarte, J. Klemm, S.O. Klemm, K.J. Mayrhofer, M. Stratmann, S. Borodin, A.H. Romero, M. Madinehei, D. Crespo, J. Serrano, S.S. Gerstl, P.P. Choi, D. Raabe, F.U. Renner, Element-resolved corrosion analysis of stainless-type glass-forming steels, Science, 341 (2013) 372-376.
[243] Y. Yan, P. Zhou, O. Gharbi, Z. Zeng, X. Chen, P. Volovitch, K. Ogle, N. Birbilis, Investigating ion release using inline ICP during in situ scratch testing of an Mg-Li(-Al-Y-Zr) alloy, Electrochemistry Communications, 99 (2019) 46-50.
[244] E.P. George, D. Raabe, R.O. Ritchie, High-entropy alloys, Nature Reviews Materials, 4 (2019) 515-534.
[245] A. Rodriguez, J.H. Tylczak, M. Ziomek-Moroz, Corrosion Behavior of CoCrFeMnNi High-Entropy Alloys (HEAs) Under Aqueous Acidic Conditions, ECS Transactions, 77 (2017) 741-752.
[246] A. Nishimoto, T. Fukube, T. Maruyama, Microstructural, mechanical, and corrosion properties of plasma-nitrided CoCrFeMnNi high-entropy alloys, Surface and Coatings Technology, 376 (2019) 52-58.
[247] Z. Han, W. Ren, J. Yang, A. Tian, Y. Du, G. Liu, R. Wei, G. Zhang, Y. Chen, The corrosion behavior of ultra-fine grained CoNiFeCrMn high-entropy alloys, Journal of Alloys and Compounds, 816 (2020).
[248] H. Baba, T. Kodama, Y. Katada, Role of nitrogen on the corrosion behavior of austenitic stainless steels, Corrosion Science, 44 (2002) 2393-2407.
[249] H. Feng, H. Li, X. Wu, Z. Jiang, S. Zhao, T. Zhang, D. Xu, S. Zhang, H. Zhu, B. Zhang, M. Yang, Effect of nitrogen on corrosion behaviour of a novel high nitrogen medium-entropy alloy CrCoNiN manufactured by pressurized metallurgy, Journal of Materials Science & Technology, 34 (2018) 1781-1790.

Curriculum Vitae

Xuejie LI

(33) 661960281 | xuejieli.buaa@gmail.com | 10 Rue Madeleine Brès, 75013, Paris, France

EDUCATION

École nationale supérieure de chimie de Paris, Paris, France

Doctor of Philosophy, Analytical Chemistry, 09/2017 – 11/2020

Beihang University, Beijing, P. R. China

Master of Science, Materials Science and Engineering, 09/2014 – 06/2017

Yantai University, Yantai, Shandong Province, P. R. China

Bachelor of Science, Materials Science and Engineering, 09/2009 –06/2013

RESEARCH EXPERIENCE

In-situ investigation of elemental behavior during passivation of Ni alloys

Interfaces, Electrochemistry & Energy (I2E), École nationale supérieure de chimie de Paris, PSL University

- Employing atomic emission spectroelectrochemistry (AESEC) to investigate the release of species into solution under different electrochemical methods.

Study of ion release of stainless-steel alloys as bipolar plates at fuel cell (in associate with Sandvik)

Interfaces, Electrochemistry & Energy (I2E), École nationale supérieure de chimie de Paris, PSL University

- AESEC was used to monitor the ion release of 304L, 316L and 904L stainless-steel during local or global hydrogen starvation.

Surface modification of $Zr_{56}Al_{16}Co_{28}$ biomedical bulk metallic glass

Bulk Metallic Glass (BMG) Lab, Beihang University

- Adopting anodic oxidation method to modify the surface of biomedical metallic glass to obtain better biocompatibility.

PUBLICATION

(*****indicates equal contribution)

1. X. Li, H. Xu, Y. Jin, T. Zhang, Fabrication of highly ordered nanotube layer on Zr-based bulk metallic glass for biomedical uses, Materials Letters, 200 (2017) 63-66.
2. J. D. Henderson*, X. Li*, D.W. Shoesmith, J.J. Noël, K. Ogle, Molybdenum surface enrichment and release during transpassive dissolution of Ni-based alloys, Corrosion Science, 147 (2019) 32-40.
3. X. Li, K. Ogle, The Passivation of Ni-Cr-Mo Alloys: Time Resolved Enrichment and Dissolution of Cr and Mo during Passive-Active Cycles, Journal of The Electrochemical Society, 166 (2019) C3179-C3185.
4. P. Zhou, W. Cai, Y. Yang, X. Li, T. Zhang, F. Wang, Effect of ultrasonic agitation during the activation process on the microstructure and corrosion resistance of electroless Ni-W-P coatings on AZ91D magnesium alloy, Surface and Coatings Technology, 374 (2019) 103-115.
5. X. Li, P. Zhou, K. Ogle, S. Proch, M. Paliwal, A. Jansson, J. Westlinder, Transient stainless-steel dissolution and its consequences on ex-situ bipolar plate testing procedures, International Journal of Hydrogen Energy, 45 (2020) 984-995.
6. Y.M. Yan, A. Maltseva, P. Zhou, X.J. Li, Z.R. Zeng, O. Gharbi, K. Ogle, M. La Haye, M. Vaudescal, M. Esmaily, N. Birbilis, P. Volovitch, On the in-situ aqueous stability of an Mg-Li-(Al-Y-Zr) alloy: Role of Li, Corrosion Science, 164 (2020).
7. X. Li, J. Han, P. Lu, J.E. Saal, G.B. Olson, G.S. Frankel, J.R. Scully, K. Ogle, Communication—Dissolution and Passivation of a Ni-Cr-Fe-Ru-Mo-W High Entropy Alloy by Elementally Resolved Electrochemistry, Journal of The Electrochemical Society, 167 (2020).
8. X. Li*, J. D. Henderson*, F. P. Filice, D. Zagidulin, M. C. Biesinger, F. Sun, B. Qian, D. W. Shoesmith, J. J. Noël, K. Ogle, The contribution of Cr and Mo to the passivation of Ni22Cr and Ni22Cr10Mo alloys in sulfuric acid, Corrosion Science, in press.

CONFERENCE

- **Poster presentation**

1. X. Li, H. Xu, Y Jin, T Zhang, Fabrication of self-organized nanotube coating on $Zr_{56}Al_{16}Co_{28}$ bulk metallic glass surface, The International Union of Materials Research Societies (IUMRS) International Conference, 21-23 October 2016, Qingdao, China.

- **Oral Presentation**

2. X. Li, J. D. Henderson, D. W. Shoesmith, J. J. Noël, K. Ogle, Surface enrichment of Mo during transpassive dissolution of Ni-alloys, European Corrosion Congress (Eurocorr), 9-13 September 2019, Seville, Spain.

RÉSUMÉ

Dans cette thèse, le rôle des éléments d'alliage sur le comportement de passivation des alliages synthétiques Ni-Cr, Ni-Cr-Mo, des alliages Ni commerciaux et d'un nouveau HEA Ni-Cr-Fe-Ru-Mo-W a été étudié. Les courants élémentaires ont été décomposés à partir de la courbe de polarisation, qui donne le comportement élémentaire pendant le domaine de transition actif-passif, le domaine passif et le domaine transpassif pour ces alliages à base de Ni. La passivation spontanée et la passivation anodique des alliages de Ni ont été étudiées. Mo joue un rôle critique dans la passivation spontanée. Il a été constaté que le Mo s'enrichissait en Mo (IV) à la surface pendant la passivation spontanée et s'oxydait en Mo soluble (VI) pendant la passivation anodique. La passivation spontanée des alliages Ni commerciaux dans HCl a été décidée par la teneur en Mo. La passivation anodique suivante a été influencée par la passivation spontanée. En solution neutre de NaCl, Mo enrichi pendant le domaine transpassif et dissous pendant la repassivation. Il a été conclu que la présence de Mo dans le film passif était étroitement associée à l'histoire de l'alliage et largement influencée par le potentiel et le pH. Le nouveau Ni-Cr-Fe-Ru-Mo-W HEA a présenté une excellente résistance à la corrosion dans la solution H_2SO_4 indiquée par la passivation spontanée, le faible courant passif dans la courbe de polarisation et l'absence de dissolution élémentaire détectable pendant le pic actif. La passivation spontanée du HEA était différente de celle des alliages Ni-Cr-Mo, qui ne se produisait pas immédiatement après l'élimination cathodique de l'oxyde de surface.

MOTS CLÉS

in situ, dissolution, passivation, alliages à haute entropie, alliages à Ni-Cr-Mo

ABSTRACT

In this dissertation, the role of alloying elements on the passivation behavior of synthetic Ni-Cr, Ni-Cr-Mo alloys, commercial Ni alloys and a novel Ni-Cr-Fe-Ru-Mo-W HEA was investigated. Elemental currents were decomposed from the polarization curve which gives new insights into the active-passive transition for these Ni-based alloys. Spontaneous passivation and anodic passivation of Ni alloys were studied. Mo plays critical role in the spontaneous passivation. It was found that Mo enriched as Mo(IV) on surface during spontaneous passivation and oxidized to soluble Mo(VI) during anodic passivation. Spontaneous passivation of the commercial Ni alloys in HCl was decided by the Mo content. The following anodic passivation was influenced by the spontaneous passivation. In neutral NaCl solution, Mo enriched during transpassive domain and dissolved during the subsequent repassivation. It was concluded that the presence of Mo in the passive film was closely associated with the history of the alloy, and largely influenced by potential and pH. The novel Ni-Cr-Fe-Ru-Mo-W HEA exhibited excellent corrosion resistance in H_2SO_4 solution indicated by spontaneous passivation, the low passive current in the polarization curve and the absence of detectable elemental dissolution during the active peak. Spontaneous passivation of the HEA was different from that observed for Ni-Cr-Mo alloys, which did not occur immediately after the surface oxide was cathodically removed.

KEYWORDS

in situ, dissolution, passivation, high entropy alloys, Ni-Cr-Mo alloys